Organic trace analysis in the atmosphere using HPLC-HRMS: Determination of retention coefficients of secondary organic aerosol (SOA) constituents and molecular characterization of SOA in different environments

Dissertation

zur Erlangung des Grades

„Doktor der Naturwissenschaften“

im Promotionsfach Chemie

am Fachbereich Chemie, Pharmazie,

Geographie und Geowissenschaften

der Johannes Gutenberg-Universität Mainz

Vorgelegt von

Christine Borchers

Geboren in Ludwigshafen am Rhein

Mainz, 2025

Dekanin: Prof. Dr. Eva Rentschler

1. Gutachter:

2. Gutachter:

Tag der mündlichen Prüfung: 27.03.2025

D77 Dissertation der Johannes Gutenberg-Universität Mainz

I hereby declare that I wrote the dissertation submitted without any unauthorized external assistance and used only sources acknowledged in the work. All textual passages which are appropriated verbatim or paraphrased from published and unpublished texts as well as all information obtained from oral sources are duly indicated and listed in accordance with bibliographical rules. I used DeepL Translate and DeepL Write for grammatical corrections and better readability. In carrying out this research, I complied with the rules of standard scientific practice as formulated in the statutes of Johannes Gutenberg University Mainz to insure standard scientific practice.

Mainz, January 2025

"Shoot for the moon. Even if you miss, you'll land among the stars."

Norman Vincent Peale

Zusammenfassung

Organische Aerosole (OA) spielen eine wichtige Rolle in der Atmosphäre. Sie werden aus verschiedenen natürlichen und anthropogenen Quellen in die Atmosphäre eingetragen und können dort das Klima beeinflussen, indem sie Strahlung streuen oder zur Wolkenbildung beitragen. Vor allem im Submikrometerbereich trägt die organische Fraktion einen großen Teil zur Partikelmasse der Atmosphäre bei. In Gebieten mit konvektiven Wolkensystemen wurden in Studien eine große Anzahl kleiner Partikel in der oberen Troposphäre gefunden, was auf die Bildung neuer Partikel (*new particle formation*, NPF) durch homogene Nukleation und anschließendes Partikelwachstum zurückzuführen ist. Die Transportmechanismen organischer Verbindungen in diese Regionen sind noch nicht vollständig geklärt, aber von großer Bedeutung.

Der erste Teil dieser Arbeit beschäftigt sich mit dem möglichen Transport von semivolatilen organischen Verbindungen (SVOCs) in höhere Troposhärenschichten durch hochreichende Konvektionswolken, wo sie zur NPF beitragen können. Die zuvor in Wassertropfen gelösten SVOCs werden durch die Konvektionswolke in Höhen transportiert, in denen Mischphasenwolken und damit sowohl unterkühlte Wassertropfen als auch gefrorene Hydrometeore vorhanden sind. Durch die Kollision von unterkühlten Wolkentropfen mit z.B. Graupel kommt es zum Gefrieren der Lösung. Während dieses Gefrierprozesses können die im Wolkentropfen gelösten Stoffe entweder im Eis verbleiben oder in die Gasphase übergehen. Dieser Vorgang wird durch den Retentionskoeffizienten beschrieben, der Werte zwischen 0 und 1 annehmen kann, wobei 1 für einen vollständigen Verbleib im Eis steht. Wenn die Stoffe im Eis verbleiben, können sie durch Niederschlag effektiv aus der Atmosphäre entfernt werden. Ein Übergang der SVOC in die Gasphase kann dagegen zu einer vertikalen Neuverteilung, und damit zu einem Anstieg der Konzentration in der oberen Troposphäre, dieser Verbindungen durch konvektive Wolkenprozesse führen. Um das Retentionsverhalten von drei α-Pinenoxidationsprodukten (*cis*-Pinsäure, *cis*-Pinonsäure, und (−)-Pinandiol), sowie von vier nitroaromatischen Verbindungen (4-Nitrophenol, 4-Nitrocatechol, 2-Nitrobenzoesäure, und 2-Nitrophenol) zu untersuchen, wurden Experimente im vertikalen Windkanal der Johannes Gutenberg-Universität in Mainz durchgeführt. Dabei wurden Trocken- und Nasswachstumsbedingungen (Temperatur von -12 bis -3 °C) bei verschiedenen pH-Werten (pH 4,0 und 5,6) der Wassertropfen untersucht. Nur der Retentionskoeffizient von 2-Nitrophenol zeigte eine Abhängigkeit von Temperatur und pH-Wert.

Im zweiten Teil dieser Arbeit wurde ein miniaturisierter Aerosolpartikelsammler für den Einsatz mit Drohnen entwickelt. Dieser dient dazu, Erkenntnisse über Quellen und Senken sowie die Bedeutung von Mischungs- und Alterungsprozessen für OA zu gewinnen, indem vertikale Konzentrationsprofile organischer Aerosole ermittelt werden. Solche Messungen werden gegenwärtig an speziellen Messtürmen, wie zum Beispiel dem 325 m hohen ATTO-Turm im brasilianischen Regenwald, durchgeführt. Der Einsatz von Drohnen ermöglicht eine

kostengünstige Probenahme in verschiedenen Höhen und in Regionen, die sonst nur schwer zugänglich wären. Das System wurde im Rahmen der Kampagne BISTUM23 erfolgreich getestet, wobei Aerosolproben in einer Höhe von bis zu 500 m über Grund gesammelt wurden. Die Proben wurden mittels hochauflösender Flüssigchromatographie-Massenspektrometrie (HPLC-HRMS) analysiert. Dadurch konnten Höhenprofile bekannter biogener und anthropogener Markerverbindungen erstellt werden. Die biogenen Verbindungen zeigen einen Konzentrationsanstieg zwischen 1,5 m und 120 m, gefolgt von einer Abnahme bei 500 m. Generell kommt es zu einem Anstieg der Konzentrationen im Tagesverlauf. Dies steht in guter Übereinstimmung mit der ebenfalls durchgeführten Non-Target-Analyse, die eine Zunahme höher oxidierter Verbindungen im Tagesverlauf zeigt.

Der letzte Teil dieser Arbeit befasst sich mit maritimen Aerosolen. Obwohl die Ozeane mehr als 70% der Erdoberfläche bedecken, ist der Einfluss maritimer VOC und der daraus resultierenden SOA noch nicht vollständig geklärt. Um ein besseres Verständnis über die Rolle der Ozeane bei der Entstehung von SOA zu erlangen, wurden Proben mittels HPLC-HRMS untersucht, die auf dem Forschungssegelschiff *Eugen Seibold* in den Jahren 2020 und 2021 zwischen dem nördlichen Polarkreis und dem Äquator gesammelt wurden. Ziel war es, neue maritime Markerverbindungen zu finden und ein besseres Verständnis maritimer Aerosolquellen zu erlangen. Zu diesem Zweck wurden die Proben mit einer Non-Target HPLC-HRMS-Analyse untersucht und die Ergebnisse in einer Serie von Van-Krevelen-Diagrammen dargestellt. Dabei wurde eine Gruppe von Verbindungen mit den Summenformeln $C_{9\text{-}12}H_{22\text{-}32}N_{6\text{-}12}O_{1\text{-}5}S$ als mögliche neue maritime Markerverbindungen identifiziert. Darüber hinaus wurde in allen Proben eine organische Iodverbindung ($C_9H_7IO_3$) nachgewiesen, die ebenfalls eine Verbindung maritimen Ursprungs sein könnte.

Abstract

Organic aerosols (OA) play an important role in the atmosphere. They are introduced into the atmosphere from various natural and anthropogenic sources and can influence the climate by scattering radiation or contributing to cloud formation. The organic fraction contributes a large fraction of the atmospheric particle mass, especially in the submicron range. Studies show a large number of small particles in the upper troposphere in areas with convective cloud systems, which can be attributed to new particle formation (NPF) by homogeneous nucleation and subsequent particle growth. The transport mechanisms of organic compounds into these regions are not fully understood but are of high interest.

The first part of this thesis focuses on the possible transport of semi-volatile organic compounds (SVOCs) by deep convective clouds to high altitudes in the troposphere, where they can contribute to NPF. The SVOCs, previously dissolved in water droplets, are transported by the convective cloud to altitudes where mixed-phase clouds, and thus both supercooled water droplets and frozen hydrometeors, are present. The collision of supercooled cloud droplets with e.g. graupel results in the freezing of the solution. During the freezing process, the substances dissolved in the cloud droplets can either remain in the ice or be transferred to the gas phase. This process is described by the retention coefficient, which can have values between 0 and 1, where 1 represents complete retention in the ice. If the substances remain in the ice, they can be effectively removed from the atmosphere by precipitation. A transition of SVOCs to the gas phase, on the other hand, can lead to a vertical redistribution and thus to an increase in the concentration of these compounds in the upper troposphere due to convective cloud processes. To investigate the retention behavior of three α-pinene oxidation products (*cis*-pinic acid, *cis*-pinonic acid, and (−)-pinanediol) and four nitroaromatic compounds (4-nitrophenol, 4-nitrocatechol, 2-nitrobenzoic acid, and 2-nitrophenol), experiments were performed in the vertical wind tunnel of the Johannes Gutenberg-University in Mainz, Germany. Dry and wet growth conditions (temperature from −12 to −3 °C) at different pH values (pH 4.0 and 5.6) of the water droplets were investigated. Only the retention coefficient of 2-nitrophenol showed a dependence on temperature and pH.

In the second part of this work, a miniaturized aerosol particle collector for use with drones was developed. This system was used to determine the vertical concentration profiles of organic aerosols in order to gain insight into sources and sinks as well as the importance of mixing and aging processes for OA. Such measurements are currently carried out on high towers, such as the 325 m ATTO tower in the Brazilian rainforest. The use of drones allows cost-effective sampling at different heights and in regions that would otherwise be difficult to access. The system was successfully tested during the BISTUM23 campaign, where aerosol samples were collected at up to 500 m above ground. The samples were analyzed by HPLC-HRMS. This allowed the generation of altitude profiles of known biogenic and anthropogenic marker compounds. The biogenic compounds show an increase in concentration between 1.5 m and 120 m, followed by a decrease at 500 m. In general, there is an increase in

concentrations during the course of the day. This is in good agreement with the non-target analysis, which also showed an increase in higher oxidized compounds over the course of the day.

The last part of this thesis deals with marine aerosol particles. Although the oceans cover more than 70% of the Earth's surface, the influence of marine VOCs and the resulting SOA is not fully understood. To gain a better understanding of the role of the oceans in the formation of SOA, samples collected on the research sailing vessel *Eugen Seibold* between the northern polar circle and the equator in 2020 and 2021 were analyzed by HPLC-HRMS. The aim was to find new marine marker compounds and to gain a better understanding of marine aerosol sources. For this purpose, the samples were analyzed by non-target HPLC-HRMS and the results were presented in a series of Van Krevelen diagrams. A group of compounds with the molecular formulas $C_{9\text{-}12}H_{22\text{-}32}N_{6\text{-}12}O_{1\text{-}5}S$ were identified as possible new marine marker compounds. In addition, an organic iodine compound ($C_9H_7IO_3$) was detected in all samples, which could also be a compound of marine origin.

Table of Contents

Abbreviations

ACN	acetonitrile
APCI	atmospheric pressure chemical ionization
CCN	cloud condensation nuclei
CI^*	excited Criegee intermediate
DMS	dimethyl sulfide
EI	electron ionization
ELVOC	extremely low volatility organic compound
ESI	electrospray ionization
HOM	highly oxygenated organic molecule
HPLC	high performance liquid chromatography
HRMS	high-resolution mass spectrometry
IEPOX	isoprene epoxy diol
INP	ice nucleation particle
IS	internal standard
IVOC	intermediate-volatility organic compound
LC	liquid chromatography
LN	liquid nitrogen
LVOC	low-volatility organic compound
LWC	liquid water content
MBTCA	3-methyl-1,2,3-butanetricarboxylic acid
MeOH	methanol
MT	monoterpene
MS	mass spectrometry
MSA	methanesulfonic acid
MSIA	methanesulfinic acid
NPF	new particle formation
OA	organic aerosol
POA	primary organic aerosols
SA	sulfuric acid

SCI	stabilized Criegee intermediate
SOA	secondary organic aerosols
SVOC	semi-volatile organic compound
UAV	uncrewed aerial vehicles
UHPLC	ultra high performance liquid chromatography
ULVOC	ultralow-volatility organic compound
VOC	volatile organic compound

1. Introduction

1.1 Atmospheric aerosols

An aerosol is defined as a suspension of liquid or solid particles in a gas. These particles have a diameter ranging from a few nanometers to around a hundred micrometers. Aerosols in the atmosphere can have an impact on Earth's radiative budget and the climate. Aerosols have the potential to exert both a warming and a cooling effect on global warming (Seinfeld and Pandis, 2006; Pöschl, 2005). Observations and model calculations indicate that an increase in global temperature resulting from the rise in greenhouse gases, including CO_2, CH_4, N_2O, and halocarbons, may be reduced by an increase in aerosol particle concentration. Aerosols are more challenging to characterize than trace gases due to their complex chemical composition and extensive size range (van Dingenen et al., 2004).

The impact of aerosols on climate can be classified into two categories: direct and indirect effects. Direct effects include the scattering and absorption of radiation. The indirect effects of aerosols can be observed in their influence on cloud formation and precipitation, acting as both cloud condensation nuclei (CCN) and ice nucleation particles (INP) (Seinfeld and Pandis, 2006; Pöschl, 2005). The lifetime and properties of clouds can be influenced by a high number of aerosol particles. As long as the liquid water content remains constant, a higher number of aerosol particles leads to a greater potential for CCN, resulting in a greater number of smaller cloud droplets. This phenomenon, described as the Twomey effect, results in an increased reflection of radiation. The greater number of smaller cloud droplets also lead to a lower precipitation efficiency, which means that the lifetime of the clouds is longer (Lohmann and Feichter, 2005).

Organic aerosol (OA) particles are responsible for a large fraction (20-90%) of the submicron particle mass in the lower troposphere (Jimenez et al., 2009). They are classified as primary or secondary particles, depending on their origin (Iavorivska et al., 2016). Figure 1.1 shows potential sources and sinks for aerosol particles. Primary organic aerosols (POA) are emitted directly, for example from volcanoes, sea spray, fossil fuel combustion, or biomass burning. Particles of dust, pollen, plant fragments, and sea salt often exceed one micrometer in size. In contrast, combustion-related particles may range in size from a few nanometers to one micrometer. Secondary organic aerosols (SOA) are formed by the oxidation of previously emitted volatile organic compounds (VOCs) followed by homogeneous nucleation, i.e., gas-to-particle conversion, in the atmosphere (Kroll and Seinfeld, 2008). Following the initial formation, there is a potential for subsequent growth through condensation and self-coagulation, reaching a size capable of serving as cloud condensation nuclei. In order to act as a CCN, the particle size must be greater than 50 to 140 nm, depending on the supersaturation. The SOA particles typically remain in a size range of below one micrometer (Reddington et al., 2011; Seinfeld and Pandis, 2006; Kerminen et al., 2005).

In-cloud reactions are efficient in cloud droplets. Upon evaporation of the cloud droplets, the modified aerosol particles are reintroduced into the atmosphere. However, precipitation can also occur, leading to what is known as wet deposition. This process not only removes CCN particles but also particles that are picked up while the drops are falling from the cloud to the Earth's surface. This represents the largest sink for atmospheric aerosol particles. Another mechanism is dry deposition, in which aerosols are removed from the atmosphere by convective transport, diffusion, and adhesion to the Earth's surface (Pöschl, 2005). In addition to classifying OA as primary or secondary, OA can also be classified according to their sources as biogenic, anthropogenic, or caused by biomass burning (Gouw and Jimenez, 2009).

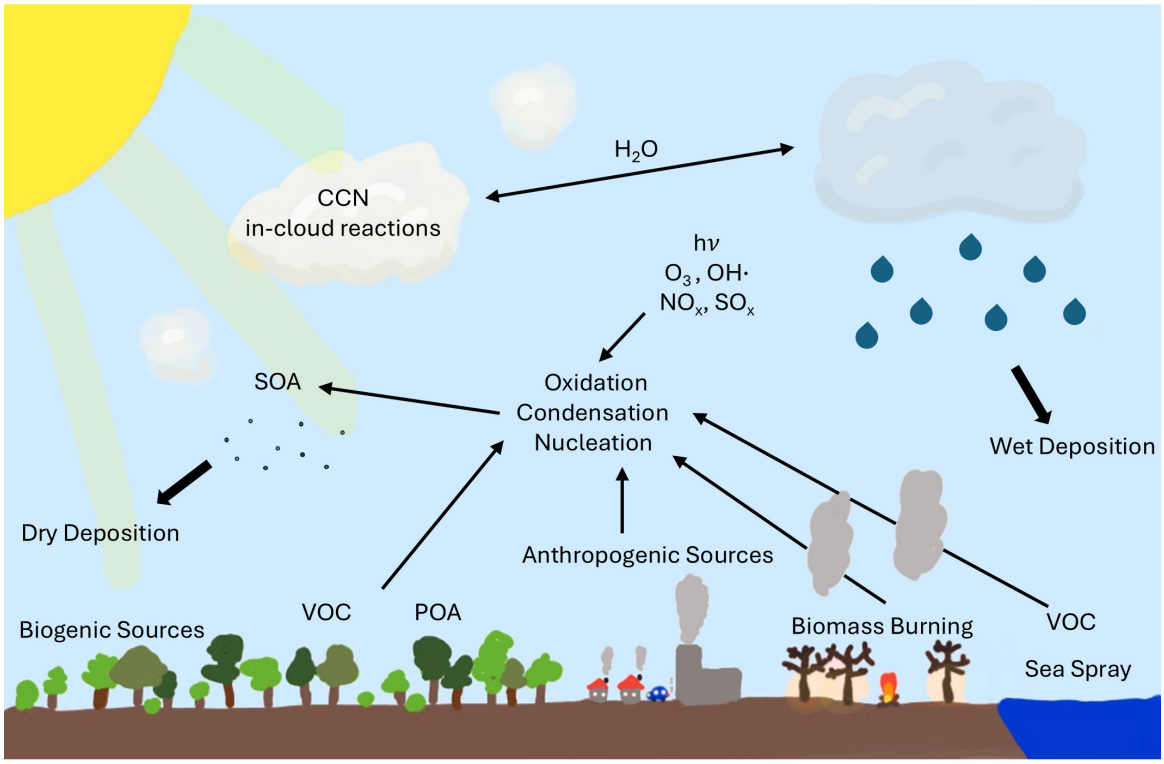

Figure 1.1: Schematic of sources and sinks of aerosol particles. After Krishnan et al. (2020) and Iavorivska et al.(2016) (VOC: volatile organic compound, SOA: secondary organic aerosol, POA: primary organic aerosol, CCN: cloud condensation nuclei)

The sources and sinks of atmospheric aerosols are highly dependent on the size of the aerosol particle (see Figure 1.2). Aerosols are distinguished between fine and coarse particles. In general, coarse particles are defined as particles with an aerodynamic diameter of exceeding 2.5 µm. In some cases, a further restriction is that the diameter must be less than 10 µm. Conversely, fine particles are characterized as particles with a diameter below 2.5 µm (Seinfeld and Pandis, 2006; Brunekreef and Forsberg, 2005). The fine particles are further subdivided into three distinct modes: nucleation mode (particles smaller than 10 nm), Aitken mode (particles with a diameter between 10 and 100 nm) and accumulation mode (particles between 0.1 µm and 2.5 µm). The formation of nucleation mode particles is attributed to the condensation of hot vapor or the process of nucleation in the atmosphere, which results in the generation of new particles. The sink of these particles, as well as those of the Aitken mode, is

the coagulation with larger particles. Accumulation mode particles are formed by the coagulation of particles and by the condensation of vapors on existing particles. They are mainly removed from the atmosphere by wet deposition. Coarse particles are created by mechanical processes and usually consist of dust. They have a short atmospheric lifetime and sediment quickly (Seinfeld and Pandis, 2006).

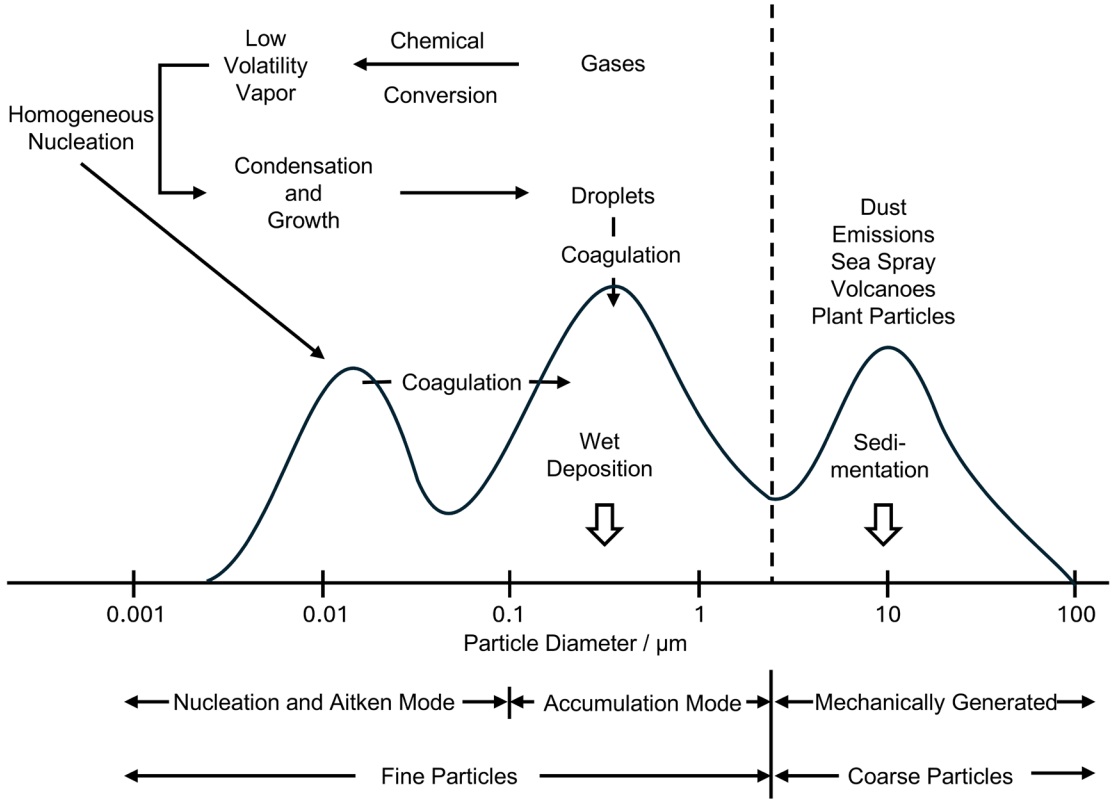

Figure 1.2: Schematic of an idealized distribution of particle diameter, including modes, sinks and formation. Modified after Whitby (1978).

In addition to the previously described effects of aerosols on the climate, a number of studies have demonstrated a negative impact of aerosols on human health. The inhalation of aerosol particles, particularly those measuring less than 2.5 µm in diameter, has been linked to the development of allergic reactions, reduced lung function, and an increased risk of cancer (Lelieveld et al., 2015; Bernstein et al., 2004).

1.2 Secondary organic aerosols

Secondary organic aerosols (SOA) are formed through the processing of volatile trace gases such as isoprene, alpha-pinene, and benzene, resulting in the formation of less volatile organic compounds (Carlton et al., 2009; Ng et al., 2007). They account for a large fraction of OA in the atmosphere (Jimenez et al., 2009). It is notable that numerous atmospheric models tend to underestimate the mass of organic aerosols present in the atmosphere (Williamson et al., 2019; Bernstein et al., 2004). This illustrates the necessity for further investigation into the composition and processing of SOA in the atmosphere.

1.2.1 Formation of SOA

The diversity of volatile organic compounds (VOCs) emitted to the atmosphere is reflected in their structural and functional variability. These compounds can be divided into various categories based on their chemical composition and functional groups. The most common groups are alkanes, alkenes, alcohols, acids, carbonyls, esters, halocarbons, and aromatics (Li et al., 2021; Kesselmeier and Staudt, 1999). Among the biogenic VOCs, the so-called isoprenoids exert the most significant influence. These are constituted of C_5 units. The categorization of these compounds is dependent on the number of C_5 units they contain. Thus, they are classified as hemiterpenes (C_5, e.g. isoprene), monoterpenes (C_{10}, e.g. α-pinene, camphor), sesquiterpenes (C_{15}, e.g. β -caryophyllene, abscisic acid), and so on. Of these, isoprene and monoterpenes are the most atmospherically relevant (Kesselmeier and Staudt, 1999; McGarvey and Croteau, 1995). The proportion of biogenic VOCs emitted is approximately eight times greater than that of anthropogenic VOCs (Goldstein and Galbally, 2007).

The VOCs emitted into the atmosphere can undergo a series of reactions, including gas-phase oxidation with hydroxyl radicals (OH), ozone (O_3), or nitrate radicals (NO_3). These reactions can result in the formation of compounds with lower volatility. This is shown exemplarily in Figure 1.3 (Kroll and Seinfeld, 2008).

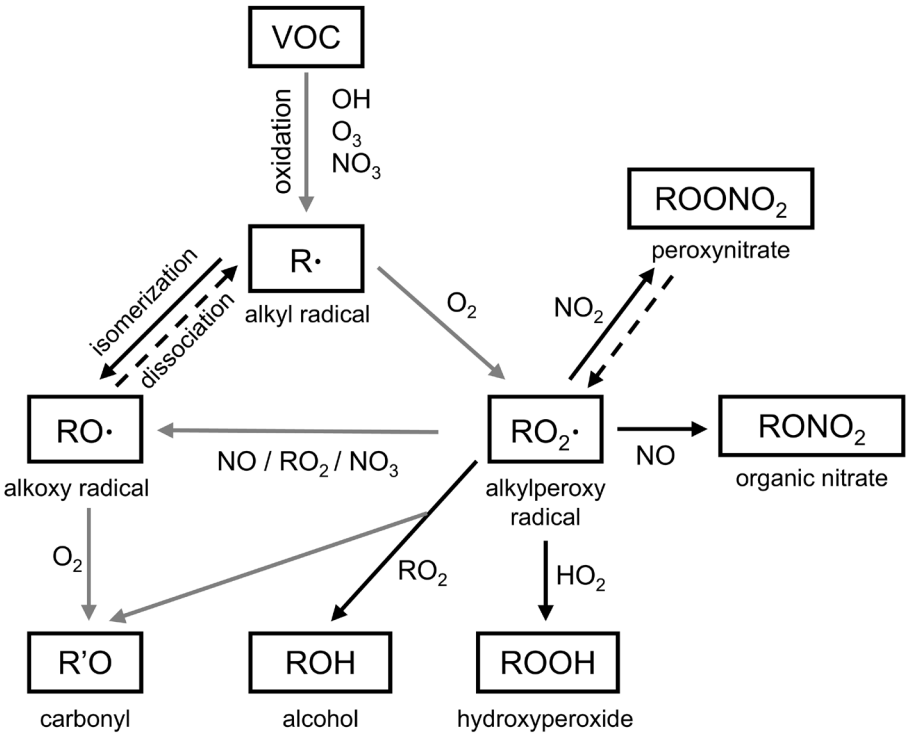

Figure 1.3: Simplified reaction diagram of the gas phase oxidation of a VOC by the atmospheric oxidants OH·, NO_3· and O_3. The black arrows indicate a potential decrease in vapor pressure, while the dashed black arrows indicate a potential increase in vapor pressure due to the reaction. After Kroll and Seinfeld (2008).

The addition of either OH or NO_3 to an unsaturated system, or the abstraction of a hydrogen by, for example, OH, can initiate the reaction scheme with the formation of an alkyl radical (R) as the initial step. This alkyl radical can then undergo oxidation in the presence of oxygen, forming an alkylperoxy radical (RO_2). A multitude of diverse chemical classes can be generated from the alkylperoxy radical. This is often associated with a reduction in vapor pressure. The reaction with NO_2 results in the formation of peroxynitrates, whereas the reaction with NO leads to the production of organic nitrates. Moreover, the reaction with HO_2 and RO_2 can yield hydroperoxides and alcohols or carbonyls. Additionally, the alkyl radical can undergo reversible isomerization to form an alkoxy radical, which can then undergo oxidation with oxygen to result in the formation of a carbonyl. In addition to the previously mentioned reactions, the formation of compounds with a higher vapor pressure than that of the original VOC is also a possibility. These include, for example, carbon dioxide (CO_2) and formaldehyde (CH_2O). (Kroll and Seinfeld, 2008; Atkinson and Arey, 2003).

An example of a radical oxidation mechanism is what is known as autoxidation. In this process, alkylperoxy radicals (RO_2) undergo an intramolecular hydrogen shift, forming a compound with a hydroperoxide functionality and an alkyl radical. This can then react rapidly with oxygen, resulting in the formation of a new, more highly oxidized alkylperoxy radical. The hydroperoxyl group may undergo decomposition, resulting in the generation of an OH, which was only required for catalytic purposes. The resulting highly oxidized compounds are

classified as highly oxygenated organic molecules (HOM) (Bianchi et al., 2019; Crounse et al., 2013). This is exemplarily shown in Figure 1.4.

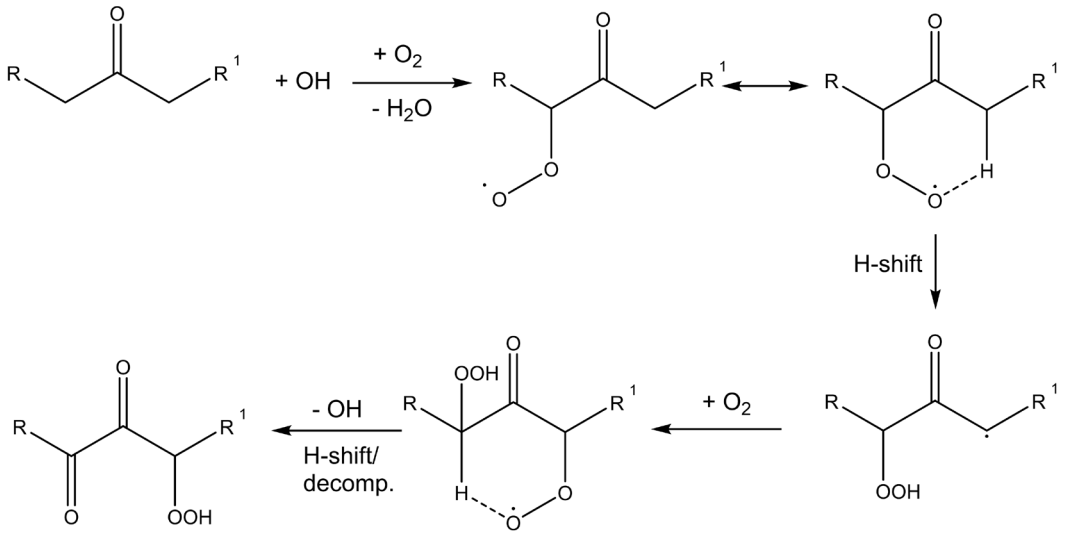

Figure 1.4: Reaction mechanism of OH-initiated autoxidation with a ketone as the example. Adapted from Crounse et al. (2013).

In addition to the radical oxidations described above, the oxidation with ozone also occurs on double bonds, which follows a different mechanism. The first step in the process is the addition of ozone to the double bond (see Figure 1.5), which results in the formation of a primary ozonide. This compound rapidly decomposes into an excited Criegee intermediate (CI*) and a carbonyl compound. The activated Criegee intermediate can undergo two distinct reactions. One possibility is that it can be stabilized by collisions, resulting in a stabilized Criegee intermediate (SCI). This SCI can form an α-hydroxyhydroperoxide by the addition of water or a secondary ozonide by reaction with a carbonyl. This reaction pathway is known as the "SCI channel". Alternatively, the intermediate can undergo a unimolecular reaction, resulting in the "hydroperoxide channel". The CI* decomposes, releasing an OH radical and an alkyl radical, which can then undergo the reactions shown in Figure 1.3. Which of the two reaction pathways is preferred depends on the molecular structure (Kroll and Seinfeld, 2008; Chuong et al., 2004; Atkinson and Arey, 2003).

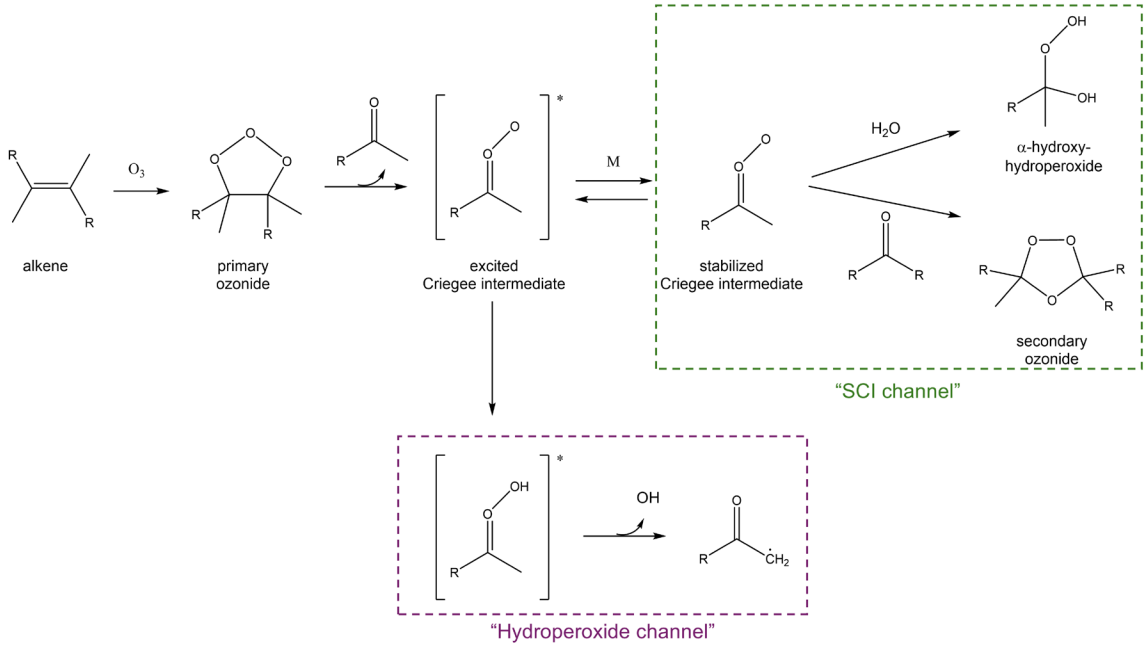

Figure 1.5: Simplified mechanism of ozonolysis of an alkene via the SCI channel or the hydroperoxide channel. Modified after Kroll and Seinfeld (2008).

Aqueous phase oxidation in clouds represents a significant process in the formation of SOA (Lim et al., 2010). This reaction pathway provides an explanation for the discrepancy between the higher oxygen-to-carbon ratio observed in atmospheric samples compared to the ratio measured in smog chamber experiments (Aiken et al., 2008). SOA formation via vapor pressure reduction through oxidation processes requires large precursors with six or more carbon atoms to achieve high yields (Seinfeld and Pankow, 2003). In contrast, aqueous SOA precursors are most often small molecules with two to three carbon atoms, as they have to be water-soluble. This makes it easier to achieve a high oxygen to carbon ratio (Volkamer et al., 2007). The oxidation of volatile but water-soluble organics is enabled by the presence of fog, cloud droplets, and wet aerosols. The oxidation of organic compounds in aqueous droplets can be initiated by a variety of compounds, including radicals (OH, NO_3, HO_2), radical anions (O_2^-, Cl_2^-, Br_2^-, SO_4^-) and non-radical compounds (O_3, H_2O_2). The OH radical is the most relevant oxidation reagent in atmospheric water droplets. (Hallquist et al., 2009; Faust and Allen, 1993). The sources of the OH radicals are dependent on the conditions. Nitrite (NO_2^-) photolysis in the aqueous phase is the major source of OH radicals in the boundary layer. This is a consequence of the anthropogenic influence on the boundary layer, which results in the presence of HONO in the atmosphere (Anastasio and McGregor, 2001). The photolysis of nitrite is shown in Equation (1.1) (Hallquist et al., 2009).

$$NO_2^- + H_2O \xrightarrow{h\nu\ (\lambda<400\ \mathrm{nm})} OH + NO + OH^- \qquad (1.1)$$

In the case of clouds in the free troposphere, the formation pathway of OH radicals occurs via the aqueous-phase photolysis of nitrate, as illustrated in Equation (1.2). Alternatively, at pH values less than or equal to 4, the photo-Fenton reaction, which is a photochemical cycle, can occur (see Equation (1.3) and (1.4)) (Hallquist et al., 2009; Arakaki et al., 2006). Finally, the photolysis of H_2O_2 contributes to this process to a lesser extent (Equation (1.5)) (Arakaki and Faust, 1998).

$$NO_3^- + H_2O \xrightarrow{h\nu\ (\lambda<355\ \text{nm})} OH + NO_2 + OH^- \quad (1.2)$$

$$FeOH^{2+} \xrightarrow{h\nu\ (\lambda<370\ \text{nm})} OH + Fe^{2+} \quad (1.3)$$

$$Fe^{2+} + H_2O_2 \longrightarrow OH + FeOH^{2+} \quad (1.4)$$

$$H_2O_2 \xrightarrow{h\nu\ (\lambda<320\ \text{nm})} 2\ OH \quad (1.5)$$

During the oxidation process, low-volatile products are formed. For instance, glyoxal is generated in the atmosphere as a result of photochemical processes. Subsequently, it can be dissolved in aqueous droplets. Under the influence of light, glyoxal can react with OH radicals to form oxalic acid within cloud or fog droplets. During the evaporation of the droplet, oxalic acid is introduced to the atmosphere, and unreacted glyoxal can reversibly form oligomers (Lim et al., 2010). The oxalic acid released into the atmosphere through droplet evaporation largely remains in the particle phase (Carlton et al., 2006). Additionally, the reaction of organic compounds with other water-soluble substances, such as sulfate, ammonium, or amides, leads to the formation of sulfur- or nitrogen-containing species (Lim et al., 2010).

1.2.2 Gas-particle partitioning

The reactions described above can result in a reduction in the vapor pressure of the compounds. If the vapor pressure decreases to a point where condensation occurs, this can result in the formation of new particles or, in the case of condensation on existing particles, particle growth (Ng et al., 2007; Pankow et al., 2001). It is important to note that SOA can be composed of semi-volatile compounds that are distributed between the gas and particle phases. The theoretical foundations of gas-particle partitioning were initially developed by Pankow in the 1990s, with later extensions being made by Odum (Odum et al., 1996; Pankow, 1994). The partitioning of each compound is described by its partitioning coefficient $K_{p,i}$ [$m^3\ \mu g^{-1}$], which is equivalent to the inverse saturation vapor pressure concentration C_i^* [$\mu g\ m^{-3}$] (Hallquist et al., 2009; Donahue et al., 2006). This correlation is illustrated in Equation (1.6).

$$\frac{C_{\mathrm{i}}^{\mathrm{p}}}{C_{\mathrm{i}}^{\mathrm{g}}} = K_{\mathrm{p,i}} \cdot C_{\mathrm{OA}} = \frac{C_{\mathrm{OA}}}{C_{\mathrm{i}}^{*}} \tag{1.6}$$

In this equation $C_{\mathrm{i}}^{\mathrm{g}}$ is the mass concentration of a species i per unit volume of air in the gas phase, $C_{\mathrm{i}}^{\mathrm{p}}$ is the mass concentration per unit volume of air in the particulate phase, and C_{OA} is the mass concentration per unit volume of air of the total absorbing particle phase (all in [µg m^{-3}]). Equation (1.6) shows that as the amount of aerosol that allows partitioning into the particle phase increases, the proportion of a semi-volatile compound present in the particle phase also increases, even if the gas phase concentration of this compound is still below the saturation concentration (C_{i}^{*}). The proportion of the semi-volatile compound present in the particle phase (F_{i}) can be calculated using Equation (1.7) (Hallquist et al., 2009).

$$F_{\mathrm{i}} = \frac{C_{\mathrm{i}}^{\mathrm{p}}}{C_{\mathrm{i}}^{\mathrm{p}} + C_{\mathrm{i}}^{\mathrm{g}}} = \frac{C_{\mathrm{OA}} \cdot K_{\mathrm{p,i}}}{1 + C_{\mathrm{OA}} \cdot K_{\mathrm{p,i}}} = \frac{1}{1 + C_{\mathrm{i}}^{*}/C_{\mathrm{OA}}} \tag{1.7}$$

This demonstrates that an increase in the quantity of absorbing particulate material results in the partitioning of compounds with higher volatility into the particle phase. If C_{i}^{*} is equal to C_{OA}, 50% of the mass of the semi-volatile compound i is present in the particle phase. Consequently, if $C_{\mathrm{OA}} \gg C_{\mathrm{i}}^{*}$, the entire semi-volatile compound i is present in the particle phase (Hallquist et al., 2009).

Additionally, the saturation concentration can be used to categorize compounds into different volatility classes (Donahue et al., 2012). The categories are (Simon et al., 2020):

- Intermediate-volatility organic compound (IVOC): $300 < C^{*}(T) < 3 \cdot 10^{6}$ µg m^{-3}
- Semi-volatile organic compound (SVOC): $0.3 < C^{*}(T) < 300$ µg m^{-3}
- Low-volatility organic compound (LVOC): $3 \cdot 10^{-5} < C^{*}(T) < 0.3$ µg m^{-3}
- Extremely low volatility organic compound (ELVOC): $3 \cdot 10^{-9} < C^{*}(T) < 3 \cdot 10^{-5}$ µg m^{-3}
- Ultralow-volatility organic compound (ULVOC): $C^{*}(T) < 3 \cdot 10^{-9}$ µg m^{-3}

IVOCs are typically present in the gas phase. In contrast, a significant proportion of semi-volatile compounds are found both in the particle phase and in the gas phase. LVOCs and ELVOCs are predominantly present in the condensed phase and play a role in the growth of particles in the atmosphere. ULVOCs have a saturation vapor pressure that is so low that they can reach supersaturation, which can result in nucleation and, consequently, the formation of new particles (Bianchi et al., 2019; Donahue et al., 2012; Donahue et al., 2009; Simon et al., 2020).

The sampling of aerosol particles is a challenging process because semi-volatile compounds are known to undergo phase transitions between the gas and particle phases depending on the temperature and relative humidity conditions (van Dingenen et al., 2004).

1.2.3 Isoprene SOA

Biogenic emissions play a significant role in the formation of SOA. Isoprene is primarily emitted by terrestrial ecosystems (Hallquist et al., 2009). Model calculations indicate that isoprene emissions, which exceed 500 Tg per year, account for approximately half of the biogenic VOC emission and about one-third of the annual global VOC emission (Guenther et al., 2012; Guenther et al., 2006). At the beginning of the 1990s, it was hypothesized that isoprene did not play a substantial role in the formation of SOA (Pandis et al., 1991). However, polar compounds, including 2-methyltetrols and 2,3-dihydromethacrylic acid, were detected in significant amounts in both natural forest aerosol samples and chamber experiments and were identified as isoprene SOA (Kroll et al., 2006; Edney et al., 2005; Claeys et al., 2004a; Claeys et al., 2004b).

Oxidation of isoprene in the atmosphere results in a multitude of compounds (Figure 1.6). The photochemical reaction between isoprene, OH radicals, and NO_x ($NO_x = NO + NO_2$) leads to the formation of methacrylic acid epoxide through the intermediate formation of methacrolein. Subsequent reactions involving the epoxide, sulfate ions, nitrate ions, or water result in the production of organosulfates, organic nitrates, or 2-methylglyceric acid, which may also form a dimer. These chemical reactions lead to a reduction in vapor pressure, with the resulting compounds being present in the particle phase (Lin et al., 2013b). In low-NOx conditions higher SOA yields are observed. Under these conditions the isoprene epoxy diol (IEPOX) is initially formed through gas phase photooxidation reactions. This subsequently undergoes acid-catalyzed ring opening with water or sulfate, resulting in the formation of alkene triols, 2-methyltetrol, or hydroxy sulfate ester. As is the case with high NO_x conditions, the formation of dimers or oligomers might also occur. This generates a multitude of compounds with low volatility that contribute to the composition of SOA (Lin et al., 2013a; Surratt et al., 2010).

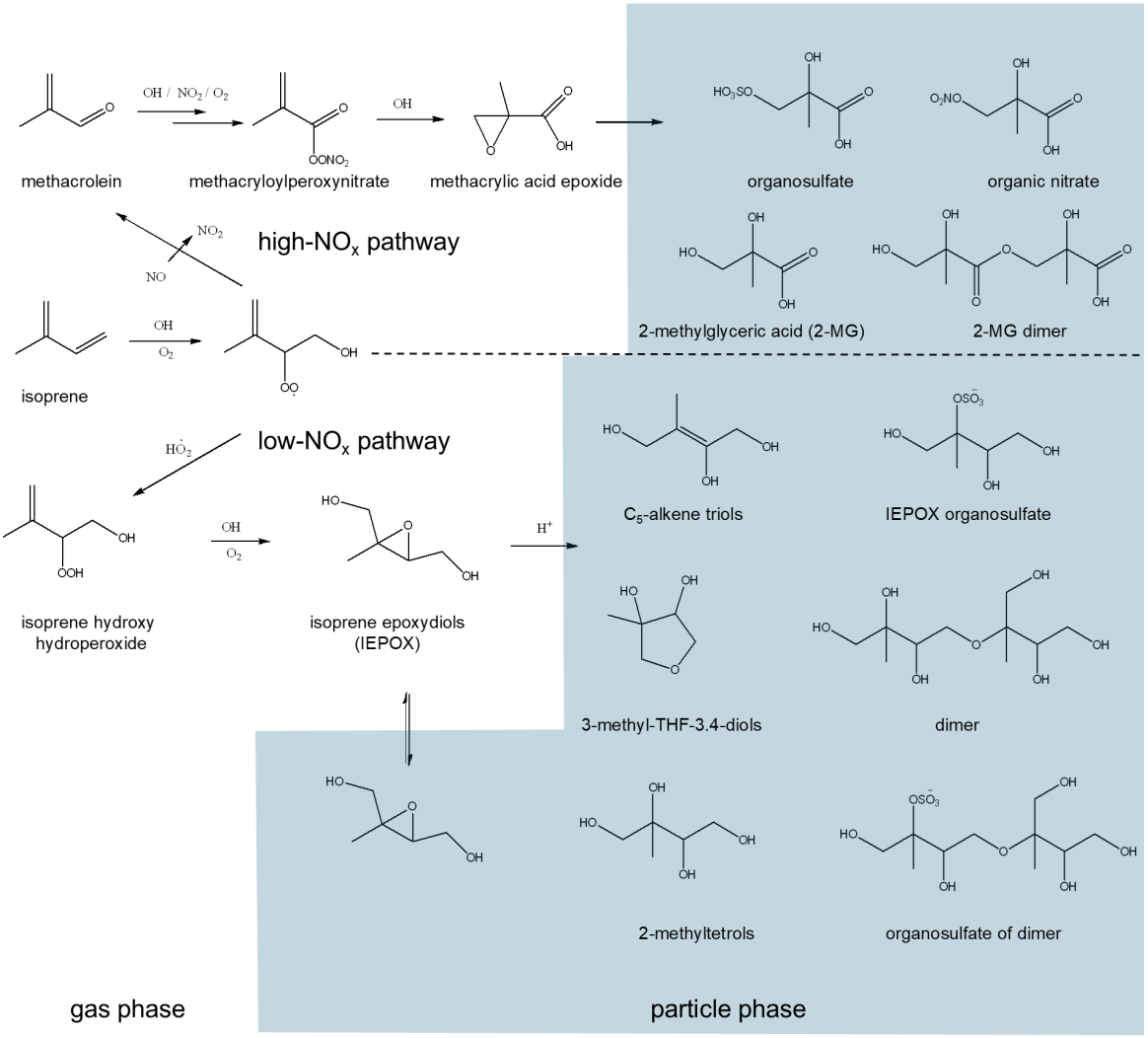

Figure 1.6: Different reaction pathways of isoprene that lead to isoprene SOA. The upper reaction pathway takes place under high-NO_x conditions, the one below under low-NO_x conditions. The compounds shaded in blue are in the particle phase. Adapted after Lin et al. (2013a) and Surratt et al. (2010).

1.2.4 α-Pinene SOA

In addition to isoprene (C_5H_8), monoterpenes ($C_{10}H_{16}$) represent a significant source of biogenic VOCs. Terrestrial vegetation emits many different monoterpenes (MT), with the most important MT α-pinene contributing around one third of global MT emissions (Sindelarova et al., 2014). Despite their lower emissions in comparison to isoprene, the oxidation of monoterpenes may contribute up to 50% of the fine organic aerosol in specific regions (Zhang et al., 2018; Guenther et al., 1995). Figure 1.7 shows the atmospheric oxidation of α-pinene by OH radicals during the day, NO_3 radicals at night, and ozone, resulting in the formation of

various functional groups, including ketones, alcohols, aldehydes, and carboxylic acids, which are added to the α-pinene skeleton (Kołodziejczyk et al., 2019).

Important first generation oxidation products are, among others, *cis*-pinic acid, *cis*-pinonic acid, and *cis*-norpinic acid (Lignell et al., 2013; Jenkin et al., 2000). In addition to the previously mentioned oxidation products, higher-generation oxidation products, including 3-methyl-1,2,3-butanetricarboxylic acid (MBTCA) and 3-hydroxyglutaric acid, are also formed. These findings were confirmed through laboratory and field measurements (Kourtchev et al., 2008).

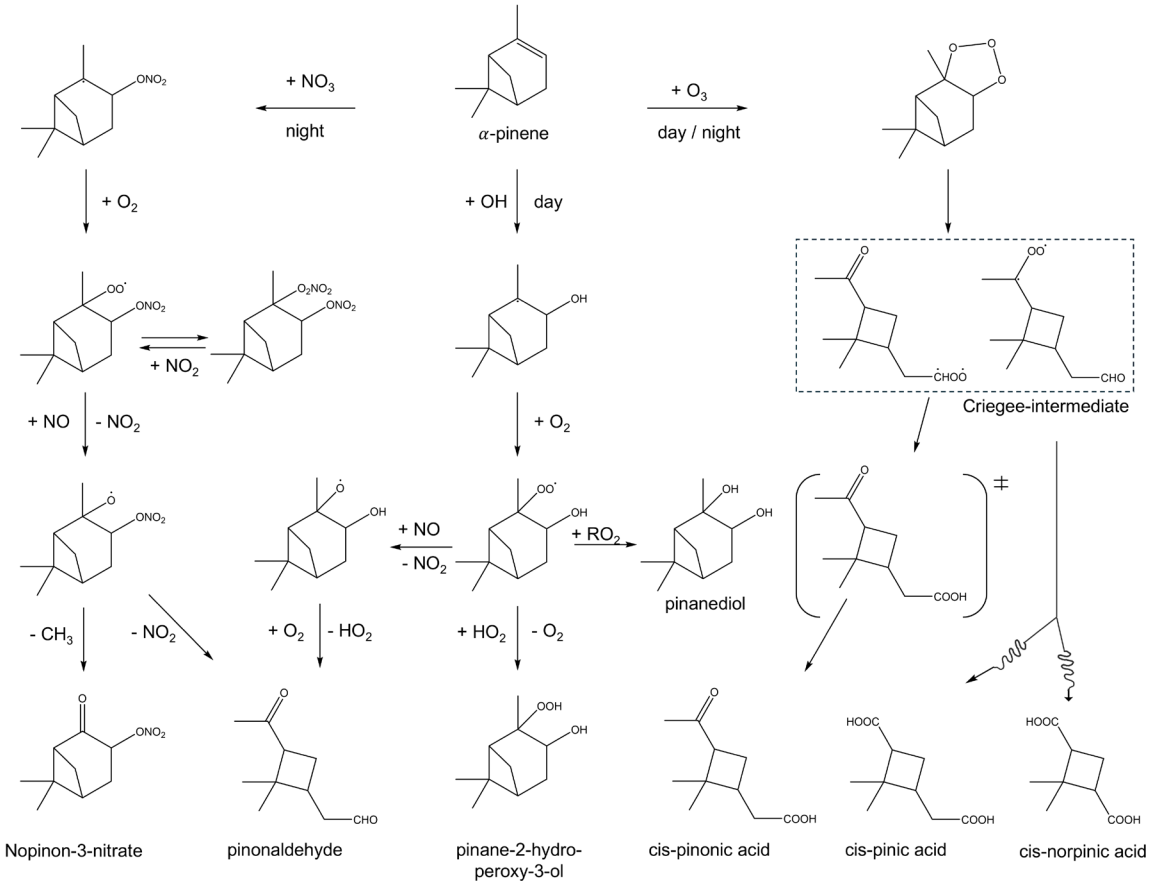

Figure 1.7: Simplified reaction scheme for the oxidation of α-pinene with NO_3 radicals, OH radicals and ozone. Modified after Jenkin (2004) and Hoffmann and Klockow (1998).

In addition to the 6- and 4-ring compounds shown above, γ-lactones such as terpenylic acid or terebic acid are also formed during ozonolysis. This is illustrated in Figure 1.8. The formation of terpenylic acid and terebic acid is primarily the result of the oxidation of myrtenal, which is derived from the oxidation of α-pinene.

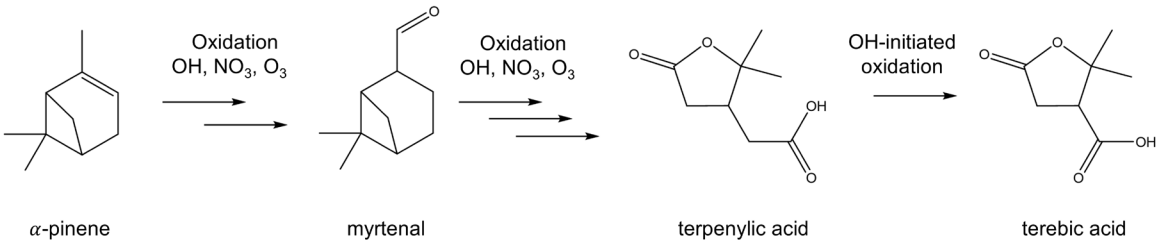

Figure 1.8: Simplified reaction scheme for the oxidation of α-pinene forming gamma lactones. After Florou et al.(2024).

The aldehyde function of myrtenal is highly reactive with OH or NO_3 radicals, resulting in the formation of terpenylic acid and terebic acid through subsequent oxidation with OH radicals (Florou et al., 2024). Terebic acid was identified as a significant constituent of SOA, which is generated from α-pinene, in field measurements (Kourtchev et al., 2013; Gómez-González et al., 2012).

It is commonly assumed that biogenic SOA cannot be controlled because the emission of biogenic VOCs cannot be prevented. However, model simulations indicate that the formation of biogenic SOA is significantly influenced by the concentration of NO_x and the presence of primary carbonaceous particulate matter. Removal of controllable anthropogenic emissions could result in a decrease of greater than 50% in biogenic SOA in the eastern United States (Carlton et al., 2010).

1.2.5 Marine aerosol

Marine aerosols are a significant contributor to the global aerosol budget. The focus has long been on aerosols formed by sea salt and non-sea salt sulfates (O'Dowd et al., 1997; Charlson et al., 1987; Shaw, 1983). However, a study shows that during plankton blooms, the fraction of organic matter in submicron particles dominates (O'Dowd et al., 2004). The composition of the organic components of marine aerosol is dependent upon both the primary emission and the transformation to SOA (Facchini et al., 2008a; Facchini et al., 2008b). One source of marine aerosol is the so-called bubble bursting. The action of wind above the water's surface results in the formation of air bubbles within the water column, caused by the breaking of waves. Following a period of residence in the water, the air bubbles return to the surface and cause a break in the surface layer of the water, resulting in the formation of aerosol particles (Resch et al., 1986). The presence of phytoplankton has the potential to affect the composition of the aerosol generated by bubble bursting (Kuznetsova et al., 2005). The resulting aerosols contain a variety of compounds, including organic acids, amines, carbonyls, and amino acids (Saxena and Hildemann, 1996). This compounds may be further oxidized in the atmosphere to form SOA (Schmitt-Kopplin et al., 2012).

In addition to the primary aerosols, marine SOA can also form in the atmosphere through the processing of VOCs present in marine environments. The process of marine SOA formation

remains poorly understood. Seawater contains a highly complex mixture of VOCs, the distribution and emission of which is still poorly understood. Additionally, the global contribution of the oceans to the Earth's VOC budget is not yet fully elucidated (Yu and Li, 2021). Dimethyl sulfide (DMS) is a biogenic sulfur-containing VOC that is responsible for the majority of organic sulfur in the atmosphere (Andreae et al., 1985). DMS, produced by phytoplankton, is often the dominant source of sulfur in the marine environment (Yang et al., 2011). Following its release into the atmosphere, DMS is oxidized to a number of volatile and semi volatile compounds. Additionally, it is oxidized to compounds with such low volatility that they contribute to particle growth or even new particle formation (NPF) (Beck et al., 2021; Barnes et al., 2006). Oxidation may occur through two principal pathways (see Figure 1.9).

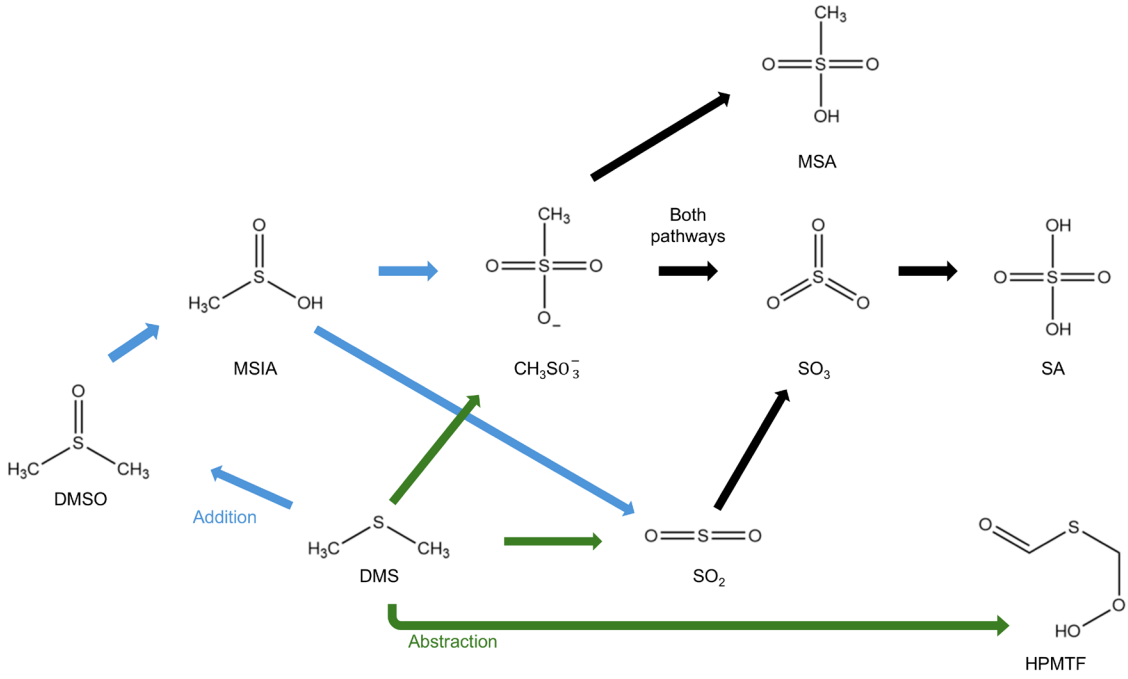

Figure 1.9: Simplified oxidation mechanism of DMS in the atmosphere. The green arrows indicate the reaction pathway via hydrogen abstraction, forming MSA, hydroperoxymethyl thioformate (HPMTF), and sulfuric acid via SO_2 and SO_3. The blue arrows represent the addition of hydroxyl radicals, resulting in the formation of DMSO, MSIA, MSA, and SA via SO_2 and SO_3 or via methanesulfonate. Adapted after Siegel et al. (2023).

One reaction pathway includes the addition of OH, NO_3, or halogen radicals, whereas the second reaction pathway involves the abstraction of an H atom (Siegel et al., 2023). In the addition reaction pathway, the earliest stable oxidation product is dimethyl sulfoxide (DMSO), which is subsequently oxidized to methanesulfinic acid (MSIA) (Barnes et al., 2006). MSIA is now able to undergo a reactive uptake in particle phase or to be oxidized to form either methanesulfonic acid (MSA), sulfuric acid (SA), or sulfur dioxide. In the abstraction pathway, the predominant products are sulfuric acid, which is primarily generated through the oxidation of SO_2 and SO_3, and MSA (Siegel et al., 2023).

In addition to organic sulfur compounds, water-soluble organic nitrogen compounds also play a significant role in marine aerosol particles. Many of these compounds originate from gas-to-particle conversion in the atmosphere. Additionally, nitrogen containing compounds introduced to the atmosphere through mechanical processes, such as sea spray, and subsequently oxidized, also significantly contribute to marine submicron aerosol (Cornell et al., 2003). An important fraction of the organic nitrogen compounds are amines and amino acids (Barbaro et al., 2015; Facchini et al., 2008b).

Isoprene and monoterpenes are produced not only by terrestrial vegetation, but also by bacteria, macroalgae (seaweed), or marine phytoplankton, and consequently may contribute to marine SOA (Yassaa et al., 2008; Broadgate et al., 2004). In addition to the monoterpenes that have been identified in terrestrial vegetation, halogenated monoterpenes have also been found in algae. This can be attributed to the presence of halogenides in seawater, which allows for the formation of these compounds (O'Dowd et al., 2004). However, these emissions are not a significant contributor to the formation of marine aerosol. A model study indicates that the marine SOA has an origin that can be attributed to approximately 78% from the oxidation of DMS, approximately 21% from dialkylamine salts, and a minor fraction of 0.1% from marine hydrocarbon oxidation (Myriokefalitakis et al., 2010).

1.2.6 Biomass burning

Biomass burning is also a significant contributor to the formation of primary aerosols, as well as a source of VOCs (Hodshire et al., 2019; Gilman et al., 2015; Yokelson et al., 2011). Biomass burning emissions originate from both natural and anthropogenic sources. On a global scale, the combustion of vegetation represents the most significant biomass burned (Simoneit et al., 1999).

Lignocellulose, representing the most abundant biomass resource on Earth, is composed of cellulose, hemicellulose, and lignin (Malherbe and Cloete, 2002). Cellulose decomposes at temperatures exceeding 300 °C, resulting in the cleavage of bonds into anhydrous sugars and volatile products. Among these products, the 1,6-anhydride of glucose, or levoglucosan, is observed to be a prominent constituent (Simoneit et al., 1999). Levoglucosan is well suited to act as a biomass combustion marker due to its high abundance and long stability in different environmental conditions (Bhattarai et al., 2019). Lignin, when subjected to combustion, gives rise to the production of phenolic compounds with aldehyde functionalities. These include 4-hydroxybenzaldehyde, vanillin, and syringaldehyde, among others. Phenolic aldehydes are known to undergo oxidation in the atmosphere by OH radicals, NO_3 radicals, or ozone, resulting in the production of carboxylic acids (Cao et al., 2022; Rana and Guzman, 2022; Net et al., 2011).

Another group of marker compounds are nitro-aromatic compounds. The formation of these compounds can occur as a direct result of the combustion of coal or wood or the emission of vehicle exhaust gases. Additionally, they can be generated as a result of the reaction between phenols or cresols and NO_x. (Wang et al., 2020; Harrison et al., 2005; Lu et al., 2019).

1.3 Cloud condensation nuclei

Aerosols play a significant role in the formation of clouds. The activation of aerosols, dependent on their size, concentration, composition and hygroscopicity, can result in the formation of fog or cloud droplets when there is a supersaturation of water. (Andreae and Rosenfeld, 2008; Gunthe et al., 2009). The number of particles that can act as CCN is dependent on the level of supersaturation (Seinfeld and Pandis, 2006). An increase in CCN results in an elevated number of cloud droplets, accompanied by a reduction in droplet size. This phenomenon may potentially suppress precipitation in shallow and short-lived clouds. Conversely, it may also lead to an increase in precipitation in convective clouds (Rosenfeld et al., 2008; Gunthe et al., 2009).

The formation of cloud droplets can be described using the Köhler theory (Andreae and Rosenfeld, 2008; Köhler, 1936). This is based on the existence of two effects: the Kelvin effect and the Raoult effect. The Kelvin effect describes the fact that the equilibrium vapor pressure is significantly higher for small particles than it is for a flat surface, due to the strong curvature of the surface of the small particles (Lin et al., 2020). In the absence of CCN, this effect would require that a supersaturation, corresponding to a relative humidity of 800%, is reached before cloud droplets can form (Pruppacher and Klett, 2010). This is counteracted by the Raoult effect. It describes that the equilibrium water vapor pressure above a solution is lower than that which would be observed above pure water. The greater influence of the Raoult effect over the Kelvin effect allows for the condensation of water vapor on water-soluble aerosol particles. The Köhler theory states that for each dry water-soluble particle, there is a "critical supersaturation" at which the difference between the Raoult effect and the Kelvin effect is at its maximum. At this point, an infinitesimal growth of the droplet ensures that the droplet grows to a cloud droplet, as the Kelvin effect decreases with increasing particle size. The Köhler theory predicts that the required "critical supersaturation" decreases with increasing particle size (Pruppacher and Klett, 2010; Andreae and Rosenfeld, 2008; Seinfeld and Pandis, 2006).

1.4 Aerosol cloud interactions

In addition to aerosols, clouds also exert a significant influence on the Earth's climate. Clouds can exert a cooling or a warming effect on the climate. This is due to their capacity to reflect radiation back into space, thereby reducing the amount of heat absorbed by the Earth, or to trap energy near the surface, which increases the temperature of the atmosphere. In total, the effect of clouds on the Earth's climate is cooling (Seinfeld and Pandis, 2006). Low, bright clouds exert a significant cooling effect due to their capacity to effectively reflect radiation back into space. In contrast, semi-transparent clouds have a net warming effect, as the reflection of radiation into space is relatively low. However, they also have the potential to absorb heat, which is redirected back into space by the Earth (Rosenfeld et al., 2014).

Aerosols can directly impact the characteristics of clouds, thereby influencing their overall climate impact. An increase in the concentration of CCN results in the formation of a greater number of smaller cloud droplets. This results in an increase in the albedo of the cloud. This phenomenon is known as the first indirect aerosol effect, or the Twomey effect (Werner et al., 2014; Twomey, 1977).

In addition to the sink for aerosols through precipitation, deep convective clouds can also be a source of aerosols in the upper troposphere. These clouds may play a significant role in the transport of trace substances and aerosols into the upper troposphere. In this region, these substances have a longer atmospheric lifetime, increasing the probability of long-range transport. It is also possible that they contribute to the NPF. (Bardakov et al., 2022; Barth et al., 2007a; Barth et al., 2007b). Figure 1.10 shows the evolution of deep convective clouds in a pristine and a polluted atmosphere. In the pristine atmosphere, cloud droplets grow by coalescence into raindrops, which are removed from the lower levels of the cloud by precipitation. Additionally, the early precipitation initiates an early downdraft, which subsequently replaces the updrafts. This results in the early maturation and dissipation of the cloud. In regions with higher levels of pollution, cloud droplets are smaller, which allows them to reach supercooled levels before precipitation can occur. The supercooled droplets have the potential to freeze on existing graupel or hail, releasing latent heat, which can result in the formation of higher and more extensive clouds. The melting of ice hydrometeors during precipitation at lower levels results in a reduction in temperature, which in turn gives rise to more intense downdrafts and a higher precipitation amount (Rosenfeld et al., 2008; Rosenfeld, 2007).

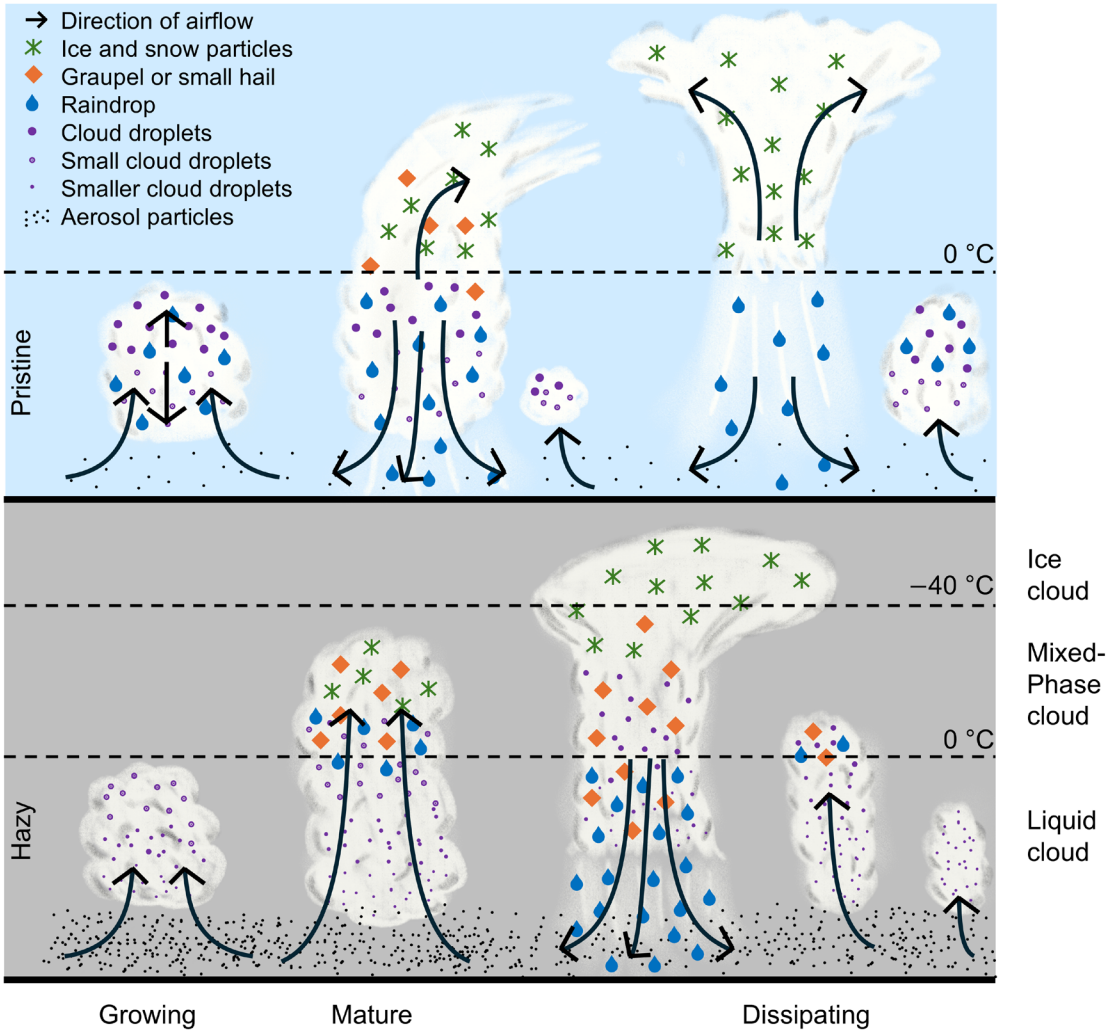

Figure 1.10: Evolution of deep convective clouds in (top) pristine and (bottom) polluted regions. After (Korolev et al., 2017; Rosenfeld et al., 2008).

1.4.1 Retention

In addition to the updrafts illustrated in Figure 1.10, riming in the mixed-phase zones of clouds can also facilitate the transport of intermediate and semi volatile compounds to higher altitudes (Jost et al., 2017). Water-soluble compounds, such as those resulting from the oxidation of biogenic or anthropogenic VOCs, can dissolve in cloud droplets. Such compounds may then be transported upwards, for instance via deep convection, to regions of lower temperature. Upon reaching the mixed-phase zone of the cloud, supercooled water droplets can undergo a freezing process upon contact with graupel or hail. This process is known as riming (Pruppacher and Klett, 2010). During the freezing process, the dissolved substances can either remain in the ice or return to the gas phase. The re-release of these substances during freezing can lead to vertical redistribution, which can explain the presence of, for example, semi-volatile compounds at high altitudes. However, if the organic compounds

remain in the ice phase during freezing, they may continue to be transported upward and released into the gas phase through the sublimation of the ice particles at even higher levels (Pruppacher and Klett, 2010; Snider and Huang, 1998).

The release of latent heat during the freezing process results in the warming of the surface of the rime collectors. In conditions of dry growth, the rime collector surface temperature consistently remains well below 0°C. The accreted cloud water freezes within milliseconds upon contact with the collector, preserving a close to spherical shape. With increasing droplet size, liquid water content and collision frequency, the surface temperature of the hydrometeor rises until it reaches a maximum of 0°C. At this point, the conditions for wet growth are achieved. Under these conditions, the colliding water droplets freeze more slowly, allowing for the formation of a dense ice structure (Pruppacher and Klett, 2010; Macklin, 1961; List, 1960).

The proportion of the compound that is retained within the ice during the riming process can be quantified by the retention coefficient R, which provides a relative amount of the compound remaining in the ice within the range of 0 to 1 (Bela et al., 2018; Stuart and Jacobson, 2003; Snider et al., 1992; Iribarne and Pyshnov, 1990). The retention of a compound is influenced by a number of factors, including its chemical properties, such as the dimensionless effective Henry's law solubility constant (H^*), as well as physical factors, including temperature, ventilation, cloud liquid water content, droplet size, and potentially the pH of the droplet. The volatilization of compounds with lower H^* during riming results in a reduction in the retention coefficient. Moreover, external conditions exert a more pronounced influence on the retention of these compounds, in contrast to those with higher H^*(Cuchiara et al., 2023; Jost et al., 2017; Stuart and Jacobson, 2004, 2003).

1.4.2 Henry’s law constant

Henry's law constant H describes the solubility behavior of an ideal gas in an ideal solution. It is observed that the quantity of a dissolved gas is proportional to the partial pressure of that gas above the liquid. The proportionality factor is defined as Henry's constant, and this relationship is expressed in equation 1.8 (Sander, 2023; Kish et al., 2013; Kühne et al., 2005; Mackay and Shiu, 1981; Henry, 1803).

$$H = \frac{P}{c} \tag{1.8}$$

There are numerous methodologies for determining Henry’s law constant. The definition presented in equation 1.8 represents the Henry’s law solubility constant. Conversely, if the reciprocal value is calculated, it would correspond to the Henry’s law volatility constant (Sander, 2023). An alternative definition of Henry's constant is provided by the ratio of the concentration of a substance in air (c_{air}) to that in water (c_{water}). This is known as the air/water partition coefficient K_{aw} or dimensionless Henry's law constant (see Equation 1.9) (Kühne et al., 2005).

$$K_{aw} = \frac{c_{air}}{c_{water}} \quad (1.9)$$

The Henry's constants described above refer to substances that exhibit identical physical and chemical properties in both the aqueous and gaseous phases. These are referred to as intrinsic Henry's law constants. However, if the substance in question undergoes an irreversible reaction with water, the Henry's law constant is no longer applicable. In the case of a rapid equilibrium reaction in an aqueous solution, a so-called effective Henry's law constant (H^*) can be determined. This refers to the "total concentration" of the substance in the water, which depends, for example, on the dissociation constant or the pH value of the solution (Sander, 2023; Jost et al., 2017).

1.5 Analytical methods

1.5.1 High performance liquid chromatography (HPLC)

Chromatography is a separation method based on the constant distribution of the analyte between two phases. A schematic setup of a HPLC system is provided in Figure 1.11. The system consists of two eluent reservoirs, which allow the solvent mixture to be changed during a measurement. This is known as a gradient. It also contains a degasser, which removes gases dissolved in the solvent, such as nitrogen, to minimize fluctuations in the flow. It also contains a pump to enable a stable flow, a mixing chamber, an injector, a column with an optional column oven, and a detector. The detector can be a UV/Vis, fluorescence detector, or mass spectrometer (see 1.5.2) (Gey, 2021; Ritgen, 2019).

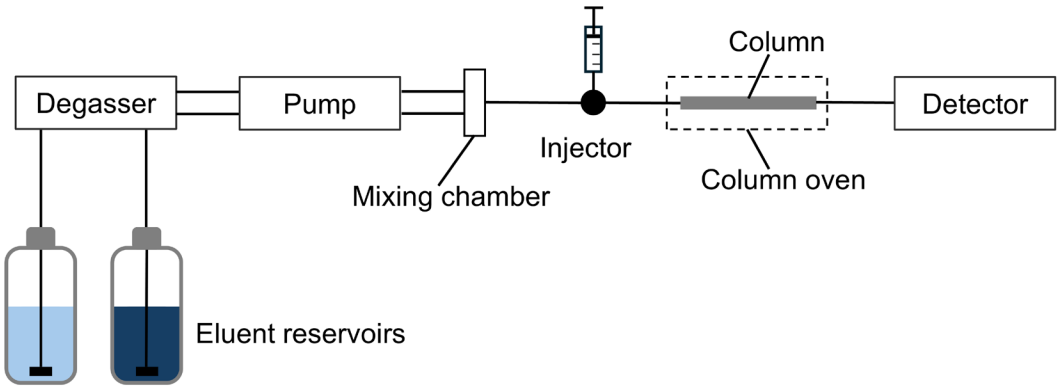

Figure 1.11: Schematic of a HPLC system including eluent reservoirs, a degasser, a pump, a mixing chamber, the injector, a column with optional column oven, and a detector.

In liquid chromatography (LC), a liquid mobile phase is used whose polarity can be adapted to the separation problem. Modified silica gel particles are used as the stationary phase. Reversed phase LC uses silica gel particles modified with non-polar groups such as C_8 chains, alkyl nitrile, C_{18} chains, or fluorophenyl. The non-polar stationary phase requires the use of polar solvents such as methanol or acetonitrile/water mixtures as the mobile phase. Since not all silanol groups are occupied by non-polar residues for steric reasons, these are derivatized,

for example, with trimethylchlorosilane. This modification is called "endcapping" (Harris et al., 2014).

The efficiency of the separation process is dependent upon the particle size used. In classical HPLC, particles with a diameter of 5-10 µm are typically selected. To enhance the efficiency of the separation process, smaller particles are employed. Ultra high performance LC (UHPLC) systems utilize columns with a particle diameter of less than 2 µm. The use of smaller particles requires the application of a higher pressure of up to 1000 bar to ensure a sufficient flow through the column (Gey, 2021).

1.5.2 Mass spectrometry

The determination of the chemical composition of OA provides information on the sources and processing of organic aerosol constituents. This includes the contribution of biogenic sources in terrestrial environments and the role of anthropogenic contributions to atmospheric aerosols. Mass spectrometry (MS) offers the possibility of this chemical composition determination and therefore plays an important role in this research field (Li et al., 2024; Laskin et al., 2012).

The configuration of a mass spectrometer is presented in Figure 1.12. The analyte is first converted into positively or negatively charged gaseous ions in the ion source. Subsequently, the ions are separated in the mass analyzer based on their mass-to-charge ratio (m/z) and thereafter detected. The m/z ratio can then be utilized to draw conclusions about the substance analyzed. To prevent collisions between the ions, the mass analyzer and the detector are situated within a high vacuum. Depending on the type of ionization, the ion source can be employed in a vacuum or under atmospheric pressure (Gey, 2021).

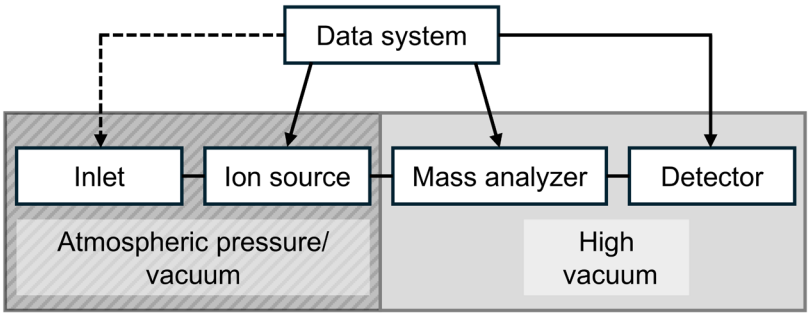

Figure 1.12: Boxplot of a mass spectrometer., including the inlet, ion source, mass analyzer and detector. Modified after Gross (2013).

The selection of an appropriate ion source is dependent on the specific substances to be analyzed. Figure 1.13 provides an overview of the various ion sources that are commonly used in combination with gas or liquid chromatography (Li et al., 2015). In gas chromatography, electron ionization (EI) is an appropriate ionization method for less polar and low molecular

compounds, which is a compatible approach with GC. In liquid chromatography, ionization methods are often used that are conducted under atmospheric pressure. The most commonly applied techniques are electrospray ionization (ESI) and atmospheric pressure chemical ionization (APCI). These two types of ionization are referred to as soft ionization techniques, resulting in the formation of protonated or deprotonated "quasi molecular ions" (Gross, 2013).

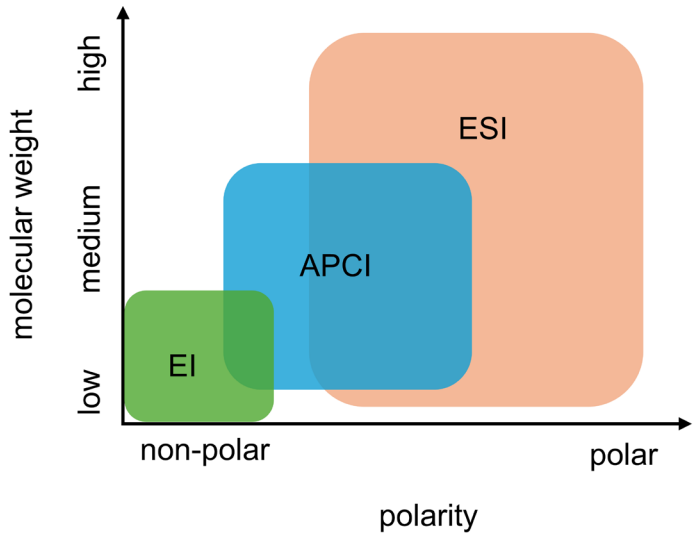

Figure 1.13: Schematic the dependence of the ionization techniques EI, APCI, and ESI on the polarity and molecular weight of the compounds. Adapted after (Li et al., 2015).

1.5.2.1 Electrospray ionization

A schematic setup of an ESI source is shown in Figure 1.14 (a). The solution containing the analyte is introduced into the ion source via a stainless steel capillary. A voltage of 2–4 kV is applied between the tip of the capillary and the inlet of the mass spectrometer, resulting in the formation of a high electric field at the tip of the capillary. This causes charge separation in the solution, leading to the formation of a Taylor cone. Once the electric field strength exceeds the surface tension, a liquid jet is generated in the direction of the counter electrode. This jet subsequently breaks up into numerous small droplets, which are dispersed due to their charge and the resulting Coulomb repulsion, leading to the formation of a spray. The formation of the spray is supported by a nebulizing gas (typically N_2), which concentrically encloses the spray. (Gross, 2013; Konermann et al., 2013; Kebarle and Verkerk, 2009; Wilm and Mann, 1994; Kebarle and Tang, 1993; Taylor, 1964).

The formation of ions from charged droplets is a process that can be described by a number of different theories. Initially, the droplets, which have a significant excess charge, undergo a reduction in size as the solvent evaporates. This results in an increase in the charge density

on the surface. Once the electrostatic repulsion reaches a point where it is greater than the surface tension (Rayleigh limit), the droplets break up into smaller droplets (Rayleigh, 1882).

Figure 1.14 (b) illustrates two different ion release models. The ion evaporation model (IEM) describes the formation of ions through the direct evaporation of desolvated ions from the droplet. To achieve the necessary electric field for desolvation, droplets with a diameter of approx. 10 nm are required (Thomson and Iribarne, 1979). The charged residue model (CRM) describes the formation of ions through the continuous evaporation of the solvent, which causes the droplets to break up into smaller droplets until only a single ion remains in the droplet at the end. The evaporation of the remaining solvent produces a gaseous ion (Gross, 2013; Konermann et al., 2013).

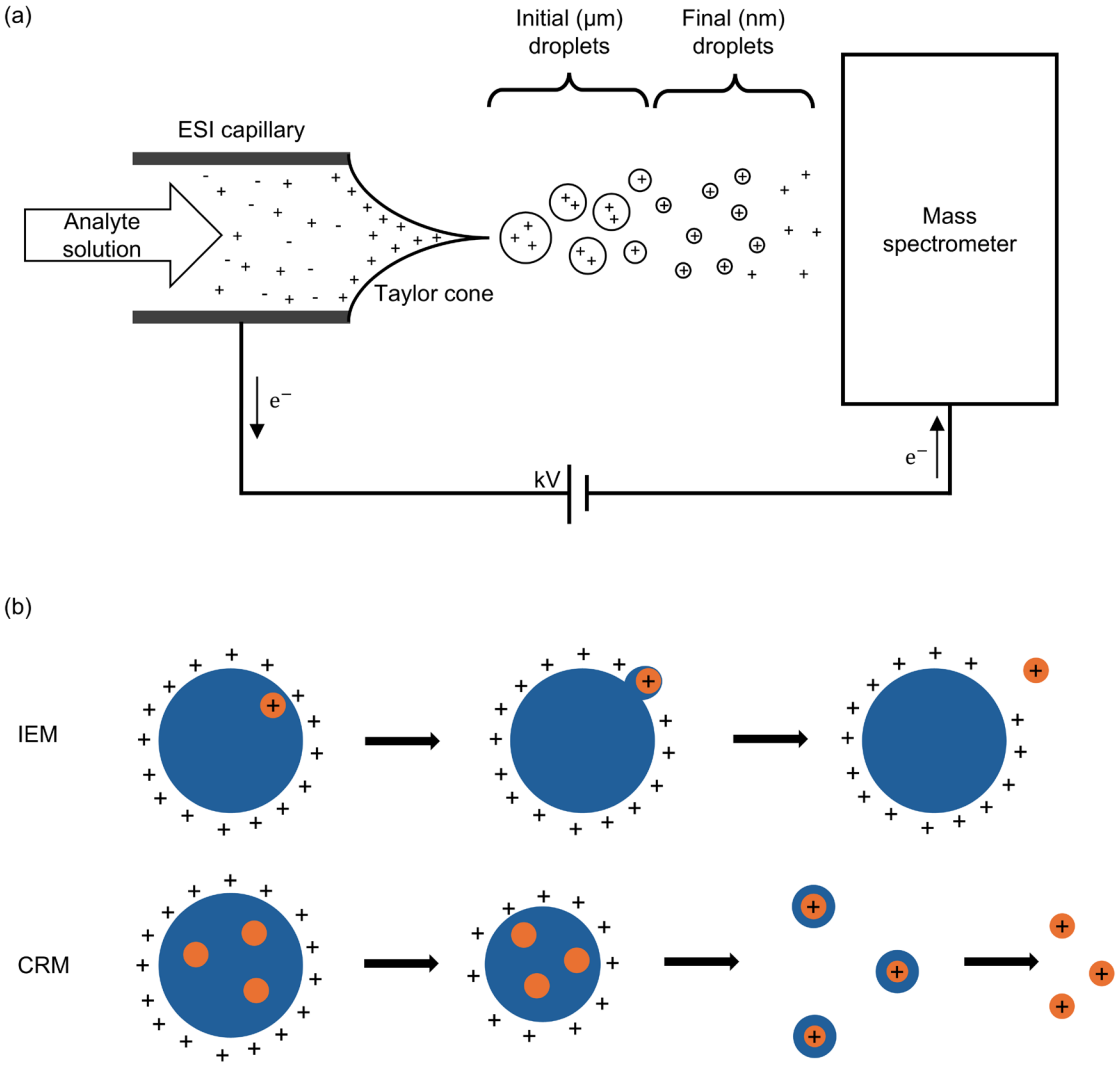

Figure 1.14: (a) Schematic representation of an electrospray ionization (ESI) source in positive ion mode. Modified after Konermann et al. (2013) and Kebarle and Tang (1993). (b) Ionization models of ESI: the ion evaporation model (IEM) and the charge residue model (CRM). After (Konermann et al., 2013) and (Banerjee and Mazumdar, 2012).

When using an ESI source, the production of ions depends on the polarity of the analyte, the properties of the solvent, and the presence of impurities. In positive mode, the protonated $[M+H]^+$ (M: molecule) quasi-molecular ions are typically detected. However, other ions, including alkali metal ions and ammonium ions, may also participate in the process, forming species such as $[M+alkali]^+$ and $[M+NH_4]^+$, respectively. In negative mode, it is the deprotonated compounds $[M-H]^-$ that represent the most important species (Gross, 2013; Konermann et al., 2013).

1.5.2.2 Atmospheric pressure chemical ionization

Another important ionization technique that is commonly used in conjunction with HPLC is atmospheric pressure chemical ionization (APCI). The setup of the ion source is illustrated schematically in Figure 1.15. The solution containing the analyte is atomized via a pneumatic nebulizer. Subsequent to this, the aerosol is vaporized in a heater, thus resulting in the analytes being present in the gas phase. Ions are generated by ion-molecule reactions. For this purpose, a voltage of 4-6 kV is applied to a corona needle, resulting in a corona discharge between the needle tip and the spray chamber, which serves as a counter electrode. This initiates a reaction cascade (Equation 1.10-1.15), which starts with nitrogen and ultimately leads to the formation of an $[M + H]^+$ ion in positive mode via protonated water clusters. (Gross, 2013). One of the most significant benefits of APCI over ESI is that the ions are generated actively from neutral molecules, which allows for the analysis of less polar analytes (Hayen and Karst, 2003).

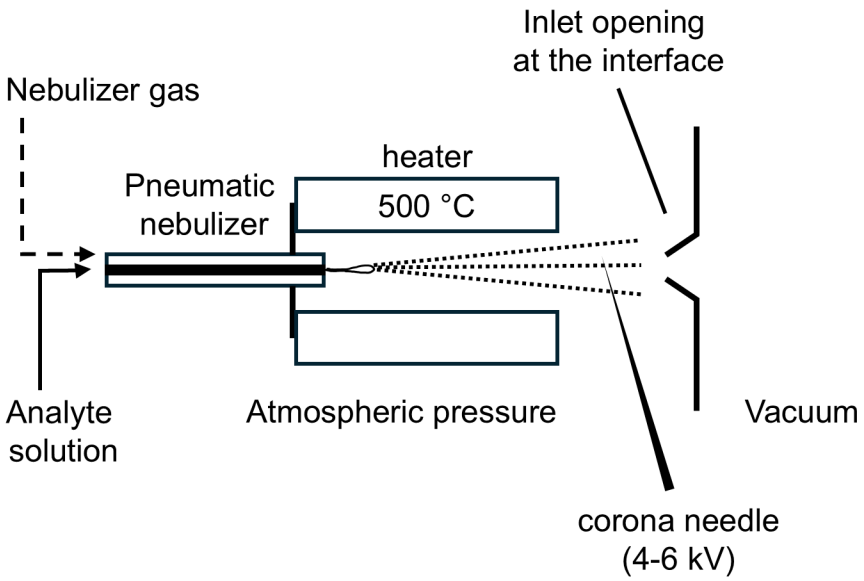

Figure 1.15: Schematic illustration of an atmospheric pressure chemical ionization (APCI) source. After (Gross, 2013).

$$N_2 + e^- \rightarrow N_2^{+\cdot} + 2\,e^- \quad (1.10)$$

$$N_2^{+\cdot} + 2N_2 \rightarrow N_4^{+\cdot} + N_2 \quad (1.11)$$

$$N_4^{+\cdot} + H_2O \rightarrow H_2O^{+\cdot} + 2N_2 \quad (1.12)$$

$$H_2O^{+\cdot} + H_2O \rightarrow H_3O^+ + OH^{\cdot} \quad (1.13)$$

$$H_3O^+ + H_2O + N_2 \rightarrow [(H_2O)_2 + H]^+ + N_2 \quad (1.14)$$

$$[(H_2O)_n + H]^+ + M \rightarrow [M + H]^+ + n\,H_2O \quad (1.15)$$

In the negative mode (equations 1.16-1.18), the reaction cascade starts with oxygen and ends with the formation of $[M\text{-}H]^-$ ions (Osaka et al., 2009).

$$O_2 + e^- \rightarrow O_2^{-\cdot} \quad (1.16)$$

$$O_2^{-\cdot} + n\,H_2O \rightarrow O_2^{-\cdot} \cdot (H_2O)_n \quad (1.17)$$

$$O_2^{-\cdot} \cdot (H_2O)_n + M \rightarrow [M - H]^- + HO_2^{\cdot} + n\,H_2O \quad (1.18)$$

1.5.2.3 Orbitrap mass analyzer

A crucial parameter of mass spectrometry is the resolution R', which is defined as the ratio of the mass (m_1) of an ion to the mass difference (Δm) of a neighboring ion (m_2). This is illustrated in equation 1.19 (Gey, 2021; Murray et al., 2013).

$$R' = \frac{m}{\Delta m} \quad (1.19)$$

The resolution achieved determines whether the analyzers are classified as low resolution (R'=500-2000), high resolution (R'>5000) or ultrahigh resolution ($R' > 100\,000$) (Hawkes et al., 2016; Gross, 2013). The Orbitrap mass analyzer, which can achieve ultrahigh resolution (e.g., $R' = 140\,000$ at *m/z* 200), was first described in 2000 and became commercially available in 2005 (Michalski et al., 2011; Scigelova and Makarov, 2006; Makarov, 2000).

The Orbitrap mass analyzer is an ion trap comprising an inner, spindle-shaped electrode and an outer barrel-like electrode, which is partitioned into two sections (see Figure 1.16). A voltage is applied between the two electrodes. Upon entering the Orbitrap, the ions are directed into a circular trajectory around the inner electrode, which is determined by the equilibrium between the centrifugal force and the electrostatic force. In addition to the movement in the r-direction, the ions also oscillate harmonically along the z-axis, creating an image current. The frequency of this oscillation is proportional to the square root of the reciprocal *m/z* ratio (see equation 1.20) (Makarov and Scigelova, 2010; Makarov, 2000).

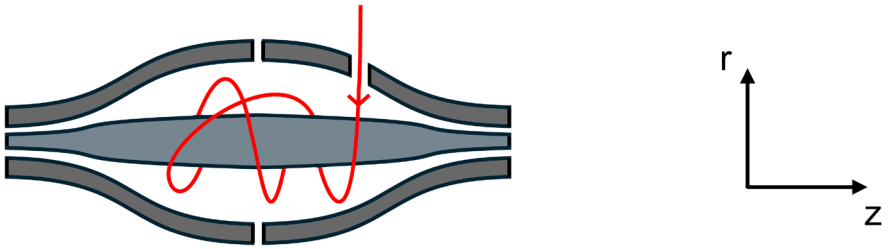

Figure 1.16: Schematic of an Orbitrap analyzer with an outer barrel-like electrode (grey); an inner, spindle-shaped electrode (blue), and an ion trajectory (red). Modified after Makarov and Scigelova (2010).

$$\omega = \sqrt{\frac{z}{m} \cdot k} \tag{1.20}$$

In this equation, ω is defined as the frequency of oscillation along the z-axis, m/z represents the mass-to-charge ratio of the ion of interest, and k is a constant. k is understood as the axial restoring force and is dependent on the precise shape of the electrodes and the applied potential. The m/z can be determined using image current detection and a Fourier transformation. It is important to note that the frequency being considered is independent of the initial properties of the ions, which allows for particularly high resolution. (Perry et al., 2008; Makarov, 2000).

2. Retention measurements

This chapter has been published in *Atmospheric Chemistry and Physics (Borchers et al., 2024)*:

Retention of α-pinene oxidation products and nitro-aromatic compounds during riming

Christine Borchers, Jackson Seymore, Martanda Gautam, Konstantin Dörholt, Yannik Müller, Andreas Arndt, Laura Gömmer, Florian Ungeheuer, Miklós Szakáll, Stephan Borrmann, Alexander Theis, Alexander L. Vogel, Thorsten Hoffmann

2.1 Abstract

Riming is an important growth process of graupel and hailstones in the mixed-phase zones of clouds, during which supercooled liquid droplets freeze on the surface of ice particles by contact. Compounds dissolved in the supercooled cloud droplets can remain in the ice or be released to the gas phase during freezing, which might play an important role in the vertical redistribution of these compounds in the atmosphere by convective cloud processes. This is important for estimating the availability of these compounds in the upper troposphere, where organic matter can promote new particle formation and growth. The amount of organic material remaining in the ice phase can be described by the retention coefficient. Experiments were performed in the Mainz vertical wind tunnel under dry and wet growth conditions (temperature from -12 to -3 °C and a liquid water content (LWC) of 0.9 ± 0.2 g m^{-3} and 2.2 ± 0.2 g m^{-3}) as well as with different pH values (4 and 5.6) to obtain the retention coefficients of α-pinene oxidation products and nitro-aromatic compounds. For *cis*-pinic acid, *cis*-pinonic acid, and (−)-pinanediol, mean retention coefficients of 0.96 ± 0.07, 0.92 ± 0.11, and 0.98 ± 0.08 were obtained. 4-Nitrophenol, 4-nitrocatechol, 2-nitrobenzoic acid, and 2-nitrophenol showed mean retention coefficients of 1.01 ± 0.07, 1.01 ± 0.14, 0.99 ± 0.04, and 0.21 ± 0.12. Only the retention coefficient of 2-nitrophenol showed a dependence on temperature, growth regime, and pH. This is in accordance with previous studies, which showed a dependence between the dimensionless effective Henry's law constant H^* and the retention coefficient for inorganic and small organic molecules. Our results reveal that this correlation can also be applied to more complex organic molecules, and that retention under these conditions is not a significant factor for molecules with H^* below 10^3, while retention close to 1 can be expected for compounds with H^* above 10^8.

2.2 Introduction

The observation of a large number of small particles at high altitudes, which has already been made several times, is attributed to the formation of new particles (new particle formation, NPF) through the process of homogeneous nucleation and early growth. The rate of NPF is strongly dependent on the concentration of low-volatility vapors, the temperature, and the number of particles that are present. Low-volatility vapors are for example sulfuric acid, which is formed from the reaction of sulfur dioxide and hydroxyl radicals or via oxidation of dimethyl sulfide, as well as highly oxidized organic compounds (Xiao et al., 2023; Williamson et al., 2019; Andreae et al., 2018; Kerminen et al., 2018; Twohy et al., 2002). A common explanation for the presence of this high number of small particles at high altitudes is the uplift of condensable vapors with simultaneous removal of existing aerosol particles in deep convective clouds. This removal of larger particles reduces the sinks for small particles and condensable vapors, supporting NPF (Clarke et al., 1998). However, Williamson et al. (2019) showed that tropical convection does not lead to uniquely low particle numbers for larger particles. They then argue that there must be a stronger source of condensable vapors at high altitudes in the marine tropics than in other regions and that most of the models used underestimated available organic matter at high altitudes and predict less NPF in these regions. It is therefore important to investigate the possible transport mechanism of organic precursor components that could lead to NPF at high altitudes (Bardakov et al., 2022).

Among other mechanisms, deep convection plays an important role in the transport of trace substances and aerosols into the upper troposphere. In this region, these substances have a longer atmospheric lifetime, thereby increasing the likelihood of long-range transport. Additionally, they can contribute to NPF (Bardakov et al., 2022; Barth et al., 2007a; Barth et al., 2007b). The fraction that arrives in the upper troposphere is influenced by the liquid-phase and mixed-phase scavenging of the substances. Aircraft measurements from the USA in thunderstorm inflow and outflow regions demonstrate that water-soluble trace gases, such as H_2O_2, are removed with efficiencies between 79% and 97%, which are also influenced by the process of retention (Bela et al., 2018; Barth et al., 2016).

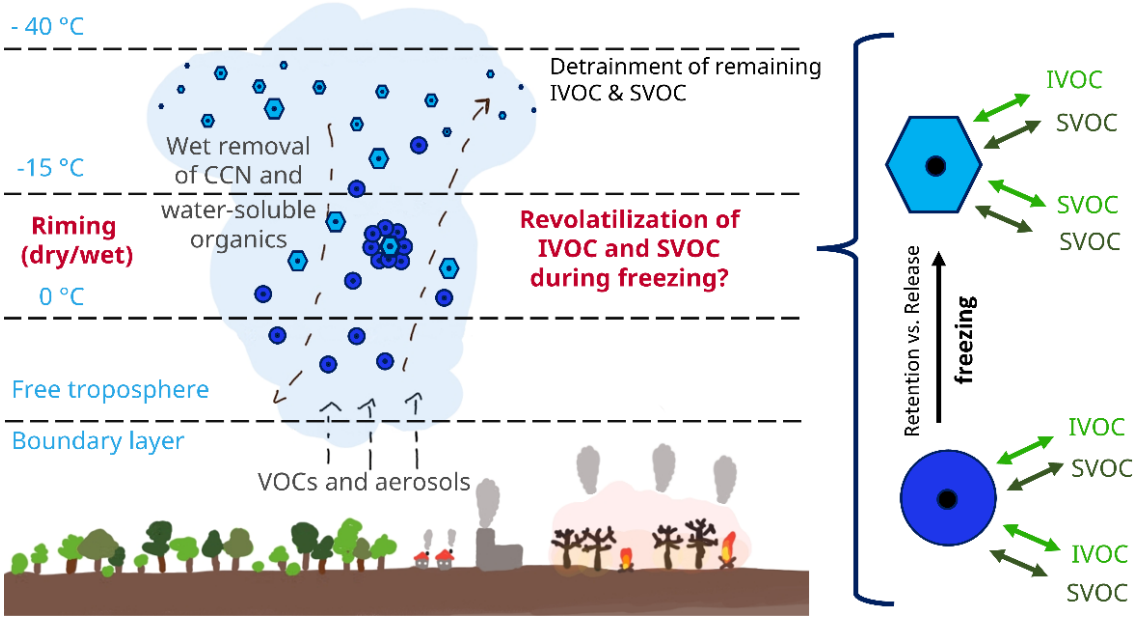

Figure 2.1 : Water-soluble intermediate-volatile and semi-volatile organic compounds (IVOCs and SVOCs) can be dissolved in water droplets (dark blue circles), which can be transported upwards by deep convection. In the mixed-phase zone of the clouds, the water droplets can collide with ice particles (light blue hexagons), resulting in riming.

Figure 2.1 shows vertical transport mechanisms of intermediate-volatile and semi-volatile organic compounds (IVOCs and SVOCs). Organic compounds in the atmosphere can be categorized into different groups depending on their source, such as biogenic, anthropogenic, or compounds originating from the combustion of biomass (Gouw and Jimenez, 2009). Nitro-aromatic compounds can be formed directly from the combustion of coal or wood but can also be formed as secondary products from the reaction of phenols or cresols with NOx (Wang et al., 2020; Harrison et al., 2005). Terrestrial vegetation emits large quantities of volatile organic compounds (VOCs) such as isoprene and various monoterpenes (MTs), with the most important MT, α-pinene contributing around one-third of global MT emissions (Sindelarova et al., 2014). In the atmosphere, oxidation by OH radicals, ozone, or NO_3 radicals results in various products spanning orders of magnitude in volatility. Products such as 2-methyl tetrols, pinanediol, terpenylic acid, pinonic acid, and pinic acid, have been described as major oxidation products (Kołodziejczyk et al., 2020; Bianchi et al., 2019; Nozière et al., 2015; Müller et al., 2012; Kroll and Seinfeld, 2008; Claeys et al., 2004b; Hoffmann et al., 1997). At standard conditions, the saturation vapor pressure of these oxidation products is too large to be relevant for new particle formation. Highly oxygenated organic molecules (HOMs) exhibit a sufficient low vapor pressure for NPF (Bianchi et al., 2019); however, their formation via autoxidation, a rapid OH-radical–induced oxidation process in the atmosphere, is suppressed at low temperatures (Stolzenburg et al., 2018). Hence, the higher-volatility major oxidation products of isoprene and monoterpenes might be relevant for NPF in the upper troposphere, where HOM formation is suppressed and the colder temperatures cause saturation of the major oxidation products, which are classified as SVOCs at standard conditions. Both classes

of compounds focused on in this study, i.e., pinene oxidation products and nitro-aromatic compounds, are IVOCs (saturation mass concentration C^*, $300 < C^* < 3 \cdot 10^6$ µg m^{-3}) or SVOCs ($0.3 < C^* < 300$ µg m^{-3}) (Simon et al., 2020; Andreae et al., 2018).

Water-soluble IVOCs and SVOCs can be dissolved in water droplets (dark blue circles in Figure 2.1), which can be transported upwards via deep convection. In the mixed-phase zone of clouds, retention or release of IVOCs and SVOCs during riming can occur. Riming describes the collision and freezing of supercooled water droplets on the surface of hydrometeors such as a graupel or snowflakes (light blue hexagon in Figure 2.1) which leads to their growth. The organic compounds can be trapped in the ice phase and then washed out by precipitation, or they can return to the gas phase by volatilization during freezing. This revolatilization leads to a vertical redistribution in the atmosphere and could explain the occurrence of semi-volatile organic compounds at high altitudes in regions with deep convection. However, if the organic substances remain in the ice phase during freezing, they could also be transported further upwards and released into the gas phase by sublimation of the ice particles there (Pruppacher and Klett, 2010; Snider and Huang, 1998).

The proportion of the compound that remains in the ice can be described by the retention coefficient *R*, which indicates the relative fraction of the trapped compound with a value between 0 and 1 (Bela et al., 2018; Stuart and Jacobson, 2003; Snider et al., 1992; Iribarne and Pyshnov, 1990). The retention of a compound is influenced by its chemical properties, such as the dimensionless effective Henry's law solubility constant H^*, as well as physical parameters such as temperature, droplet size, liquid water content in the cloud, ventilation, and potentially the pH of the droplet, which also influences H^*. Compounds with a small H^* are more likely to return to the gas phase during riming, which results in a lower retention coefficient. In addition, external conditions have a greater influence on retention for these kind of compounds, which is in contrast to compounds with high H^* (Cuchiara et al., 2023; Jost et al., 2017; Stuart and Jacobson, 2004, 2003).

Previous measurements of inorganic and small organic species in the wind tunnel in Mainz confirm the correlation between H^* and R as well as the stronger dependence of retention on external factors such as temperature for lower H^*. Hydrochloric acid, nitric acid, malonic acid, and oxalic acid are characterized by a high H^* value and remain completely in the ice phase during freezing. Compounds with more moderate H^* values such as ammonia, hydrogen peroxide, formic acid, and acetic acid have retention factors of 0.92 ± 0.21, 0.64 ± 0.11, 0.68 ± 0.09, and 0.72 ± 0.16. Retention of the organic compounds shows a dependence on temperature and ventilation. Additionally, sulfur dioxide shows both the lowest H^* value and retention coefficient (0.46 ± 0.16) of the compounds discussed, with a dependence on external conditions as well (Jost et al., 2017; v. Blohn et al., 2013; 2011).

Up to now, only inorganic and small organic molecules have been investigated with regard to their retention during the freezing process. Measurements of rain, hail and cloud water have already shown that they contain α-pinene oxidation products and nitrophenols (Spolnik et al., 2020; Desyaterik et al., 2013; Ganranoo et al., 2010). It is therefore likely that these

compounds are also present in the supercooled droplets within the mixed-phase zones of clouds. In contrast to the smaller organic molecules and inorganic compounds, the retention coefficients for α-pinene oxidation products and nitrophenols are unknown. In this study, therefore, the retention coefficients of three α-pinene oxidation products (pinonic acid, pinic acid, and pinanediol) and four nitro-aromatic compounds (2-nitrobenzoic acid, 4-nitrocatechol, 4-nitrophenol, and 2-nitrophenol) are investigated in a series of wind tunnel experiments under simulated atmospheric conditions.

2.3 Experimental procedures

2.3.1 Mainz vertical wind tunnel

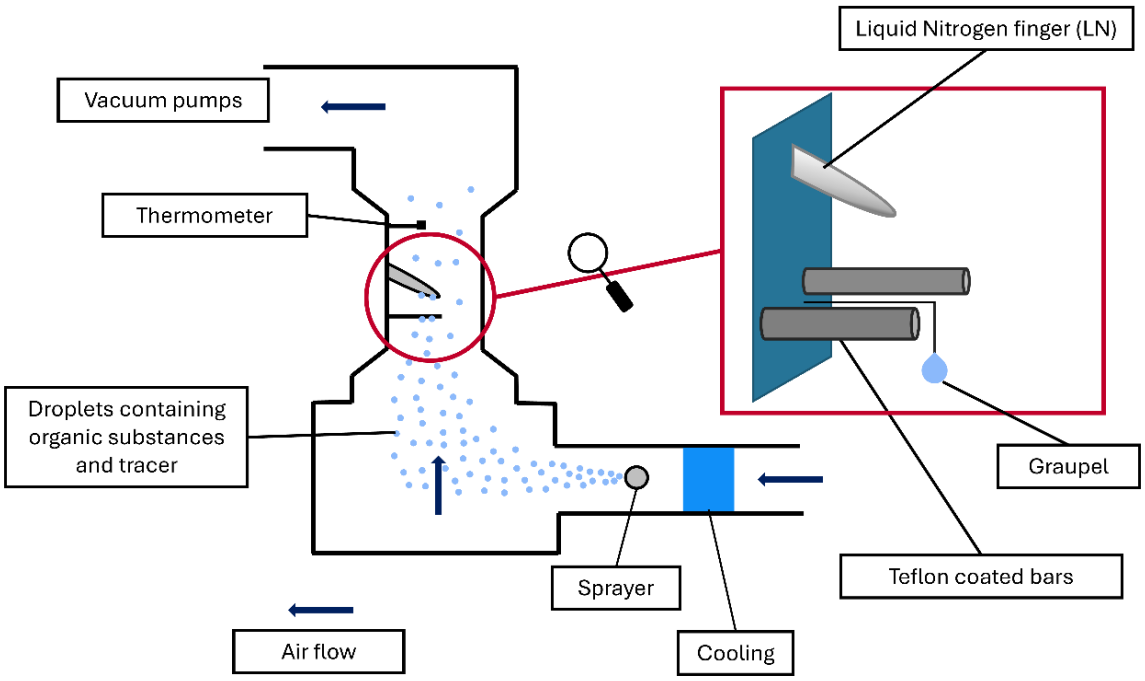

Figure 2.2: Schematic of the wind tunnel. Cooled air transported the generated water droplets containing the compounds into the experimental region (red circle). Red rectangle – the enlarged experimental area shows the three surfaces on which the riming took place: graupel, the liquid nitrogen finger and Teflon-coated bars.

The experiments were carried out in the vertical wind tunnel of Johannes Gutenberg University of Mainz, shown schematically in Figure 2.2. Here, hydrometeors ranging from a few tens of micrometers to centimeters can float freely in a vertical airstream at their terminal fall velocity. The prevailing conditions such as ventilation, mass, and heat transfer are very similar to those in the atmosphere (Pruppacher and Klett, 2010). A vacuum pump continuously sucked dried ambient air through the system to produce an airflow in the wind tunnel. For riming experiments the tunnel was cooled down to −18 °C, and water droplets were produced using up to four spray nozzles. These droplets were transported via the airflow to the experimental region (red circle, zoomed-in: red rectangle in Figure 2.2). In the

experimental region the supercooled droplets collided with three different surfaces—a simulated graupel, a liquid nitrogen finger, and Teflon-coated bars— and froze on the substrate. A detailed description of the experiments is provided in Sect. 2.3.3 Retention measurements. Further details on the wind tunnel can be found in two reviews by Diehl et al. (2011) and Szakáll et al. (2010).

2.3.2 Growth regimes

For riming, a distinction is made between dry and wet growth conditions, which are determined by the combination of temperature, liquid water content and ventilation. During freezing latent heat is released, which warms the surface of the rime collectors. Under dry growth conditions the surface temperature of the rime collector remains well below 0 °C and all the accreted cloud water freezes within some milliseconds on the rime collector, preserving a close-to-spherical shape. The surface temperature increases with increasing liquid water content, droplet size, and collision frequency of the droplets with the hydrometeor. If the temperature rises to a maximum value of 0 °C, wet growth conditions are reached. At this point, not all the water that has collided with the rime collector freezes immediately. During wet growth, the freezing rate of an element of liquid input is rather low in comparison to dry growth conditions, resulting in a dense ice structure (Pruppacher and Klett, 2010; Macklin, 1961; List, 1960).

The earlier wind tunnel measurements on retention coefficients (Jost et al., 2017; v. Blohn et al., 2013; 2011) focused solely on retention during dry growth conditions. Thus, the question of to what extent wet growth conditions affect retention remained. For example, Michael and Stuart (2009) found in their theoretical study that during wet growth conditions, H^* is an important but not a dominant factor. They observed that retention increased with increasing H^* (from 300 to $3 \cdot 10^6$) and then leveled off with further increasing H^*, resulting in low retention values for compounds with high H^* such as HCl. Here other factors like the ice–liquid interface supercooling and the liquid water content are major determiners of the extent of retention. In the present study, the measurements were carried out under dry and wet growth conditions. However, unlike the study of Michael and Stuart (2009), we did not observe the droplets shedding off during these experiments. Calculations of the surface temperature during the growth of graupel reveals that under our wet growth conditions the surface temperature varied between −0.8 and −2.2 °C for −3 and −5 °C ambient temperature, respectively, and had a measured LWC of 2.2 g m^{-3} (Theis et al., 2022; v. Blohn et al., 2009; Pflaum and Pruppacher, 1979). For temperatures higher than −3 °C, no freezing was observed on the Teflon-coated bars and little freezing could be observed on the graupel. During wet growth experiments small cloud droplets coalesced and formed larger millimeter-sized drops before freezing. A photo of an example ice sample is provided in the Supplement (Figure 7.1). This coalescence of droplets during our experiments is representative of the wet growth of graupel rather than the wet growth of hail—where the accreted liquid water is shed off from the surface due to the faster fall speeds.

2.3.3 Retention measurements

Dilute aqueous solutions with different compositions were used for the experiments. Single-component measurements were carried out for the α-pinene oxidation products and 2-nitrophenol. The aqueous solution to be analyzed contained one of the compounds of interest (pinonic acid, pinic acid, pinanediol, or 2-nitrophenol) and sodium bromide (NaBr; Sigma-Aldrich, ≥99 %). For the other nitro-aromatic compounds (2-nitrobenzoic acid, 4-nitrocatechol, and 4-nitrophenol), a mixture of all organics and NaBr was used, an experimental setup that comes closer to the complex conditions in the atmosphere. All samples contained NaBr as an internal standard (IS) to account for dilution and evaporation effects. The retention of NaBr is assumed to be 1; i.e., NaBr remains completely in the droplets during freezing. HCl (30 %) was added if the measurements were carried out at a pH value of 4. The concentrations of the chemicals used are shown in Table 2.1.

Table 2.1: Concentrations of the investigated solutions.

Compound	Concentration (µmol L^{-1})	Label, purity	IS concentration NaBr (µmol L^{-1})
cis-Pinonic acid	10	Sigma Aldrich, 98 %	10
cis-Pinic acid	10	Synthesized, N/A	10
(1R,2R,3S,5R)-(−)-Pinanediol	15	Merck, 99 %	10
2-Nitrophenol	30	Thermo Scientific, 99 %	10
2-Nitrobenzoic acid	10	Thermo Scientific, 95 %	10
4-Nitrocatechol	10	Thermo Scientific, ≥98 %	10
4-Nitrophenol	10	Alfa Aesar, 99 %	10

To generate the supercooled droplets, the solution containing the analyte and the IS was nebulized with a gas stream of nitrogen (>99.8 %) and either two or four spray nozzles depending on the experiment. Two spray nozzles and a nitrogen flow of 20 L min^{-1} were used for dry growth and four spray nozzles and a flow of 24 L min^{-1} for wet growth conditions. The number of spray nozzles influences the liquid water content (LWC) and thus the growth regime.

For dry growth conditions a lower LWC is required, therefore only two spray nozzles were used. The resulting droplet size distribution in the wind tunnel was measured using a custom in-line digital holographic instrument, similar to the "holographic imaging and velocimetry instrument for small cloud ice" (HIVIS) described by Weitzel et al. (2020). The measurements were not taken simultaneously to each retention experiment but measured independently under the same conditions during the retention experiments. After the cloud of droplets was produced, a camera (Basler acA2040) captured the holograms containing the images of the droplets at 90 fps (frames per second). Typical measurement time was 1 minute. Approximately 5400 holograms were reconstructed and analyzed for each measurement with two and four nozzles. Using a telecentric lens with a 0.5 magnification, the pixel size of the holograms was 2.72 µm x 2.72 µm, which yielded a sample area and volume of 5.57 x 5.57 mm^2 and 2.48 cm^3, respectively. For the reconstruction of the holograms, a depth of 8 cm was chosen as this represents the central part of the measurement section where the collectors were exposed to the cloud of supercooled droplets during the experiments. The holograms were reconstructed at each $\Delta z = 100$ µm distance along the optical axis using the method of Fugal et al.(2004). This produced an in-focus image of the droplets independent of their location within the sample volume. The particle sizes were obtained from the particle detection algorithm of Fugal et al. (2009), which determined the normalized number and volume distributions. Figure 2.3 (a) shows the number distribution of the supercooled droplets in the measurement section of the tunnel when two spray nozzles were used. Figure 2.3 (b) shows the volume distribution of the droplets, which represents the normalized cloud liquid water content (LWC) per size interval. We observed no difference in the distribution when using four nozzles (see SI Figure 7.2). The LWC was measured using a dew-point meter (DP3-D/SH, MBW Calibration Ltd., Wettingen, Switzerland) in conjunction with a 5 m long heated pipe. Wind tunnel air was sampled isokinetically through the heated pipe to evaporate the droplets. The absolute humidity was then obtained from the dew point measurement. In a second step, a droplet separator was installed at the inlet to the heated tube to measure the dew point of the wind tunnel air without droplets. The difference between the two absolute humidities gives an LWC of 0.9 ± 0.2 g m^{-3} for dry growth and 2.2 ± 0.2 g m^{-3} for wet growth conditions.

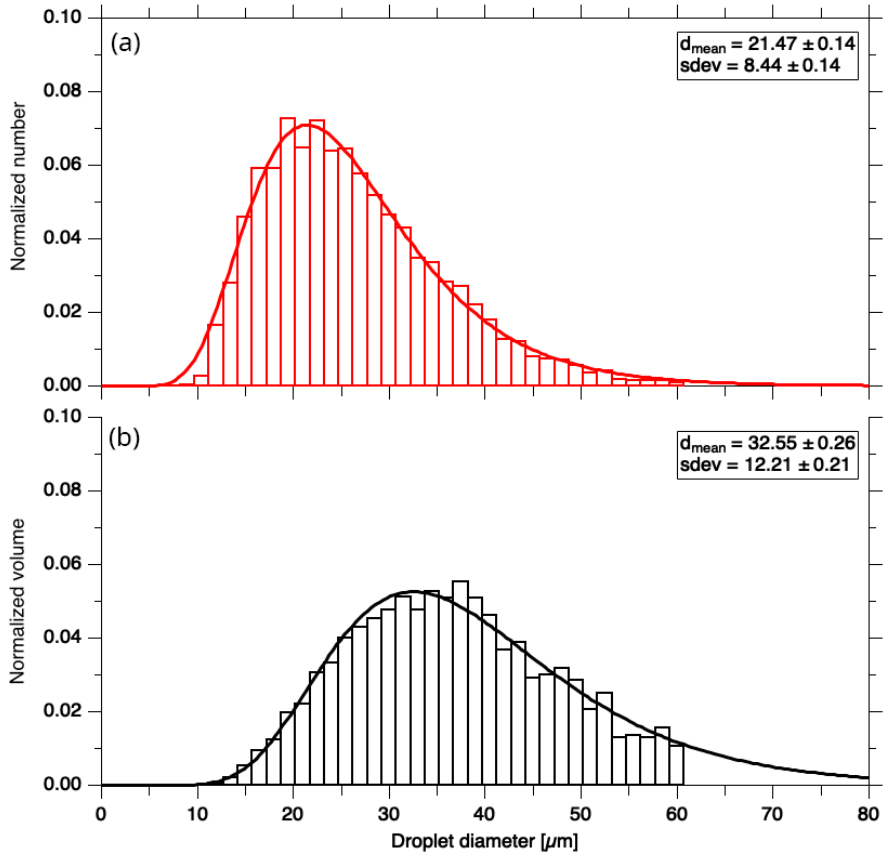

Figure 2.3: Normalized droplet number (a) and volume distribution (b) of the supercooled droplets generated using two spraying nozzles. The lines represent log-normal fit functions.

During retention measurements, the droplets were transported downstream of the sprayer into the experimental section. The distance between the sprayer and the experimental region is approx. 3 m (Jost, 2012). In the experimental section, the supercooled droplets collided with three different surfaces, that were used as rime ice collectors and froze on them. The first surface was a Teflon-coated bar (FEP; outer diameter 6 mm) and the second was an ice sphere (graupel) with a diameter of 7 mm, which comes closer to real atmospheric sizes for graupel. According to the American Meteorological Society glossary of meteorology, graupel is defined as rimed particles with diameters less than 5 mm; larger ones are called hailstones. However, we refer to the particle investigated as graupel according to the flow conditions present rather than the of particle size. The larger diameter was necessary to obtain a sufficient sample volume for analysis. The last surface was a cold tube made of Teflon (PFA) that was constantly filled with liquid nitrogen (LN finger tube). This sample determined the liquid-phase concentration of the droplets immediately before riming occurs. At the surface of the LN finger tube, freezing is so fast that the retention can be assumed to be 1, and the concentration of the droplets can be determined before riming.

To produce the simulated graupel, a silicon mold was filled with ultra-pure water and frozen. The graupel were “captively floated” to avoid the loss of graupel and any contamination on contact with the wind tunnel walls. For this purpose, they were attached to a nylon fiber with a diameter of 80 µm. Under these conditions, the rime collectors were exposed to the airflow

containing the supercooled droplets at 3 m s^{-1}, which corresponds to a typical fall velocity of graupel. (Wang and Kubicek, 2013; Pruppacher and Klett, 2010). The ice samples were collected after each experimental run and stored at -25 °C until they were melted for the chemical analysis.

2.3.4 UHPLC-HRMS analysis

For analysis, the ice samples were melted and filtered through polyamide (PA) membranes (pore size – 0.20 µm; Altmann Analytik) to remove potential particles, without affecting the concentration of the analytes. Analysis was performed in triplicate using a Dionex UltiMate 3000 ultra-high-performance liquid chromatography (UHPLC) system coupled to a heated electrospray ionization source (HESI) or atmospheric pressure chemical ionization (APCI) and with a high-resolution Q-Exactive Orbitrap mass spectrometer (HRMS) (all Thermo Fisher Scientific). A Hypersil GOLD, C18, 50 x 2.0 mm column with 1.9 µm particle size (Thermo Fisher Scientific) was used for the chromatography. Eluent A consisted of 98 % liquid chromatography-mass spectrometry (LC-MS) grade water (Thermo Fisher Scientific) with 0.04 % formic acid and acetonitrile (VWR Chemicals); eluent B consisted of 98 % acetonitrile (ACN) and water, and the injection volume was 5 µL. Different H_2O/ACN gradients were used for the different compounds. For pinonic acid, pinic acid, pinanediol, 2-nitrobenzoic acid, 4-nitrocatechol, and 4-nitrophenol, a flow rate of 0.5 mL min^{-1} and a gradient as described in the following were used: starting with 2 % eluent B isocratically for 1 min, increasing to 20 % B over 2.5 min, then further increasing to 90 % over 1.5 min, after which B was held at 90 % for 4 min, decreased to 2 % over 0.5 min, and held again for 1.5 min. For pinanediol, a post-column flow of 50 mmol L^{-1} NH_4OH in MeOH was added after 1 min at a flow rate of 0.1 mL min^{-1} to enhance ionization. The HESI source was used in negative mode, resulting in the formation of deprotonated molecular ions. Sheath gas and auxiliary gas flow were 40 and 20 a. u.(arbitrary unit), respectively. The temperature of the auxiliary gas heater was 150 °C, and the capillary temperature was 350 °C. The sprayer voltage was set to -4.00 kV.

A different gradient with a flow rate of 0.3 mL min^{-1} was used for 2-nitrophenol. Starting with 2 % eluent B isocratically for 1 min, increasing to 20 % B over 2.5 min, then further increasing to 90 % over 1.5 min, after which B was again held at 90 % for 0.3 min, decreased to 2 % over 0.2 min, and held again for 0.5 min. To further enhance ionization, a post-column flow of 50 mmol L^{-1} NH_4OH in MeOH was added after 1 min at a flow rate of 0.1 mL min^{-1}. The APCI source was used in negative mode, resulting in the formation of deprotonated molecular ions. Sheath gas and auxiliary gas flow were 23 and 5 a. u., respectively. The vaporizer temperature was 375 °C, and the capillary temperature was 350 °C.

2.3.5 Calculation of the retention coefficient

Eq. (2.1) was used for compounds with a retention coefficient *R* close to 1:

$$R = \frac{c_{\text{compound}}^{\text{sample}} / c_{\text{compound}}^{\text{LN}}}{c_{\text{IS}}^{\text{sample}} / c_{\text{IS}}^{\text{LN}}} \quad (2.1)$$

The numerator describes the ratio between the concentration of the compound of interest in the ice sample ($c_{\text{compound}}^{\text{sample}}$) (Teflon coated bars or graupel) and in the LN finger sample ($c_{\text{compound}}^{\text{LN}}$). The denominator describes the same ratio but for the IS ($c_{\text{IS}}^{\text{sample}} / c_{\text{IS}}^{\text{LN}}$). Thus, it is not necessary to consider a dilution, evaporation, and desorption correction as these effects change both the compound and IS concentrations in the nitrogen finger sample accordingly. Therefore, a change in this ratio is solely an effect of the retention of the compound during the riming process.

The calculation is different for compounds with a lower effective Henry's law constant (below 10^4), which leads to higher desorption. These compounds are transferred to the gas-phase in larger amounts before and during the freezing process, resulting in a higher gas phase concentration in the tunnel. Therefore, it cannot be ruled out that the measured concentrations of the LN finger tube samples could be influenced by additional adsorption out of gas-phase components. This would no longer provide a suitable correction for determining the retention coefficient.

As the LN finger sample is not available, the sprayer sample (the solution from which the droplets are produced) is used instead. As the distance between the two sampling points (sprayer and graupel/bar) is large, it is necessary to determine the amount of compound that is transferred to the gas phase before freezing. The desorption correction coefficient *D* (see Supplement Eq. (7.1)) will be utilized. A detailed description of the desorption correction coefficient can be found in the Supplement.

To calculate the retention coefficient *R* for compounds with a lower retention coefficient, Eq. (2.1) was extended to include the desorption correction coefficient using the sprayer solution sample instead of the LN finger (see Eq. (2.2)):

$$R = \frac{c_{\text{compound}}^{\text{sample}} / c_{\text{compound}}^{\text{sprayer}}}{c_{\text{IS}}^{\text{sample}} / c_{\text{IS}}^{\text{sprayer}} \cdot D} \quad (2.2)$$

Equation 2.1 and 2.2 yield identical results for compounds with a desorption correction coefficient of approximately 1. This is illustrated using pinic acid as a representative example in the Supplement (Figure 7.3).

2.4 Results and discussion

2.4.1 Retention measurements

The results of the retention measurements for the α-pinene oxidation products are shown in Figure 2.4; those for 4-nitrocatechol, nitrobenzoic acid, and 4-nitrophenol are shown in Figure 2.5; and the desorption-corrected *R* for 2-nitrophenol in Figure 2.6.

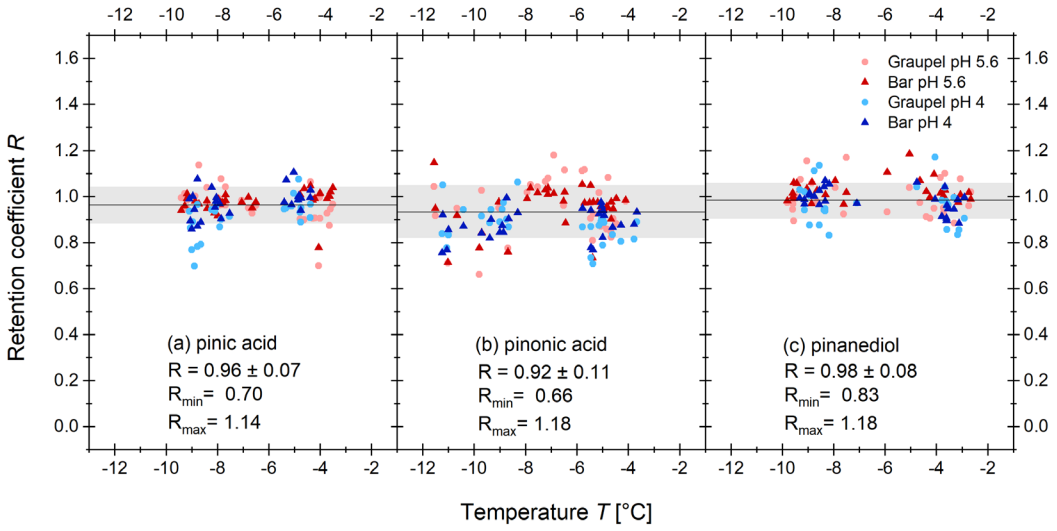

Figure 2.4: Experimentally determined retention coefficients of (a) pinic acid, (b) pinonic acid, and (c) pinanediol as a function of the temperature during the experiment for different rime collectors. The circles represent the graupel samples and the triangles the Teflon-coated bars. For the blue symbols, the pH was adjusted to 4 by adding HCl (30 %), the red symbols are without adding HCl. The solid black line represents the mean of all measurements, and the gray area represents 1 standard deviation.

2.4.1.1 Pinic acid and pinonic acid

Figure 2.4 shows the results for (panel a) pinic and (panel b) pinonic acids. Pinic acid and pinonic acid both show no pH dependence, temperature dependence, or influence from the rime regime. This agrees with the earlier findings for compounds with high H^*. The retention coefficients for pinic acid vary between 0.70 and 1.14 with a mean value of 0.96 ± 0.07. For pinonic acid, a mean retention coefficient of 0.92 ± 0.11 was determined. The variation in the measured values of *R* is greater than that for pinic acid and lies between 0.66 and 1.18. This is probably due to the lower H^*, which makes pinonic acid more sensitive to slight changes in the experimental conditions. The scatter of the values is comparable to that observed in other studies on retention. Theoretical and experimental studies have demonstrated that the retention of compounds with a low H^* is dependent on the freezing conditions (Jost et al., 2017; v. Blohn et al., 2013; 2011; Stuart and Jacobson, 2004, 2003). The results shown here indicate that slight differences in freezing conditions across the experiments may exert an influence on the retention of compounds despite their high H^* values.

2.4.1.2 Pinanediol

The results for pinanediol are depicted in Figure 2.4 (c). No effect on the investigated parameters could be found for this diol. The mean retention coefficient was 0.98 ± 0.08 with a minimum value of 0.83 and a maximum value of 1.18, which is an exception to previous findings (Jost et al., 2017). In comparison to pinic and pinonic acid, pinanediol showed a lower H^* (see Table 2.3). A lower retention coefficient is expected for compounds in this range as well as a dependence on temperature. However, no temperature, pH, or growth regime dependence was seen. This deviation from the expected behavior could be because the Henry's law constant for pinanediol is estimated using the bond method implemented in the HENRYWIN™ software as part of EPI Suite™. The bond method breaks down the molecule into a sum of the individual bonds that make up the compound. The exact structure and spatial orientation of the molecule is not considered. Due to the large deviations of the polyols in the original method by Hine and Mookerjee (1975), further correction factors were included in the method. However, the predictions are less accurate for molecules with a more complex structure (Meylan and Howard, 1991; Hine and Mookerjee, 1975). Pinanediol is a cyclic diol. Due to its capped ring form, it is sterically hindered, and thus the potential interactions between the OH groups are not considered by the model. Since there are no experimental data for the Henry's law constant, there is no current alternative to the estimation.

2.4.1.3 4-Nitrocatechol and 4-nitrophenol

The results for 4-nitrocatechol and 4-nitrophenol are shown in Figure 2.5 (a) and Figure 2.5 (b). Overall, no pH or temperature dependence is recognizable. Furthermore, no difference between wet and dry growth conditions can be observed. This agrees with the current literature. As Stuart and Jacobson (2004, 2003) have shown, a temperature or pH dependence is not expected for compounds with high effective Henry's law constants, such as 4-nitrocatechol or 4-nitrophenol. Mean retention coefficients of 1.01 ± 0.14 and 1.01 ± 0.07 were determined for 4-nitrocatechol and 4-nitrophenol, respectively. For 4-nitrocatechol, the derived retention coefficients showed a large scatter that has no current explanation. A minimum value of 0.63 and a maximum value of 1.41 was obtained. 4-Nitrophenol showed a smaller scatter with values between 0.79 and 1.28.

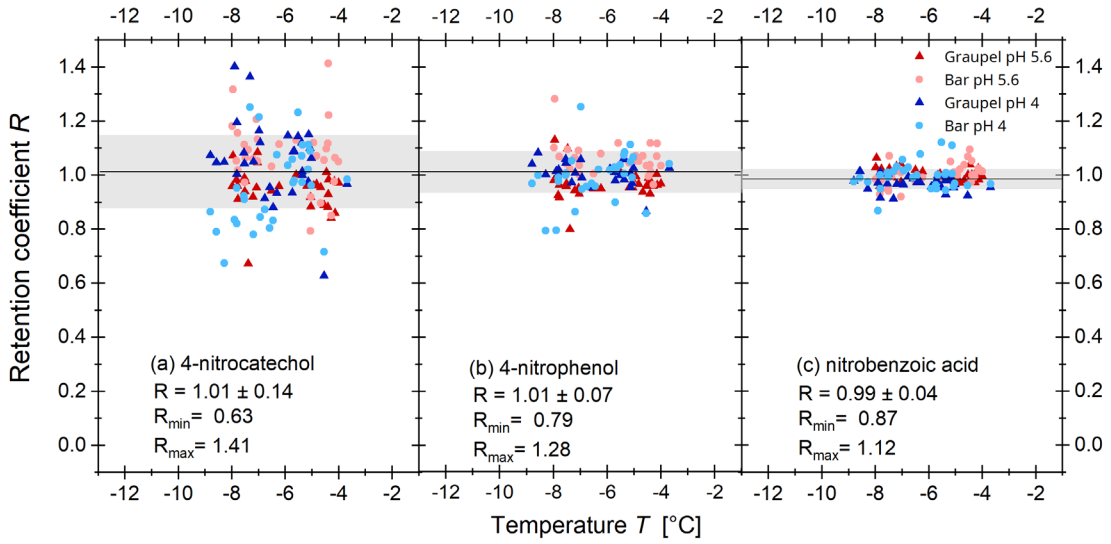

Figure 2.5: Experimentally determined retention coefficients of (a) 4-nitrocatechol, (b) 4-nitrophenol, and (c) nitrobenzoic acid as a function of the temperature during the experiment for different riming collectors. The circles represent the graupel samples and the triangles the bars. For the blue symbols, the pH was adjusted to 4 by adding HCl (30 %), the red symbols are without adding HCl. The black line represents the mean of all measurements, and the gray area represents 1 standard deviation.

2.4.1.4 2-Nitrobenzoic acid

For 2-nitrobenzoic acid in Figure 2.5 (c), no dependence on the investigated parameters was found. The average retention coefficient is 0.99 $\pm$ 0.04, with the lowest scatter among the measured compounds. The smallest value measured was 0.87 and the largest 1.12. This is probably because 2-nitrobenzoic acid has the lowest pK_a value of all the compounds studied. In the pH range investigated, most of the 2-nitrobenzoic acid molecules are deprotonated, unlike the other components studied. This makes a transition into the gas phase less likely, and therefore small differences in the measurement conditions have less influence on the results.

2.4.1.5 2-Nitrophenol

2-Nitrophenol (Figure 2.6) showed significantly lower retention coefficients than the other compounds presented above. The retention coefficients shown here are desorption corrected according to Eq. 2.2. At pH 4, the different rime collectors (Teflon-coated bar, graupel) showed a statistically significant (significance level $\alpha = 0.05$) negative temperature dependence (lines and equations in Figure 2.6; Table 2.2). The bar samples show a slightly stronger temperature dependence than the graupel samples. This is probably due to the metal rod inside the Teflon-coated bar and the resulting faster heat transfer. It is also noticeable in these measurements that the graupel samples (light red and light blue circles in Figure 2.6 (b)) have an overall lower retention coefficient than the bar samples (red and blue triangles in Figure 2.6 (a)). This might also be explained by the metal rod inside the Teflon-coated bar. The faster

heat transfer leads to a shorter freezing time and thus to a higher retention coefficient. At a pH value of 5.6, no statistically significant negative temperature trend could be determined. This could be attributed to the greater scattering of the values, which is presumably caused by fluctuations in the conditions in the wind tunnel and slight variations in the pH value of the solution utilized. The fluctuation in the values could conceal an existing temperature trend.

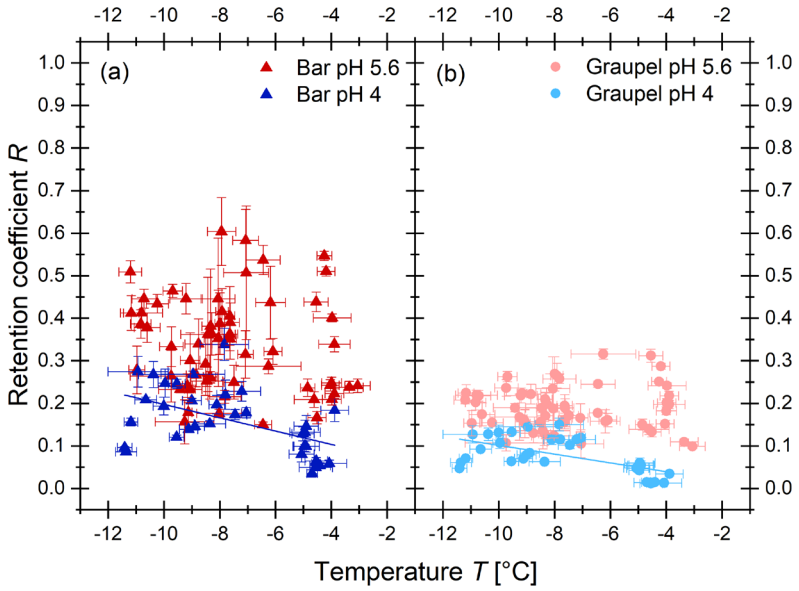

Figure 2.6: Experimentally determined desorption-corrected retention coefficients of 2-nitrophenol as function of the temperature during the experiment for different rime collectors. The triangles represent the Teflon-coated bar samples (a) and the circles the graupel (b). For the blue symbols, the pH was adjusted to 4 by adding HCl (30 %); the red symbols are without adding HCl. The line represents a linear fit.

The data points (Figure 2.6) below −6 °C were obtained from dry growth conditions, while the ones higher than that represent wet growth conditions. A closer inspection of the data reveals that the temperature dependency might also be a result of the riming regimes. When separating the data between the two regimes, the temperature dependency vanishes. Therefore, the difference in retention values between wet and dry growth conditions might be due to the longer freezing times of the accreted and coalesced droplets. The droplets accreted during the wet growth regime remained liquid for some time and formed a larger millimeter-sized drop before they froze. This means that dissolved 2-nitrophenol was able to further desorb from the drops before ice shell formation occurred, which reduces further expulsion from the freezing droplet. This resulted in slightly lower retention values for the rime collectors grown during wet growth. Considering the absolute retention values for wet growth, it becomes apparent that 2-nitrophenol will not be retained in atmospherically significant amounts during wet growth conditions. However, as the values between dry and wet growth overlap within the experimental uncertainty, a temperature dependency is provided here, which is applicable within the investigated temperature and growth condition range simulated in the present study. As the temperature dependence in the analyzed range

has only a minor influence on the retention compared to the data scattering, the mean values were determined for all sets of measurements. The mean retention coefficients for the various riming conditions are shown in Table 2.2. The overall mean retention coefficient was determined to be 0.21 ± 0.12. The measured values of R were between a minimum of 0.01 and a maximum of 0.60.

In addition to the dependence on temperature, growth regime, and the riming collectors already discussed, the pH dependence was also analyzed as retention is also strongly dependent on the dissociation of the molecules. As the retention for the rime collectors is different, the comparisons are only carried out within the same collectors. The mean retention coefficients for the graupel samples at pH 5.6 and pH 4 were 0.19 ± 0.05 and 0.08 ± 0.04, respectively. At pH 5.6 it is more likely that 2-nitrophenol is dissociated in comparison to at pH 4. A dissociated molecule needs to be neutralized by a proton before leaving the droplet during riming. At pH 5.6, more molecules are available that do not evaporate without recombination, which might explain the higher retention coefficient.

Table 2.2: Measured retention coefficients of 2-nitrophenol and their temperature dependencies.

Conditions	Mean retention coefficient R	Temperature dependency of R
Bar pH 5.6	0.34 ± 0.11	-
Graupel pH 5.6	0.19 ± 0.05	-
Bar pH 4	0.16 ± 0.07	$R_{B_4} = (-0.016 \pm 0.005)\,T + (0.041 \pm 0.037)$
Graupel pH 4	0.08 ± 0.04	$R_{G_4} = (-0.010 \pm 0.002)\,T + (-0.002 \pm 0.019)$

2.4.2 Relationship between the Henry's law constant and retention

Jost et al. (2017) have shown a correlation between the retention coefficient R and the dimensionless effective Henry's law constant H^* ($H^* = K_H \cdot \bar{R}T$, with K_H – effective Henry's law constant; $\bar{R}$ – gas constant; and T – temperature) for inorganic and small organic molecules, which can be described by Eq (2.3).

$$R(H^*) = \left(1 + (a\,/\,H^*)^b\right)^{-1}, \tag{2.3}$$

where R is the retention coefficient, H^* is the dimensionless effective Henry's law constant, and a and b are constants that are determined by a fit. To test whether this relationship is also applicable to the larger organic molecules investigated here, the mean values of retention coefficients of the compounds were plotted against their dimensionless effective Henry's law constants (Figure 2.7). H^* was determined for the investigated pH values and at 298 K. Since

most of the compounds analyzed in this study did not show any pH dependence within the pH range of 4-5.6, a pH value of 4 was used for the calculation of H^* for these compounds. This is a typical value found in cloud water samples (Pye et al., 2020; Löflund et al., 2002). For 2-nitrophenol, the mean retention coefficient for each of the pH values (pH 4 and 5.6) was calculated and plotted (Figure 2.7). The fact that a pH dependence was only found for 2-nitrophenol is consistent with the literature. A pH dependence is only to be expected for compounds with low H^*. Additionally, a dependence is expected primarily in a pH range near the pK_a value, as the impact on the ratio between dissociated and non-dissociated molecules is most pronounced in this range (Reijenga et al., 2013; Stuart and Jacobson, 2003). The pK_a values of pinic acid and pinonic acid are the most similar to the investigated pH values. However, the H^* values seem to be too high to detect an influence of pH on the measurements. The calculated values of H^* are listed in Table 2.3. Since there are no measured Henry's law constants nor reaction enthalpies for some of the more complex organic compounds, these were predicted using the bond method of the HENRYWIN™ software which provides the values for 298 K.

Table 2.3: Retention coefficient of the measured compounds and their pK_a values, Henry's law constants, and dimensionless effective Henry's law constants at 298 K and pH 4 for all compounds except 2-nitrophenol (pH 4 and 5.6).

Compound	Mean retention coefficient R	Acid dissociation constant pK_a	Henry's law constant[1] / M atm^{-1}	Dimensionless effective Henry's law constant
4-Nitrocatechol	1.01 ± 0.14	7.23[2]	$4.35 \cdot 10^9$	$1.06 \cdot 10^{11}$
2-Nitrobenzoic acid	0.99 ± 0.04	2.17[3]	$2.08 \cdot 10^6$	$3.49 \cdot 10^9$
cis-Pinic acid	0.96 ± 0.07	4.64[2]	$1.02 \cdot 10^8$	$3.06 \cdot 10^9$
cis-Pinonic acid	0.92 ± 0.11	5.19[4]	$1.12 \cdot 10^6$	$2.93 \cdot 10^7$
4-Nitrophenol	1.01 ± 0.07	7.15[3]	$4.52 \cdot 10^5$	$1.11 \cdot 10^7$
(−)-Pinanediol	0.98 ± 0.08	14.68[2]	$4.08 \cdot 10^3$	$9.97 \cdot 10^4$
2-Nitrophenol (pH 5.6)	0.27 ± 0.11	7.23[3]	$1.43 \cdot 10^2$	$3.50 \cdot 10^3$
2-Nitrophenol (pH 4)	0.12 ± 0.07	7.23[3]	$1.43 \cdot 10^2$	$3.58 \cdot 10^3$

[1] Calculated using US EPA. [2012]. Estimation Programs Interface Suite™ for Microsoft® Windows, v 4.11. United States Environmental Protection Agency, Washington, DC, US; [2] Calculated using Advanced Chemistry Development (ACD/Labs) Software V11.02 (© 1994-2024 ACD/Labs); [3] (Haynes, 2014); [4] (Kołodziejczyk et al., 2019).

The compounds measured in this study are the colored, filled symbols in Figure 2.7; the ones measured by Jost et al.(2017), v. Blohn et al. (2013; 2011) and in earlier investigations in the wind tunnel are the gray, half-filled symbols. The dashed gray line represents the fit for the gray, half-filled symbols, i.e. previous measurements. Since the retention of formaldehyde, as shown in Jost et al. (2017), depends on not only on H^* but also the hydration to the diol, the value is not taken into account when determining the fit. The resulting parameters are $a_{\mathrm{gray}} = (2.41 \pm 1.06) \cdot 10^4$ and $b_{\mathrm{gray}} = 0.27 \pm 0.04$. The solid red line is the new fit function in which all compounds are considered. Here again formaldehyde was not included into the fit. Pinanediol was also excluded from the fit as it appears to be an outlier (see Sect. 2.4.1.2). The values $a_{\mathrm{red}} = (3.34 \pm 1.61) \cdot 10^4$ and $b_{\mathrm{red}} = 0.36 \pm 0.06$ result for the fit function.

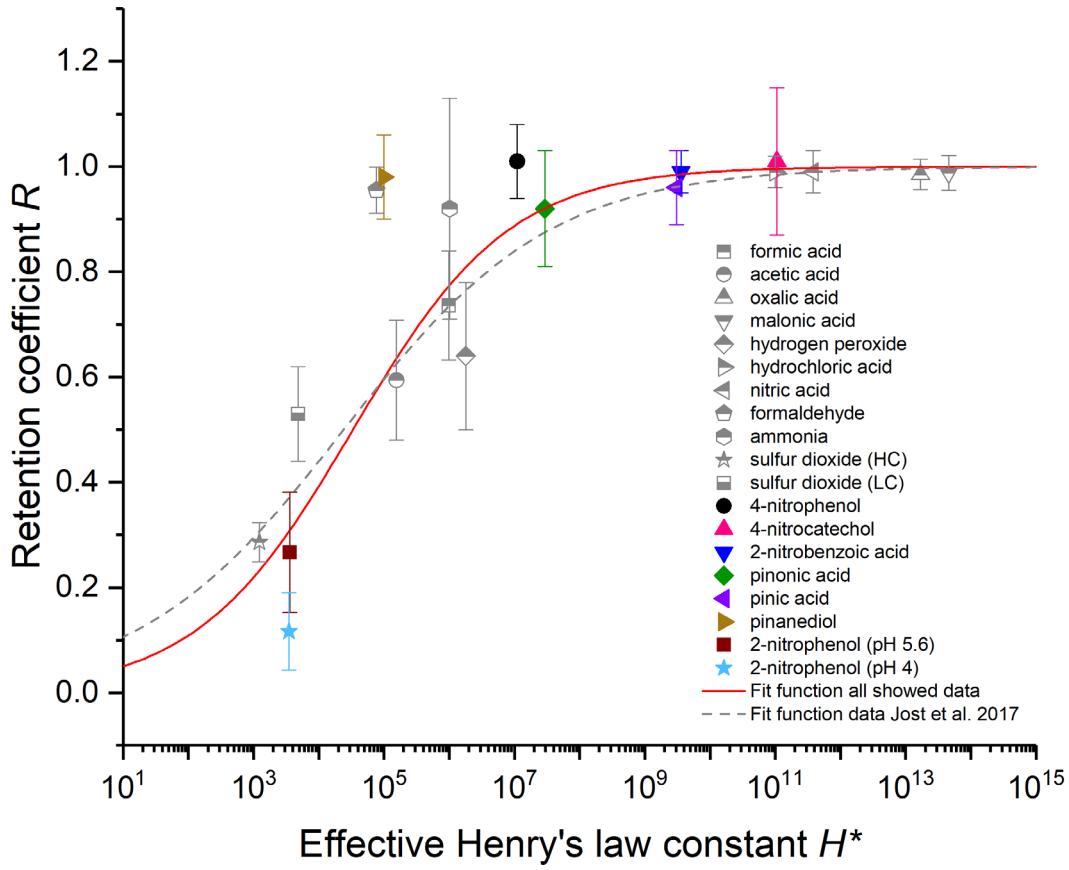

Figure 2.7: Measured retention coefficients as a function of H^*. Colorful filled symbols – compounds investigated in the present study. Gray symbols – wind tunnel data from earlier studies (Jost et al., 2017; v. Blohn et al., 2013; v. Blohn et al., 2011) Solid red line – new fit to wind tunnel data. Dashed gray line – fit of the gray data points only.

As Figure 2.7 shows, the retention coefficients of larger organic molecules do also scale with H^* which agrees with the previous measurements. Only pinanediol and formaldehyde do not fit at first glance. A comparison of the new fit function (solid red line) with the values already known from the literature (dashed gray line) shows that the inflection in the fit function is steeper than was previously assumed. Our results show that the retention of compounds with an H^* below 10^3 is close to 0; i.e., most of the compound dissolved in water is released into the gas phase during riming. This is also evident from the equilibrium distribution of species between the liquid and gas phase in a confined system, which is a function of the LWC (see Supplement Figure 7.9). For species with $H^* < 10^4$ just a maximum of 10 % is present in the liquid droplets, even for LWCs of up to 10 g m^{-3}, which are only reached within severe storms (Lohmann et al., 2020). For $H^* > 10^3$ the compounds are present in significant amounts. For compounds with an H^* value above 10^8, a retention of 1 is expected with most of the compound remaining in the ice phase during freezing. This finding is in accordance with the literature. Stuart and Jacobson (2004) suggest a threshold value between 10^6 and 10^{10} M/atm for dry growth riming, which is on the same order of magnitude as the values presented here. For the compounds in-between 10^3 and 10^8, the retention coefficient is highly dependent on H^*. However, the retention estimation is still afflicted by some degree of uncertainty especially in this H^* range. A close inspection of the data shows that it is not obvious that pinanediol and formaldehyde are outliers. It might also be that the transition from low to high retention values occurs in a smaller range of H^*, and retention is 1 already for $H^* > 10^5$. We cannot ultimately clarify the steepness of the curve, and the limiting regimes might be closer than assumed here. Jost et al. (2017) argued that formaldehyde cannot be explained solely by H^*, and aqueous-phase kinetics must be considered. However, such explanations are lacking for pinanediol. This might indicate that the transition from low to high retention values occurs at lower H^*. Support for that is given from the fit when taking all measurements into account, i.e., also formaldehyde and pinanediol (see Supplement Figure 7.10). To finally answer the question about the transition behavior of the function, further retention measurements in the range $10^4 < H^* < 10^6$ are needed. However, to our current knowledge, and particularly because of the lack of reliable measurements of H^* for pinanediol, we believe that the parameterization given above (Eq. (2.3), with $a_{\mathrm{red}} = (3.34 \pm 1.61) \cdot 10^4$ and $b_{\mathrm{red}} = 0.36 \pm 0.06$ is most trustworthy to calculate retention in the transition regime.

2.5 Conclusions

Wind tunnel experiments were carried out in the vertical wind tunnel of Johannes Gutenberg University, Mainz to determine the retention coefficients R of three α-pinene oxidation products and four nitro-aromatic compounds. The experiments were performed in the temperature range from -12 to -3 °C with a liquid water content of $0.9 \pm 0.2\ \mathrm{g\,m^{-3}}$ and $2.2 \pm 0.2\ \mathrm{g\,m^{-3}}$ to represent dry and wet growth conditions and to simulate mixed-phase cloud conditions. The wind speed ($3\ \mathrm{m\,s^{-1}}$) was chosen to match the typical fall velocity of graupel. The temperature and pH dependences (pH 4 and 5.6) of the compounds were

studied, as well as the dependence on the growth regimes. Two different rime collectors were also considered: a Teflon-coated metal bar and graupel. Stuart and Jacobson (2004; 2003) hypothesized a dependence on external influences such as temperature and pH for compounds with a low dimensionless effective Henry's law constant H^*. Of the compounds investigated, 2-nitrophenol has the lowest H^*. In agreement with the current literature, the retention coefficients of 2-nitrophenol determined show a significant dependence on pH and on the type of rime collector. The mean retention coefficients for the graupel samples are $R_{G5.6} = 0.19 \pm 0.05$ (pH 5.6) and $R_{G4} = 0.08 \pm 0.04$ (pH 4). This indicates that changes in the pH value can influence retention and must be taken into account. At pH 4, 2-nitrophenol also showed a dependence between dry and wet growth conditions. The temperature dependence and the dependence on growth conditions seem to overlap, as the growth conditions differ in not only in liquid water content but also temperature. Since the measured values between dry and wet growth overlap within the experimental uncertainty, a temperature dependence is reported in this study. The higher scattering of the values obtained from the measurements with pH 5.6 could be the reason why the temperature trend and the difference between the growth regimes found at pH 4 are not visible at pH 5.6.

2-Nitrobenzoic acid, 4-nitrophenol, and 4-nitrocatechol showed retention coefficients of 0.99 ± 0.04, 1.01 ± 0.07, and 1.01 ± 0.14, respectively, with no significant dependence on temperature, pH, type of rime collector, or growth-regime. For *cis*-pinic acid and *cis*-pinonic acid, retention coefficients of 0.96 ± 0.07 and 0.92 ± 0.11 were obtained, which also showed no dependence on the parameters investigated. This study shows that there appears to be no difference between dry and wet growth conditions for compounds with a high effective Henry's law constant and that H^* can also be used to estimate retention coefficients for wet growth conditions, at least for graupel and the ambient conditions used in this study (wet growth conditions – ambient temperature of −3 and −5 °C, LWC of 2.2 g m^{-3}, surface temperature of −0.8 and −2.2 °C, and no shedding of water). This is in contrast to a modeling study by Michael and Stuart (2009), which indicates a lower influence of H^* and low retention coefficients even for compounds with high H^* under wet growth conditions for hailstones. However, it should be noted that in this study, hail was investigated at a surface temperature of 0°C with a shedding of water. It is therefore possible that the differences in the experimental conditions are responsible for the discrepancies in the observed outcomes. The retention coefficient for pinanediol was determined to be 0.98 ± 0.08 with no significant temperature dependence. This was not expected due to the comparably low H^*. However, the Henry's law constant is only predicted and may be subject to errors due to the specific structure of the molecule. For this reason, it is important to determine Henry's law constants of more and different molecules to aid in the understanding and modeling of processes in the atmosphere.

The retention coefficients for 4-nitrophenol and 2-nitrophenol differ considerably. Since they are structural isomers, it is obvious that they have the same molecular formula and the same functional groups, although they are arranged differently. The different arrangement allows for the formation of an intramolecular hydrogen bond between the OH and the nitro group in 2-nitrophenol. This can result in the non-dissociated form being stabilized, which may explain

why 4-nitrophenol exhibits greater solubility than 2-nitrophenol. This could be due to the fact that 4-nitrophenol undergoes easier solvation and displays the capacity to form intermolecular hydrogen bonds. This property may also be responsible for the observed differences in Henry's law constants and retention (Achard et al., 1996; Schwarzenbach et al., 1988). In contrast to the bond method used in this study, the group method of the HENRYWIN™ software predicts the same Henry's law constant for both isomers. This clearly shows the importance of reliable prediction or measurement of H^* and the importance of chemical structure.

We demonstrated here that the retention coefficients of more complex organic molecules depend mainly on the dimensionless effective Henry's law constant. These experiments have improved the parameterization of retention coefficients using the dimensionless effective Henry's law constant. The results show that the retention of compounds with an H^* below 10^3 is not a significant factor, and thus most of the compound dissolved in the supercooled drops is released into the gas phase during freezing. For compounds with an H^* value above 10^8, retention close to 1 is expected, and the compound remains completely in the ice phase during freezing. These compounds can be effectively washed out by precipitation or transported further upwards and released by sublimation of the ice particles. At high altitudes and low temperatures, the volatility of these compounds is even lower, and it is possible that particulate residuals form after sublimation. This probably has an impact on the chemistry of the upper troposphere and ultimately on the Earth's radiative budget. In the intermediate range of H^*, the improved fit of R vs H^* (Eq. (2.3), with $a_{\mathrm{red}} = (3.34 \pm 1.61) \cdot 10^4$ and $b_{\mathrm{red}} = 0.36 \pm 0.06$) can be used to estimate the retention coefficient and thus further improve cloud models that account for transport of organic trace components. However, the present results show that more retention measurements are needed for compounds with $10^4 < H^* < 10^6$ to clarify the sharpness of the transition between the two boundaries of zero retention and full retention.

Data availability

Data are available upon request from the corresponding author, Thorsten Hoffmann (t.hoffmann@uni-mainz.de).

Author contribution

CB, JS, MG, KD, YM, AA, LG, AT, AV, and TH designed and performed the wind tunnel experiments; FU synthesized pinic acid; CB performed the analytical measurement, analyzed the data and wrote the manuscript draft; and JS, MG, MS, AT, AV, and TH reviewed and edited the paper.

Competing interests

The authors declare that they have no conflict of interest.

Financial support: This research has been supported by the Deutsche Forschungsgemeinschaft (grant. no. TRR 301 – project-ID 428312742).

This open-access publication was funded

by Johannes Gutenberg University Mainz.

Review statement. This paper was edited by Anne Perring and reviewed by Jefferson Snider and Amy L. Stuart.

3. Height-selective drone-based measurements of aerosol particles

This chapter has been published as preprint in *Atmospheric Measurement Techniques (Borchers et al., 2025)*:

Development and use of a lightweight sampling system for height-selective drone-based measurements of organic aerosol particles

Christine Borchers, Lasse Moormann, Bastien Geil, Niklas Karbach and Thorsten Hoffmann

3.1 Abstract

Organic aerosols (OA) are introduced into the atmosphere from a variety of natural or anthropogenic sources. Especially in the sub micrometer range, the organic fraction contributes to a large proportion of the particle mass and thus has an impact on climate and air quality. To gain insights into sources and sinks and the significance of dispersion, mixing and ageing processes for OA, vertical profiling of the concentration of organic aerosols is particularly helpful. Therefore, the aim of this study is to present an aerosol particle sampler that is suitable to be used onboard uncrewed aerial vehicles (UAVs). The sampler consists of a three-dimensionally printed filter holder connected to a lightweight high-performance pump that can generate a flow rate of up to 19 L min^{-1} for up to 30 minutes. The sampler was characterized and applied on a proof-of-concept study during the BISTUM23 campaign in August 2023 in Southern Germany. Vertical profiles were measured with three samplers mounted on ground and drones and collected aerosol particles in an altitude of 1.5 m, 120 m and 500 m above ground level simultaneously. The filters were analyzed with UHPLC-HRMS, and a targeted approach was used to determine vertical profiles and diurnal trends of biogenic, anthropogenic and biomass burning marker compounds. A non-targeted analysis revealed a high number of CHO-containing compounds, which were oxidized to a greater extent during the course of the day and at increasing altitudes. The system presented here provides a comparatively simple and cost-effective way to sample OA at different altitudes and at different locations and thus obtain vertical concentration profiles of the organic aerosol composition.

3.2 Introduction

Organic aerosol particles (OA) are accountable for a large proportion (20–90%) of the sub-micron particle mass in the lower troposphere. They affect air quality, climate and human health (Benoit et al., 2023; Jimenez et al., 2009; Kanakidou et al., 2005). Primary organic aerosols (POA) are emitted directly, for example from biogenic sources such as plant debris or in the form of spores, bacteria or viruses, or from sources that are mostly anthropogenic such as combustion processes. Secondary organic aerosols (SOA) are formed by oxidation of volatile organic precursors and subsequent condensation of the products (gas-to-particle conversion) (Reddington et al., 2011; Kroll and Seinfeld, 2008; Kerminen et al., 2005). The chemical composition of OA provides information on the individual sources and source processes (Gouw and Jimenez, 2009). Nitroaromatic compounds, for example, are released during the combustion of coal or wood, and are contained in vehicle exhaust gases. They can also be formed as secondary products from the reaction of phenols or cresols with NO_x (Wang et al., 2020; Harrison et al., 2005; Lu et al., 2019). The combustion of lignocellulose, the most abundant biomass resource on Earth, leads to the production of phenolic compounds with aldehyde functionalities, including 4-hydroxybenzaldehyde, vanillin and syringaldehyde. Phenol aldehydes can be oxidized in the atmosphere by OH radicals, NO_3 radicals or ozone, leading to the production of carboxylic acids (Cao et al., 2022; Rana and Guzman, 2022; Net et al., 2011). Vegetation on Earth emits large amounts of volatile organic compounds (VOCs) such as isoprene and various monoterpenes (MTs), with the most important MT, α-pinene, accounting for about one third of global MT emissions (Sindelarova et al., 2014). In the atmosphere, oxidation by OH radicals, NO_3 radicals or ozone leads to various products that differ in their volatility by several orders of magnitude. Products such as 2-methyl tetrols, terpenylic acid, terebic acid, and pinonic acid are described as the main oxidation products (Kołodziejczyk et al., 2020; Bianchi et al., 2019; Nozière et al., 2015; Müller et al., 2012; Kroll and Seinfeld, 2008; Claeys et al., 2004b; Hoffmann et al., 1997). It can be concluded that the elucidation of the chemical composition of OA can provide valuable information about the sources, source strengths and processing of organic aerosol components, such as the contribution of biogenic sources in terrestrial ecosystems or the role of anthropogenic contributions to organic aerosols.

The implementation of atmospheric concentration measurements in the form of vertical gradient measurements offers several advantages: firstly, measurements at multiple heights allow the identification of sources and sinks, as they can distinguish between local plumes and emission sources at ground level and atmospheric background concentrations. The latter are particularly characterized by aging in the case of OA (Li et al., 2024). Vertical profiling can also be used to investigate the transport and distribution of OA. Therefore, many monitoring stations also perform atmosphere-related observations from tall towers, as they enable measurements at several heights within the planetary boundary layer or even beyond, and can thus reflect both local processes at lower altitudes and regional influences at higher altitudes (Li et al., 2024; Mikhailov et al., 2017; Andreae et al., 2015; Williams et al., 2011).

This is where drones can also be used without the need for a suitable tower infrastructure. The use of miniaturized sampling systems in conjunction with drones has attracted considerable attention in recent years (Böhmländer et al., 2024). Compared to conventional sampling methods that use towers, balloons or aircraft, these systems offer the advantages of smaller size, environmental friendliness and the ability to collect samples in remote locations that are difficult to access (Thivet et al., 2024; Pusfitasari et al., 2022; Lan et al., 2020; Bieber et al., 2020).

The aim of this proof-of-concept study was therefore to develop a new low-cost and lightweight aerosol sampling system for drones. To do this, a filter holder was designed and produced using 3D printing and connected to a lightweight high-performance pump. The sampled filters were then extracted and analyzed using UHPLC-MS. The system was characterized and vertical concentration profiles of OA compounds at different times of the day were determined as part of the BISTUM23 campaign in August in the Swabian Jura, Southern Germany.

3.3 Experimental procedures

3.3.1 Sampling system

For aerosol sampling, a home-made 3D-printed filter holder was connected to an electric fan motor with an impeller (CDS-R540-QA012; DC 7.2 V; 70 W; SIP Cinderson Motor CO., LTD), which enables high gas flow rates. The inlet diameter of the filter holder was 20 mm. The filters with a diameter of 70 mm were placed on a stainless steel mesh to prevent the filter from tearing even at high flow rates (see Figure 3.1). The sampling unit was powered by a lithium polymer battery (LiPO 7.4 V; 5000 mAh; Conrad Energy), which allows an operating time of about 30 minutes, which is slightly above the approximate maximum flight time of the drones on which the sampler is mounted on. The total weight of the filter holder and electric blade motor is 280 grams, which corresponds to the weight of the battery.

To check the stability of the flow rate through the sampling unit, a filter holder (equipped with PallflexTM EmfabTM filters TX40HI20WW, 70 mm) was connected to a flow meter (model 4148, TSI GmbH, USA) and the flow rate was recorded at 30-second intervals over a total period of 30 minutes.

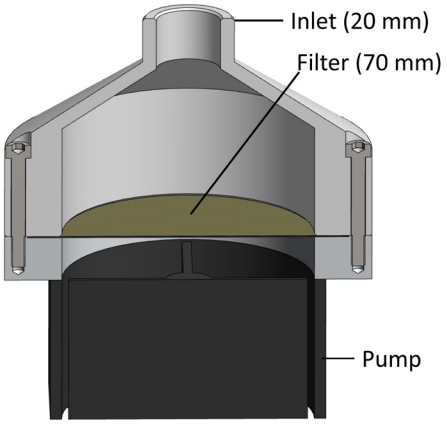

Figure 3.1: Schematic representation of the filter holder. The air containing aerosol particles is sucked through the filter, which is positioned on a stainless steel mesh.

3.3.2 Sampling procedure

The filter holders were attached below the drones with the filter opening facing to the side (Figure 7.11). During a deployment near the village of Essenheim near Mainz (49° 55‘ N, 8° 10’ E), the drones (model Matrice 200 and Matrice 300, both DJI) and the third filter holder were operated at the same height, approx. 5 m above the ground, and with a horizontal distance of approx. 5 m. Borosilicate glass microfibers, reinforced with glass cloth and bonded with PTFE (PallflexTM EmfabTM Filters TX40HI20WW, 70 mm), were used for aerosol sampling. Sampling time was between 20 and 30 minutes depending on the battery power of the drones. To conduct the vertical profile measurements, the system was operated near the village of Albstadt, in the Swabian Jura (48° 15‘ N, 8° 59’ E). The two drones were simultaneously operated at 120 m and 500 m (one above the other with a horizontal offset of about 10 m), while the third filter holder was attached to a wooden frame at a height of about 1.5 m above the ground, with again a vertical offset of about 10 m (Figure 7.12). A third measurement drone, FLab (Moormann et al., 2024), was used to simultaneously quantify gas tracers and meteorological data in hourly vertical profiles over the course of a day at the same measurement location.

3.3.3 Analysis

The filters were stored at -25 °C until analysis. The filters were extracted according to the following protocol. They were cut into small pieces and placed in a vial that had been previously baked at 450 °C for at least 8 hours. They were then extracted with 3 mL and twice 1.5 mL of a 9:1 (v/v) mixture of LC/MS grade methanol (Carl Roth) and LC/MS grade water (Thermo Fisher Scientific) for 30 minutes on a shaking plate. The supernatant was transferred to a 1.5 mL HPLC vial and concentrated at 30 °C under a gentle N_2 stream. The residue was then filtered with a PTFE filter (pore size: 0.20 µm; Altmann Analytik) and filled up to about 50 µL with water. Since the volume of the solution is not known, a camphor sulfonic acid

standard was added to obtain a correction factor for potential volume discrepancies (See Supplement: Determination of the concentration).

Analysis was performed in triplicate using a Dionex UltiMate 3000 ultra-high-performance liquid chromatography system coupled to a heated electrospray ionization source (HESI) and a high-resolution Q-Exactive Orbitrap mass spectrometer (HRMS) (all Thermo Fisher Scientific). An Acquity UPLC CSH Fluoro Phenyl (PFP) column, 100 mm×2.1 mm with 1.7 µm particle size (Waters) was used for chromatography. The eluent A was 98% LC/MS grade water (Thermo Fisher Scientific) with 0.04% formic acid and acetonitrile (VWR Chemicals), the eluent B was 98% acetonitrile and water, and the injection volume was 5 µL. An H_2O/ACN gradient was used for the analysis. A flow rate of 0.5 mL min^{-1} and a gradient as described below was used: Starting with 10% B, increasing to 99% B in 11 min, after which B was held at 99% for 1 min, decreased to 10% in 0.5 min, and held again for 0.5 min. The HESI source was used in negative mode, resulting in the formation of deprotonated molecular ions. The sheath gas and auxiliary gas pressures were 40 and 20 a. u. (arbitrary unit) respectively. The auxiliary gas heater temperature was 150 °C and the capillary temperature was 350 °C. The sprayer voltage was set to -4.00 kV. Further details on the additional chemicals used, including their respective purities, can be found in Supplement.

3.4 Results and discussion

3.4.1 Sampler characteristics

Figure 3.2 shows the airflow through the filter holder as a function of time. During the measurement, the recorded airflow decreases from 19.0 L min^{-1} to 17.8 L min^{-1}. This may be due to the fact that no voltage regulator was installed between the battery and the motor, so the voltage in the battery decreases over time, and thus the power of the motor also decreases. A statistically significant (significance level $\alpha = 0.05$) linear relationship was obtained between flow rate and time. A linear fit ($y = mx + b$) was performed, with $m = (-0.027 \pm 0.002)$ L min^{-2} and $b = (18.97 \pm 0.04)$ L min^{-1} as fit parameters. This function can then be used to determine the volume of air collected within the sampling time (see Supplement: Determination of the concentration).

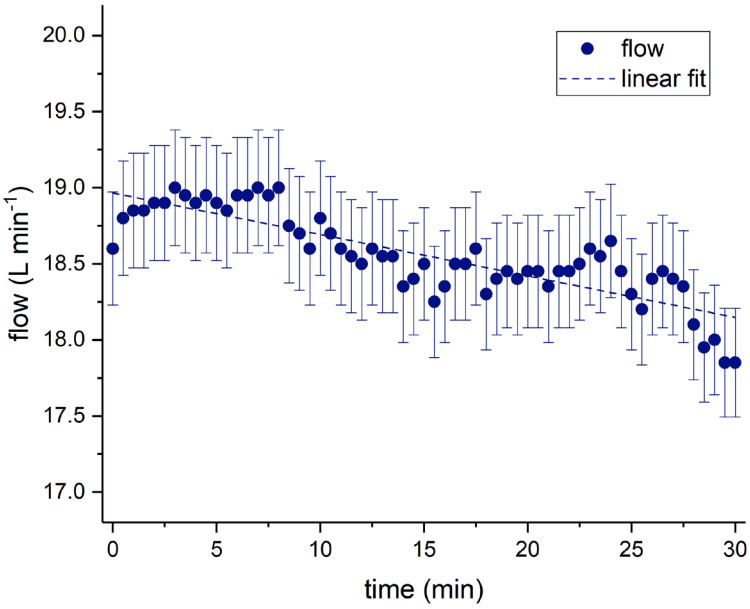

Figure 3.2: Flow through the filter holder as a function of time (blue dots), the dashed line represents a linear fit of the data. The errors correspond to 2% of the measured value, which represents the measurement uncertainty of the flow meter.

Most aerosol particle collectors operate at flow rates between 10 and 500 L min^{-1} to collect aerosol particles over periods of several hours or days (Ma et al., 2022; Leppla et al., 2023). Since the presented system is designed for use onboard drones, a lightweight configuration is crucial. These constraints result in an operational time of 20 to 30 minutes and a flow rate of approximately 18 L min^{-1}. However, sample preparation is essential to be able to detect individual components despite these restrictions. Due to the extraction method and the reduction of the sample volume to only 50 µL of liquid, it is possible to detect a wide range of biogenic and anthropogenic substances. Figure 3.3 shows an excerpt of an extracted ion chromatogram (EIC) of a LC-MS run for *m/z* 185.0819 (red line) and *m/z* 157.0506 (blue line), which originate from a loaded and a blank filter (red and blue dashed lines). The mass traces refer to biogenic maker substances. As the mass spectrometer was operated with a HESI ion source in negative mode, the EICs demonstrate the deprotonated compounds. The signal observed at a retention time of approximately 2 min in the EIC at *m/z* 157.0506 can be attributed to terebic acid, which is an oxidation product of α-pinene (Kołodziejczyk et al., 2020). The second mass trace (*m/z* 185.0819) shows several signals. The occurrence of these signals can be attributed to several constitutional isomers of pinic acid, an oxidation product of α-pinene, which exhibit identical mass-to-charge ratios. However, not only α-pinene is emitted in the atmosphere, but also various other terpenes such as 3-carene, sabinene or limonene. These terpenes oxidize and form compounds such as 3-caric acid, sabinic acid, or limonic acid, which have the same sum formula as pinic acid. This results in the occurrence of different compounds at a single mass trace (Glasius et al., 2000).

It is evident that the signals of the loaded filters differ by an order of magnitude from those of the blank filter and that a high signal-to-noise ratio is achieved for both mass traces. This demonstrates that with the light aerosol sampling system presented here, in conjunction with the extraction method described, it is possible to detect and quantify various marker substances despite the relatively short sampling time. As a result, the presented system is ideally suited for use onboard drones.

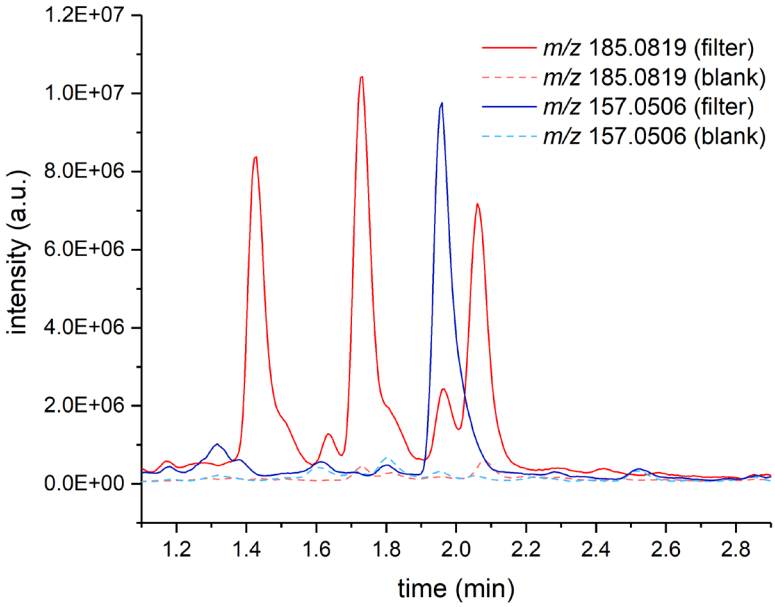

Figure 3.3: Extracted ion chromatogram for *m/z* 185.0819 (red line) and *m/z* 157.0506 (blue line) for a loaded filter and the corresponding EIC for a blank filter (red and blue dashed line). This EIC is representative of biogenic marker compounds like pinic acid, limonic acid, sabinic acid, 3-caric acid (red line), or terebic acid (blue line).

3.4.2 Influence of the sampling drone on the measured concentrations

To evaluate whether differences in the drone models or sample device mounting positions (see Figure 7.11) impact analysis results (e.g., due to aspiration flow variations), two sampler onboard drones and one at a metal framework were operated simultaneously at ~5 m height near Essenheim during a test flight. Figure 3.4 compares the concentrations of a few selected exemplary compounds (pinic acid, 4-nitrophenol, terebic acid and 2,6-dimethyl-4-nitrophenol) at different sampling times for the respective systems. The results of these replicate measurements at the three different sampling periods are shown in brown, blue and green. According to these results, the concentrations of the individual compounds fluctuate noticeably between the different sampling periods, which is plausible due to the approximately one-hour delay between the three sampling periods. The differences between these measurement flights can be attributed to the different time of the flights and the resulting changes in the composition of the collected aerosol particles. The discrepancy between the second and third measurements is particularly evident for the anthropogenic

markers 4-nitrophenol and 2,6-dimethyl-4-nitrophenol. Such fluctuations can be attributed, for example, to a change in wind direction and thus to a different origin of the sampled air mass. However, it is crucial that the differences between the different sampling systems within a measurement flight are comparatively low for the analytes. It can be concluded that the type of drone used, or minor differences in the mounting position of the sampler on the drone and the resulting differences in air turbulence around the filter holder, have no significant influence on the analytical results.

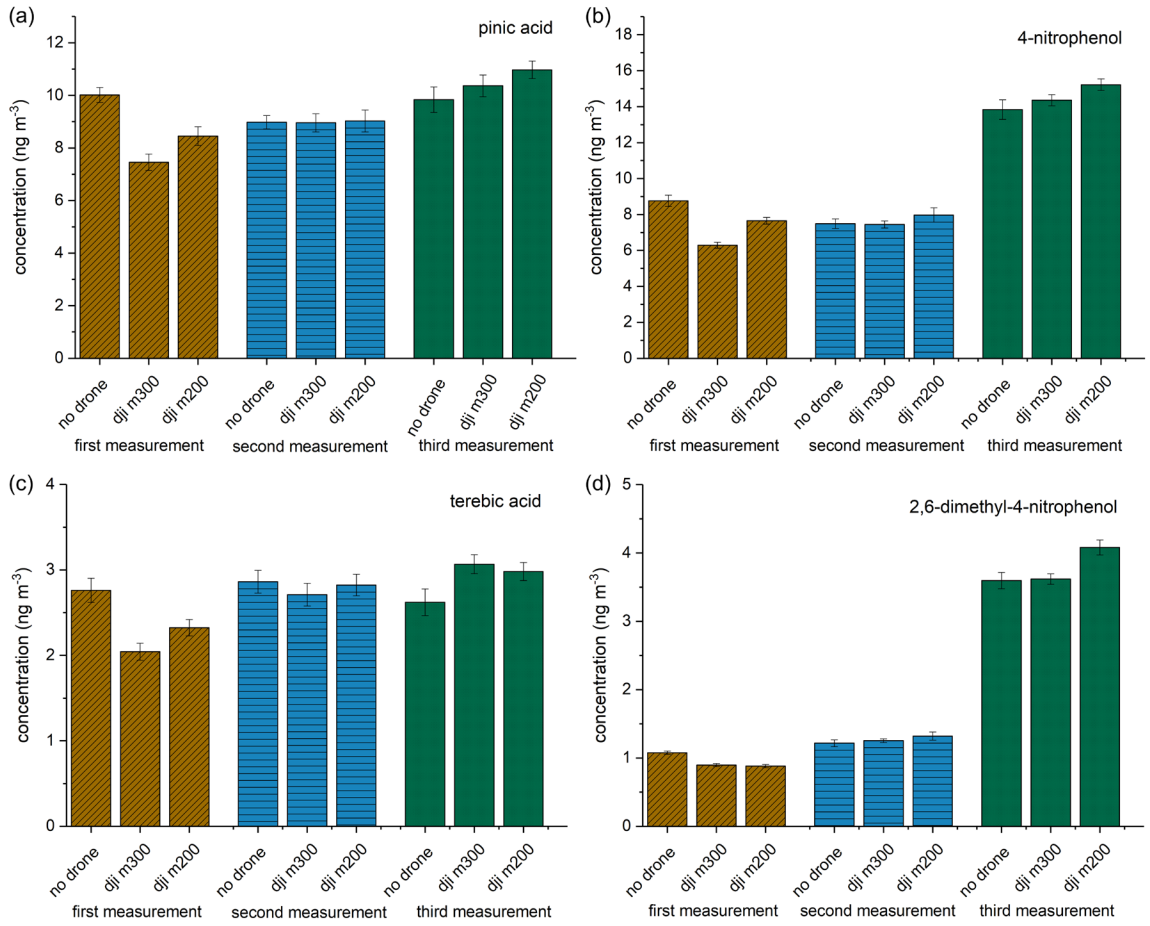

Figure 3.4: Mean concentration of pinic acid, 4-nitrophenol, terebic acid and 2,6-dimethyl-4-nitrophenol, for the three measurement setups (no drone; dji m300; dji m200) during three measurement flights (brown, blue and green). The error bar is the result of two error sources: the standard deviation derived from the triple determination made by the LC-MS measurement; and the error associated with the flow measurement of the filter holder.

3.4.3 Vertical profiles of biogenic, biomass burning and anthropogenic marker compounds

The characterized filter sampler was used to sample aerosol particles simultaneously to measurements of a third measurement drone, FLab (Moormann et al., 2024) during the BISTUM23 campaign in August 2023 in Albstadt, Germany. This approach allowed for the acquisition of daily and height trends for OA at a measurement site, which is surrounded in all directions by a mixture of grassland, forest, agricultural land, and urban infrastructure (see Figure 7.12).

Figure 3.5 shows three height profiles at 10:35 am, 1:35 pm and 4:30 pm local time (UCT+2) for concentrations of the three biogenic marker components pinic acid (black square), terpenylic acid (blue triangle) and terebic acid (green diamond) in 1.5 m, 120 m and 500 m.

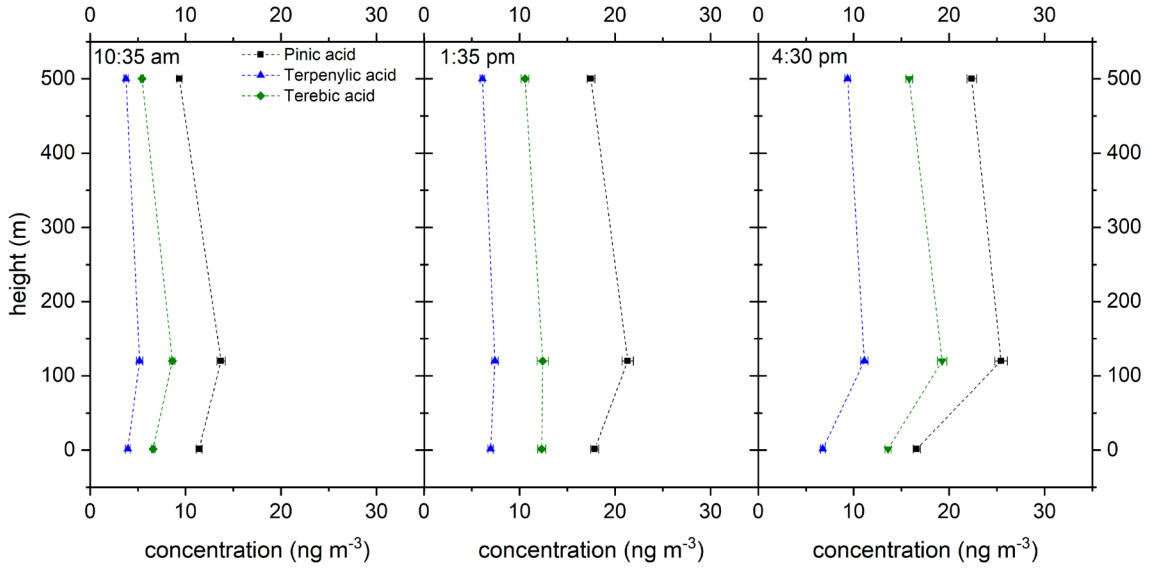

Figure 3.5: Vertical profiles of the biogenic marker compounds pinic acid (black square), terpenylic acid (blue triangle) and terebic acid (green diamond) at the different times (all times are in UTC+2). For better clarity, these points are connected by dashed lines The error bar is the result of two error sources: the standard deviation derived from the triple determination made by the LC-MS measurement; and the error associated with the flow measurement of the filter holder.

It can be seen that the concentrations at a height of 120 m are higher than at ground level (1.5 m). This observation can have multiple causes, for example the different footprint areas attributable to the various heights or also dry deposition of corresponding aerosol-borne components on the ground (Spielmann et al., 2017; Bamberger et al., 2011). Actually, this trend between 1.5 m and 120 m also coincides with the measured ozone concentration (Figure 7.13). The ozone concentration is slightly lower at ground level than in the higher region. However, the concentrations of the selected oxidation products decrease up to a height of 500 m. This finding could be attributed to the higher average residence time of the

corresponding aerosol populations. One potential explanation for the concentration decrease is, among others, the further oxidation of the compounds measured here, which could lead to the formation of more highly oxidized compounds. In addition to the altitude trend, a distinct daytime trend can also be seen. From morning to afternoon, the concentrations of all three compounds increase at all altitude levels, although the relative increase depends on the individual compound. This is also in good agreement with the measured ozone concentration. The ozone concentration increases during the day at all altitudes.

Figure 3.6 shows the altitude profile of some marker compounds for anthropogenic sources of OA and biomass burning, salicylic acid (purple circle), 4-hydroxybenzaldehyde (pink hexagon), 4-nitrophenol (turquoise pentagon), 2,6-dimethyl-4-nitrophenol (light blue half-filled circle), and 2,4-dinitrophenol (brown star). The actually measured concentrations are shown as symbols. For these marker substances, no clear trend can be seen in terms of altitude or time of day. It can be observed that the trend in terms of altitude or time of day is comparable for salicylic acid and 4-hydroxybenzaldehyde, as well as for 4-nitrophenol and 2,4-dinitrophenol. The differences between the trends are probably due to different sources of the marker substances. For example, salicylic acid and 4-hydroxybenzaldehyde are formed during the combustion of lignin (Cao et al., 2022; Rana and Guzman, 2022; Fleming et al., 2020). In addition, salicylic acid has been detected in vehicle exhausts, making it both an anthropogenic and a biomass-burning marker compound (Li et al., 2020). The nitroaromatic compounds may originate from the combustion of biomass and the nitration of phenols or vehicle exhaust gases (Zhang et al., 2022; Kulakova et al., 2020; Lu et al., 2019). Consequently, they can also be considered as marker substances for biomass burning and anthropogenic substances. The highest concentrations of salicylic acid, 4-nitrophenol, 2,6-dimethyl-4-nitrophenol and 2,4-dinitrophenol were observed in the morning at a height of 120 m. This indicates that the air mass sampled at 10:35 am had crossed an area where biomass had been burned or where there was heavy traffic. The wind direction determined by FLab is southwest with a wind speed of 2 to 3 m s^{-1} (Figure 7.14 and Figure 7.15). A federal highway is also located in this direction. The backward trajectory for the 120 m sample created with the NOAA HYSPLIT model (Rolph et al., 2017; Stein et al., 2015; Draxler and Hess, 1998) indicates that the sampled air masses crossed the federal highway at around 8 am (Figure 7.16). Higher concentrations of anthropogenic markers can be attributed to rush-hour traffic. At ground level, the plume is less extended due to the surface layer (Stull, 2017), while at 500 m, it is diluted by dynamic air mixing or different origin of the air masses (Figure 7.16). Thus, compound concentrations from the federal road, especially in the morning, are lower at 1.5 m and 500 m.

The measured concentrations of the anthropogenic markers are lower than those of the biogenic ones. The lower concentrations can be explained by the fact that the sampling site was in a rural area where anthropogenic influences are possibly less significant than biogenic ones.

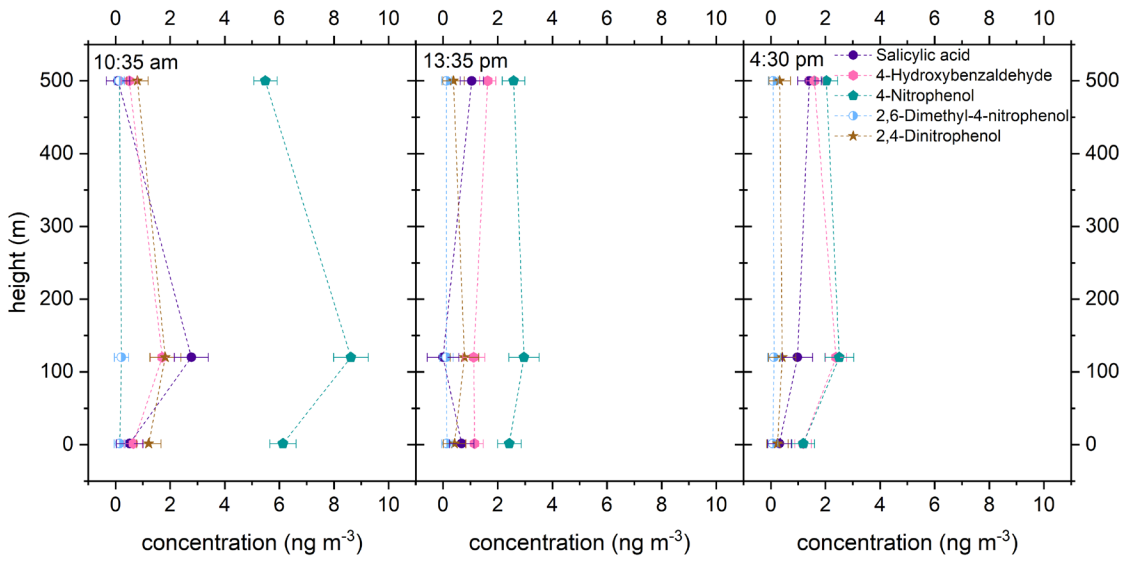

Figure 3.6: Vertical profiles of the anthropogenic marker compounds salicylic acid (purple circle), 4-hydroxybenzaldehyde (pink hexagon), 4-nitrophenol (turquoise pentagon), 2,6-dimethyl-4-nitrophenol (light blue half-filled circle), and 2,4-dinitrophenol (brown star). The actually measured concentrations are shown as symbols. For better clarity, these are connected with dashed lines. The error bar is the result of two error sources: the standard deviation derived from the triple determination made by the LC-MS measurement; and the error associated with the flow measurement of the filter holder.

3.4.4 Height dependent Van Krevelen diagrams

In addition to the targeted analysis of individual marker compounds described above, a non-target analysis was also carried out. The results are shown in a series of Van Krevelen diagrams in Figure 3.7. The underlying molecular formulas of the compounds shown can be unambiguously assigned due to the use of a high-resolution mass spectrometer with accurate mass determination and were determined using MZmine 2.53 software (Pluskal et al., 2010). These were used to determine the H/C and O/C ratios, which were then plotted against each other. The compounds were assigned to the four substance classes CHO (blue), CHON (green), CHOS (orange) and CHONS (pink), with CHO being the most abundant class. The size of the dots is defined by the measured peak intensity of the respective LC-MS measurement. All signals were normalized to the duration of the sampling. Since a HESI source was used as the ion source, it is important to consider the potentially different ionization efficiencies of the compounds. The ionization efficiency can differ by several orders of magnitude for differently functionalized compounds (Liigand et al., 2021; Oss et al., 2010). Therefore, the dot size essentially provides an overview of the concentration changes of the respective compounds as a function of time or height. However, it does not provide any information about the relative amounts between different compounds. The Van Krevelen diagrams are divided into five sections for better clarity. These are based on the maximum carbonyl ratio (MCR) of the compounds. This describes the maximum contribution of the carbonyl/epoxy functionalities of the components and thus provides an indication of their

degree of oxidation. The five groups are *V*: highly unsaturated (combustion related), *IV*: oxidized unsaturated (primary organic carbon, oxidation products from aromatic VOC), *III*: intermediately oxidized (monoterpene first generation oxidation products), *II*: highly oxidized (monoterpene oxidation products, oxidative aging), and *I:* very highly oxidized (isoprene oxidation products) (Zhang et al., 2021).

The composition of the aerosols should not differ significantly regardless of the origin of the air mass due to the remote location. At first glance, however, it can be seen that the Van Krevelen diagram at a height of 120 m in the morning (Figure 3.7 (d)) differs significantly from all the others. This sample shows a strikingly high number of CHO-containing compounds with high peak areas in the region between areas *III* and *IV* and in area *V*, likely originating from combustion processes. Studies link these regions of the Van Krevelen diagram to biomass combustion (Tang et al., 2020). Compounds in this area ($C_{20}H_{26}O_3$, $C_{20}H_{28}O_2$, $C_{20}H_{28}O_3$, $C_{20}H_{30}O_2$, $C_{20}H_{30}O_4$) are identified as biomass combustion markers in previous research (Ramteke et al., 2024; Smith et al., 2009). The intense biomass burning and anthropogenic tracers in the 120 m morning sample (section 3.4.3) may result from vehicle exhaust and biomass burning, as discussed for the vertical profiles of anthropogenic substances in Figure 3.6 and Section 3.4.3. However, the change in the surface layer and atmospheric boundary layer heights in the morning hours is likely related to these observations. To examine general trends over height and time of day, the Van Krevelen diagram for a height of 120 m in the morning is not considered in the discussion below.

The vertical profiles at 1:35 pm and 4:30 pm are very similar. At a height of 1.5 m, there are several substances in area *IV* that are no longer present at heights of 120 m and 500 m, or are present in significantly lower concentrations. This can be attributed to the oxidation of the substances to more highly oxidized compounds. In addition, a shift of the points to higher O/C and H/C ratios is observed between 120 m and 500 m, which leads to an increased number of substances in section *II*. This also indicates that the observed compounds at higher altitudes are evolving into more highly oxidized substances. The observed tendency towards higher concentrations of higher-oxidized compounds at higher altitudes can be explained by the longer residence time in the atmosphere before reaching these altitudes. Consequently, terpenes, isoprene and their oxidation products are exposed to oxidizing species for a longer period of time, resulting in the formation of more highly oxidized compounds.

For the variation during the day, the diagrams at the same altitudes can be compared with each other. It is noticeable that the size of the points and thus the associated measured concentration increases during the course of the day, particularly for the CHO-containing compounds. This finding is also consistent with the targeted approach, which detects an increase in the concentrations of biogenic SOA compounds (in this case CHO compounds) during the course of the day. The higher concentration of CHO-containing compounds can be attributed to the rising temperature and the accumulating oxidation product concentrations over the course of the day. As the temperature rises, more biogenic substances such as

terpenes are emitted by the trees, which are then oxidized to CHO-containing compounds over the course of the day (Vettikkat et al., 2023; Niinemets et al., 2004).

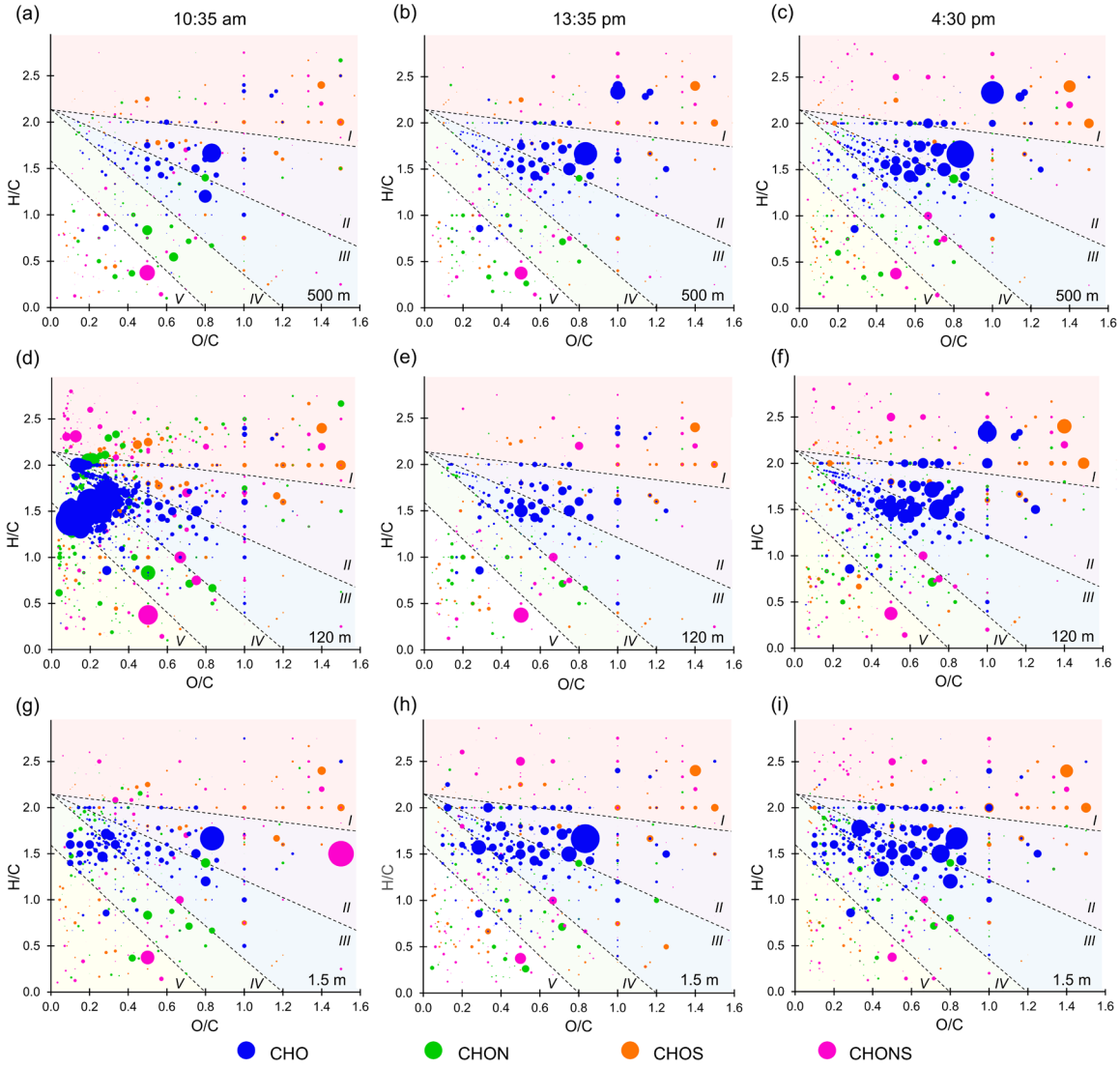

Figure 3.7: Van Krevelen diagrams in the morning (left), at noon (middle) and in the afternoon (right). The different substance classes are represented by different colors (CHO blue; CHON green; CHOS orange; CHONS pink) The size of the dots correlate with the measured peak area of the compounds. The Van Krevelen diagrams are divided into 5 areas depending on the MCR, which are separated by dashed lines (Zhang et al., 2021).

3.5 Conclusions

This study demonstrates that drones can also be used as a sampling platform for detailed chemical characterization of organic aerosol components using UHPLC-MS. The developed aerosol sampling unit allows the collection of sufficient aerosol mass for both targeted and non-targeted analysis of primary and secondary organic aerosol components within the maximum flight time of the drones used. The newly developed, very light aerosol sampling

system with a weight of approx. 560 g was successfully tested at two locations in Germany. Comparative measurements with three identical aerosol samplers on different drones (Matrice 200 and Matrice 300 models, both DJI) showed that the drones themselves and slight differences of the mounting position on the drones had no significant influence on the results. During a measurement campaign (BISTUM23), a series of filters were sampled in parallel using two drones and a ground-based framework, supported by another measurement UAV that measured the gas phase and meteorological conditions throughout the day. The aim was to perform vertical concentration measurements to investigate the variations in aerosol composition during the course of a day. For this purpose, aerosol samples were collected simultaneously at ground level, 120 m above ground and 500 m above ground.

The primary aim of the measurements shown above is a proof-of-concept, as the amount of data alone is of course not sufficient to make general statements about vertical concentration profiles of organic aerosol components. Nevertheless, some initial conclusions can be drawn about the measured analytes. The biogenic SOA markers pinic acid, terebic acid, and terpenylic acid show increasing concentrations from the morning hours to the afternoon hours. This result is consistent with the observed increase in ozone concentrations during the day. Both the rising temperatures during the day and thus the increasing release of precursor VOCs during the day and the increasing importance of oxidation reactions can explain this concentration trend (Vettikkat et al., 2023; Niinemets et al., 2004). Interestingly, the vertical concentration measurement showed that the maximum concentration of these compounds was often observed at a height of 120 m, an observation that may be attributed to different footprint regions, dry deposition and chemical ageing (Spielmann et al., 2017; Bamberger et al., 2011). The highest concentrations of anthropogenic markers were observed in the morning hours. The wind data (Figure 7.14and Figure 7.15) and HYSPLIT back trajectories (Figure 7.16) indicate that this phenomenon may be due to the main road during rush hour. In general, the concentration of anthropogenic marker compounds is lower than that of biogenic compounds, which can be explained by the remote location of the sampling site, where biogenic processes can have a greater influence than anthropogenic activities.

The results of the non-targeted analysis of the filter samples are consistent with the trends identified in the targeted analysis and show an increase of oxidized compounds throughout the day and with increasing altitude. Consistent with the targeted approach, compounds associated with automobile exhaust and biomass combustion products are particularly present in the morning samples. In summary, this study highlights the use of drones as an innovative platform for the sampling and chemical characterization of organic aerosols using UHPLC-MS. The developed sampling unit collects sufficient aerosol mass within the drones' flight time, enabling both targeted and non-targeted analysis of primary and secondary organic aerosols. This approach facilitates cost-effective, height-selective sampling, allowing the measurement of vertical concentration profiles and access to otherwise challenging or inaccessible locations for aerosol sampling.

Author contribution

CB and TH developed the filter holder and planed the measurements; CB performed the analytical measurement of the OA samples, analyzed the data and wrote the manuscript draft; BG, NK and TH performed the drone flights; LM performed the flights of FLab and analyzed the ozone and wind data; TH, LM, BG and NK reviewed and edited the paper.

Competing interests

The authors declare that they have no conflict of interest.

Data availability

The measured concentration of the targets can be found in the supplement. The non-target data is available upon request from the corresponding author, Thorsten Hoffmann (t.hoffmann@uni-mainz.de).

Acknowledgements: This work was funded by the Deutsche Forschungsgemeinschaft (DFG, German Research Foundation) – TRR 301 – Project-ID 428312742 and HO 1748/24-1 (Project-ID 541033130).

4. Characterization of marine aerosol particles

Investigation of organic aerosol particles collected on board the research vessel *Eugen Seibold* between Iceland and the equator

4.1 Abstract

Organic aerosols (OA) are a significant component of particulate matter in the atmosphere, thereby influencing climate and public health. These particles have the capacity to absorb or scatter radiation, consequently exerting a direct influence on temperature. Functioning as cloud condensation nuclei, they play a crucial role in the process of cloud and precipitation formation. The chemical composition of OA offers insights into their sources and processing, including contributions from biogenic sources in largely undisturbed marine or terrestrial ecosystems, as well as the role of anthropogenic activities in organic aerosol formation. High-resolution mass spectrometry (HRMS) is currently regarded as one of the most significant analytical techniques, including for the analysis of atmospheric aerosols. The combination of high mass resolution and accurate mass determination allows for the elucidation of the elemental composition of numerous compounds and ultimately facilitates a more profound understanding of biosphere-atmosphere cycles. In this study, we present findings on the chemical composition of 18 aerosol partilce samples collected aboard the sailing research vessel *S/Y Eugen Seibold* in various marine regions between the northern polar circle and the equator. A variety of biogenic marker compounds were observed, along with the presence of novel potential marine compounds that contained carbon, hydrogen, oxygen, nitrogen, and sulfur atoms. Additionally, a possible organic iodine compound was postulated as a potential new marine marker compound.

4.2 Introduction

Marine aerosols are crucial for the global aerosol budget. Historically, research has focused on aerosols originating from sea salt and non-sea salt sulfates (O'Dowd et al., 1997; Charlson et al., 1987; Shaw, 1983). However, a recent study highlights the importance of organic matter, particularly during plankton blooms, where submicron organic particles dominate (O'Dowd et al., 2004). The organic components of marine aerosols are influenced by both primary emissions and atmospheric processing, leading to the formation of secondary organic aerosols (SOA) (Facchini et al., 2008a; Facchini et al., 2008b).

One significant source of marine aerosols is the process known as bubble bursting. This occurs when wind causes the formation of air bubbles in the water column due to wave breaking. As these bubbles rise to the surface, they disrupt the water's surface layer and release particles (Resch et al., 1986). Phytoplankton in the water can influence the composition of the aerosols produced through this process (Kuznetsova et al., 2005). The resulting aerosols contain a variety of compounds, such as organic acids, amines, carbonyls, and amino acids (Saxena and Hildemann, 1996), which may undergo further oxidation in the atmosphere to form SOA (Schmitt-Kopplin et al., 2012).

Marine SOA can also form in the atmosphere through the oxidation of volatile organic compounds (VOCs) from marine environments. Seawater contains a complex mixture of VOCs, whose distribution and emissions are not fully characterized. Furthermore, the oceans' contribution to the Earth's VOC budget is not yet fully understood (Yu and Li, 2021). One major VOC, dimethyl sulfide (DMS), is produced by phytoplankton and is the primary source of organic sulfur in the atmosphere (Yang et al., 2011; Andreae et al., 1985). Once released, DMS undergoes oxidation, forming various gas-phase compounds, some of which are low-volatility and contribute to particle growth or new particle formation (NPF) (Beck et al., 2021; Barnes et al., 2006). There are two main pathways for DMS oxidation: one involves the addition of OH, NO_3, or halogen radicals, while the other involves the abstraction of a hydrogen atom (Siegel et al., 2023). In the addition pathway, DMS is first oxidized to dimethyl sulfoxide (DMSO), which then converts to methanesulfinic acid (MSIA) (Barnes et al., 2006). MSIA can either transition into the particle phase or be further oxidized into methanesulfonic acid (MSA), sulfuric acid (SA), or sulfur dioxide. In the abstraction pathway, sulfuric acid and MSA are the primary products (Siegel et al., 2023).

In addition to sulfur compounds, organic nitrogen compounds also play a significant role in marine aerosols. Many of these compounds are derived from gas-to-particle conversion in the atmosphere, while others are introduced via mechanical processes such as sea spray and subsequently oxidized (Cornell et al., 2003). A large proportion of the organic nitrogen compounds are amines and amino acids (Barbaro et al., 2015; Facchini et al., 2008b).

Marine aerosols can also be influenced by isoprene and monoterpenes, which are produced not only by terrestrial vegetation but also by bacteria, macroalgae (seaweed), and marine phytoplankton (Yassaa et al., 2008; Broadgate et al., 2004). The occurrence of halogenated

monoterpenes in marine algae has been documented, suggesting a potential source of these compounds in the marine environment. This phenomenon is hypothesized to be a result of halogenides present in seawater (O'Dowd et al., 2004). However, these emissions play a minor role in marine aerosol formation. A model study estimates that around 78% of marine SOA originates from the oxidation of DMS, 21% from dialkylamine salts, and a small fraction of 0.1% from the oxidation of marine hydrocarbons (Myriokefalitakis et al., 2010).

4.3 Experimental procedure

4.3.1 Filter sampling

The filters were collected on board the research vessel *S/Y Eugen Seibold*. The sample inlet was located at an approximate height of 13 m above the waterline. A low-volume sampler with a flow rate of up to 50 L/min was utilized. Further details about the *S/Y Eugen Seibold* and the sampling process can be found in the literature (Schiebel et al., 2024). Pallflex™ Emfab™ filters (TX40HI20WW, 47 mm) were utilized for the collection of samples. A summary of the samples can be found in the supplement (Table 7.20). The samples were collected between July 2020 and May 2021. The sampling locations spanned a latitudinal range from the northern polar circle near Iceland to the equator. A total of 26 filters were subjected to analysis, of which 8 filters were classified as blank filters and were not sampled. The collection time for each filter ranged from 1:33 h to 24:05 h, with an average duration of 15:03 h.

4.3.2 Filter analysis

The filters were stored at -25 °C until analysis. The filters were extracted according to the following protocol. They were cut into small pieces and placed in a vial that had been previously baked at 450 °C for at least 8 hours to remove any remaining organics. They were then extracted three times with 1.5 mL each of a 9:1 (v/v) mixture of LC/MS grade acetonitrile (ACN)(Carl Roth) and LC/MS grade water (Thermo Fisher Scientific) for 30 minutes on a shaking plate (see Figure 4.1). The supernatant was transferred to a 1.5 mL HPLC vial and concentrated at 30 °C under a gentle N_2 stream to dryness. The residue was then filled up to 700 µL with 50/50 (v/v) water/acetonitrile mixture and filtered with a PTFE syringe filter (pore size: 0.20 µm; Altmann Analytik).

Analysis was performed in triplicate using a Dionex UltiMate 3000 ultra-high-performance liquid chromatography system coupled to a heated electrospray ionization source (HESI) and a high-resolution Q-Exactive Orbitrap mass spectrometer (HRMS) (all Thermo Fisher Scientific). A Hypersil Gold, C18, 50 x 2.0 mm column with 1.9 µm particle size (Thermo Fisher Scientific) was used for the chromatography. Eluent A consisted of 98 % LC/MS grade water (Thermo Fisher Scientific) with 0.04 % formic acid and acetonitrile (VWR Chemicals), eluent B consisted of 98 % acetonitrile and water, and the injection volume was 5 µL. An H_2O/ACN gradient was used for the analysis. A flow rate of 0.5 mL min^{-1} and a gradient as described in the following were used: Starting with 2 % B isocratically for 1 min, increasing

to 20 % B in 2.5 min, then further increasing to 90 % in 1.5 min, after which B was held at 90 % for 4 min, decreased to 2 % in 0.5 min, and held again for 1.5 min. The HESI source was used in negative mode, resulting in the formation of deprotonated molecular ions. The sheath gas and auxiliary gas pressures were 40 and 20 a. u. (arbitrary unit) respectively. The auxiliary gas heater temperature was 150 °C and the capillary temperature was 350 °C. The sprayer voltage was set to -4.00 kV.

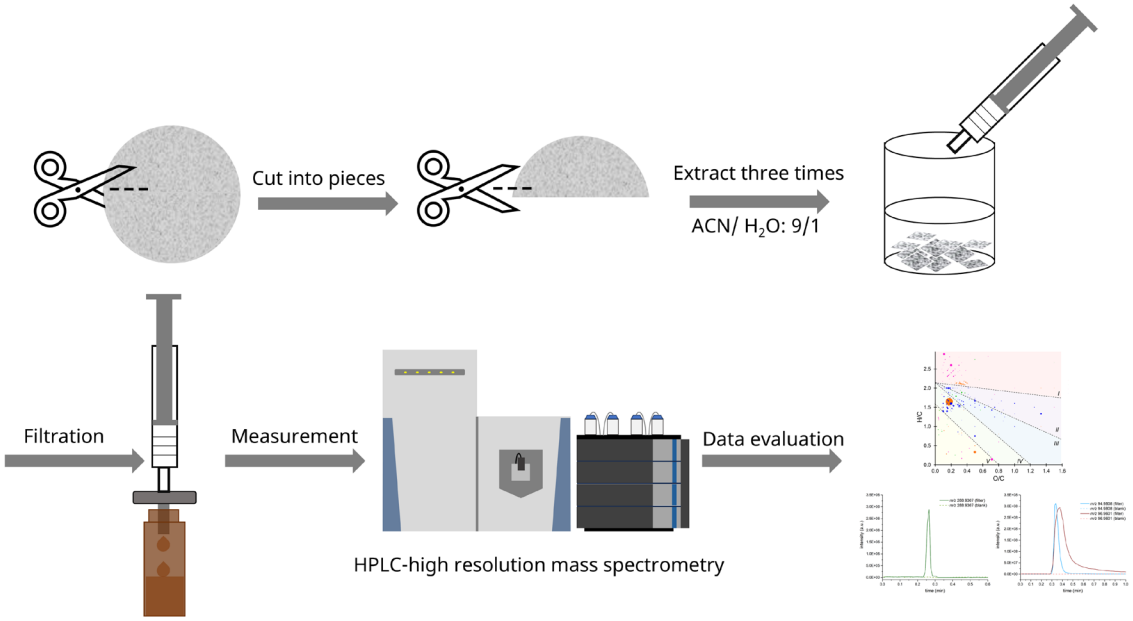

Figure 4.1: Schematic of the sample preparation and analytical analysis process. The filters are initially cut in half, and half of each filter is subsequently cut into small pieces. The filter pieces are then mixed with solvent for extraction, shaken for approximately 30 minutes, filtered, and concentrated under a stream of nitrogen. The resulting solution is then taken up in solvent and analyzed using HPLC-HRMS. The resulting data is subsequently analyzed.

4.4 Results and discussion

4.4.1 Non-target analysis

The filters were subjected to a non-target analysis. The results are presented in a series of Van Krevelen diagrams, as illustrated in Figure 4.2. Each Van Krevelen diagram represents the sum of three filters in the corresponding region. The underlying molecular formulas of the compounds shown can be assigned due to the use of a high-resolution mass spectrometer with accurate mass determination and were determined using MZmine 2.53 software (Pluskal et al., 2010). These were used to ascertain the H/C and O/C ratios, which were subsequently plotted against one another. The compounds were classified into one of four substance classes: CHO (blue), CHON (green), CHOS (orange), and CHONS (pink). The size of the dots is proportional to the measured peak intensity of the respective LC-MS measurement. Given that a HESI source was employed as the ion source, it is essential to take into account the potential variations in ionization efficiency among the compounds. The ionization efficiency can differ

by several orders of magnitude for compounds with different functional groups (Liigand et al., 2021; Oss et al., 2010). Consequently, the size of the dot provides an overview of the concentration changes of the respective compounds. However, it does not provide any information regarding the relative amounts of different compounds. For enhanced clarity, the Van Krevelen diagrams are divided into five sections. These are based on the maximum carbonyl ratio (MCR) of the compounds. This ratio describes the maximum contribution of the carbonyl/epoxy functionalities of the components, thereby providing an indication of their degree of oxidation. The five groups are as follows: *V*: highly unsaturated (combustion related), *IV*: oxidized unsaturated (primary organic carbon, oxidation products from aromatic VOC), *III*: intermediately oxidized (monoterpene first generation oxidation products), *II*: highly oxidized (monoterpene oxidation products, oxidative aging), and *I:* very highly oxidized (isoprene oxidation products) (Zhang et al., 2021).

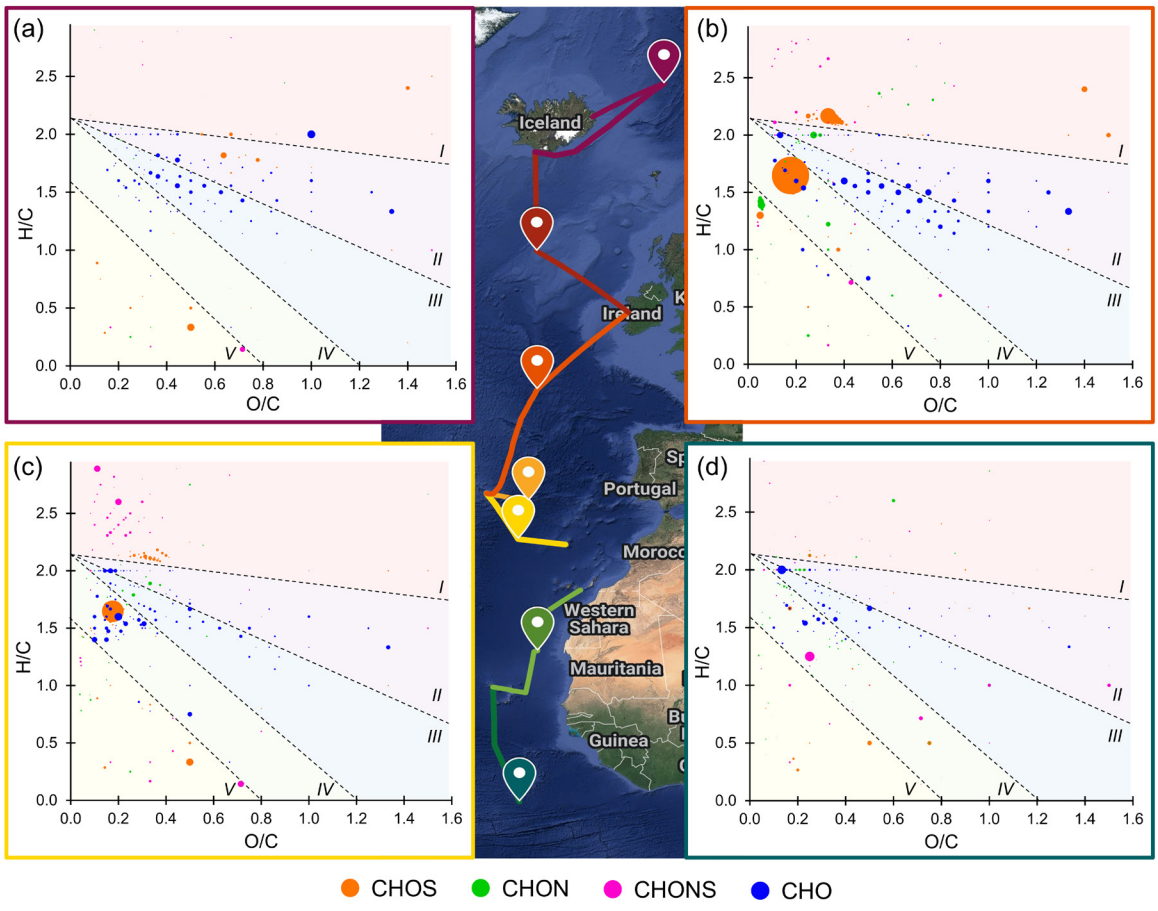

Figure 4.2: Van Krevelen diagrams for the filter samples from the various regions traversed by the *Eugen Seibold* during its 2020 (red to yellow) and 2021 cruises (light to dark green) (© Google Earth). The Van Krevelen diagram of the corresponding region is indicated by a colored frame.

The Van Krevelen diagram, which depicts the samples near Iceland (Figure 4.2 (a)), demonstrates a substantial presence of CHO-containing compounds, particularly in regions *II* and *III* of the diagram. This observation suggests a significant presence of biogenic

compounds, as monoterpene oxidation products are predominantly found in this region. Given the coastal vicinity of the sampling site, a combination of terpenes from terrestrial vegetation and algae may be present (Fu et al., 2011; Yassaa et al., 2008). The anthropogenic influence on these samples appears to be minimal, as the presence of relatively few compounds in areas *IV* and *V* suggests a low level of combustion or oxidation of aromatics.

The Van Krevelen diagram representing the samples collected on the cruise from Ireland to the Azores (Figure 4.2 (b)) shows some intense CHOS compounds in addition to the potentially biogenic CHO compounds in region *II* and *III*. Of notable significance is the CHOS signal in area *IV,* which exhibited the highest peak area among all the samples that were analyzed. This signal corresponds to the compound $C_{17}H_{28}O_3S$. This signal is overlaid on the signals also present in the sample, which can be attributed to the compounds $C_{16}H_{26}O_3S$, $C_{18}H_{30}O_3S$, and $C_{19}H_{32}O_3S$. The presence of these compounds is most likely a consequence of the combustion of heavy fuel, which is either due to the presence of other ships or to the engine of the *Eugen Seibold* being operated (Bai et al., 2020; Rüger et al., 2015; Antipenko and Melenevskii, 2012; Liu et al., 2010). In addition, the presence of certain CHOS compounds in area *I* has been observed, some of which also exhibit high intensity. These include a number of molecular formulas, such as $C_{12}H_{26}O_4S$, $C_{14}H_{30}O_4S$ and $C_{16}H_{34}O_4S$. Laranjeiro et al.(2024) discovered in a study that these sulfates can be introduced into the water by biodegradable plastics. This indicates that these compounds have probably been introduced into the ocean as contaminants and therefore have no biological background. Furthermore, area *I* contains a compound with the molecular formula $C_{15}H_{32}O_3S$. This compound was detected in extracts of seaweed, suggesting a probable biological origin (Mofeed et al., 2022). In addition to this CHOS ($C_{15}H_{32}O_3S$) compound previously described three other CHO compounds ($C_{14}H_{28}O_2$, $C_{17}H_{34}O_2$, $C_{20}H_{40}O_2$) were identified. These compounds had also been detected in the extract of the seaweed *Corallina officinalis*. This finding suggests that this plant may not only contains the substances, but also emits them (Mofeed et al., 2022).

The Van Krevelen diagram of the samples near the Azores (Figure 4.2 (c)) also shows combustion markers of heavy oil ($C_{16}H_{26}O_3S$, $C_{17}H_{28}O_3S$, $C_{18}H_{30}O_3S$, and $C_{19}H_{32}O_3S$), albeit not as high as in the previous Van Krevelen diagram. In addition to the CHOS compounds present in heavy oil, the formation of more saturated and more oxidized organosulfates, such as $C_{18}H_{38}O_6S$, can also result from reactions in the atmosphere (Zhao et al., 2013; Hatch et al., 2011). These compounds are identified in area *I* of the Van Krevelen diagram. Two different formation mechanisms for CHOS compounds have been described in the literature. Firstly, ester formation of alcohols with sulfuric acid has been observed. Secondly, acid-catalyzed reactions of epoxides have been reported (Minerath and Elrod, 2009; Liggio et al., 2005). It has been established that both mechanisms are dependent on the presence of sulfuric acid anions, which are known to be produced in a marine environment through the emission of DMS and subsequent reactions in the atmosphere (Siegel et al., 2023; Minerath and Elrod, 2009; Liggio et al., 2005). The importance of organosulfates for marine organic aerosol is also supported by studies that have identified organosulfate functionalities in coastal areas influenced by maritime and continental sources, as well as in remote areas with exclusively

biogenic influences (Hawkins et al., 2010; Claeys et al., 2010). Consequently, the CHOS compounds present in area *I* may be partly of marine biogenic origin. Another notable finding in the Van Krevelen diagram is the presence of certain CHONS compounds within area *I*. These compounds are characterized by their high molecular weight, with a molecular weight greater than 250 u. The molecular formulas of these compounds are $C_{9\text{-}12}H_{22\text{-}32}N_{6\text{-}12}O_{1\text{-}5}S$, with the compounds $C_{10}H_{26}N_6O_2S$ and $C_9H_{26}N_6O_2S$ exhibiting the highest signal intensity. The H/C ratio of the molecules indicates an aliphatic character. It is expected that low molecular weight aliphatic amines are of marine origin(Facchini et al., 2008b; Müller et al., 2009). A comparison of the marine samples ((Figure 4.2 (c)) with samples from tropical terrestrial ecosystems (amazon rainforest (Leppla, 2021)) and industrial regions (Beijing (Ma et al., 2022)) reveals interesting differences. The CHONS-containing compounds in area *I* in the samples taken near the Azores are only found in these marine samples. Therefore, it is very promising that these substances are of marine origin. Further filter samples need to be investigated to determine if the increased occurrence of CHONS-containing compounds is a seasonal or a regional effect.

As illustrated in the Van Krevelen diagram (Figure 4.2 (d)), which is based on samples collected in regions close to the equator, there are comparatively few compounds present. Once more, as previously observed in Figure 4.2 (a), the largest fraction is comprised of CHO compounds. These CHO compounds are primarily found in area *III* and *IV*, indicating that they are monoterpene oxidation products and primary organic compounds. The compound exhibiting the highest signal intensity of the CHO compounds is $C_{15}H_{30}O_2$, which is likely to be a *n*-fatty acid. Fatty acids may have terrestrial sources, such as higher plant waxes or soil microbes. Alternatively, they may have marine sources, such as cellular lipids or phytoplankton, which are present at the ocean surface. These fatty acids were previously detected in marine aerosol samples (Bikkina et al., 2019; Tyagi et al., 2017; Mochida et al., 2002). In addition to the presence of the C_{15} fatty acid, C_{12} to C_{20} fatty acids were also detected in the samples. Given the remote nature of the sampling location, it is plausible that the fatty acids are of marine origin.

4.4.2 semi-target analysis

Furthermore, the filters were subjected to a semi-targeted analysis. This entailed the search for masses of known biogenic and marine marker compounds in the chromatograms. In Table 4.1, the utilized marker compounds, along with the exact mass of the corresponding ion used for the analysis and their presence in the filter samples, are presented. Methanesulfonic acid and sulfuric acid are maritime marker compounds that are formed from the oxidation of dimethylsulfide and contribute to NPF (Siegel et al., 2023; Katoshevski et al., 1999). Pinic acid and 3-methyl-1,2,3-butantricarboxylic acid (MBTCA) are oxidation products of α-pinene. These compounds are typically used as biogenic terrestrial marker compounds; however, they could also be used as maritime markers since algae also emits α-pinene (Yassaa et al., 2008; Kourtchev et al., 2008; Jenkin et al., 2000). The exact masses of the analyzed ions that could correspond to methanesulfonic acid, sulfuric acid, pinic acid, and MBTCA were detected in all

the analyzed samples. This finding indicates that all of the samples were influenced by biogenic emissions.

Decesari et al.(2020) have proposed creatinine as a new biogenic marine marker that they found in the Weddell Sea. The precise origin of this substance remains to be elucidated; however, one hypothesis suggests that it might be a byproduct of the excrement of sea lions. Alternatively, the marker may be the result of an enzymatic conversion process of creatine to creatinine within the marine environment (Decesari et al., 2020). In contrast to the findings reported by Decesari et al. (2020), no creatinine was detected in the samples collected on the *Eugen Seibold*. Given that the samples were collected at disparate locations and under differing climatic conditions, it can be hypothesized that creatinine cannot be used as a universal marine marker. Further studies are necessary to investigate the sources of creatinine in order to obtain a reliable marker compound.

The ocean plays a significant role in the global iodine cycle, serving as a main source of atmospheric iodine. The primary mechanism for iodine input into the atmosphere is the evaporation of organic iodides (Carpenter, 2003; Lovelock et al., 1973). Macroalgae (seaweeds) and microalgae (phytoplankton) represent the predominant sources of organic iodine compounds within the oceanic ecosystem (Carpenter, 2003). Consequently, the non-target analysis was conducted with a specific focus on the identification of organic iodine compounds. The predicted compound $C_9H_7IO_3$ may potentially serve as a novel marker compound for biogenic maritime emissions, as it was detected in all of the analyzed samples. However, it is crucial to conduct additional measurements, including MS/MS experiments, to verify the molecular formula and potentially suggest structural hypotheses.

Table 4.1: Possible marker substances, including their molecular formula, the exact mass of the quasi-molecular ion and their presence in the filter samples.

Substance	Sum formula	Exact mass of the analyzed ion / u	Found in samples
Methanesulfonic acid	CH_4O_3S	94.9808	Yes
Sulfuric acid	H_2SO_4	96.9601	Yes
Pinic acid	$C_9H_{14}O_4$	185.0819	Yes
MBTCA	$C_8H_{12}O_6$	203.0561	Yes
creatinine	$C_4H_7N_3O$	114.0662	No
Organic iodine compound	$C_9H_7IO_3$	288.9367	Yes

Figure 4.3 presents the extracted ion chromatograms (EICs) of the exact masses of the ions suspected in the semi-target analysis. The solid line corresponds to a loaded filter, while the dashed line corresponds to a blank filter and can therefore be used to correct for background. However, it is important to note that direct comparison of the absolute intensities of the compounds is hindered by the use of HESI as an ion source. This is due to the fact that the ionization efficiency can vary by several orders of magnitude for compounds with different functional groups (Liigand et al., 2021; Oss et al., 2010).

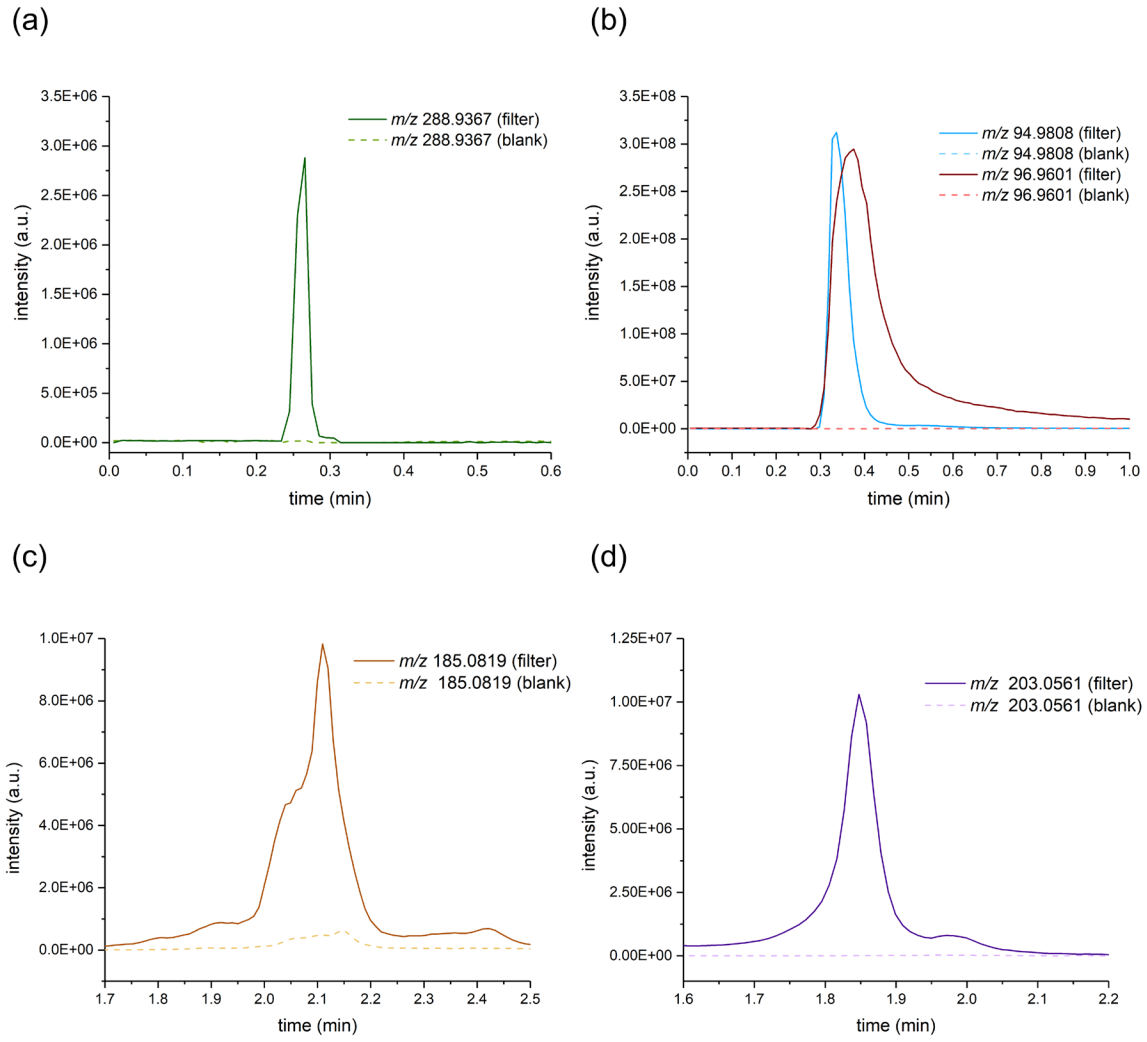

Figure 4.3: Extracted ion chromatogram for (a) *m/z* 288.9367 (green line), (b) *m/z* 94.9808 (blue line) and *m/z* 96.9601 (red line), (c) *m/z* 185.0819 and (d) *m/z* 203.0561 for a loaded filter and the corresponding EIC for a blank filter (green, blue, and red dashed lines). The EIC in (a) might correspond to the sum formula C_9H_7IO, the ones in (b) are representative of the marine marker compounds like MSA (blue line), or sulfuric acid (red line). The EIC in (c) might correspond to the pinene oxidation product pinic acid and the EIC in (d) is representative for the biogenic aging marker MBTCA.

As illustrated in Figure 4.3, the signals observed for the loaded filters differ significantly from those of the blank filter, and the EICs exhibit a high signal-to-noise ratio. The mass trace of the ion with *m/z* 185.0819 (Figure 4.3 (c)) displays a notable deviation in its peak form when compared to the other EICs presented. The mass trace in Figure 4.3 (c) appears to be composed of two overlapping signals, which may be attributed to the presence of other molecules with identical sum formulas. The mass trace is associated with pinic acid, a product of α-pinene oxidation. However, it is important to note that α-pinene is not the sole contributor to atmospheric terpene emissions; various other terpenes, including 3-carene, sabinene, and limonene, also contribute to these emissions. These terpenes undergo oxidation, resulting in the formation of compounds such as 3-carboxylic acid, sabinic acid, and limonic acid, which share the same sum formula as pinic acid. This phenomenon results in the presence of multiple compounds within a single mass trace (Glasius et al., 2000). Nevertheless, these mass traces definitively demonstrate that the sampling and extraction method presented herein enables the analysis of various biogenic marker compounds.

4.5 Conclusions

In this study, samples were collected over the course of a year between the northern polar circle and the equator and analyzed in a non-target analysis. The most intense signal detected is assigned to the molecular formula $C_{17}H_{28}O_3S$. Studies have shown that this is likely to be a component of heavy fuel oil and was therefore emitted either from the *Eugen Seibold* itself or from surrounding ships (Bai et al., 2020; Rüger et al., 2015; Antipenko and Melenevskii, 2012; Liu et al., 2010). However, biogenic CHOS compounds, such as $C_{15}H_{32}O_3S$, which has also been detected in extracts of seaweed, were also detected (Mofeed et al., 2022). In addition to this biogenic CHOS compound, molecular formulas were predicted ($C_{14}H_{28}O_2$, $C_{20}H_{40}O_2$, $C_{17}H_{34}O_2$), belonging to CHO compounds which were also detected in a study of extracts from *Corallina officinalis* (Mofeed et al., 2022). It is also notable that some CHONS compounds within area *I* of the Van Krevelen diagram were found in the samples near the Azores. These compounds are characterized by their high molecular weight of more than 250 u. The molecular formulas of these compounds are $C_{9\text{-}12}H_{22\text{-}32}N_{6\text{-}12}O_{1\text{-}5}S$. Notably, these compounds were not detected in samples from the Amazon rainforest or in the urban environment of Beijing, suggesting a probable marine origin (Ma et al., 2022; Leppla, 2021). The H/C ratio indicates aliphatic characteristics, but further studies are necessary to determine the structures of these compounds. Obtaining additional samples is also essential to ascertain the source of these compounds and to determine whether the presence of the compounds is a regional or seasonal effect, as they have only been detected near the Azores.

In addition to non-target analysis, a semi-targeted approach was employed, focusing on the detection of mass traces of known biogenic marker compounds. The mass traces that can be associated with methanesulfonic acid and sulfuric acid, two typical marine marker compounds, are present in all analyzed samples (Siegel et al., 2023; Katoshevski et al., 1999).

Additionally, pinic acid and MBTCA were detected in all samples. These compounds have been observed to originate from both terrestrial and marine sources (Yassaa et al., 2008; Kourtchev et al., 2008; Jenkin et al., 2000). A marine marker compound (creatinine) proposed by Decesari et al. (2020) could not be detected in any sample, suggesting that creatinine cannot be used universally as a marine marker and that its use may be linked to specific conditions, such as the location of the sampling point.

The ocean is a significant source of atmospheric iodine (Carpenter, 2003). Thus, there was a focus on the presence of organic iodine compounds. The molecular formula $C_9H_7IO_3$ was proposed for *m/z* 288.9367, which was also detected in all samples. The predicted compound $C_9H_7IO_3$ may potentially serve as a novel marker compound for biogenic maritime emissions. To verify the molecular formula and potentially suggest structural hypotheses, additional measurements, including MS/MS experiments, must be conducted.

A total of 26 samples were successfully collected and analyzed between Iceland and the equator, 8 of which were blank samples. Several biogenic marker compounds were observed, as well as potentially new marine compounds containing CHONS. In addition, an organic iodine compound was postulated. Further measurements are necessary to investigate regional and seasonal effects on the CHONS compounds and their potential sources.

4.6 Acknowledgements

I would like to thank Isabella Hrabe de Angelis and the working group on board the Eugen Seibold for their contribution in collecting the filter samples.

5. Summary and outlook

The aim of this work was to investigate the transport mechanisms, sources and sinks, and aging processes of organic aerosols (OA) in the atmosphere using chromatography with high-resolution mass spectrometry. For this purpose, the retention coefficients of three α-pinene oxidation products and four nitroaromatic compounds were determined in the vertical wind tunnel of the Johannes Gutenberg University under close to atmospheric conditions in mixed-phased clouds. Additionally, a miniaturized aerosol particle sampler was successfully developed for application in conjunction with drones to obtain vertical concentration profiles of secondary organic aerosol (SOA). In a third study, samples from the sailing vessel *Eugen Seibold* were utilized to investigate maritime sources in addition to the terrestrial and anthropogenic SOA.

Wind tunnel experiments were conducted within a temperature range of -12 to -3 °C, under dry and wet growth conditions. The wind speed was set at 3 m/s to simulate the fall velocity of graupel. These experiments were designed to elucidate the impact of temperature, pH (4 and 5.6), and growth regimes on the retention of organic compounds during riming. The retention coefficient of 2-nitrophenol demonstrated a variation with pH, exhibiting values of 0.19 ± 0.05 at pH 5.6 and 0.08 ± 0.04 at pH 4 for graupel samples. These findings indicate that pH can influence retention and should be taken into account when developing models of atmospheric processes involving such compounds. Additionally, a notable negative temperature trend was observed at pH 4, which aligns with the findings reported in the literature. Stuart and Jacobson (2004; 2003) had hypothesized that external factors such as temperature and pH could influence compounds with a low dimensionless effective Henry's law constant, H^*. This hypothesis is supported by the experimental observations, which indicate a dependence on these environmental variables for 2-nitrophenol. The retention coefficients of 2-nitrobenzoic acid, 4-nitrophenol, and 4-nitrocatechol were found to be close to 1 (0.99 ± 0.04, 1.01 ± 0.07, and 1.01 ± 0.14, respectively), showing no significant influence of temperature, pH, or growth regime. A similar observation was made with *cis*-pinic acid and *cis*-pinonic acid, which showed retention coefficients of 0.96 ± 0.07 and 0.92 ± 0.11, respectively. These findings indicate that compounds with a higher H^* value tend to exhibit stable retention behavior, independent of environmental factors. Pinanediol's retention coefficient was determined to be 0.98 ± 0.08, which was unexpected given its relatively low H^*. However, it should be noted that the Henry's law constant is only predicted and may be subject to errors due to the specific structure of the molecule. Given the absence of experimental data for H^* for a significant number of atmospherically relevant organic molecules, it is essential to measure the Henry's law constants of a larger variety of molecules to enhance understanding and improve modeling of atmospheric processes. The wind tunnel experiments demonstrated that molecular structure is a significant factor in retention. 2-Nitrophenol and 4-nitrophenol, despite being structural isomers, exhibited substantial differences in their retention coefficients. The different spatial arrangement of these

molecules allows for the formation of an intramolecular hydrogen bond between the hydroxyl group and the nitro group in 2-nitrophenol. This structural modification can potentially stabilize the non-dissociated form, which might contribute to the observed differences in solubility between the two isomers (Achard et al., 1996; Schwarzenbach et al., 1988). Additionally, this property may be a factor in the variation of Henry's law constants and retention. The wind tunnel measurements indicate that compounds with an H^* value below 10^3 experience minimal retention and are released into the gas phase during the freezing process. In contrast, compounds with an H^* value above 10^8 remain predominantly in the ice phase and can be removed from the atmosphere through precipitation. For compounds with intermediate H^* values, an improved fit for the relationship between R and H^* is provided, which could be used to estimate retention coefficients and further refine cloud models that simulate the transport and fate of organic trace components.

A lightweight aerosol sampling unit was developed to collect aerosol particles for detailed chemical characterization of organic aerosol components using UHPLC-MS. This unit allows for the collection of sufficient aerosol mass for both targeted and non-targeted analysis of primary and secondary organic aerosol components within the maximum flight time of the drones used. The newly developed system was tested during the BISTUM23 campaign, where aerosol samples were collected from varying altitudes to study vertical concentration profiles of organic aerosols. The findings indicated an increase in concentrations of biogenic SOA markers, such as pinic acid and terebic acid, from morning to afternoon. This observation correlated with rising ozone levels and increasing temperatures, indicating an increase in the release of precursor volatile organic compounds (VOCs), during the day (Vettikkat et al., 2023; Niinemets et al., 2004). The vertical concentration measurements indicated that the highest concentrations of these compounds were observed at 120 m, likely due to dry deposition and chemical aging (Spielmann et al., 2017; Bamberger et al., 2011). Non-targeted analysis of filter samples further supported these findings, showing an increase in oxidized compounds throughout the day and with increased altitude. The analysis also identified anthropogenic markers, particularly in morning samples, likely due to emissions from nearby road traffic. This finding highlights the potential of drones for cost-effective, height-selective sampling. To further extend the drone's flight duration or utilize smaller drones, there is a potential for miniaturization of the novel lightweight aerosol particle sampler. This reduction in weight would enable prolonged drone flight times, thereby facilitating extended sampling periods. A reduction in filter size, from the current 47 mm to 8 mm, has the potential to decrease the amount of solvent required, thereby reducing or even eliminating evaporation during sample preparation, thus enhancing the efficiency of the sample preparation process.

In the final section of the presented work, filter samples collected in the region between the northern polar circles and the equator in the years 2020 and 2021 were analyzed. These samples were collected with the help of the research sailing vessel *Eugen Seibold*. In the semi-targeted analysis, marine and biogenic marker compounds (methanesulfonic acid, sulfuric acid, pinic acid, and MBTCA) were detected in all samples. In the non-target analysis, certain biogenic compounds were identified, which have previously been detected in seaweed

extracts and are therefore likely to have a maritime origin. In addition, CHONS ($C_{9\text{-}12}H_{22\text{-}32}N_{6\text{-}12}O_{1\text{-}5}S$) compounds were detected, which were not detected in samples from the Amazon rainforest or in the urban environment of Beijing, suggesting a probable marine origin (Ma et al., 2022; Leppla, 2021). The H/C ratio indicates aliphatic characteristics; however, further studies are necessary to determine the structures of these compounds. Obtaining additional samples is also essential to ascertain the source of these compounds and to determine whether the presence of the compounds is a regional or seasonal effect, as they have only been detected near the Azores. Moreover, an organic iodine compound was detected in all samples, for which a molecular formula of $C_9H_7IO_3$ was postulated. The postulated compound $C_9H_7IO_3$ may potentially serve as a novel marker compound for biogenic maritime emissions. However, additional measurements, including MS/MS experiments, must be conducted to verify the molecular formula and suggest structural hypotheses.

6. References

Achard, C., Jaoui, M., Schwing, M., and Rogalski, M.: Aqueous Solubilities of Phenol Derivatives by Conductivity Measurements, J. Chem. Eng. Data, 41, 504–507, https://doi.org/10.1021/je950202o, 1996.

Aiken, A. C., Decarlo, P. F., Kroll, J. H., Worsnop, D. R., Huffman, J. A., Docherty, K. S., Ulbrich, I. M., Mohr, C., Kimmel, J. R., Sueper, D., Sun, Y., Zhang, Q., Trimborn, A., Northway, M., Ziemann, P. J., Canagaratna, M. R., Onasch, T. B., Alfarra, M. R., Prevot, A. S. H., Dommen, J., Duplissy, J., Metzger, A., Baltensperger, U., and Jimenez, J. L.: O/C and OM/OC ratios of primary, secondary, and ambient organic aerosols with high-resolution time-of-flight aerosol mass spectrometry, Environ. Sci. Technol., 42, 4478–4485, https://doi.org/10.1021/es703009q, 2008.

Anastasio, C. and McGregor, K. G.: Chemistry of fog waters in California's Central Valley: 1. In situ photoformation of hydroxyl radical and singlet molecular oxygen, Atmospheric Environment, 35, 1079–1089, https://doi.org/10.1016/S1352-2310(00)00281-8, 2001.

Andreae, M. O. and Rosenfeld, D.: Aerosol–cloud–precipitation interactions. Part 1. The nature and sources of cloud-active aerosols, Earth-Science Reviews, 89, 13–41, https://doi.org/10.1016/j.earscirev.2008.03.001, 2008.

Andreae, M. O., Acevedo, O. C., Araùjo, A., Artaxo, P., Barbosa, C. G. G., Barbosa, H. M. J., Brito, J., Carbone, S., Chi, X., Cintra, B. B. L., Da Silva, N. F., Dias, N. L., Dias-Júnior, C. Q., Ditas, F., Ditz, R., Godoi, A. F. L., Godoi, R. H. M., Heimann, M., Hoffmann, T., Kesselmeier, J., Könemann, T., Krüger, M. L., Lavric, J. V., Manzi, A. O., Lopes, A. P., Martins, D. L., Mikhailov, E. F., Moran-Zuloaga, D., Nelson, B. W., Nölscher, A. C., Santos Nogueira, D., Piedade, M. T. F., Pöhlker, C., Pöschl, U., Quesada, C. A., Rizzo, L. V., Ro, C.-U., Ruckteschler, N., Sá, L. D. A., Oliveira Sá, M. de, Sales, C. B., dos Santos, R. M. N., Saturno, J., Schöngart, J., Sörgel, M., Souza, C. M. de, Souza, R. A. F. de, Su, H., Targhetta, N., Tóta, J., Trebs, I., Trumbore, S., van Eijck, A., Walter, D., Wang, Z., Weber, B., Williams, J., Winderlich, J., Wittmann, F., Wolff, S., and Yáñez-Serrano, A. M.: The Amazon Tall Tower Observatory (ATTO): overview of pilot measurements on ecosystem ecology, meteorology, trace gases, and aerosols, Atmos. Chem. Phys., 15, 10723–10776, https://doi.org/10.5194/acp-15-10723-2015, 2015.

Andreae, M. O., Ferek, R. J., Bermond, F., Byrd, K. P., Engstrom, R. T., Hardin, S., Houmere, P. D., LeMarrec, F., Raemdonck, H., and Chatfield, R. B.: Dimethyl sulfide in the marine atmosphere, J. Geophys. Res., 90, 12891–12900, https://doi.org/10.1029/JD090iD07p12891, 1985.

Andreae, M. O., Afchine, A., Albrecht, R., Holanda, B. A., Artaxo, P., Barbosa, H. M. J., Borrmann, S., Cecchini, M. A., Costa, A., Dollner, M., Fütterer, D., Järvinen, E., Jurkat, T., Klimach, T., Konemann, T., Knote, C., Krämer, M., Krisna, T., Machado, L. A. T., Mertes, S., Minikin, A., Pöhlker, C., Pöhlker, M. L., Pöschl, U., Rosenfeld, D., Sauer, D., Schlager, H., Schnaiter, M., Schneider, J., Schulz, C., Spanu, A., Sperling, V. B., Voigt, C., Walser, A., Wang, J., Weinzierl, B.,

Wendisch, M., and Ziereis, H.: Aerosol characteristics and particle production in the upper troposphere over the Amazon Basin, Atmos. Chem. Phys., 18, 921–961, https://doi.org/10.5194/acp-18-921-2018, 2018.

Antipenko, V. R. and Melenevskii, V. N.: Composition of volatile products of flash pyrolysis of natural asphaltite and its resin-asphaltene and oil components, Pet. Chem., 52, 373–382, https://doi.org/10.1134/S0965544112060035, 2012.

Arakaki, T. and Faust, B. C.: Sources, sinks, and mechanisms of hydroxyl radical (• OH) photoproduction and consumption in authentic acidic continental cloud waters from Whiteface Mountain, New York: The role of the Fe(r) (r = II, III) photochemical cycle, J. Geophys. Res., 103, 3487–3504, https://doi.org/10.1029/97JD02795, 1998.

Arakaki, T., Kuroki, Y., Okada, K., Nakama, Y., Ikota, H., Kinjo, M., Higuchi, T., Uehara, M., and Tanahara, A.: Chemical composition and photochemical formation of hydroxyl radicals in aqueous extracts of aerosol particles collected in Okinawa, Japan, Atmospheric Environment, 40, 4764–4774, https://doi.org/10.1016/j.atmosenv.2006.04.035, 2006.

Atkinson, R. and Arey, J.: Atmospheric degradation of volatile organic compounds, Chemical reviews, 103, 4605–4638, https://doi.org/10.1021/cr0206420, 2003.

Bai, Z., Zhang, L., Cheng, Y., Zhang, W., Mao, J., Chen, H., Li, L., Wang, L., and Chen, J.: Water/Methanol-Insoluble Brown Carbon Can Dominate Aerosol-Enhanced Light Absorption in Port Cities, Environ. Sci. Technol., 54, 14889–14898, https://doi.org/10.1021/acs.est.0c03844, 2020.

Bamberger, I., Hörtnagl, L., Ruuskanen, T. M., Schnitzhofer, R., Müller, M., Graus, M., Karl, T., Wohlfahrt, G., and Hansel, A.: Deposition Fluxes of Terpenes over Grassland, J. Geophys. Res. Atmos., 116, https://doi.org/10.1029/2010JD015457, 2011.

Banerjee, S. and Mazumdar, S.: Electrospray ionization mass spectrometry: a technique to access the information beyond the molecular weight of the analyte, International journal of analytical chemistry, 2012, 282574, https://doi.org/10.1155/2012/282574, 2012.

Barbaro, E., Zangrando, R., Vecchiato, M., Piazza, R., Cairns, W. R. L., Capodaglio, G., Barbante, C., and Gambaro, A.: Free amino acids in Antarctic aerosol: potential markers for the evolution and fate of marine aerosol, Atmos. Chem. Phys., 15, 5457–5469, https://doi.org/10.5194/acp-15-5457-2015, 2015.

Bardakov, R., Thornton, J. A., Riipinen, I., Krejci, R., and Ekman, A. M. L.: Transport and chemistry of isoprene and its oxidation products in deep convective clouds, Tellus B: Chemical and Physical Meteorology, 73, 1979856, https://doi.org/10.1080/16000889.2021.1979856, 2022.

Barnes, I., Hjorth, J., and Mihalopoulos, N.: Dimethyl sulfide and dimethyl sulfoxide and their oxidation in the atmosphere, Chemical reviews, 106, 940–975, https://doi.org/10.1021/cr020529+, 2006.

Barth, M. C., Bela, M. M., Fried, A., Wennberg, P. O., Crounse, J. D., St. Clair, J. M., Blake, N. J., Blake, D. R., Homeyer, C. R., Brune, W. H., Zhang, L., Mao, J., Ren, X., Ryerson, T. B., Pollack, I. B., Peischl, J., Cohen, R. C., Nault, B. A., Huey, L. G., Liu, X., and Cantrell, C. A.: Convective transport and scavenging of peroxides by thunderstorms observed over the central U.S. during DC3, Journal of Geophysical Research: Atmospheres, 121, 4272–4295, https://doi.org/10.1002/2015JD024570, 2016.

Barth, M. C., Kim, S.-W., Wang, C., Pickering, K. E., Ott, L. E., Stenchikov, G., Leriche, M., Cautenet, S., Pinty, J.-P., Barthe, C., Mari, C., Helsdon, J. H., Farley, R. D., Fridlind, A. M., Ackerman, A. S., Spiridonov, V., and Telenta, B.: Cloud-scale model intercomparison of chemical constituent transport in deep convection, Atmos. Chem. Phys., 7, 4709–4731, https://doi.org/10.5194/acp-7-4709-2007, 2007a.

Barth, M. C., Kim, S.-W., Skamarock, W. C., Stuart, A. L., Pickering, K. E., and Ott, L. E.: Simulations of the redistribution of formaldehyde, formic acid, and peroxides in the 10 July 1996 Stratospheric-Tropospheric Experiment: Radiation, Aerosols, and Ozone deep convection storm, J. Geophys. Res., 112, D13310, https://doi.org/10.1029/2006JD008046, 2007b.

Beck, L. J., Sarnela, N., Junninen, H., Hoppe, C. J. M., Garmash, O., Bianchi, F., Riva, M., Rose, C., Peräkylä, O., Wimmer, D., Kausiala, O., Jokinen, T., Ahonen, L., Mikkilä, J., Hakala, J., He, X.-C., Kontkanen, J., Wolf, K. K. E., Cappelletti, D., Mazzola, M., Traversi, R., Petroselli, C., Viola, A. P., Vitale, V., Lange, R., Massling, A., Nøjgaard, J. K., Krejci, R., Karlsson, L., Zieger, P., Jang, S., Lee, K., Vakkari, V., Lampilahti, J., Thakur, R. C., Leino, K., Kangasluoma, J., Duplissy, E.-M., Siivola, E., Marbouti, M., Tham, Y. J., Saiz-Lopez, A., Petäjä, T., Ehn, M., Worsnop, D. R., Skov, H., Kulmala, M., Kerminen, V.-M., and Sipilä, M.: Differing Mechanisms of New Particle Formation at Two Arctic Sites, Geophys. Res. Lett., 48, https://doi.org/10.1029/2020GL091334, 2021.

Bela, M. M., Barth, M. C., Toon, O. B., Fried, A., Ziegler, C., Cummings, K. A., Li, Y., Pickering, K. E., Homeyer, C. R., Morrison, H., Yang, Q., Mecikalski, R. M., Carey, L., Biggerstaff, M. I., Betten, D. P., and Alford, A. A.: Effects of Scavenging, Entrainment, and Aqueous Chemistry on Peroxides and Formaldehyde in Deep Convective Outflow Over the Central and Southeast United States, J. Geophys. Res. Atmos., 123, 7594–7614, https://doi.org/10.1029/2018jd028271, 2018.

Benoit, R., Vernier, H., Vernier, J.-P., Joly, L., Dumelié, N., Wienhold, F. G., Crevoisier, C., Delpeux, S., Bernard, F., Dagaut, P., and Berthet, G.: The first balloon-borne sample analysis of atmospheric carbonaceous components reveals new insights into formation processes, Chemosphere, 326, 138421, https://doi.org/10.1016/j.chemosphere.2023.138421, 2023.

Bernstein, J. A., Alexis, N., Barnes, C., Bernstein, I. L., Nel, A., Peden, D., Diaz-Sanchez, D., Tarlo, S. M., and Williams, P. B.: Health effects of air pollution, The Journal of allergy and clinical immunology, 114, 1116–1123, https://doi.org/10.1016/j.jaci.2004.08.030, 2004.

Bhattarai, H., Saikawa, E., Wan, X., Zhu, H., Ram, K., Gao, S., Kang, S., Zhang, Q., Zhang, Y., Wu, G., Wang, X., Kawamura, K., Fu, P., and Cong, Z.: Levoglucosan as a tracer of biomass burning: Recent progress and perspectives, Atmospheric Research, 220, 20–33, https://doi.org/10.1016/j.atmosres.2019.01.004, 2019.

Bianchi, F., Kurtén, T., Riva, M., Mohr, C., Rissanen, M. P., Roldin, P., Berndt, T., Crounse, J. D., Wennberg, P. O., Mentel, T. F., Wildt, J., Junninen, H., Jokinen, T., Kulmala, M., Worsnop, D. R., Thornton, J. A., Donahue, N., Kjaergaard, H. G., and Ehn, M.: Highly Oxygenated Organic Molecules (HOM) from Gas-Phase Autoxidation Involving Peroxy Radicals: A Key Contributor to Atmospheric Aerosol, Chemical reviews, 119, 3472–3509, https://doi.org/10.1021/acs.chemrev.8b00395, 2019.

Bieber, P., Seifried, T. M., Burkart, J., Gratzl, J., Kasper-Giebl, A., Schmale, D. G., and Grothe, H.: A Drone-Based Bioaerosol Sampling System to Monitor Ice Nucleation Particles in the Lower Atmosphere, Remote Sensing, 12, 552, https://doi.org/10.3390/rs12030552, 2020.

Bikkina, P., Kawamura, K., Bikkina, S., Kunwar, B., Tanaka, K., and Suzuki, K.: Hydroxy Fatty Acids in Remote Marine Aerosols over the Pacific Ocean: Impact of Biological Activity and Wind Speed, ACS Earth and Space Chemistry, 3, 366–379, https://doi.org/10.1021/acsearthspacechem.8b00161, 2019.

Böhmländer, A. J., Lacher, L., Brus, D., Doulgeris, K.-M., Brasseur, Z., Boyer, M., Kuula, J., Leisner, T., and Möhler, O.: A novel aerosol filter sampler for measuring the vertical distribution of ice-nucleating particles via fixed-wing uncrewed aerial vehicles, Atmos. Meas. Tech. Discuss. [preprint], 2024.

Borchers, C., Moormann, L., Geil, B., Karbach, N., and Hoffmann, T.: Development and use of a lightweight sampling system for height-selective drone-based measurements of organic aerosol particles, EGUsphere [preprint], https://doi.org/10.5194/egusphere-2024-4015, 2025.

Borchers, C., Seymore, J., Gautam, M., Dörholt, K., Müller, Y., Arndt, A., Gömmer, L., Ungeheuer, F., Szakáll, M., Borrmann, S., Theis, A., Vogel, A. L., and Hoffmann, T.: Retention of α -pinene oxidation products and nitro-aromatic compounds during riming, Atmos. Chem. Phys., 24, 13961–13974, https://doi.org/10.5194/acp-24-13961-2024, 2024.

Broadgate, W., Malin, G., Küpper, F., Thompson, A., and Liss, P.: Isoprene and other non-methane hydrocarbons from seaweeds: a source of reactive hydrocarbons to the atmosphere, Marine Chemistry, 88, 61–73, https://doi.org/10.1016/j.marchem.2004.03.002, 2004.

Brunekreef, B. and Forsberg, B.: Epidemiological evidence of effects of coarse airborne particles on health, The European respiratory journal, 26, 309–318, https://doi.org/10.1183/09031936.05.00001805, 2005.

Cao, M., Li, W., Ge, P., Chen, M., and Wang, J.: Seasonal variations and potential sources of biomass burning tracers in particulate matter in Nanjing aerosols during 2017-2018,

Chemosphere, 303, 135015, https://doi.org/10.1016/j.chemosphere.2022.135015, 2022.

Carlton, A. G., Wiedinmyer, C., and Kroll, J. H.: A review of Secondary Organic Aerosol (SOA) formation from isoprene, Atmos. Chem. Phys., 9, 4987–5005, https://doi.org/10.5194/acp-9-4987-2009, 2009.

Carlton, A. G., Pinder, R. W., Bhave, P. V., and Pouliot, G. A.: To what extent can biogenic SOA be controlled?, Environ. Sci. Technol., 44, 3376–3380, https://doi.org/10.1021/es903506b, 2010.

Carlton, A. G., Turpin, B. J., Lim, H.-J., Altieri, K. E., and Seitzinger, S.: Link between isoprene and secondary organic aerosol (SOA): Pyruvic acid oxidation yields low volatility organic acids in clouds, Geophys. Res. Lett., 33, https://doi.org/10.1029/2005GL025374, 2006.

Carpenter, L. J.: Iodine in the marine boundary layer, Chemical reviews, 103, 4953–4962, https://doi.org/10.1021/cr0206465, 2003.

Charlson, R. J., Lovelock, J. E., Andreae, M. O., and Warren, S. G.: Oceanic phytoplankton, atmospheric sulphur, cloud albedo and climate, Nature, 326, 655–661, https://doi.org/10.1038/326655a0, 1987.

Chuong, B., Zhang, J., and Donahue, N. M.: Cycloalkene ozonolysis: collisionally mediated mechanistic branching, Journal of the American Chemical Society, 126, 12363–12373, https://doi.org/10.1021/ja0485412, 2004.

Claeys, M., Wang, W., Vermeylen, R., Kourtchev, I., Chi, X., Farhat, Y., Surratt, J. D., Gómez-González, Y., Sciare, J., and Maenhaut, W.: Chemical characterisation of marine aerosol at Amsterdam Island during the austral summer of 2006–2007, Journal of Aerosol Science, 41, 13–22, https://doi.org/10.1016/j.jaerosci.2009.08.003, 2010.

Claeys, M., Wang, W., Ion, A. C., Kourtchev, I., Gelencsér, A., and Maenhaut, W.: Formation of secondary organic aerosols from isoprene and its gas-phase oxidation products through reaction with hydrogen peroxide, Atmospheric Environment, 38, 4093–4098, https://doi.org/10.1016/j.atmosenv.2004.06.001, 2004a.

Claeys, M., Graham, B., Vas, G., Wang, W., Vermeylen, R., Pashynska, V., Cafmeyer, J., Guyon, P., Andreae, M. O., Artaxo, P., and Maenhaut, W.: Formation of secondary organic aerosols through photooxidation of isoprene, Science (New York, N.Y.), 303, 1173–1176, https://doi.org/10.1126/science.1092805, 2004b.

Clarke, A. D., Varner, J. L., Eisele, F., Mauldin R. L., Tanner, D., and Litchy, M.: Particle production in the remote marine atmosphere: Cloud outflow and subsidence during ACE 1, J. Geophys. Res., 103, 16397–16409, 1998.

Cornell, S., Jickells, T., Cape, J., Rowland, A., and Duce, R.: Organic nitrogen deposition on land and coastal environments: a review of methods and data, Atmospheric Environment, 37, 2173–2191, https://doi.org/10.1016/S1352-2310(03)00133-X, 2003.

Crounse, J. D., Nielsen, L. B., Jørgensen, S., Kjaergaard, H. G., and Wennberg, P. O.: Autoxidation of Organic Compounds in the Atmosphere, J. Phys. Chem. Lett., 4, 3513–3520, https://doi.org/10.1021/jz4019207, 2013.

Cuchiara, G. C., Fried, A., Barth, M. C., Bela, M. M., Homeyer, C. R., Walega, J., Weibring, P., Richter, D., Woods, S., Beyersdorf, A., Bui, T. V., and Dean-Day, J.: Effect of Marine and Land Convection on Wet Scavenging of Ozone Precursors Observed During a SEAC 4 RS Case Study, J. Geophys. Res. Atmos., 128, e2022JD037107, https://doi.org/10.1029/2022JD037107, 2023.

Decesari, S., Paglione, M., Rinaldi, M., Dall'Osto, M., Simó, R., Zanca, N., Volpi, F., Facchini, M. C., Hoffmann, T., Götz, S., Kampf, C. J., O'Dowd, C., Ceburnis, D., Ovadnevaite, J., and Tagliavini, E.: Shipborne measurements of Antarctic submicron organic aerosols: an NMR perspective linking multiple sources and bioregions, Atmos. Chem. Phys., 20, 4193–4207, https://doi.org/10.5194/acp-20-4193-2020, 2020.

Desyaterik, Y., Sun, Y., Shen, X., Lee, T., Wang, X., Wang, T., and Collett, J. L.: Speciation of "brown" carbon in cloud water impacted by agricultural biomass burning in eastern China, J. Geophys. Res. Atmos., 118, 7389–7399, https://doi.org/10.1002/jgrd.50561, 2013.

Diehl, K., Mitra, S. K., Szakáll, M., Blohn, N. von, Borrmann, S., and Pruppacher, H. R.: The Mainz vertical wind tunnel facility: a review of 25 years of laboratory experiments on cloud physics and chemistry: Aerodynamics, models, and experiments, Wind Tunnels: Aerodynamics, Models, and Experiments, Nova Science Publisher's, New York, 69-92, 2011.

Donahue, N. M., Kroll, J. H., Pandis, S. N., and Robinson, A. L.: A two-dimensional volatility basis set – Part 2: Diagnostics of organic-aerosol evolution, Atmos. Chem. Phys., 12, 615–634, https://doi.org/10.5194/acp-12-615-2012, 2012.

Donahue, N. M., Robinson, A. L., Stanier, C. O., and Pandis, S. N.: Coupled partitioning, dilution, and chemical aging of semivolatile organics, Environ. Sci. Technol., 40, 2635–2643, https://doi.org/10.1021/es052297c, 2006.

Donahue, N. M., Robinson, A. L., and Pandis, S. N.: Atmospheric organic particulate matter: From smoke to secondary organic aerosol, Atmospheric Environment, 43, 94–106, https://doi.org/10.1016/j.atmosenv.2008.09.055, 2009.

Draxler, R. R. and Hess, G. D.: An overview of the HYSPLIT_4 modelling system for trajectories, Australian Meteorological Magazine, 47, available at: https://www.researchgate.net/profile/g-hess/publication/239061109_an_overview_of_the_hysplit_4_modelling_system_for_trajectories, 1998.

Edney, E. O., Kleindienst, T. E., Jaoui, M., Lewandowski, M., Offenberg, J. H., Wang, W., and Claeys, M.: Formation of 2-methyl tetrols and 2-methylglyceric acid in secondary organic aerosol from laboratory irradiated isoprene/NOX/SO2/air mixtures and their detection in

ambient PM2.5 samples collected in the eastern United States, Atmospheric Environment, 39, 5281–5289, https://doi.org/10.1016/j.atmosenv.2005.05.031, 2005.

Facchini, M. C., Rinaldi, M., Decesari, S., Carbone, C., Finessi, E., Mircea, M., Fuzzi, S., Ceburnis, D., Flanagan, R., Nilsson, E. D., Leeuw, G. de, Martino, M., Woeltjen, J., and O'Dowd, C. D.: Primary submicron marine aerosol dominated by insoluble organic colloids and aggregates, Geophys. Res. Lett., 35, 396, https://doi.org/10.1029/2008GL034210, 2008a.

Facchini, M. C., Decesari, S., Rinaldi, M., Carbone, C., Finessi, E., Mircea, M., Fuzzi, S., Moretti, F., Tagliavini, E., Ceburnis, D., and O'Dowd, C. D.: Important source of marine secondary organic aerosol from biogenic amines, Environ. Sci. Technol., 42, 9116–9121, https://doi.org/10.1021/es8018385, 2008b.

Faust, B. C. and Allen, J. M.: Aqueous-phase photochemical formation of hydroxyl radical in authentic cloudwaters and fogwaters, Environ. Sci. Technol., 27, 1221–1224, https://doi.org/10.1021/es00043a024, 1993.

Fleming, L. T., Lin, P., Roberts, J. M., Selimovic, V., Yokelson, R., Laskin, J., Laskin, A., and Nizkorodov, S. A.: Molecular composition and photochemical lifetimes of brown carbon chromophores in biomass burning organic aerosol, Atmos. Chem. Phys., 20, 1105–1129, https://doi.org/10.5194/acp-20-1105-2020, 2020.

Florou, K., Błaziak, A., Jorga, S., Uruci, P., Vasilakopoulou, C. N., Szmigielski, R., and Pandis, S. N.: Properties and Atmospheric Oxidation of Terebic Acid Aerosol, ACS Earth and Space Chemistry, 8, 2090–2100, https://doi.org/10.1021/acsearthspacechem.4c00201, 2024.

Fu, P., Kawamura, K., and Miura, K.: Molecular characterization of marine organic aerosols collected during a round-the-world cruise, J. Geophys. Res., 116, 482603, https://doi.org/10.1029/2011JD015604, 2011.

Fugal, J. P., Schulz, T. J., and Shaw, R. A.: Practical methods for automated reconstruction and characterization of particles in digital in-line holograms, Meas. Sci. Technol., 20, 75501, https://doi.org/10.1088/0957-0233/20/7/075501, 2009.

Fugal, J. P., Shaw, R. A., Saw, E. W., and Sergeyev, A. V.: Airborne digital holographic system for cloud particle measurements, Applied optics, 43, 5987–5995, https://doi.org/10.1364/ao.43.005987, 2004.

Ganranoo, L., Mishra, S. K., Azad, A. K., Shigihara, A., Dasgupta, P. K., Breitbach, Z. S., Armstrong, D. W., Grudpan, K., and Rappenglueck, B.: Measurement of nitrophenols in rain and air by two-dimensional liquid chromatography-chemically active liquid core waveguide spectrometry, Analytical chemistry, 82, 5838–5843, https://doi.org/10.1021/ac101015y, 2010.

Gey, M. H.: Instrumentelle Analytik und Bioanalytik: Biosubstanzen, Trennmethoden, Strukturanalytik, Applikationen, 4. Aufl. 2021, Springer Berlin Heidelberg, Berlin, Heidelberg, 563 pp., 2021.

Gilman, J. B., Lerner, B. M., Kuster, W. C., Goldan, P. D., Warneke, C., Veres, P. R., Roberts, J. M., Gouw, J. A. de, Burling, I. R., and Yokelson, R. J.: Biomass burning emissions and potential air quality impacts of volatile organic compounds and other trace gases from fuels common in the US, Atmos. Chem. Phys., 15, 13915–13938, https://doi.org/10.5194/acp-15-13915-2015, 2015.

Glasius, M., Lahaniati, M., Calogirou, A., Di Bella, D., Jensen, N. R., Hjorth, J., Kotzias, D., and Larsen, B. R.: Carboxylic Acids in Secondary Aerosols from Oxidation of Cyclic Monoterpenes by Ozone, Environ. Sci. Technol., 34, 1001–1010, https://doi.org/10.1021/es990445r, 2000.

Goldstein, A. H. and Galbally, I. E.: Known and unknown organic constituents in the Earth' s atmosphere, Environ. Sci. Technol., 41, 1514–1521, https://doi.org/10.1021/es072476p, 2007.

Gómez-González, Y., Wang, W., Vermeylen, R., Chi, X., Neirynck, J., Janssens, I. A., Maenhaut, W., and Claeys, M.: Chemical characterisation of atmospheric aerosols during a 2007 summer field campaign at Brasschaat, Belgium: sources and source processes of biogenic secondary organic aerosol, Atmos. Chem. Phys., 12, 125–138, https://doi.org/10.5194/acp-12-125-2012, 2012.

Gouw, J. de and Jimenez, J. L.: Organic aerosols in the Earth's atmosphere, Environ. Sci. Technol., 43, 7614–7618, https://doi.org/10.1021/es9006004, 2009.

Gross, J. H.: Massenspektrometrie: Ein Lehrbuch, SpringerLink Bücher, Springer Berlin Heidelberg, Berlin, Heidelberg, 802 pp., 2013.

Guenther, A., Karl, T., Harley, P., Wiedinmyer, C., Palmer, P. I., and Geron, C.: Estimates of global terrestrial isoprene emissions using MEGAN (Model of Emissions of Gases and Aerosols from Nature), Atmos. Chem. Phys., 6, 3181–3210, https://doi.org/10.5194/acp-6-3181-2006, 2006.

Guenther, A. B., Jiang, X., Heald, C. L., Sakulyanontvittaya, T., Duhl, T., Emmons, L. K., and Wang, X.: The Model of Emissions of Gases and Aerosols from Nature version 2.1 (MEGAN2.1): an extended and updated framework for modeling biogenic emissions, Geosci. Model Dev., 5, 1471–1492, https://doi.org/10.5194/gmd-5-1471-2012, 2012.

Guenther, A., Hewitt, C. N., Erickson, D., Fall, R., Geron, C., Graedel, T., Harley, P., Klinger, L., Lerdau, M., Mckay, W. A., Pierce, T., Scholes, B., Steinbrecher, R., Tallamraju, R., Taylor, J., and Zimmerman, P.: A global model of natural volatile organic compound emissions, J. Geophys. Res., 100, 8873–8892, https://doi.org/10.1029/94JD02950, 1995.

Gunthe, S. S., King, S. M., Rose, D., Chen, Q., Roldin, P., Farmer, D. K., Jimenez, J. L., Artaxo, P., Andreae, M. O., Martin, S. T., and Pöschl, U.: Cloud condensation nuclei in pristine tropical rainforest air of Amazonia: size-resolved measurements and modeling of atmospheric aerosol composition and CCN activity, Atmos. Chem. Phys., 9, 7551–7575, https://doi.org/10.5194/acp-9-7551-2009, 2009.

Guo, X. X. and Brimblecombe, P.: Henry's law constants of phenol and mononitrophenols in water and aqueous sulfuric acid, Chemosphere, 68, 436–444, https://doi.org/10.1016/j.chemosphere.2007.01.011, available at: https://www.sciencedirect.com/science/article/pii/S0045653507000069, 2007.

Hallquist, M., Wenger, J. C., Baltensperger, U., Rudich, Y., Simpson, D., Claeys, M., Dommen, J., Donahue, N. M., George, C., Goldstein, A. H., Hamilton, J. F., Herrmann, H., Hoffmann, T., Iinuma, Y., Jang, M., Jenkin, M. E., Jimenez, J. L., Kiendler-Scharr, A., Maenhaut, W., McFiggans, G., Mentel, T. F., Monod, A., Prévôt, A. S. H., Seinfeld, J. H., Surratt, J. D., Szmigielski, R., and Wildt, J.: The formation, properties and impact of secondary organic aerosol: current and emerging issues, Atmos. Chem. Phys., 9, 5155–5236, https://doi.org/10.5194/acp-9-5155-2009, 2009.

Harris, D. C., Werner, G., and Werner, T.: Lehrbuch der Quantitativen Analyse, 8. Aufl. 2014, Werner, G. and Werner, T. (Eds.), Springer Berlin Heidelberg, Berlin, Heidelberg, 977 pp., 2014.

Harrison, M. A., Barra, S., Borghesi, D., Vione, D., Arsene, C., and Iulian Olariu, R.: Nitrated phenols in the atmosphere: a review, Atmospheric Environment, 39, 231–248, https://doi.org/10.1016/j.atmosenv.2004.09.044, 2005.

Hatch, L. E., Creamean, J. M., Ault, A. P., Surratt, J. D., Chan, M. N., Seinfeld, J. H., Edgerton, E. S., Su, Y., and Prather, K. A.: Measurements of isoprene-derived organosulfates in ambient aerosols by aerosol time-of-flight mass spectrometry - part 1: single particle atmospheric observations in Atlanta, Environ. Sci. Technol., 45, 5105–5111, https://doi.org/10.1021/es103944a, 2011.

Hawkes, J. A., Dittmar, T., Patriarca, C., Tranvik, L., and Bergquist, J.: Evaluation of the Orbitrap Mass Spectrometer for the Molecular Fingerprinting Analysis of Natural Dissolved Organic Matter, Anal. Chem., 88, 7698–7704, https://doi.org/10.1021/acs.analchem.6b01624, 2016.

Hawkins, L. N., Russell, L. M., Covert, D. S., Quinn, P. K., and Bates, T. S.: Carboxylic acids, sulfates, and organosulfates in processed continental organic aerosol over the southeast Pacific Ocean during VOCALS-REx 2008, J. Geophys. Res., 115, https://doi.org/10.1029/2009JD013276, 2010.

Hayen, H. and Karst, U.: Strategies for the liquid chromatographic-mass spectrometric analysis of non-polar compounds, Journal of chromatography. A, 1000, 549–565, https://doi.org/10.1016/S0021-9673(03)00505-3, 2003.

Haynes, W. M.: CRC Handbook of Chemistry and Physics, CRC Press, 2014.

Henry, W.: III. Experiments on the quantity of gases absorbed by water, at different temperatures, and under different pressures, Phil. Trans. R. Soc., 93, 29–274, https://doi.org/10.1098/rstl.1803.0004, 1803.

Hine, J. and Mookerjee, P. K.: Structural effects on rates and equilibriums. XIX. Intrinsic hydrophilic character of organic compounds. Correlations in terms of structural contributions, The Journal of Organic Chemistry, 3, 292–298, available at: https://doi.org/10.1021/jo00891a006, 1975.

Hodshire, A. L., Akherati, A., Alvarado, M. J., Brown-Steiner, B., Jathar, S. H., Jimenez, J. L., Kreidenweis, S. M., Lonsdale, C. R., Onasch, T. B., Ortega, A. M., and Pierce, J. R.: Aging Effects on Biomass Burning Aerosol Mass and Composition: A Critical Review of Field and Laboratory Studies, Environ. Sci. Technol., 53, 10007–10022, https://doi.org/10.1021/acs.est.9b02588, 2019.

Hoffmann, T. and Klockow, D.: Atmosphärenchemie biogener Kohlenwasserstoffe, Chemie in nserer Zeit, 32, 182–191, https://doi.org/10.1002/ciuz.19980320403, 1998.

Hoffmann, T., Odum, J. R., Bowman, F., Collins, D., Klockow, D., Flagan, R. C., and Seinfeld, J. H.: Formation of Organic Aerosols from the Oxidation of Biogenic Hydrocarbons, J Atmos Chem, 26, 189–222, https://doi.org/10.1023/A:1005734301837, 1997.

Iavorivska, L., Boyer, E. W., and DeWalle, D. R.: Atmospheric deposition of organic carbon via precipitation, Atmospheric Environment, 146, 153–163, https://doi.org/10.1016/j.atmosenv.2016.06.006, 2016.

Iribarne, J. V. and Pyshnov, T.: The effect of freezing on the composition of supercooled droplets—I. Retention of HCl, HNO3, NH3 and H2O2, Atmospheric Environment. Part A. General Topics, 24, 383–387, https://doi.org/10.1016/0960-1686(90)90118-7, 1990.

Jenkin, M. E.: Modelling the formation and composition of secondary organic aerosol from α- and β-pinene ozonolysis using MCM v3, Atmos. Chem. Phys., 4, 1741–1757, https://doi.org/10.5194/acp-4-1741-2004, 2004.

Jenkin, M. E., Shallcross, D. E., and Harvey, J. N.: Development and application of a possible mechanism for the generation of cis-pinic acid from the ozonolysis of α- and β-pinene, Atmospheric Environment, 34, 2837–2850, https://doi.org/10.1016/S1352-2310(00)00087-X, 2000.

Jimenez, J. L., Canagaratna, M. R., Donahue, N. M., Prevot, A. S. H., Zhang, Q., Kroll, J. H., DeCarlo, P. F., Allan, J. D., Coe, H., Ng, N. L., Aiken, A. C., Docherty, K. S., Ulbrich, I. M., Grieshop, A. P., Robinson, A. L., Duplissy, J., Smith, J. D., Wilson, K. R., Lanz, V. A., Hueglin, C., Sun, Y. L., Tian, J., Laaksonen, A., Raatikainen, T., Rautiainen, J., Vaattovaara, P., Ehn, M., Kulmala, M., Tomlinson, J. M., Collins, D. R., Cubison, M. J., Dunlea, J., Huffman, J. A., Onasch, T. B., Alfarra, M. R., Williams, P. I., Bower, K., Kondo, Y., Schneider, J., Drewnick, F., Borrmann, S., Weimer, S., Demerjian, K., Salcedo, D., Cottrell, L., Griffin, R., Takami, A., Miyoshi, T., Hatakeyama, S., Shimono, A., Sun, J. Y., Zhang, Y. M., Dzepina, K., Kimmel, J. R., Sueper, D., Jayne, J. T., Herndon, S. C., Trimborn, A. M., Williams, L. R., Wood, E. C., Middlebrook, A. M., Kolb, C. E., Baltensperger, U., and Worsnop, D. R.: Evolution of Organic Aerosols in the Atmosphere,

Science (New York, N.Y.), 326, 1525–1529, https://doi.org/10.1126/science.1180353, 2009.

Jost, A.: Bereifungsexperimente zur Bestimmung des SO2 - Retentionskoeffizienten; durchgeführt am vertikalen Windkanal der Johannes Gutenberg Universität Mainz, Diplomarbeit, Institut für Physik der Atmosphäre, Johannes Gutenberg Universität Mainz, Mainz, 189 pp., 2012.

Jost, A., Szakáll, M., Diehl, K., Mitra, S. K., and Borrmann, S.: Chemistry of riming: the retention of organic and inorganic atmospheric trace constituents, Atmos. Chem. Phys., 17, 9717–9732, https://doi.org/10.5194/acp-17-9717-2017, 2017.

Kanakidou, M., Seinfeld, J. H., Pandis, S. N., Barnes, I., Dentener, F. J., Facchini, M. C., van Dingenen, R., Ervens, B., Nenes, A., Nielsen, C. J., Swietlicki, E., Putaud, J. P., Balkanski, Y., Fuzzi, S., Horth, J., Moortgat, G. K., Winterhalter, R., Myhre, C. E. L., Tsigaridis, K., Vignati, E., Stephanou, E. G., and Wilson, J.: Organic aerosol and global climate modelling: a review, Atmos. Chem. Phys., 5, 1053–1123, https://doi.org/10.5194/acp-5-1053-2005, 2005.

Katoshevski, D., Nenes, A., and Seinfeld, J. H.: A study of process that govern the maintenance of aerosols in the marine boundary layer, Journal of Aerosol Science, 30, 503–532, https://doi.org/10.1016/S0021-8502(98)00740-X, 1999.

Kebarle, P. and Verkerk, U. H.: Electrospray: from ions in solution to ions in the gas phase, what we know now, Mass spectrometry reviews, 28, 898–917, https://doi.org/10.1002/mas.20247, 2009.

Kebarle, P. and Tang, L.: From ions in solution to ions in the gas phase - the mechanism of electrospray mass spectrometry, Anal. Chem., 65, 972A-986A, https://doi.org/10.1021/ac00070a001, 1993.

Kerminen, V.-M., Chen, X., Vakkari, V., Petäjä, T., Kulmala, M., and Bianchi, F.: Atmospheric new particle formation and growth: review of field observations, Environ. Res. Lett., 13, 103003, https://doi.org/10.1088/1748-9326/aadf3c, 2018.

Kerminen, V.-M., Lihavainen, H., Komppula, M., Viisanen, Y., and Kulmala, M.: Direct observational evidence linking atmospheric aerosol formation and cloud droplet activation, Geophys. Res. Lett., 32, https://doi.org/10.1029/2005GL023130, 2005.

Kesselmeier, J. and Staudt, M.: Biogenic Volatile Organic Compounds (VOC): An Overview on Emission, Physiology and Ecology, J Atmos Chem, 33, 23–88, https://doi.org/10.1023/A:1006127516791, 1999.

Kind, T. and Fiehn, O.: Seven Golden Rules for heuristic filtering of molecular formulas obtained by accurate mass spectrometry, BMC bioinformatics, 105, https://doi.org/10.1186/1471-2105-8-105, 2007.

Kish, J. D., Leng, C., Kelley, J., Hiltner, J., Zhang, Y., and Liu, Y.: An improved approach for measuring Henry's law coefficients of atmospheric organics, Atmospheric Environment, 79, 561–565, https://doi.org/10.1016/j.atmosenv.2013.07.023, 2013.

Köhler, H.: The nucleus in and the growth of hygroscopic droplets, Trans. Faraday Soc., 32, 1152–1161, https://doi.org/10.1039/TF9363201152, 1936.

Kołodziejczyk, A., Pyrcz, P., Błaziak, K., Pobudkowska, A., Sarang, K., and Szmigielski, R.: Physicochemical Properties of Terebic Acid, MBTCA, Diaterpenylic Acid Acetate, and Pinanediol as Relevant α-Pinene Oxidation Products, ACS omega, 5, 7919–7927, https://doi.org/10.1021/acsomega.9b04231, 2020.

Kołodziejczyk, A., Pyrcz, P., Pobudkowska, A., Błaziak, K., and Szmigielski, R.: Physicochemical Properties of Pinic, Pinonic, Norpinic, and Norpinonic Acids as Relevant α-Pinene Oxidation Products, The journal of physical chemistry. B, 123, 8261–8267, https://doi.org/10.1021/acs.jpcb.9b05211, 2019.

Konermann, L., Ahadi, E., Rodriguez, A. D., and Vahidi, S.: Unraveling the mechanism of electrospray ionization, Analytical chemistry, 85, 2–9, https://doi.org/10.1021/ac302789c, 2013.

Korolev, A., McFarquhar, G., Field, P. R., Franklin, C., Lawson, P., Wang, Z., Williams, E., Abel, S. J., Axisa, D., Borrmann, S., Crosier, J., Fugal, J., Krämer, M., Lohmann, U., Schlenczek, O., Schnaiter, M., and Wendisch, M.: Mixed-Phase Clouds: Progress and Challenges, Meteorological Monographs, 58, 5.1-5.50, https://doi.org/10.1175/AMSMONOGRAPHS-D-17-0001.1, 2017.

Kourtchev, I., Fuller, S., Aalto, J., Ruuskanen, T. M., McLeod, M. W., Maenhaut, W., Jones, R., Kulmala, M., and Kalberer, M.: Molecular composition of boreal forest aerosol from Hyytiälä, Finland, using ultrahigh resolution mass spectrometry, Environ. Sci. Technol., 47, 4069–4079, https://doi.org/10.1021/es3051636, 2013.

Kourtchev, I., Warnke, J., Maenhaut, W., Hoffmann, T., and Claeys, M.: Polar organic marker compounds in PM2.5 aerosol from a mixed forest site in western Germany, Chemosphere, 73, 1308–1314, https://doi.org/10.1016/j.chemosphere.2008.07.011, 2008.

Krishnan, R., Sanjay, J., Gnanaseelan, C., Mujumdar, M., Kulkarni, A., and Chakraborty, S.: Assessment of Climate Change over the Indian Region: A Report of the Ministry of Earth Sciences (MoES), Government of India, Springer Singapore, Singapore, 1 online resource, 2020.

Kroll, J. H. and Seinfeld, J. H.: Chemistry of secondary organic aerosol: Formation and evolution of low-volatility organics in the atmosphere, Atmospheric Environment, 42, 3593–3624, https://doi.org/10.1016/j.atmosenv.2008.01.003, 2008.

Kroll, J. H., Ng, N. L., Murphy, S. M., Flagan, R. C., and Seinfeld, J. H.: Secondary organic aerosol formation from isoprene photooxidation, Environmental science & technology, 40, 1869–1877, https://doi.org/10.1021/es0524301, 2006.

Kühne, R., Ebert, R.-U., and Schüürmann, G.: Prediction of the temperature dependency of Henry's law constant from chemical structure, Environmental science & technology, 39, 6705–6711, https://doi.org/10.1021/es050527h, 2005.

Kulakova, E. S., Safarov, A. M., Safarova, V. I., Malkova, M. A., and Kantor, E. A.: Phenol monitoring in the air of the city residential part, IOP Conf. Ser.: Earth Environ. Sci., 579, 12102, https://doi.org/10.1088/1755-1315/579/1/012102, 2020.

Kuznetsova, M., Lee, C., and Aller, J.: Characterization of the proteinaceous matter in marine aerosols, Marine Chemistry, 96, 359–377, https://doi.org/10.1016/j.marchem.2005.03.007, 2005.

Lan, H., Hartonen, K., and Riekkola, M.-L.: Miniaturised air sampling techniques for analysis of volatile organic compounds in air, TrAC Trends in Analytical Chemistry, 126, 115873, https://doi.org/10.1016/j.trac.2020.115873, 2020.

Laranjeiro, F., Rotander, A., López-Ibáñez, S., Vilas, A., Södergren Seilitz, F., Clérandeau, C., Sampalo, M., Rial, D., Bellas, J., Cachot, J., Almeda, R., and Beiras, R.: Comparative assessment of the acute toxicity of commercial bio-based polymer leachates on marine plankton, The Science of the total environment, 946, 174403, https://doi.org/10.1016/j.scitotenv.2024.174403, 2024.

Laskin, A., Laskin, J., and Nizkorodov, S. A.: Mass spectrometric approaches for chemical characterisation of atmospheric aerosols: critical review of the most recent advances, Environ. Chem., 9, 163, https://doi.org/10.1071/EN12052, 2012.

Lelieveld, J., Evans, J. S., Fnais, M., Giannadaki, D., and Pozzer, A.: The contribution of outdoor air pollution sources to premature mortality on a global scale, Nature, 525, 367–371, https://doi.org/10.1038/nature15371, 2015.

Leppla, D.: Comprehensive Study of Secondary Organic Aerosol Particles from the Amazon Rainforest by High-Resolution Mass Spectrometry, Johannes Gutenberg-Universität Mainz, 2021.

Leppla, D., Zannoni, N., Kremper, L., Williams, J., Pöhlker, C., Sá, M., Solci, M. C., and Hoffmann, T.: Varying chiral ratio of pinic acid enantiomers above the Amazon rainforest, Atmos. Chem. Phys., 23, 809–820, https://doi.org/10.5194/acp-23-809-2023, 2023.

Li, B., Ho, S. S. H., Li, X., Guo, L., Chen, A., Hu, L., Yang, Y., Di Chen, Lin, A., and Fang, X.: A comprehensive review on anthropogenic volatile organic compounds (VOCs) emission estimates in China: Comparison and outlook, Environment international, 156, 106710, https://doi.org/10.1016/j.envint.2021.106710, 2021.

Li, D.-X., Gan, L., Bronja, A., and Schmitz, O. J.: Gas chromatography coupled to atmospheric pressure ionization mass spectrometry (GC-API-MS): review, Analytica chimica acta, 891, 43–61, https://doi.org/10.1016/j.aca.2015.08.002, 2015.

Li, M., Wang, X., Lu, C., Li, R., Zhang, J., Dong, S., Yang, L., Xue, L., Chen, J., and Wang, W.: Nitrated phenols and the phenolic precursors in the atmosphere in urban Jinan, China, Science of The Total Environment, 714, 136760, https://doi.org/10.1016/j.scitotenv.2020.136760, 2020.

Li, Y., Ren, H., Zhou, S., Pei, C., Gao, M., Liang, Y., Ye, D., Sun, X., Li, F., Zhao, J., Hang, J., Fan, S., and Fu, P.: Tower-based profiles of wintertime secondary organic aerosols in the urban boundary layer over Guangzhou, The Science of the total environment, 950, 175326, https://doi.org/10.1016/j.scitotenv.2024.175326, 2024.

Liggio, J., Li, S.-M., and McLaren, R.: Heterogeneous reactions of glyoxal on particulate matter: identification of acetals and sulfate esters, Environ. Sci. Technol., 39, 1532–1541, https://doi.org/10.1021/es048375y, 2005.

Lignell, H., Epstein, S. A., Marvin, M. R., Shemesh, D., Gerber, B., and Nizkorodov, S.: Experimental and theoretical study of aqueous cis-pinonic acid photolysis, The journal of physical chemistry. A, 117, 12930–12945, https://doi.org/10.1021/jp4093018, 2013.

Liigand, P., Liigand, J., Kaupmees, K., and Kruve, A.: 30 Years of research on ESI/MS response: Trends, contradictions and applications, Analytica chimica acta, 1152, 238117, https://doi.org/10.1016/j.aca.2020.11.049, 2021.

Lim, Y. B., Tan, Y., Perri, M. J., Seitzinger, S. P., and Turpin, B. J.: Aqueous chemistry and its role in secondary organic aerosol (SOA) formation, Atmos. Chem. Phys., 10, 10521–10539, https://doi.org/10.5194/acp-10-10521-2010, 2010.

Lin, J. J., Kristensen, T. B., Calderón, S. M., Malila, J., and Prisle, N. L.: Effects of surface tension time-evolution for CCN activation of a complex organic surfactant, Environmental science. Processes & impacts, 22, 271–284, https://doi.org/10.1039/c9em00426b, 2020.

Lin, Y.-H., Knipping, E. M., Edgerton, E. S., Shaw, S. L., and Surratt, J. D.: Investigating the influences of SO_2 and NH_3 levels on isoprene-derived secondary organic aerosol formation using conditional sampling approaches, Atmos. Chem. Phys., 13, 8457–8470, https://doi.org/10.5194/acp-13-8457-2013, 2013a.

Lin, Y.-H., Zhang, H., Pye, H. O. T., Zhang, Z., Marth, W. J., Park, S., Arashiro, M., Cui, T., Budisulistiorini, S. H., Sexton, K. G., Vizuete, W., Xie, Y., Luecken, D. J., Piletic, I. R., Edney, E. O., Bartolotti, L. J., Gold, A., and Surratt, J. D.: Epoxide as a precursor to secondary organic aerosol formation from isoprene photooxidation in the presence of nitrogen oxides, Proceedings of the National Academy of Sciences of the United States of America, 110, 6718–6723, https://doi.org/10.1073/pnas.1221150110, 2013b.

List, R.: Zur Thermodynamik teilweise wässriger Hagelkörner, Journal of Applied Mathematics and Physics (ZAMP), 11, 273–306, https://doi.org/10.1007/BF01602676, 1960.

Liu, P., Shi, Q., Chung, K. H., Zhang, Y., Pan, N., Zhao, S., and Xu, C.: Molecular Characterization of Sulfur Compounds in Venezuela Crude Oil and Its SARA Fractions by Electrospray

Ionization Fourier Transform Ion Cyclotron Resonance Mass Spectrometry, Energy Fuels, 24, 5089–5096, https://doi.org/10.1021/ef100904k, 2010.

Löflund, M., Kasper-Giebl, A., Schuster, B., Giebl, H., Hitzenberger, R., and Puxbaum, H.: Formic, acetic, oxalic, malonic and succinic acid concentrations and their contribution to organic carbon in cloud water, Atmospheric Environment, 36, 1553–1558, https://doi.org/10.1016/S1352-2310(01)00573-8, 2002.

Lohmann, U. and Feichter, J.: Global indirect aerosol effects: a review, Atmos. Chem. Phys., 5, 715–737, https://doi.org/10.5194/acp-5-715-2005, 2005.

Lohmann, U., Lüönd, F., and Mahrt, F.: An introduction to clouds: From the microscale to climate, First published 2016. Reprinted 2020, Cambridge University Press, Cambridge, 2020.

Lovelock, J. E., Maggs, R. J., and Wade, R. J.: Halogenated Hydrocarbons in and over the Atlantic, Nature, 241, 194–196, https://doi.org/10.1038/241194a0, 1973.

Lu, C., Wang, X., Dong, S., Zhang, J., Li, J., Zhao, Y., Liang, Y., Xue, L., Xie, H., Zhang, Q., and Wang, W.: Emissions of fine particulate nitrated phenols from various on-road vehicles in China, Environmental Research, 179, 108709, https://doi.org/10.1016/j.envres.2019.108709, 2019.

Ma, J., Ungeheuer, F., Zheng, F., Du, W., Wang, Y., Cai, J., Zhou, Y., Yan, C., Liu, Y., Kulmala, M., Daellenbach, K. R., and Vogel, A. L.: Nontarget Screening Exhibits a Seasonal Cycle of PM2.5 Organic Aerosol Composition in Beijing, Environ. Sci. Technol., 56, 7017–7028, https://doi.org/10.1021/acs.est.1c06905, 2022.

Mackay, D. and Shiu, W. Y.: A critical review of Henry's law constants for chemicals of environmental interest, Journal of Physical and Chemical Reference Data, 10, 1175–1199, https://doi.org/10.1063/1.555654, 1981.

Macklin, W. C.: Accretion in mixed clouds, Quart J Royal Meteoro Soc, 87, 413–424, https://doi.org/10.1002/qj.49708737312, 1961.

Makarov, A.: Electrostatic axially harmonic orbital trapping: a high-performance technique of mass analysis, Anal. Chem., 72, 1156–1162, https://doi.org/10.1021/ac991131p, 2000.

Makarov, A. and Scigelova, M.: Coupling liquid chromatography to Orbitrap mass spectrometry, Journal of chromatography. A, 1217, 3938–3945, https://doi.org/10.1016/j.chroma.2010.02.022, 2010.

Malherbe, S. and Cloete, T. E.: Lignocellulose biodegradation: Fundamentals and applications, Rev Environ Sci Biotechnol, 1, 105–114, https://doi.org/10.1023/A:1020858910646, 2002.

McGarvey, D. J. and Croteau, R.: Terpenoid metabolism, The Plant cell, 7, 1015–1026, https://doi.org/10.1105/tpc.7.7.1015, 1995.

Meylan, W. M. and Howard, P. H.: Bond contribution method for estimating henry's law constants, Environmental Toxicology and Chemistry, 10, 1283–1293, available at: https://doi.org/10.1002/etc.5620101007, 1991.

Michael, R. and Stuart, A. L.: The fate of volatile chemicals during wet growth of a hailstone, Environ. Res. Lett., 4, 15001, https://doi.org/10.1088/1748-9326/4/1/015001, 2009.

Michalski, A., Damoc, E., Hauschild, J.-P., Lange, O., Wieghaus, A., Makarov, A., Nagaraj, N., Cox, J., Mann, M., and Horning, S.: Mass spectrometry-based proteomics using Q Exactive, a high-performance benchtop quadrupole Orbitrap mass spectrometer, Molecular & cellular proteomics MCP, 10, M111.011015, https://doi.org/10.1074/mcp.M111.011015, 2011.

Mikhailov, E. F., Mironova, S., Mironov, G., Vlasenko, S., Panov, A., Chi, X., Walter, D., Carbone, S., Artaxo, P., Heimann, M., Lavric, J., Pöschl, U., and Andreae, M. O.: Long-term measurements (2010–2014) of carbonaceous aerosol and carbon monoxide at the Zotino Tall Tower Observatory (ZOTTO) in central Siberia, Atmos. Chem. Phys., 17, 14365–14392, https://doi.org/10.5194/acp-17-14365-2017, 2017.

Minerath, E. C. and Elrod, M. J.: Assessing the potential for diol and hydroxy sulfate ester formation from the reaction of epoxides in tropospheric aerosols, Environ. Sci. Technol., 43, 1386–1392, https://doi.org/10.1021/es8029076, 2009.

Mochida, M., Kitamori, Y., Kawamura, K., Nojiri, Y., and Suzuki, K.: Fatty acids in the marine atmosphere: Factors governing their concentrations and evaluation of organic films on sea-salt particles, J. Geophys. Res., 107, https://doi.org/10.1029/2001JD001278, 2002.

Mofeed, J., Deyab, M., MOHAMED, A., MOUSTAFA, M., NEGM, S., and EL-BILAWY, E.: Antimicrobial activities of three seaweeds extract against some human viral and bacterial pathogens, BIOCELL, 46, 247–261, https://doi.org/10.32604/biocell.2022.015966, 2022.

Moormann, L., Böttger, T., Schuhmann, P., Valero, L., Fachinger, F., and Drewnick, F.: The Flying Laboratory FLab: Development and application of a UAS to measure aerosol particles and trace gases in the lower troposphere, EGUsphere [preprint], https://doi.org/10.5194/egusphere-2024-3566, 2024.

Müller, C., Iinuma, Y., Karstensen, J., van Pinxteren, D., Lehmann, S., Gnauk, T., and Herrmann, H.: Seasonal variation of aliphatic amines in marine sub-micrometer particles at the Cape Verde islands, Atmos. Chem. Phys., 9, 9587–9597, https://doi.org/10.5194/acp-9-9587-2009, 2009.

Müller, L., Reinnig, M.-C., Naumann, K. H., Saathoff, H., Mentel, T. F., Donahue, N. M., and Hoffmann, T.: Formation of 3-methyl-1,2,3-butanetricarboxylic acid via gas phase oxidation of pinonic acid – a mass spectrometric study of SOA aging, Atmos. Chem. Phys., 12, 1483–1496, https://doi.org/10.5194/acp-12-1483-2012, 2012.

Murray, K. K., Boyd, R. K., Eberlin, M. N., Langley, G. J., Li, L., and Naito, Y.: Definitions of terms relating to mass spectrometry (IUPAC Recommendations 2013), Pure and Applied Chemistry, 85, 1515–1609, https://doi.org/10.1351/PAC-REC-06-04-06, 2013.

Myriokefalitakis, S., Vignati, E., Tsigaridis, K., Papadimas, C., Sciare, J., Mihalopoulos, N., Facchini, M. C., Rinaldi, M., Dentener, F. J., Ceburnis, D., Hatzianastasiou, N., O'Dowd, C. D., van Weele, M., and Kanakidou, M.: Global Modeling of the Oceanic Source of Organic Aerosols, Advances in Meteorology, 2010, https://doi.org/10.1155/2010/939171, 2010.

Net, S., Alvarez, E. G., Gligorovski, S., and Wortham, H.: Heterogeneous reactions of ozone with methoxyphenols, in presence and absence of light, Atmospheric Environment, 45, 3007–3014, https://doi.org/10.1016/j.atmosenv.2011.03.026, 2011.

Ng, N. L., Kroll, J. H., Chan, A. W. H., Chhabra, P. S., Flagan, R. C., and Seinfeld, J. H.: Secondary organic aerosol formation from m-xylene, toluene, and benzene, Atmos. Chem. Phys., 7, 3909–3922, https://doi.org/10.5194/acp-7-3909-2007, 2007.

Niinemets, U., Loreto, F., and Reichstein, M.: Physiological and physicochemical controls on foliar volatile organic compound emissions, Trends in plant science, 9, 180–186, https://doi.org/10.1016/j.tplants.2004.02.006, 2004.

Nozière, B., Kalberer, M., Claeys, M., Allan, J., D'Anna, B., Decesari, S., Finessi, E., Glasius, M., Grgić, I., Hamilton, J. F., Hoffmann, T., Iinuma, Y., Jaoui, M., Kahnt, A., Kampf, C. J., Kourtchev, I., Maenhaut, W., Marsden, N., Saarikoski, S., Schnelle-Kreis, J., Surratt, J. D., Szidat, S., Szmigielski, R., and Wisthaler, A.: The molecular identification of organic compounds in the atmosphere: state of the art and challenges, Chemical reviews, 115, 3919–3983, https://doi.org/10.1021/cr5003485, 2015.

O'Dowd, C. D., Facchini, M. C., Cavalli, F., Ceburnis, D., Mircea, M., Decesari, S., Fuzzi, S., Yoon, Y. J., and Putaud, J.-P.: Biogenically driven organic contribution to marine aerosol, Nature, 431, 676–680, https://doi.org/10.1038/nature02959, 2004.

O'Dowd, C. D., Smith, M. H., Consterdine, I. E., and Lowe, J. A.: Marine aerosol, sea-salt, and the marine sulphur cycle: a short review, Atmospheric Environment, 31, 73–80, https://doi.org/10.1016/S1352-2310(96)00106-9, 1997.

Odum, J. R., Hoffmann, T., Bowman, F., Collins, D., Flagan, R. C., and Seinfeld, J. H.: Gas/Particle Partitioning and Secondary Organic Aerosol Yields, Environmental science & technology, 30, 2580–2585, https://doi.org/10.1021/es950943, 1996.

Osaka, I., Yoshimoto, A., Nozaki, K., Moriwaki, H., Kawasaki, H., and Arakawa, R.: Simultaneous LC/MS analysis of hexachlorobenzene and pentachlorophenol by atmospheric pressure chemical ionization (APCI) and photoionization (APPI) methods, Analytical sciences the international journal of the Japan Society for Analytical Chemistry, 25, 1373–1376, https://doi.org/10.2116/analsci.25.1373, 2009.

Oss, M., Kruve, A., Herodes, K., and Leito, I.: Electrospray ionization efficiency scale of organic compounds, Analytical chemistry, 82, 2865–2872, https://doi.org/10.1021/ac902856t, 2010.

Pandis, S. N., Paulson, S. E., Seinfeld, J. H., and Flagan, R. C.: Aerosol formation in the photooxidation of isoprene and β-pinene, Atmospheric Environment. Part A. General Topics, 25, 997–1008, https://doi.org/10.1016/0960-1686(91)90141-S, 1991.

Pankow, J. F., Seinfeld, J. H., Asher, W. E., and Erdakos, G. B.: Modeling the formation of secondary organic aerosol. 1. Application of theoretical principles to measurements obtained in the alpha-pinene/, beta-pinene/, sabinene/, delta3-carene/, and cyclohexane/ozone systems, Environ. Sci. Technol., 35, 1164–1172, https://doi.org/10.1021/es001321d, 2001.

Pankow, J. F.: An absorption model of the gas/aerosol partitioning involved in the formation of secondary organic aerosol, Atmospheric Environment, 28, 189–193, https://doi.org/10.1016/1352-2310(94)90094-9, 1994.

Perry, R. H., Cooks, R. G., and Noll, R. J.: Orbitrap mass spectrometry: instrumentation, ion motion and applications, Mass spectrometry reviews, 27, 661–699, https://doi.org/10.1002/mas.20186, 2008.

Pflaum, J. C. and Pruppacher, H. R.: A Wind Tunnel Investigation of the Growth of Graupel Initiated from Frozen Drops, J. Atmos. Sci., 36, 680–689, https://doi.org/10.1175/1520-0469(1979)036<0680:AWTIOT>2.0.CO;2, 1979.

Pluskal, T., Castillo, S., Villar-Briones, A., and Oresic, M.: MZmine 2: modular framework for processing, visualizing, and analyzing mass spectrometry-based molecular profile data, BMC bioinformatics, 11, 395, https://doi.org/10.1186/1471-2105-11-395, 2010.

Pöschl, U.: Atmosphärische Aerosole: Zusammensetzung, Transformation, Klima- und Gesundheitseffekte, Angewandte Chemie, 117, 7690–7712, https://doi.org/10.1002/ange.200501122, 2005.

Pruppacher, H. R. and Klett, J. D.: Microphysics of Clouds and Precipitation, 18, Springer Netherlands, Dordrecht, 975 pp., 2010.

Pusfitasari, E. D., Ruiz-Jimenez, J., Heiskanen, I., Jussila, M., Hartonen, K., and Riekkola, M.-L.: Aerial drone furnished with miniaturized versatile air sampling systems for selective collection of nitrogen containing compounds in boreal forest, The Science of the total environment, 808, 152011, https://doi.org/10.1016/j.scitotenv.2021.152011, 2022.

Pye, H. O. T., Nenes, A., Alexander, B., Ault, A. P., Barth, M. C., Clegg, S. L., Collett, J. L., Fahey, K. M., Hennigan, C. J., Herrmann, H., Kanakidou, M., Kelly, J. T., Ku, I.-T., McNeill, V. F., Riemer, N., Schaefer, T., Shi, G., Tilgner, A., Walker, J. T., Wang, T., Weber, R., Xing, J., Zaveri, R. A., and Zuend, A.: The Acidity of Atmospheric Particles and Clouds, Atmospheric chemistry and physics, 20, 4809–4888, https://doi.org/10.5194/acp-20-4809-2020, 2020.

Ramteke, S., Sahu, B. L., Patel, K. S., Pandey, P. K., Yurdakul, S., Martín-Ramos, P., Ren, H., and Fu, P.: Characterization of Organic Aerosols in the Ambient Air of Raipur, Central India: Distribution, Seasonal Variations, and Source Apportionment, Aerosol Sci Eng, https://doi.org/10.1007/s41810-024-00246-4, 2024.

Rana, M. S. and Guzman, M. I.: Oxidation of Phenolic Aldehydes by Ozone and Hydroxyl Radicals at the Air-Solid Interface, ACS Earth and Space Chemistry, 6, 2900–2909, https://doi.org/10.1021/acsearthspacechem.2c00206, 2022.

Rayleigh, J. W. S.: XX. On the equilibrium of liquid conducting masses charged with electricity, The London, Edinburgh, and Dublin Philosophical Magazine and Journal of Science, 14, 184–186, https://doi.org/10.1080/14786448208628425, 1882.

Reddington, C. L., Carslaw, K. S., Spracklen, D. V., Frontoso, M. G., Collins, L., Merikanto, J., Minikin, A., Hamburger, T., Coe, H., Kulmala, M., Aalto, P., Flentje, H., Plass-Dülmer, C., Birmili, W., Wiedensohler, A., Wehner, B., Tuch, T., Sonntag, A., O'Dowd, C. D., Jennings, S. G., Dupuy, R., Baltensperger, U., Weingartner, E., Hansson, H.-C., Tunved, P., Laj, P., Sellegri, K., Boulon, J., Putaud, J.-P., Gruening, C., Swietlicki, E., Roldin, P., Henzing, J. S., Moerman, M., Mihalopoulos, N., Kouvarakis, G., Ždímal, V., Zíková, N., Marinoni, A., Bonasoni, P., and Duchi, R.: Primary versus secondary contributions to particle number concentrations in the European boundary layer, Atmos. Chem. Phys., 11, 12007–12036, https://doi.org/10.5194/acp-11-12007-2011, 2011.

Reijenga, J., van Hoof, A., van Loon, A., and Teunissen, B.: Development of Methods for the Determination of pKa Values, Analytical chemistry insights, 8, 53–71, https://doi.org/10.4137/ACI.S12304, 2013.

Resch, F. J., Darrozes, J. S., and Afeti, G. M.: Marine liquid aerosol production from bursting of air bubbles, J. Geophys. Res., 91, 1019–1029, https://doi.org/10.1029/JC091iC01p01019, 1986.

Ritgen, U.: Analytische Chemie I, Springer Berlin Heidelberg, Berlin, Heidelberg, 2019.

Rolph, G., Stein, A., and Stunder, B.: Real-time Environmental Applications and Display sYstem: READY, Environmental Modelling & Software, 95, 210–228, https://doi.org/10.1016/j.envsoft.2017.06.025, 2017.

Rosenfeld, D.: New insights to cloud seeding for enhancing precipitation and for hail suppression, The Journal of Weather Modification, 39, 61–69, https://doi.org/10.54782/jwm.v39i1.203, 2007.

Rosenfeld, D., Andreae, M. O., Asmi, A., Chin, M., Leeuw, G. de, Donovan, D. P., Kahn, R., Kinne, S., Kivekäs, N., Kulmala, M., Lau, W., Schmidt, K. S., Suni, T., Wagner, T., Wild, M., and Quaas, J.: Global observations of aerosol-cloud-precipitation-climate interactions, Rev. Geophys., 52, 750–808, https://doi.org/10.1002/2013RG000441, 2014.

Rosenfeld, D., Lohmann, U., Raga, G. B., O'Dowd, C. D., Kulmala, M., Fuzzi, S., Reissell, A., and Andreae, M. O.: Flood or drought: how do aerosols affect precipitation?, Science (New York, N.Y.), 321, 1309–1313, https://doi.org/10.1126/science.1160606, 2008.

Rüger, C. P., Sklorz, M., Schwemer, T., and Zimmermann, R.: Characterisation of ship diesel primary particulate matter at the molecular level by means of ultra-high-resolution mass spectrometry coupled to laser desorption ionisation--comparison of feed fuel, filter

extracts and direct particle measurements, Analytical and bioanalytical chemistry, 407, 5923–5937, https://doi.org/10.1007/s00216-014-8408-1, 2015.

Sander, R.: Compilation of Henry's law constants (version 5.0.0) for water as solvent, Atmos. Chem. Phys., 23, 10901–12440, https://doi.org/10.5194/acp-23-10901-2023, 2023.

Saxena, P. and Hildemann, L. M.: Water-soluble organics in atmospheric particles: A critical review of the literature and application of thermodynamics to identify candidate compounds, J Atmos Chem, 24, 57–109, https://doi.org/10.1007/BF00053823, 1996.

Schiebel, R., Aardema, H. M., Calleja, M. L., Dragoneas, A., Heins, L., Hrabe de Angelis, I., Pöhlker, C., Slagter, H., Vonhof, H., Walter, D., Arns, A. I., Adolphs, N., Auderset, A., Basic, S., Bieler, A., Brüwer, J. D., Chaabane, S., Cheng, Y., Chiliński, M. T., Cybulski, J. D., Disper, T., Duprey, N., Eichele, G., Fiedler, B., Fischer, A., Foreman, A. D., Fuchs, B. M., Galer, S., Härri, J., Jochum, K. P., Jost, A., Jung, J., Kleta, H., Lammel, G., Larink, O., Leibold, P., Martínez-García, A., Moretti, S., Müller, J.-G., Nillius, B., Pan, X., Raj, S. S., Repschläger, J., Rodrigues, E., Ruff, S. E., Schmitt, M., Schmitter, J. L., Lara, A. S., Silva, P., Smart, S. M., Sörgel, M., Stoll, B., Su, H., Vogt, M., Wald, T., Weber, B., Weber, J., Weis, U., Amann, R., Arístegui, J., Dittmar, T., González, M., O'Dea, A., Pöschl, U., and Haug, G. H.: Preface: Special Issue on Probing the Open Ocean With the Research Sailing Yacht Eugen Seibold for Climate Geochemistry, J. Geophys. Res. Atmos., 129, https://doi.org/10.1029/2023JD040581, 2024.

Schmitt-Kopplin, P., Liger-Belair, G., Koch, B. P., Flerus, R., Kattner, G., Harir, M., Kanawati, B., Lucio, M., Tziotis, D., Hertkorn, N., and Gebefügi, I.: Dissolved organic matter in sea spray: a transfer study from marine surface water to aerosols, Biogeosciences, 9, 1571–1582, https://doi.org/10.5194/bg-9-1571-2012, 2012.

Schwarzenbach, R. P., Stierli, R., Folsom, B. R., and Zeyer, J.: Compound properties relevant for assessing the environmental partitioning of nitrophenols, Environ. Sci. Technol., 22, 83–92, https://doi.org/10.1021/es00166a009, 1988.

Scigelova, M. and Makarov, A.: Orbitrap mass analyzer--overview and applications in proteomics, Proteomics, 6 Suppl 2, 16–21, https://doi.org/10.1002/pmic.200600528, 2006.

Seinfeld, J. H. and Pandis, S. N.: Atmospheric chemistry and physics: From Air Pollution to Climate Change, 2nd ed., Wiley, New York, 203 pp., 2006.

Seinfeld, J. H. and Pankow, J. F.: Organic atmospheric particulate material, Annual review of physical chemistry, 54, 121–140, https://doi.org/10.1146/annurev.physchem.54.011002.103756, 2003.

Shaw, G. E.: Bio-controlled thermostasis involving the sulfur cycle, Climatic Change, 5, 297–303, https://doi.org/10.1007/BF02423524, 1983.

Siegel, K., Gramlich, Y., Haslett, S. L., Freitas, G., Krejci, R., Zieger, P., and Mohr, C.: Arctic observations of hydroperoxymethyl thioformate (HPMTF) – seasonal behavior and relationship to other oxidation products of dimethyl sulfide at the Zeppelin Observatory,

Svalbard, Atmos. Chem. Phys., 23, 7569–7587, https://doi.org/10.5194/acp-23-7569-2023, 2023.

Simon, M., Dada, L., Heinritzi, M., Scholz, W., Stolzenburg, D., Fischer, L., Wagner, A. C., Kürten, A., Rörup, B., He, X.-C., Almeida, J., Baalbaki, R., Baccarini, A., Bauer, P. S., Beck, L., Bergen, A., Bianchi, F., Bräkling, S., Brilke, S., Caudillo, L., Chen, D., Chu, B., Dias, A., Draper, D. C., Duplissy, J., El-Haddad, I., Finkenzeller, H., Frege, C., Gonzalez-Carracedo, L., Gordon, H., Granzin, M., Hakala, J., Hofbauer, V., Hoyle, C. R., Kim, C., Kong, W., Lamkaddam, H., Lee, C. P., Lehtipalo, K., Leiminger, M., Mai, H., Manninen, H. E., Marie, G., Marten, R., Mentler, B., Molteni, U., Nichman, L., Nie, W., Ojdanic, A., Onnela, A., Partoll, E., Petäjä, T., Pfeifer, J., Philippov, M., Quéléver, L. L. J., Ranjithkumar, A., Rissanen, M. P., Schallhart, S., Schobesberger, S., Schuchmann, S., Shen, J., Sipilä, M., Steiner, G., Stozhkov, Y., Tauber, C., Tham, Y. J., Tomé, A. R., Vazquez-Pufleau, M., Vogel, A. L., Wagner, R., Wang, M., Wang, D. S., Wang, Y., Weber, S. K., Wu, Y., Xiao, M., Yan, C., Ye, P., Ye, Q., Zauner-Wieczorek, M., Zhou, X., Baltensperger, U., Dommen, J., Flagan, R. C., Hansel, A., Kulmala, M., Volkamer, R., Winkler, P. M., Worsnop, D. R., Donahue, N. M., Kirkby, J., and Curtius, J.: Molecular understanding of new-particle formation from α-pinene between −50 and +25 °C, Atmos. Chem. Phys., 20, 9183–9207, https://doi.org/10.5194/acp-20-9183-2020, 2020.

Simoneit, B., Schauer, J. J., Nolte, C. G., Oros, D. R., Elias, V. O., Fraser, M. P., Rogge, W. F., and Cass, G. R.: Levoglucosan, a tracer for cellulose in biomass burning and atmospheric particles, Atmospheric Environment, 33, 173–182, https://doi.org/10.1016/S1352-2310(98)00145-9, 1999.

Sindelarova, K., Granier, C., Bouarar, I., Guenther, A., Tilmes, S., Stavrakou, T., Müller, J.-F., Kuhn, U., Stefani, P., and Knorr, W.: Global data set of biogenic VOC emissions calculated by the MEGAN model over the last 30 years, Atmos. Chem. Phys., 14, 9317–9341, https://doi.org/10.5194/acp-14-9317-2014, 2014.

Smith, J. S., Laskin, A., and Laskin, J.: Molecular characterization of biomass burning aerosols using high-resolution mass spectrometry, Analytical chemistry, 81, 1512–1521, https://doi.org/10.1021/ac8020664, 2009.

Snider, J. R. and Huang, J.: Factors influencing the retention of hydrogen peroxide and molecular oxygen in rime ice, J. Geophys. Res., 103, 1405–1415, https://doi.org/10.1029/97JD02847, 1998.

Snider, J. R., Montague, D. C., and Vali, G.: Hydrogen peroxide retention in rime ice, J. Geophys. Res., 97, 7569–7578, https://doi.org/10.1029/92JD00237, 1992.

Spielmann, F. M., Langebner, S., Ghirardo, A., Hansel, A., Schnitzler, J.-P., and Wohlfahrt, G.: Isoprene and α-pinene deposition to grassland mesocosms, Plant Soil, 410, 313–322, https://doi.org/10.1007/s11104-016-3009-8, 2017.

Spolnik, G., Wach, P., Rudziński, K. J., Szmigielski, R., and Danikiewicz, W.: Tracing the biogenic secondary organic aerosol markers in rain, snow and hail, Chemosphere, 251, 126439, https://doi.org/10.1016/j.chemosphere.2020.126439, 2020.

Stein, A. F., Draxler, R. R., Rolph, G. D., Stunder, B. J. B., Cohen, M. D., and Ngan, F.: NOAA's HYSPLIT Atmospheric Transport and Dispersion Modeling System, Bulletin of the American Meteorological Society, 96, 2059–2077, https://doi.org/10.1175/BAMS-D-14-00110.1, 2015.

Stolzenburg, D., Fischer, L., Vogel, A. L., Heinritzi, M., Schervish, M., Simon, M., Wagner, A. C., Dada, L., Ahonen, L. R., Amorim, A., Baccarini, A., Bauer, P. S., Baumgartner, B., Bergen, A., Bianchi, F., Breitenlechner, M., Brilke, S., Buenrostro Mazon, S., Chen, D., Dias, A., Draper, D. C., Duplissy, J., El Haddad, I., Finkenzeller, H., Frege, C., Fuchs, C., Garmash, O., Gordon, H., He, X., Helm, J., Hofbauer, V., Hoyle, C. R., Kim, C., Kirkby, J., Kontkanen, J., Kürten, A., Lampilahti, J., Lawler, M., Lehtipalo, K., Leiminger, M., Mai, H., Mathot, S., Mentler, B., Molteni, U., Nie, W., Nieminen, T., Nowak, J. B., Ojdanic, A., Onnela, A., Passananti, M., Petäjä, T., Quéléver, L. L. J., Rissanen, M. P., Sarnela, N., Schallhart, S., Tauber, C., Tomé, A., Wagner, R., Wang, M., Weitz, L., Wimmer, D., Xiao, M., Yan, C., Ye, P., Zha, Q., Baltensperger, U., Curtius, J., Dommen, J., Flagan, R. C., Kulmala, M., Smith, J. N., Worsnop, D. R., Hansel, A., Donahue, N. M., and Winkler, P. M.: Rapid growth of organic aerosol nanoparticles over a wide tropospheric temperature range, Proceedings of the National Academy of Sciences of the United States of America, 115, 9122–9127, https://doi.org/10.1073/pnas.1807604115, 2018.

Stuart, A. L. and Jacobson, M. Z.: Chemical retention during dry growth riming, J. Geophys. Res., 109, https://doi.org/10.1029/2003JD004197, available at: https://doi.org/10.1029/2003JD004197, 2004.

Stuart, A. L. and Jacobson, M. Z.: A timescale investigation of volatile chemical retention during hydrometeor freezing: Nonrime freezing and dry growth riming without spreading, J. Geophys. Res., 108, https://doi.org/10.1029/2001JD001408, 2003.

Stull, R. B.: Practical meteorology: An algebra-based survey of atomspheric science, UBC, Vancouver, 944 pp., 2017.

Surratt, J. D., Chan, A. W. H., Eddingsaas, N. C., Chan, M., Loza, C. L., Kwan, A. J., Hersey, S. P., Flagan, R. C., Wennberg, P. O., and Seinfeld, J. H.: Reactive intermediates revealed in secondary organic aerosol formation from isoprene, Proceedings of the National Academy of Sciences of the United States of America, 107, 6640–6645, https://doi.org/10.1073/pnas.0911114107, 2010.

Szakáll, M., Mitra, S. K., Diehl, K., and Borrmann, S.: Shapes and oscillations of falling raindrops — A review, Atmospheric Research, 97, 416–425, https://doi.org/10.1016/j.atmosres.2010.03.024, 2010.

Tang, J., Li, J., Su, T., Han, Y., Mo, Y., Jiang, H., Cui, M., Jiang, B., Chen, Y., Tang, J., Song, J., Peng, P., and Zhang, G.: Molecular compositions and optical properties of dissolved brown carbon in biomass burning, coal combustion, and vehicle emission aerosols illuminated by excitation–emission matrix spectroscopy and Fourier transform ion cyclotron resonance mass spectrometry analysis, Atmos. Chem. Phys., 20, 2513–2532, https://doi.org/10.5194/acp-20-2513-2020, 2020.

Taylor, G. I.: Disintegration of water drops in an electric field, Proc. R. Soc. Lond. A, 280, 383–397, https://doi.org/10.1098/rspa.1964.0151, 1964.

Theis, A., Szakáll, M., Diehl, K., Mitra, S. K., Zanger, F., Heymsfield, A., and Borrmann, S.: Vertical Wind Tunnel Experiments and a Theoretical Study on the Microphysics of Melting Low-Density Graupel, J. Atmos. Sci., 79, 1069–1087, https://doi.org/10.1175/JAS-D-21-0162.1, 2022.

Thivet, S., Bagheri, G., Kornatowski, P. M., Fries, A., Lemus, J., Simionato, R., Díaz-Vecino, C., Rossi, E., Yamada, T., Scollo, S., and Bonadonna, C.: In-situ volcanic ash sampling and aerosol-gas analysis based on UAS technologies (AeroVolc), Atmos. Meas. Tech. Discuss. [preprint], https://doi.org/10.5194/amt-2024-162, 2024.

Thomson, B. A. and Iribarne, J. V.: Field induced ion evaporation from liquid surfaces at atmospheric pressure, The Journal of Chemical Physics, 71, 4451–4463, https://doi.org/10.1063/1.438198, 1979.

Twohy, C. H., Clement, C. F., Gandrud, B. W., Weinheimer, A. J., Campos, T. L., Baumgardner, D., Brune, W. H., Faloona, I., Sachse, G. W., Vay, S. A., and Tan, D.: Deep convection as a source of new particles in the midlatitude upper troposphere, J. Geophys. Res., 107, https://doi.org/10.1029/2001JD000323, 2002.

Twomey, S.: The Influence of Pollution on the Shortwave Albedo of Clouds, J. Atmos. Sci., 34, 1149–1152, https://doi.org/10.1175/1520-0469(1977)034<1149:TIOPOT>2.0.CO;2, 1977.

Tyagi, P., Kawamura, K., Kariya, T., Bikkina, S., Fu, P., and Lee, M.: Tracing atmospheric transport of soil microorganisms and higher plant waxes in the East Asian outflow to the North Pacific Rim by using hydroxy fatty acids: Year-round observations at Gosan, Jeju Island, J. Geophys. Res. Atmos., 122, 4112–4131, https://doi.org/10.1002/2016JD025496, 2017.

US EPA.: Estimation Programs Interface Suite™ for Microsoft® Windows, v 4.1, United States Environmental Protection Agency, Washington, DC, USA, 2012.

v. Blohn, N., Diehl, K., Nölscher, A., Jost, A., Mitra, S. K., and Borrmann, S.: The retention of ammonia and sulfur dioxide during riming of ice particles and dendritic snow flakes: laboratory experiments in the Mainz vertical wind tunnel, J Atmos Chem, 70, 131–150, https://doi.org/10.1007/s10874-013-9261-x, 2013.

v. Blohn, N., Diehl, K., Mitra, S. K., and Borrmann, S.: Wind tunnel experiments on the retention of trace gases during riming: nitric acid, hydrochloric acid, and hydrogen peroxide, Atmos. Chem. Phys., 11, 11569–11579, https://doi.org/10.5194/acpd-11-17447-2011, 2011.

v. Blohn, N., Diehl, K., Mitra, S. K., and Borrmann, S.: Riming of Graupel: Wind Tunnel Investigations of Collection Kernels and Growth Regimes, J. Atmos. Sci., 66, 2359–2366, https://doi.org/10.1175/2009JAS2969.1, 2009.

van Dingenen, R., Raes, F., Putaud, J.-P., Baltensperger, U., Charron, A., Facchini, M.-C., Decesari, S., Fuzzi, S., Gehrig, R., Hansson, H.-C., Harrison, R. M., Hüglin, C., Jones, A. M., Laj, P., Lorbeer, G., Maenhaut, W., Palmgren, F., Querol, X., Rodriguez, S., Schneider, J., Brink, H. ten, Tunved, P., Tørseth, K., Wehner, B., Weingartner, E., Wiedensohler, A., and Wåhlin, P.: A European aerosol phenomenology—1: physical characteristics of particulate matter at kerbside, urban, rural and background sites in Europe, Atmospheric Environment, 38, 2561–2577, https://doi.org/10.1016/j.atmosenv.2004.01.040, 2004.

Vettikkat, L., Miettinen, P., Buchholz, A., Rantala, P., Yu, H., Schallhart, S., Petäjä, T., Seco, R., Männistö, E., Kulmala, M., Tuittila, E.-S., Guenther, A. B., and Schobesberger, S.: High emission rates and strong temperature response make boreal wetlands a large source of isoprene and terpenes, Atmos. Chem. Phys., 23, 2683–2698, https://doi.org/10.5194/acp-23-2683-2023, 2023.

Volkamer, R., San Martini, F., Molina, L. T., Salcedo, D., Jimenez, J. L., and Molina, M. J.: A missing sink for gas-phase glyoxal in Mexico City: Formation of secondary organic aerosol, Geophys. Res. Lett., 34, https://doi.org/10.1029/2007GL030752, 2007.

Wang, H., Gao, Y., Wang, S., Wu, X., Liu, Y., Li, X., Huang, D., Lou, S., Wu, Z., Guo, S., Jing, S., Li, Y., Huang, C., Tyndall, G. S., Orlando, J. J., and Zhang, X.: Atmospheric Processing of Nitrophenols and Nitrocresols From Biomass Burning Emissions, J. Geophys. Res. Atmos., 125, https://doi.org/10.1029/2020JD033401, 2020.

Wang, P. K. and Kubicek, A.: Flow fields of graupel falling in air, Atmospheric Research, 124, 158–169, https://doi.org/10.1016/j.atmosres.2013.01.003, 2013.

Weitzel, M., Mitra, S. K., Szakáll, M., Fugal, J. P., and Borrmann, S.: Application of holography and automated image processing for laboratory experiments on mass and fall speed of small cloud ice crystals, Atmos. Chem. Phys., 20, 14889–14901, https://doi.org/10.5194/acp-20-14889-2020, 2020.

Werner, F., Ditas, F., Siebert, H., Simmel, M., Wehner, B., Pilewskie, P., Schmeissner, T., Shaw, R. A., Hartmann, S., Wex, H., Roberts, G. C., and Wendisch, M.: Twomey effect observed from collocated microphysical and remote sensing measurements over shallow cumulus, J. Geophys. Res. Atmos., 119, 1534–1545, https://doi.org/10.1002/2013JD020131, 2014.

Whitby, K. T.: The physical characteristics of sulfur aerosols, Atmospheric Environment (1967), 12, 135–159, https://doi.org/10.1016/0004-6981(78)90196-8, 1978.

Williams, J., Crowley, J., Fischer, H., Harder, H., Martinez, M., Petäjä, T., Rinne, J., Bäck, J., Boy, M., Dal Maso, M., Hakala, J., Kajos, M., Keronen, P., Rantala, P., Aalto, J., Aaltonen, H., Paatero, J., Vesala, T., Hakola, H., Levula, J., Pohja, T., Herrmann, F., Auld, J., Mesarchaki, E., Song, W., Yassaa, N., Nölscher, A., Johnson, A. M., Custer, T., Sinha, V., Thieser, J., Pouvesle, N., Taraborrelli, D., Tang, M. J., Bozem, H., Hosaynali-Beygi, Z., Axinte, R., Oswald, R., Novelli, A., Kubistin, D., Hens, K., Javed, U., Trawny, K., Breitenberger, C., Hidalgo, P. J., Ebben, C. J., Geiger, F. M., Corrigan, A. L., Russell, L. M., Ouwersloot, H. G., Vilà-Guerau de Arellano, J., Ganzeveld, L., Vogel, A., Beck, M., Bayerle, A., Kampf, C. J., Bertelmann, M., Köllner, F., Hoffmann, T., Valverde, J., González, D., Riekkola, M.-L., Kulmala, M., and Lelieveld, J.: The summertime Boreal forest field measurement intensive (HUMPPA-COPEC-2010): an overview of meteorological and chemical influences, Atmos. Chem. Phys., 11, 10599–10618, https://doi.org/10.5194/acp-11-10599-2011, 2011.

Williamson, C. J., Kupc, A., Axisa, D., Bilsback, K. R., Bui, T., Campuzano-Jost, P., Dollner, M., Froyd, K. D., Hodshire, A. L., Jimenez, J. L., Kodros, J. K., Luo, G., Murphy, D. M., Nault, B. A., Ray, E. A., Weinzierl, B., Wilson, J. C., Yu, F., Yu, P., Pierce, J. R., and Brock, C. A.: A large source of cloud condensation nuclei from new particle formation in the tropics, Nature, 574, 399–403, https://doi.org/10.1038/s41586-019-1638-9, 2019.

Wilm, M. S. and Mann, M.: Electrospray and Taylor-Cone theory, Dole's beam of macromolecules at last?, International Journal of Mass Spectrometry and Ion Processes, 136, 167–180, https://doi.org/10.1016/0168-1176(94)04024-9, 1994.

Xiao, Q., Zhang, J., Wang, Y., Ziemba, L. D., Crosbie, E., Winstead, E. L., Robinson, C. E., DiGangi, J. P., Diskin, G. S., Reid, J. S., Schmidt, K. S., Sorooshian, A., Hilario, M. R. A., Woods, S., Lawson, P., Stamnes, S. A., and Wang, J.: New particle formation in the tropical free troposphere during CAMP 2 Ex: statistics and impact of emission sources, convective activity, and synoptic conditions, Atmos. Chem. Phys., 23, 9853–9871, https://doi.org/10.5194/acp-23-9853-2023, 2023.

Yang, M., Huebert, B. J., Blomquist, B. W., Howell, S. G., Shank, L. M., McNaughton, C. S., Clarke, A. D., Hawkins, L. N., Russell, L. M., Covert, D. S., Coffman, D. J., Bates, T. S., Quinn, P. K., Zagorac, N., Bandy, A. R., Szoeke, S. P. de, Zuidema, P. D., Tucker, S. C., Brewer, W. A., Benedict, K. B., and Collett, J. L.: Atmospheric sulfur cycling in the southeastern Pacific – longitudinal distribution, vertical profile, and diel variability observed during VOCALS-REx, Atmos. Chem. Phys., 11, 5079–5097, https://doi.org/10.5194/acp-11-5079-2011, 2011.

Yassaa, N., Peeken, I., Zöllner, E., Bluhm, K., Arnold, S., Spracklen, D., and Williams, J.: Evidence for marine production of monoterpenes, Environ. Chem., 5, 391, https://doi.org/10.1071/EN08047, 2008.

Yokelson, R. J., Burling, I. R., Urbanski, S. P., Atlas, E. L., Adachi, K., Buseck, P. R., Wiedinmyer, C., Akagi, S. K., Toohey, D. W., and Wold, C. E.: Trace gas and particle emissions from open biomass burning in Mexico, Atmos. Chem. Phys., 11, 6787–6808, https://doi.org/10.5194/acp-11-6787-2011, 2011.

Yu, Z. and Li, Y.: Marine volatile organic compounds and their impacts on marine aerosol-A review, The Science of the total environment, 768, 145054, https://doi.org/10.1016/j.scitotenv.2021.145054, 2021.

Zhang, H., Yee, L. D., Lee, B. H., Curtis, M. P., Worton, D. R., Isaacman-VanWertz, G., Offenberg, J. H., Lewandowski, M., Kleindienst, T. E., Beaver, M. R., Holder, A. L., Lonneman, W. A., Docherty, K. S., Jaoui, M., Pye, H. O. T., Hu, W., Day, D. A., Campuzano-Jost, P., Jimenez, J. L., Guo, H., Weber, R. J., Gouw, J. de, Koss, A. R., Edgerton, E. S., Brune, W., Mohr, C., Lopez-Hilfiker, F. D., Lutz, A., Kreisberg, N. M., Spielman, S. R., Hering, S. V., Wilson, K. R., Thornton, J. A., and Goldstein, A. H.: Monoterpenes are the largest source of summertime organic aerosol in the southeastern United States, Proceedings of the National Academy of Sciences of the United States of America, 115, 2038–2043, https://doi.org/10.1073/pnas.1717513115, 2018.

Zhang, L., Hu, B., Liu, X., Luo, Z., Xing, R., Li, Y., Xiong, R., Li, G., Cheng, H., Lu, Q., Shen, G., and Tao, S.: Variabilities in Primary N-Containing Aromatic Compound Emissions from Residential Solid Fuel Combustion and Implications for Source Tracers, Environ. Sci. Technol., 56, 13622–13633, https://doi.org/10.1021/acs.est.2c03000, 2022.

Zhang, Y., Wang, K., Tong, H., Huang, R.-J., and Hoffmann, T.: The maximum carbonyl ratio (MCR) as a new index for the structural classification of secondary organic aerosol components, Rapid communications in mass spectrometry RCM, 35, e9113, https://doi.org/10.1002/rcm.9113, 2021.

Zhao, Y., Hallar, A. G., and Mazzoleni, L. R.: Atmospheric organic matter in clouds: exact masses and molecular formula identification using ultrahigh-resolution FT-ICR mass spectrometry, Atmos. Chem. Phys., 13, 12343–12362, https://doi.org/10.5194/acp-13-12343-2013, 2013.

7. Appendix

7.1 Supplementary materials chapter 2

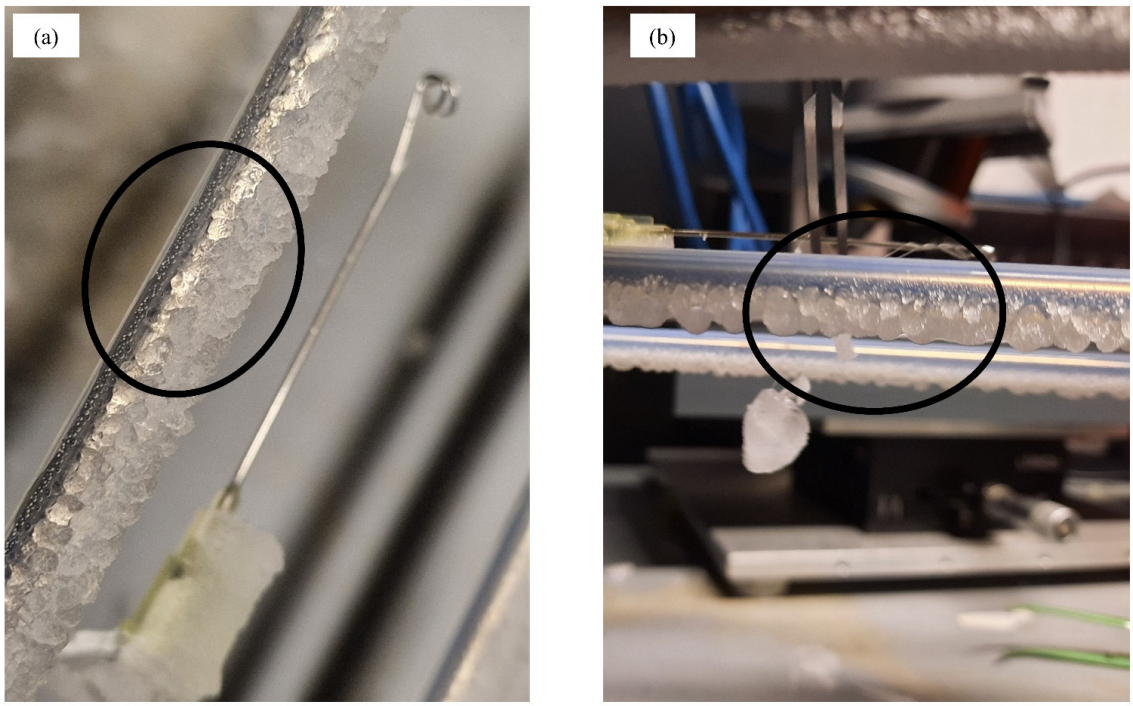

Figure 7.1: Photo of ice grown under dry (a)) and wet (b)) growth conditions.

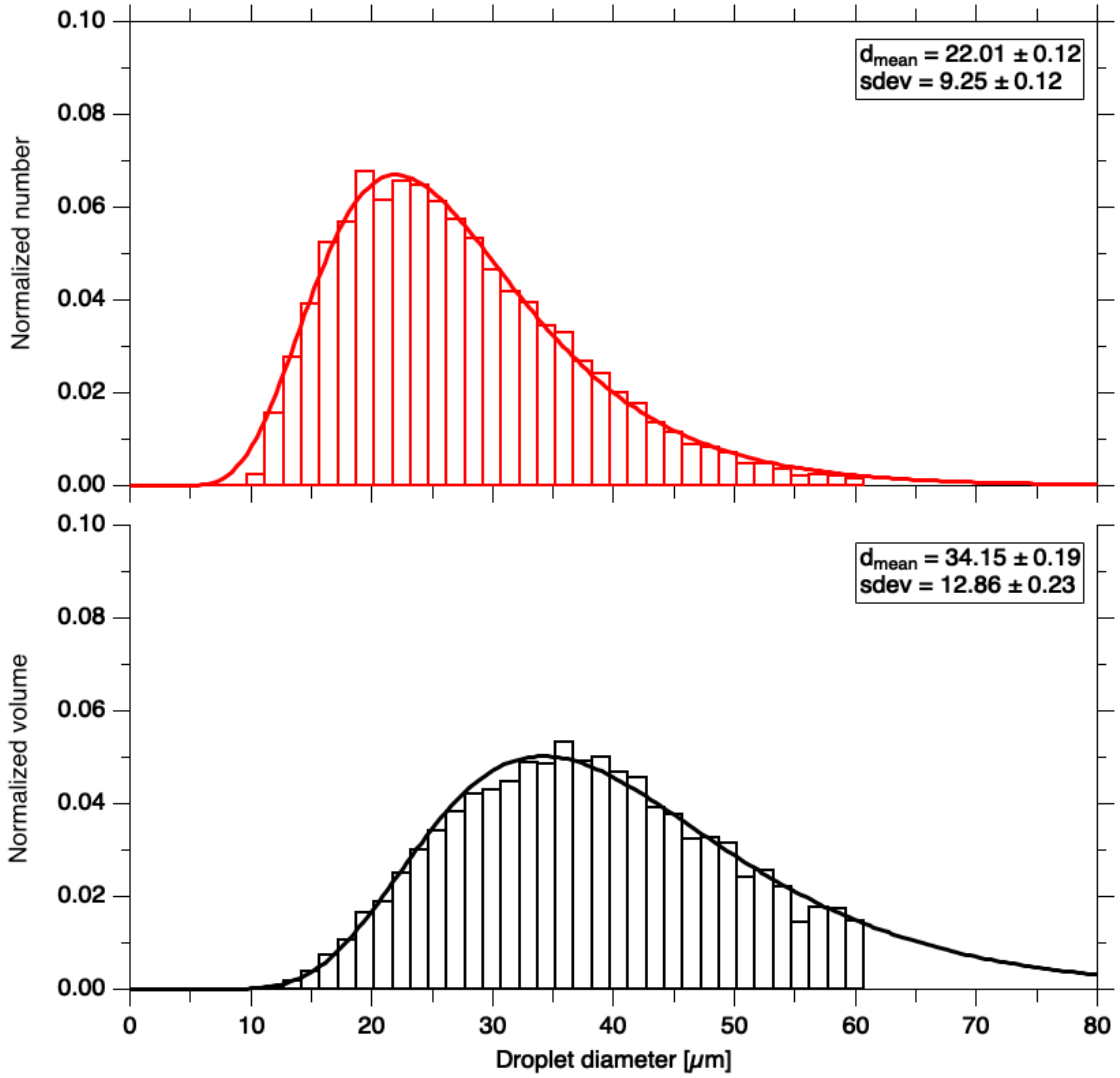

Figure 7.2: Normalized droplet number (a) and volume distribution (b) of the supercooled droplets generated using four spraying nozzles. The lines represent the log-normal fit functions.

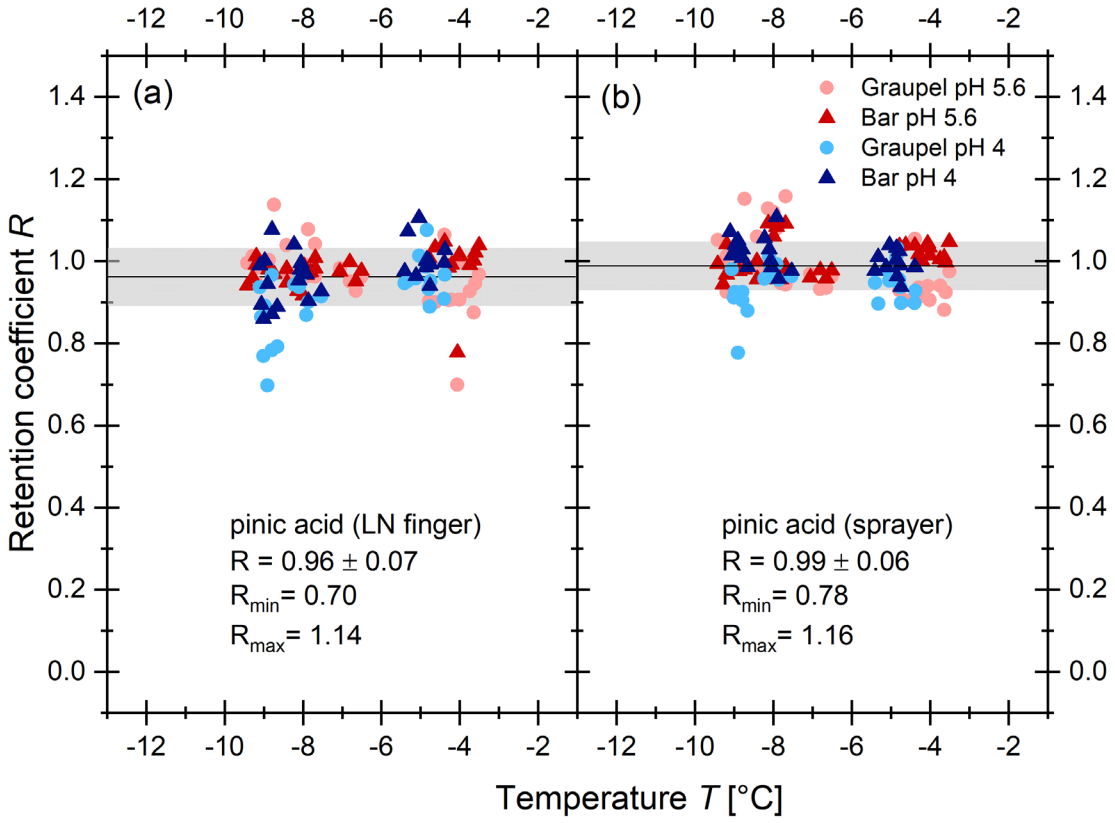

Figure 7.3: Experimentally determined retention coefficients of pinic acid using (a) the LN finger and (b) the sprayer solution as a function of the temperature during the experiment for different rime collectors. The circles represent the graupel samples and the triangles those of the Teflon-coated bars. For the blue symbols, the pH was adjusted to 4 by adding HCl (30 %), the red symbols are without adding HCl. The solid black line represents the mean of all measurements, and the grey area represents one standard deviation.

Desorption correction procedure

2-nitrophenol has the lowest effective Henry's law constant and therefore possesses the highest probability of transition from the droplet phase to the gas phase, resulting in a high gas phase concentration in the wind tunnel. For such a substance the measurement technique using the liquid nitrogen finger collection is not reliable since the gas molecules might adsorb on the liquid nitrogen cooled ice and thereby bias the retention value. Also, there is currently no other reliable measurement technique for measuring the desorption of a highly volatile substance right at the point where the retention measurements were carried out. Therefore, the desorption coefficient valid for the retention measurement was estimated based on a two step temperature and exposure time correction outlined in detail in the following.

First step: desorption measurements

The same solution (see Table 2.1) used for the retention measurements, containing 2-nitrophenol and NaBr as internal standard (IS), was nebulized and the droplets were transported downstream in the wind tunnel. The droplets were sampled in a vial in the lower horizontal part of the tunnel after a residence time of approximately 1 s (point A in Figure 7.4). The solution was then collected and measured by UHPLC-HRMS. Desorption measurements were carried out at different temperatures (between 0 °C and 19 °C) to obtain a temperature dependency.

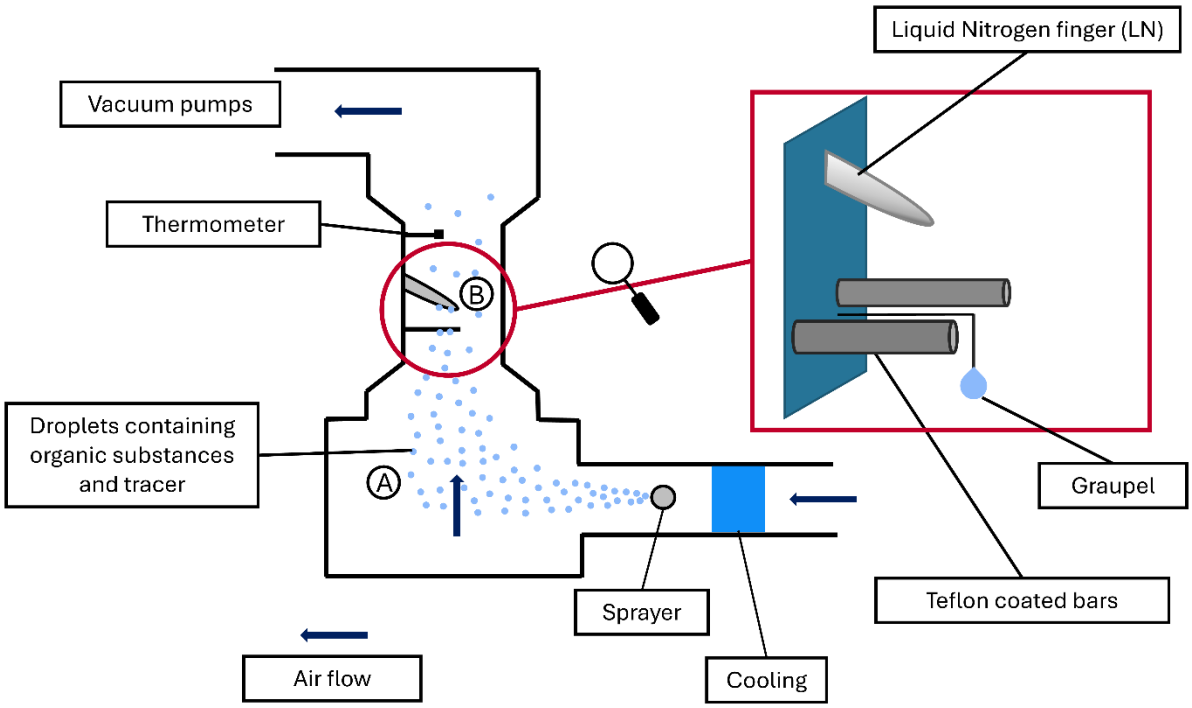

Figure 7.4: Schematic of the wind tunnel. Cooled air transported the generated water droplets containing the compounds into the experimental region (red circle). Red rectangle: The enlarged experimental area shows the three surfaces on which the riming took place: Graupel, liquid nitrogen finger and Teflon-coated bars. Desorption measurements were performed at point A and retention measurements were performed at point B.

The definition of the desorption coefficient is shown in Eq. (7.1). The numerator describes the ratio of the compound remaining in the sample (droplets sampled in a vial) to a reference sample, which is in this case the sprayer solution, which is the solution immediately before droplet formation, takes place ($c^{\text{vial}}_{\text{compound}}/c^{\text{sprayer}}_{\text{compound}}$). The denominator describes the same ratio but for the IS ($c^{\text{vial}}_{\text{IS}}/c^{\text{sprayer}}_{\text{IS}}$):

$$D_{\text{compound}} = \frac{c^{\text{vial}}_{\text{compound}}/c^{\text{sprayer}}_{\text{compound}}}{c^{\text{vial}}_{\text{IS}}/c^{\text{sprayer}}_{\text{IS}}} \quad (7.1)$$

Figure 7.5 shows the desorption coefficient as a function of the temperature as measured in the lower part of the wind tunnel. Obvious from Figure 7.5 is a strong dependence of the desorption coefficient of 2-nitrophenol on temperature, indicating less desorption at lower temperatures. This is expected since the mass transfer rate of a dissolved compound to the environment decreases for decreasing temperatures. The reason for this is that the mass transfer depends, among others on the temperature-dependent parameters like gas- and aqueous-phase diffusivities and the effective Henry's law constant. The observed variations in the values are greater than those expected due to analytical measurement error. These variations are likely attributable to fluctuations in the conditions within the wind tunnel, which were expected to be also present during the retention measurements.

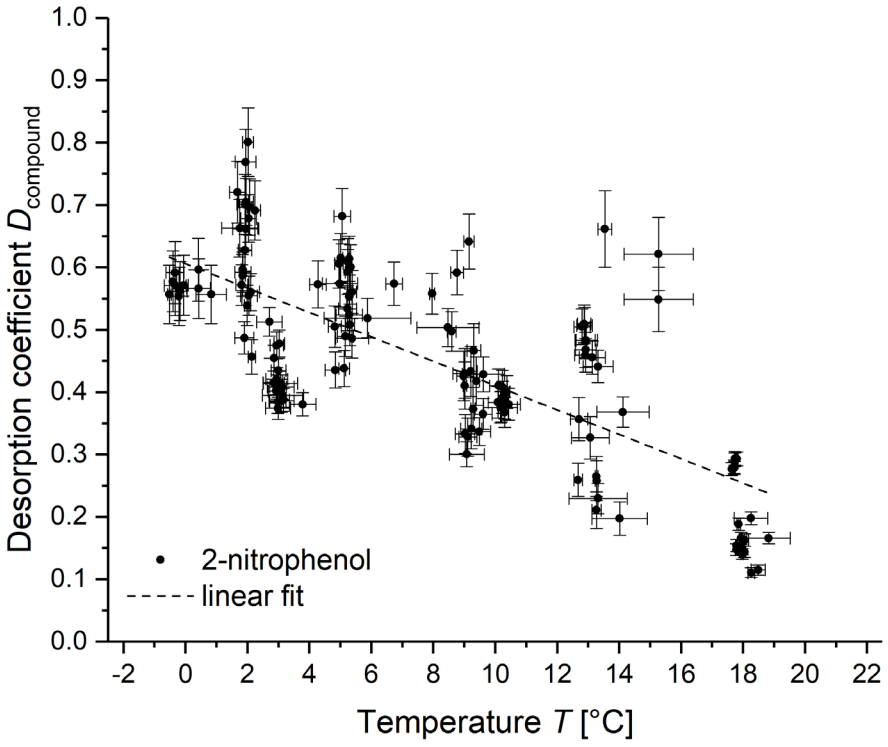

Figure 7.5: Desorption coefficient for 2-nitrophenol. The errors correspond to the error of the analytical measurement (y-axis) or the standard deviation of the temperature measurement during the collection time of each sample (x-axis). The dashed line represents a linear regression.

A statistically significant linear trend is visible in the measurement series. A linear regression with the equation $D_{\mathrm{compound}} = a_{\mathrm{D}} \cdot x \cdot [°C]^{-1} + b_{\mathrm{D}}$ was performed to extrapolate the desorption to the temperatures present during the experiments. This leads to the following equation, 7.2, for the fit function.

$$D_{\mathrm{compound}} = (-0.020 \pm 0.002) \cdot x \cdot [°C]^{-1} + (0.606 \pm 0.015) \qquad (7.2)$$

Extrapolating the results to the experimental conditions (e.g. -10 °C and -4 °C) yields $D_{\mathrm{compound}} = 0.81$ and $D_{\mathrm{compound}} = 0.67$ for typical dry and wet growth conditions respectively.

Second step: semi-empirical exposure time correction

The exposure time in the tunnel from the point of the desorption (point A in Figure 7.4) to the retention measurements (point B in Figure 7.4) is another 3 s (overall 4 s) which introduced another source of uncertainty. Thus, the measured D after one second of exposure had to be corrected for this time effect. This was done by a semi-empirical approach using theory and the results of the first step introduced above. From the convective diffusion equation assuming a well-mixed droplet, Pruppacher and Klett (2010, p. 775, Eq. 17-144) showed that the desorption of a dissociating gas with the initial condition of zero gas phase concentration follows a $1/t$ law. This functional relationship was used to fit the data from the first step to get a time dependence correction of the desorption coefficient. More specifically the following fit function was utilized:

$$D(T, L, t) = c(T, L) + \left(\frac{a(T,L)}{1 + a(T,L)b(T,L)t}\right) \qquad (7.3)$$

Here $D(T, L, t)$ is the temperature (T), liquid water content (L), and time (t) dependent desorption correction coefficient which asymptotically approaches the equilibrium value at a given temperature and liquid water content $c(T, L)$. That is, when t tends towards infinity Eq. (7.3) approaches $c(T, L)$. This coefficient describes the fraction of 2-nitrophenol in the liquid phase in equilibrium with its gas phase. It was derived from the assumption of the equilibrium gas/liquid partitioning in a confined system consisting of a single gas (2-nitrophenol) and a given amount of liquid water (1 and 2 g/m^3) (Seinfeld and Pandis 2006, p.290, Eq. 7.9). In the referenced Eq. 7.9 from Seinfeld and Pandis (2006) the temperature dependent Henry's law constant was calculated according to Guo and Brimblecombe (2007) for the temperatures used during the retention measurements. The results are shown in Figure 7.6.

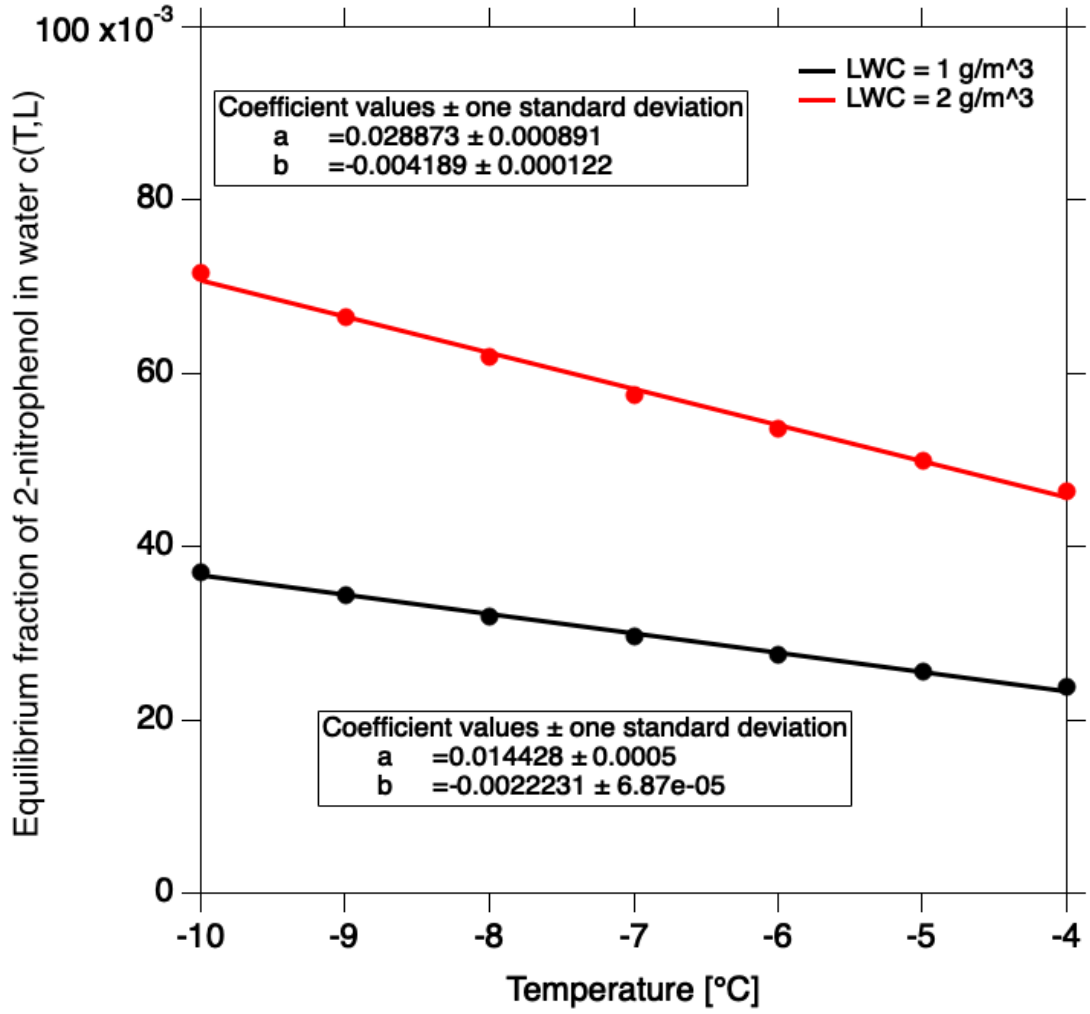

Figure 7.6: Equilibrium fraction of 2-nitrophenol in water as a function of temperature and liquid water content. Coefficients a and b represent the fit values of the intercept and slope of the linear regressions. Black: LWC = 1 g/m³. Red: LWC = 2 g/m³.

When t approaches zero Eq. (7.3) yields $c(T, L) + a(T, L) = 1$, which yields $a(T, L) = 1 - c(T, L)$. Hence, the only unknown in Eq. (7.3) is coefficient $b(T, L)$ which was used as a fit parameter and thereby parameterized as a function of T and L. Accordingly Eq. (7.3) was used along with the extrapolated desorption values to the temperatures prevailed during the retention and the equilibrium fractions (Figure 7.6) to derive a parameterization of D which depends on temperature, liquid water content and time.

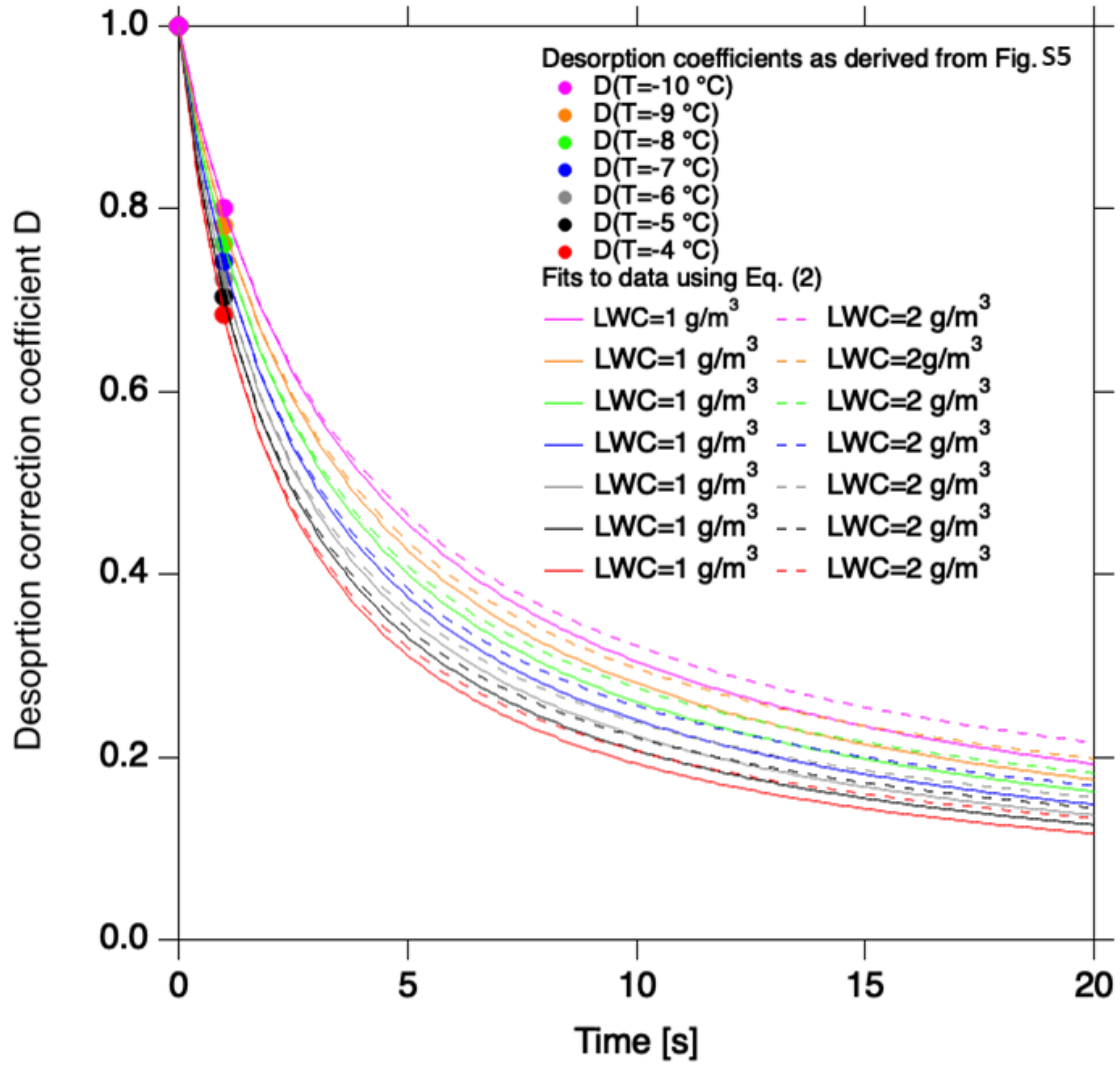

Figure 7.7: Desorption correction coefficient as a function of time for different temperatures and liquid water contents obtained from Eq. (7.3). Solid lines: LWC = 1 g/m³. Dashed lines LWC = 2 g/m³. The data points were calculated from Eq. (7.2).

From the results shown in Figure 7.7 it is obvious that a significant part (37 %) of 2-nitrophenol desorb from the droplets from the point between the desorption and retention measurements (Point A and B in Figure 7.4). For example at -10 °C the desorption between Point A and B decreases from 0.81 to 0.51. For each curve in Figure 7.7 a fit coefficient *b(T, L)* was obtained corresponding to a certain temperature and liquid water content. By plotting these as a function of temperature (Figure 7.8) a linear relationship of *b(T, L)* on the temperature and liquid water content was derived.

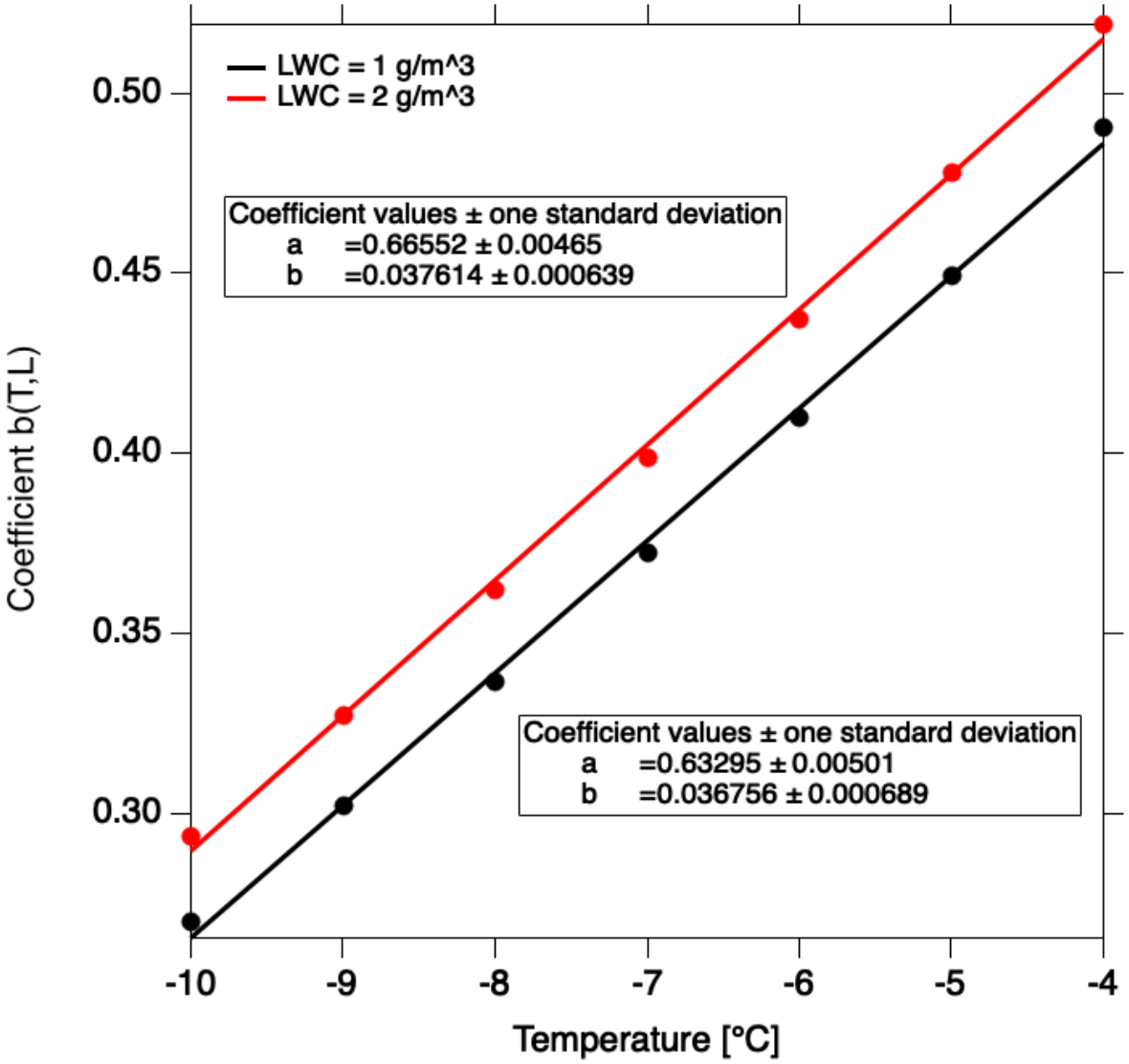

Figure 7.8: Dependency of the fit parameter *b(T,L)* on the temperature and liquid water content as derived from Figure 7.7. Red and black points: values for LWC's of 1 and 2. Red and black lines: fit to the data. Coefficients a and b represent the intercepts and the slopes of the linear regressions.

A close glance at Fig. 7.7 reveals that the difference between 1 and 2 g/m3 is below 1 %. Thus, the final desorption correction function that was used to correct the retention values for 2-nitrophenol at a given temperature and at the location of the retention measurements is given by Eq. (7.3) which was evaluated at $t = 4$ s and LWC=L= 1 g/m^3. The used parameters were:

$$c(T, L = 1) = 0.0144 - 0.0022\,T\ [°C] \tag{7.4}$$

$$a(T, L = 1) = 1 - c(T, L) \tag{7.5}$$

$$b(T, L = 1) = 0.6330 + 0.0368\,T\ [°C] \tag{7.6}$$

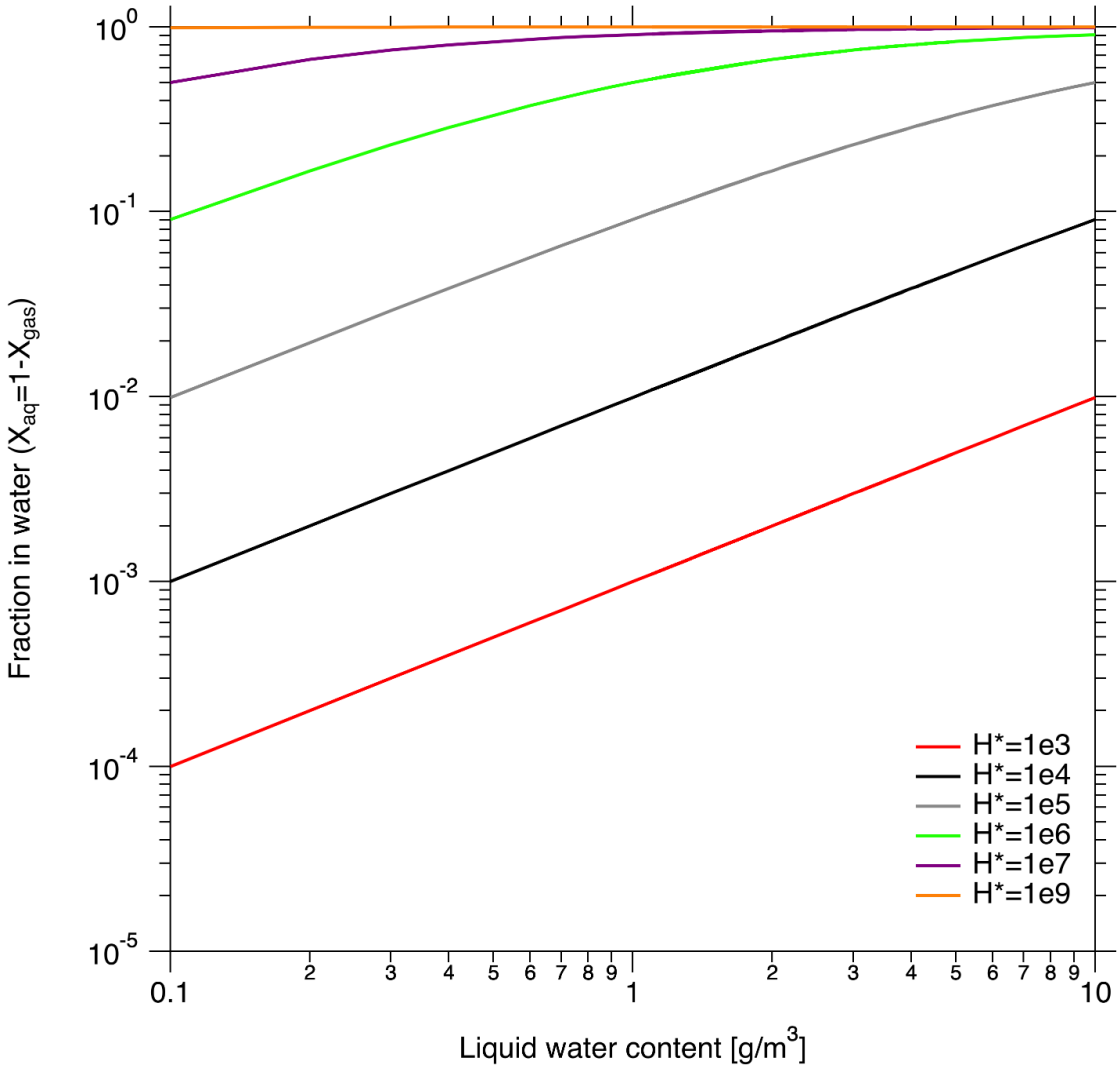

Figure 7.9: Equilibrium distribution of species between the liquid and gas phase in a confined system as function of the LWC. Figure according to Seinfeld and Pandis (2006).

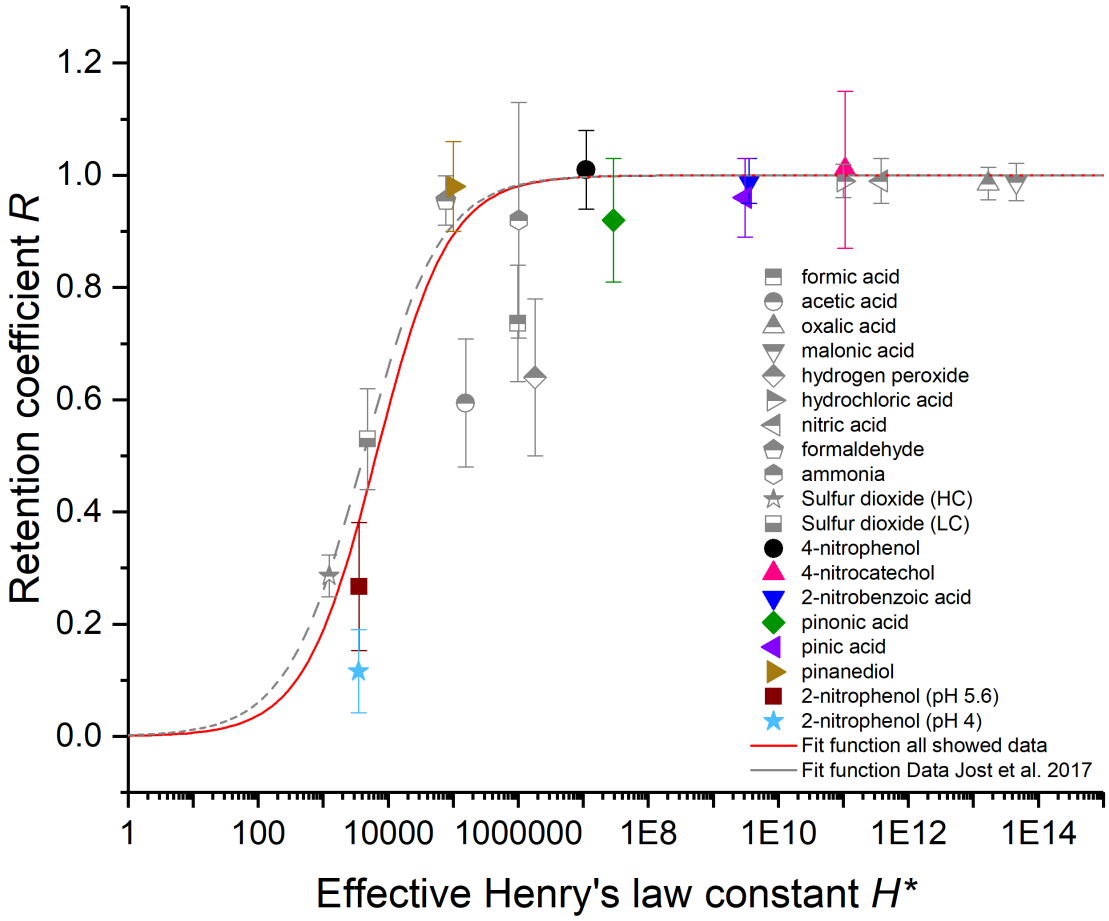

Figure 7.10: Retention coefficient as a function of H^*. Colorful filled symbols: substances investigated in the present study. Grey symbols: wind tunnel data from earlier studies (Jost et al., 2017; v. Blohn et al., 2013; 2011). Fit function: $R_{H^*} = \left(1 + (a \,/\, H^*)^b\right)^{-1}$. Red solid line: new fit to wind tunnel data with all substances ($a_{\mathrm{red}} = (6.51 \pm 2.01) \cdot 10^3$ and $b_{\mathrm{red}} = 0.78 \pm 0.16$). Grey dashed line: fit of only the grey data points $a_{\mathrm{grey}} = (4.15 \pm 1.47) \cdot 10^3$ and $b_{\mathrm{grey}} = 0.74 \pm 0.18$.

Additional material which is not included in the paper

Table 7.1: Retention coefficients for pinic acid of the measurements at pH 5.6.

T / °C	ΔT /°C	$R_{G_{5.6}}$	$\Delta R_{G_{5.6}}$	$R_{B_{5.6}}$	$\Delta R_{B_{5.6}}$
-3.51	0.37	0.97	0.03	1.04	0.03
-3.60	0.49	0.95	0.03	1.02	0.03
-3.64	0.35	0.88	0.02	1.00	0.03
-3.74	0.49	0.93	0.03	0.99	0.02
-4.01	0.56	0.91	0.03	1.02	0.03
-4.03	0.51	1.00	0.03	1.01	0.03
-4.06	0.60	0.70	0.02	0.78	0.02
-4.21	0.51	0.91	0.03	0.99	0.02
-4.29	0.51	0.91	0.02	0.98	0.02
-4.39	0.46	1.06	0.03	1.05	0.03
-4.63	0.39	0.90	0.03	1.03	0.03
-4.79	0.48	0.90	0.03	1.01	0.03
-6.51	0.46	0.96	0.05	0.98	0.03
-6.65	0.48	0.93	0.04	0.95	0.03
-6.81	0.22	0.95	0.05	1.00	0.03
-7.06	0.28	0.98	0.04	0.97	0.03
-7.69	0.21	0.96	0.04	1.01	0.03
-7.69	0.39	1.04	0.04	0.98	0.03
-7.81	0.13	0.96	0.04	0.97	0.03
-7.87	0.33	1.08	0.05	0.97	0.03
-7.92	0.49	0.96	0.05	0.97	0.03
-7.98	0.18	0.99	0.04	0.99	0.03
-7.99	0.49	0.97	0.05	0.92	0.03
-8.13	0.37	0.96	0.04	0.93	0.03
-8.41	0.34	0.98	0.04	0.95	0.03
-8.42	0.38	1.04	0.06	0.98	0.03
-8.74	0.38	1.14	0.05	0.97	0.03
-8.87	0.38	1.00	0.04	0.98	0.03
-9.19	0.38	0.98	0.04	1.01	0.03
-9.20	0.42	0.95	0.04	0.99	0.03
-9.28	0.28	1.01	0.04	0.96	0.03
-9.42	0.24	1.00	0.04	0.94	0.03

Table 7.2: Retention coefficients for pinic acid of the measurements at pH 4.

T / °C	ΔT /°C	R_{G_4}	ΔR_{G_4}	R_{B_4}	ΔR_{B_4}
-4.38	0.78	0.97	0.03	1.03	0.03
-4.40	0.67	0.91	0.03	1.00	0.03
-4.74	0.45	0.95	0.03	0.99	0.03
-4.76	0.29	0.89	0.02	0.94	0.02
-4.79	0.51	0.93	0.03	1.00	0.02
-4.84	0.78	1.08	0.03	1.00	0.03
-4.86	0.34	0.99	0.03	1.00	0.03
-4.86	0.47	0.99	0.03	0.99	0.03
-5.04	0.49	1.01	0.03	1.11	0.03
-5.12	0.42	0.96	0.03	0.96	0.03
-5.33	0.36	0.95	0.03	1.07	0.03
-5.41	0.39	0.95	0.04	0.98	0.03
-7.54	0.73	0.91	0.03	0.93	0.03
-7.86	0.56	0.90	0.03	0.90	0.03
-7.92	0.79	0.87	0.03	0.97	0.03
-8.05	0.31	0.97	0.03	1.00	0.03
-8.07	0.84	0.96	0.03	0.98	0.03
-8.11	0.64	0.94	0.03	0.95	0.03
-8.23	0.65	0.94	0.03	1.04	0.03
-8.66	0.22	0.79	0.04	0.89	0.02
-8.79	0.40	0.97	0.04	1.08	0.03
-8.79	0.41	0.78	0.05	0.87	0.02
-8.91	0.39	0.70	0.04	0.94	0.03
-8.97	0.36	0.89	0.04	1.00	0.03
-9.01	0.38	0.77	0.05	0.86	0.02
-9.06	0.29	0.86	0.03	0.89	0.02
-9.10	0.20	0.94	0.03	0.99	0.02

Table 7.3: Retention coefficients for pinonic acid of the measurements at pH 5.6.

T / °C	ΔT /°C	$R_{G_{5.6}}$	$\Delta R_{G_{5.6}}$	$R_{B_{5.6}}$	$\Delta R_{B_{5.6}}$
-4.12	0.46	0.98	0.32	0.98	0.29
-4.48	0.49	0.88	0.25	0.99	0.26
-4.60	0.35	0.90	0.11	0.95	0.11
-4.68	0.32	0.84	0.28	0.98	0.30
-4.68	0.48	0.82	0.31	0.90	0.31
-4.80	0.20	1.08	0.21	0.95	0.16
-4.85	0.38	0.86	0.30	0.96	0.31
-4.99	0.24	0.87	0.24	0.95	0.24
-5.08	0.29	0.87	0.22	0.96	0.22
-5.15	0.64	1.02	0.37	0.92	0.30
-5.20	0.24	-	-	0.98	0.31
-5.38	0.61	0.93	0.23	0.98	0.22
-5.40	0.50	0.81	0.39	0.73	0.35
-5.48	0.41	0.91	0.10	1.05	0.09
-5.52	0.31	-	-	0.97	0.21
-5.72	0.27	1.12	0.26	0.97	0.20
-5.80	0.39	1.11	0.04	1.05	0.04
-6.46	0.39	-	-	0.89	0.11
-6.48	1.50	1.12	0.04	1.02	0.04
-6.54	0.55	0.96	0.03	0.98	0.04
-6.92	0.60	1.18	0.04	1.01	0.04
-7.14	0.19	1.08	0.04	1.04	0.03
-7.14	0.29	1.03	0.04	1.01	0.04
-7.23	0.41	1.07	0.03	1.03	0.03
-7.54	0.37	1.04	0.03	1.02	0.04
-7.82	1.74	1.05	0.04	1.04	0.04
-7.95	0.31	1.02	0.04	0.99	0.03
-8.70	0.46	0.78	0.11	0.76	0.11
-9.06	0.63	0.95	0.12	0.98	0.11
-9.71	0.47	1.03	0.19	0.84	0.15
-9.81	0.15	0.66	0.10	0.78	0.12
-10.67	0.56	0.95	0.15	0.92	0.14
-11.03	0.44	0.71	0.13	0.71	0.13
-11.52	0.48	0.92	0.15	0.95	0.15
-11.57	0.63	1.04	0.17	1.15	0.19

Table 7.4: Retention coefficients for pinonic acid of the measurements at pH 4.

T / °C	ΔT /°C	R_{G_4}	ΔR_{G_4}	R_{B_4}	ΔR_{B_4}
-3.68	0.35	0.89	0.11	0.93	0.08
-3.79	0.43	0.82	0.09	0.88	0.09
-4.29	0.39	0.81	0.09	0.88	0.08
-4.62	0.40	0.84	0.08	0.87	0.10
-4.95	0.45	0.89	0.06	0.92	0.07
-4.99	0.49	0.90	0.03	0.94	0.02
-5.01	0.44	0.79	0.09	0.82	0.09
-5.04	0.48	0.91	0.06	0.96	0.04
-5.07	0.46	0.89	0.08	0.98	0.07
-5.15	0.52	0.87	0.03	0.93	0.02
-5.38	0.49	0.71	0.04	0.77	0.04
-5.46	0.58	0.73	0.04	0.78	0.04
-5.47	0.48	0.87	0.05	0.94	0.06
-5.79	0.55	0.87	0.06	0.95	0.06
-8.32	0.48	1.06	0.24	0.93	0.20
-8.67	0.24	0.87	0.05	0.90	0.05
-8.75	0.23	0.90	0.06	0.99	0.04
-8.87	0.22	0.97	0.19	0.84	0.16
-8.92	0.21	0.95	0.06	0.87	0.03
-9.02	0.21	0.89	0.06	0.84	0.03
-9.35	0.17	0.94	0.05	0.90	0.03
-9.40	0.30	0.89	0.06	0.82	0.03
-9.72	0.43	0.92	0.21	0.84	0.19
-10.42	0.71	0.94	0.21	0.87	0.19
-11.01	0.64	0.83	0.17	0.86	0.18
-11.07	0.52	0.78	0.15	0.77	0.14
-11.23	0.69	1.05	0.23	0.92	0.20
-11.25	0.71	0.84	0.20	0.76	0.17

Table 7.5: Retention coefficients for pinanediol of the measurements at pH 5.6.

T / °C	ΔT /°C	$R_{G_{5.6}}$	$\Delta R_{G_{5.6}}$	$R_{B_{5.6}}$	$\Delta R_{B_{5.6}}$
-2.67	0.49	1.02	0.04	0.99	0.04
-2.75	0.62	0.96	0.04	1.02	0.04
-3.07	0.45	1.08	0.04	1.01	0.04
-3.16	0.36	0.99	0.04	0.97	0.04
-3.31	0.49	0.89	0.04	0.99	0.04
-3.68	0.42	1.10	0.05	1.03	0.04
-3.72	0.46	0.93	0.04	1.00	0.04
-3.73	0.63	0.95	0.04	0.99	0.04
-3.85	0.56	1.08	0.05	1.02	0.04
-4.10	0.67	0.95	0.04	1.10	0.04
-4.26	0.88	0.91	0.04	1.00	0.04
-4.39	0.50	0.91	0.04	1.02	0.04
-4.65	0.43	0.97	0.05	1.07	0.04
-5.05	0.19	1.04	0.05	1.18	0.05
-5.92	0.42	0.93	0.05	1.11	0.05
-7.51	0.56	1.17	0.07	1.02	0.06
-7.62	0.76	0.92	0.05	0.97	0.05
-7.95	0.33	1.04	0.05	1.07	0.05
-8.33	0.65	-	-	1.01	0.06
-8.66	0.33	0.98	0.05	1.03	0.05
-8.85	0.20	1.06	0.05	1.06	0.05
-8.87	0.97	-	-	0.97	0.06
-9.05	0.22	1.16	0.06	1.03	0.05
-9.31	0.21	1.07	0.06	1.03	0.05
-9.45	0.24	1.00	0.05	1.06	0.05
-9.56	0.16	-	-	1.06	0.05
-9.57	0.58	0.89	0.05	0.99	0.05
-9.59	0.43	0.97	0.05	1.00	0.05
-9.60	0.30	0.95	0.05	1.02	0.05
-9.81	0.33	0.97	0.05	0.98	0.05

Table 7.6: Retention coefficients for pinanediol of the measurements at pH 4.

T / °C	ΔT /°C	R_{G_4}	ΔR_{G_4}	R_{B_4}	ΔR_{B_4}
-2.92	0.50	0.91	0.08	1.00	0.09
-3.13	0.50	0.85	0.08	0.88	0.08
-3.18	0.41	0.84	0.08	0.99	0.09
-3.32	0.42	1.00	0.09	0.95	0.08
-3.54	0.45	0.96	0.09	0.95	0.09
-3.60	0.44	0.86	0.08	0.96	0.09
-3.61	0.35	0.96	0.09	0.90	0.09
-3.62	0.43	0.98	0.09	0.91	0.08
-3.68	0.40	1.04	0.10	1.04	0.10
-3.80	0.51	0.98	0.09	0.91	0.09
-4.06	0.33	1.17	0.11	0.99	0.09
-4.76	1.85	1.04	0.10	1.06	0.10
-7.10	0.44	0.97	0.07	0.97	0.07
-8.18	0.39	0.83	0.06	1.05	0.07
-8.34	0.50	0.94	0.06	1.07	0.07
-8.34	0.50	0.95	0.07	0.98	0.07
-8.39	0.29	0.94	0.06	1.04	0.07
-8.57	0.39	0.88	0.06	0.97	0.07
-8.57	0.39	1.14	0.06	1.03	0.05
-8.77	0.28	1.11	0.07	1.00	0.06
-8.95	0.47	0.88	0.06	1.01	0.07
-8.95	0.47	1.01	0.06	1.01	0.06
-9.15	0.28	0.94	0.07	0.97	0.07
-9.15	0.28	1.02	0.06	0.99	0.06
-9.33	0.27	1.03	0.06	0.99	0.06

Table 7.7: Retention coefficients for 4-nitrocatechol of the measurements at pH 5.6.

T / °C	ΔT /°C	$R_{G_{5.6}}$	$\Delta R_{G_{5.6}}$	$R_{B_{5.6}}$	$\Delta R_{B_{5.6}}$
-4.00	0.36	1.05	0.13	0.97	0.14
-4.14	0.36	1.06	0.13	0.86	0.14
-4.16	0.43	0.98	0.12	0.98	0.14
-4.28	0.30	0.85	0.11	0.84	0.13
-4.38	0.43	1.22	0.16	0.98	0.15
-4.40	0.42	1.41	0.19	0.93	0.15
-4.41	0.35	1.12	0.15	0.88	0.15
-4.46	0.51	1.10	0.14	1.01	0.14
-4.54	0.24	1.06	0.14	0.89	0.14
-4.68	0.36	0.90	0.12	0.95	0.15
-4.84	0.35	1.07	0.14	0.97	0.14
-4.94	0.34	1.12	0.16	0.96	0.16
-5.05	0.46	0.92	0.12	0.88	0.14
-5.05	0.67	0.79	0.10	0.92	0.15
-5.18	0.46	1.02	0.15	0.96	0.16
-5.59	0.50	1.13	0.13	1.00	0.14
-6.24	0.42	1.11	0.13	0.96	0.13
-6.51	0.36	1.03	0.12	0.94	0.13
-7.04	0.70	1.05	0.15	1.08	0.18
-7.04	0.34	1.13	0.16	1.05	0.18
-7.08	0.24	1.21	0.14	0.95	0.13
-7.22	0.10	1.06	0.13	0.92	0.14
-7.39	0.26	1.09	0.12	0.67	0.10
-7.49	0.44	1.06	0.15	0.98	0.15
-7.52	0.41	0.97	0.11	0.94	0.13
-7.53	0.22	1.11	0.15	0.99	0.16
-7.78	0.27	1.02	0.11	0.91	0.13
-7.79	0.26	1.16	0.15	0.96	0.15
-7.83	0.43	1.05	0.12	0.98	0.14
-7.96	0.25	1.32	0.18	1.07	0.16
-7.98	0.22	1.18	0.15	0.96	0.15

Table 7.8: Retention coefficients for 4-nitrocatechol of the measurements at pH 4.

T / °C	ΔT /°C	R_{G_4}	ΔR_{G_4}	R_{B_4}	ΔR_{B_4}
-3.69	0.78	0.98	0.11	0.97	0.14
-4.55	0.41	0.72	0.08	0.63	0.09
-5.03	0.42	0.96	0.12	1.06	0.17
-5.08	0.40	1.09	0.13	1.10	0.17
-5.13	0.43	1.11	0.05	1.15	0.16
-5.14	0.40	1.02	0.13	0.98	0.15
-5.36	0.48	1.11	0.13	1.00	0.15
-5.37	0.38	0.97	0.12	1.01	0.15
-5.38	0.38	1.07	0.14	1.12	0.18
-5.53	0.44	1.23	0.16	1.14	0.18
-5.67	0.41	0.98	0.12	1.09	0.17
-5.71	0.38	0.97	0.12	1.09	0.17
-5.74	0.45	1.06	0.13	0.93	0.14
-5.91	0.35	1.04	0.13	1.15	0.18
-6.32	0.38	1.07	0.17	0.93	0.18
-6.45	0.57	0.83	0.12	0.88	0.16
-6.58	0.45	0.80	0.13	0.96	0.15
-6.77	0.34	0.87	0.12	0.91	0.15
-6.95	0.55	0.85	0.16	1.12	0.20
-6.99	0.94	1.22	0.21	1.16	0.20
-7.19	0.49	0.78	0.14	1.05	0.17
-7.33	0.31	1.25	0.25	1.36	0.27
-7.53	0.38	0.91	0.15	1.04	0.17
-7.55	0.23	0.92	0.15	1.08	0.17
-7.81	0.37	0.82	0.13	1.00	0.16
-7.82	0.21	0.95	0.20	1.19	0.24
-7.90	0.20	0.84	0.17	1.40	0.24
-8.29	0.37	0.67	0.15	1.05	0.19
-8.58	0.39	0.79	0.12	1.05	0.16
-8.80	0.38	0.86	0.15	1.07	0.18

Table 7.9: Retention coefficients for 4-nitrophenol of the measurements at pH 5.6.

T / °C	ΔT /°C	$R_{G_{5.6}}$	$\Delta R_{G_{5.6}}$	$R_{B_{5.6}}$	$\Delta R_{B_{5.6}}$
-4.00	0.36	1.04	0.07	0.97	0.06
-4.14	0.36	1.12	0.06	0.96	0.05
-4.16	0.43	1.07	0.07	1.00	0.07
-4.28	0.30	0.97	0.05	0.96	0.05
-4.38	0.43	1.01	0.07	0.98	0.07
-4.40	0.42	1.12	0.06	0.97	0.05
-4.41	0.35	1.04	0.06	0.93	0.05
-4.46	0.51	1.00	0.06	0.99	0.06
-4.54	0.24	1.04	0.05	0.96	0.05
-4.68	0.36	1.07	0.06	0.94	0.05
-4.84	0.35	1.05	0.07	0.97	0.06
-4.94	0.34	1.07	0.06	1.00	0.06
-5.05	0.46	1.05	0.05	0.98	0.05
-5.05	0.67	0.97	0.05	0.95	0.05
-5.18	0.46	1.05	0.06	0.95	0.05
-5.59	0.50	1.12	0.06	1.02	0.06
-6.24	0.42	1.08	0.05	0.95	0.06
-6.51	0.36	1.01	0.05	0.95	0.06
-7.04	0.70	1.04	0.06	0.95	0.06
-7.04	0.34	1.00	0.06	0.93	0.07
-7.08	0.24	1.09	0.05	0.95	0.06
-7.22	0.10	1.06	0.06	0.94	0.06
-7.39	0.26	1.02	0.05	0.80	0.05
-7.49	0.44	1.10	0.09	1.10	0.08
-7.52	0.41	1.00	0.05	0.97	0.06
-7.53	0.22	1.04	0.06	0.96	0.07
-7.78	0.27	1.01	0.05	0.92	0.06
-7.79	0.26	1.07	0.06	0.96	0.07
-7.83	0.43	0.99	0.05	0.93	0.05
-7.96	0.25	1.28	0.10	1.13	0.08
-7.98	0.22	1.10	0.06	0.98	0.06

Table 7.10: Retention coefficients for 4-nitrophenol of the measurements at pH 4.

T / °C	ΔT /°C	R_{G_4}	ΔR_{G_4}	R_{B_4}	ΔR_{B_4}
-3.69	0.78	1.04	0.08	1.03	0.08
-4.55	0.41	0.86	0.06	0.87	0.07
-5.03	0.42	1.07	0.09	1.03	0.09
-5.08	0.40	0.99	0.08	0.97	0.08
-5.13	0.43	1.05	0.04	0.96	0.04
-5.14	0.40	1.11	0.10	1.01	0.10
-5.36	0.48	1.09	0.09	1.06	0.09
-5.37	0.38	1.01	0.08	0.98	0.08
-5.38	0.38	1.07	0.09	1.06	0.09
-5.53	0.44	1.04	0.09	1.00	0.08
-5.67	0.41	1.03	0.09	1.02	0.09
-5.71	0.38	0.90	0.08	0.98	0.08
-5.74	0.45	1.03	0.08	1.01	0.09
-5.91	0.35	1.02	0.09	1.02	0.09
-6.32	0.38	1.02	0.07	-	-
-6.45	0.57	0.96	0.06	-	-
-6.58	0.45	0.97	0.17	0.95	0.18
-6.77	0.34	0.96	0.06	-	-
-6.95	0.55	0.95	0.20	0.99	0.22
-6.99	0.94	1.25	0.24	1.06	0.23
-7.19	0.49	0.87	0.16	1.01	0.20
-7.33	0.31	1.05	0.21	0.97	0.21
-7.53	0.38	1.01	0.19	1.05	0.21
-7.55	0.23	1.00	0.17	1.06	0.20
-7.81	0.37	0.98	0.17	1.00	0.19
-7.82	0.21	0.99	0.22	1.02	0.23
-7.90	0.20	0.80	0.15	1.02	0.20
-8.29	0.37	0.79	0.16	1.00	0.21
-8.58	0.39	1.00	0.17	1.08	0.21
-8.80	0.38	0.97	0.19	1.04	0.22

Table 7.11: Retention coefficients for nitrobenzoic acid of the measurements at pH 5.6.

T / °C	ΔT /°C	$R_{G_{5.6}}$	$\Delta R_{G_{5.6}}$	$R_{B_{5.6}}$	$\Delta R_{B_{5.6}}$
-4.00	0.36	1.01	0.04	1.00	0.04
-4.14	0.36	1.02	0.05	0.98	0.05
-4.16	0.43	1.02	0.04	1.02	0.04
-4.28	0.30	0.99	0.05	0.97	0.05
-4.38	0.43	1.00	0.04	0.99	0.04
-4.40	0.42	1.05	0.05	1.00	0.05
-4.41	0.35	0.97	0.05	0.99	0.06
-4.46	0.51	1.09	0.04	1.04	0.04
-4.54	0.24	1.07	0.05	1.00	0.05
-4.68	0.36	1.04	0.05	0.98	0.05
-4.84	0.35	1.02	0.04	0.97	0.04
-4.94	0.34	1.00	0.05	0.98	0.05
-5.05	0.46	1.01	0.07	0.98	0.07
-5.05	0.67	0.96	0.05	0.98	0.06
-5.18	0.46	1.05	0.06	0.99	0.05
-5.59	0.50	0.98	0.08	1.00	0.09
-6.24	0.42	0.99	0.08	1.01	0.09
-6.51	0.36	0.98	0.08	1.02	0.10
-7.04	0.70	1.01	0.08	1.04	0.09
-7.04	0.34	0.92	0.08	0.97	0.09
-7.08	0.24	1.02	0.08	1.02	0.09
-7.22	0.10	1.02	0.08	1.03	0.09
-7.39	0.26	0.99	0.08	0.99	0.09
-7.49	0.44	1.07	0.05	1.02	0.04
-7.52	0.41	0.94	0.07	1.00	0.09
-7.53	0.22	0.95	0.08	1.01	0.09
-7.78	0.27	0.98	0.08	1.02	0.10
-7.79	0.26	0.94	0.07	1.01	0.09
-7.83	0.43	0.93	0.07	0.96	0.09
-7.96	0.25	-	-	1.06	0.04
-7.98	0.22	0.98	0.07	1.03	0.09

Table 7.12: Retention coefficients for nitrobenzoic acid of the measurements at pH 4.

T / °C	ΔT /°C	R_{G_4}	ΔR_{G_4}	R_{B_4}	ΔR_{B_4}
-3.69	0.78	0.97	0.03	0.95	0.03
-4.55	0.41	0.96	0.03	0.92	0.04
-5.03	0.42	0.97	0.03	0.97	0.04
-5.08	0.40	0.96	0.03	0.95	0.04
-5.13	0.43	1.11	0.02	0.98	0.01
-5.14	0.40	1.01	0.03	0.98	0.04
-5.36	0.48	1.01	0.03	0.99	0.03
-5.37	0.38	0.94	0.03	0.93	0.03
-5.38	0.38	1.00	0.04	0.98	0.04
-5.53	0.44	1.12	0.03	0.95	0.03
-5.67	0.41	1.00	0.03	1.00	0.03
-5.71	0.38	0.95	0.03	0.98	0.03
-5.74	0.45	0.96	0.03	0.98	0.03
-5.91	0.35	0.95	0.03	0.96	0.03
-6.32	0.38	1.08	0.07	0.97	0.07
-6.45	0.57	1.00	0.07	0.97	0.08
-6.58	0.45	0.99	0.11	0.99	0.13
-6.77	0.34	1.03	0.07	0.99	0.07
-6.95	0.55	1.02	0.12	0.96	0.13
-6.99	0.94	1.06	0.14	0.97	0.15
-7.19	0.49	1.03	0.12	0.97	0.12
-7.33	0.31	1.01	0.12	0.91	0.12
-7.53	0.38	0.99	0.11	1.00	0.13
-7.55	0.23	1.01	0.12	0.97	0.12
-7.81	0.37	1.00	0.15	1.01	0.17
-7.82	0.21	0.95	0.13	0.91	0.13
-7.90	0.20	0.87	0.11	0.97	0.13
-8.29	0.37	0.98	0.14	0.95	0.14
-8.58	0.39	0.99	0.10	1.01	0.13
-8.80	0.38	0.98	0.11	0.98	0.13

Table 7.13: Retention coefficients for 2-nitrophenol of the measurements at pH 5.6.

T / °C	ΔT /°C	$R_{G_{5.6}}$	$\Delta R_{G_{5.6}}$	$R_{B_{5.6}}$	$\Delta R_{B_{5.6}}$
-3.06	0.45	0.10	0.01	0.24	0.02
-3.36	0.50	0.11	0.01	0.24	0.01
-3.89	0.33	0.22	0.01	0.22	0.01
-3.89	0.56	0.20	0.01	0.34	0.02
-3.97	0.68	0.24	0.01	0.40	0.01
-3.98	0.33	0.20	0.01	0.21	0.01
-3.99	0.36	0.18	0.01	0.25	0.01
-4.04	0.32	0.15	0.01	0.24	0.01
-4.19	0.32	0.29	0.01	0.51	0.01
-4.25	0.27	0.25	0.00	0.55	0.01
-4.51	0.33	0.13	0.01	0.17	0.01
-4.55	0.43	0.31	0.02	0.44	0.02
-4.62	0.72	0.14	0.01	0.21	0.02
-4.85	0.25	0.15	0.01	0.24	0.02
-6.09	0.32	0.16	0.02	0.32	0.03
-6.18	0.53	0.16	0.03	0.44	0.09
-6.25	1.16	0.32	0.01	0.29	0.02
-6.44	0.61	0.25	0.01	0.54	0.03
-6.45	0.31	0.18	0.00	0.15	0.01
-7.06	0.81	0.10	0.03	0.51	0.16
-7.07	0.47	-	-	0.58	0.07
-7.08	0.28	0.17	0.03	0.32	0.06
-7.49	0.35	0.17	0.01	0.25	0.04
-7.62	0.32	0.19	0.02	0.39	0.05
-7.64	0.23	0.16	0.02	0.35	0.05
-7.64	0.28	0.19	0.03	0.36	0.04
-7.64	0.18	0.16	0.02	0.41	0.07
-7.83	0.59	0.26	0.01	0.22	0.02
-7.92	0.22	0.27	0.03	0.42	0.05
-7,94	0,51	-	-	0.60	0.08
-8.00	0.17	0.27	0.04	0.39	0.07
-8.02	0.80	0.12	0.01	0.18	0.01
-8.05	0.51	0.19	0.06	0.35	0.11
-8.06	0.61	0.23	0.07	0.45	0.14
-8.29	0.13	0.20	0.04	0.36	0.05
-8.33	0.31	0.17	0.05	0.38	0.13
-8.34	0.25	0.21	0.02	0.26	0.01

T / °C	ΔT /°C	$R_{G_{5.6}}$	$\Delta R_{G_{5.6}}$	$R_{B_{5.6}}$	$\Delta R_{B_{5.6}}$
-8.36	0.21	0.13	0.03	0.26	0.05
-8.42	0.98	0.14	0.04	0.36	0.13
-8.46	0.57	0.19	0.01	0.25	0.01
-8.51	0.00	0.16	0.03	0.29	0.07
-8.76	0.48	0.13	0.02	0.34	0.06
-8.85	0.36	0.22	0.02	0.27	0.03
-9.07	0.35	0.16	0.03	0.30	0.07
-9.07	0.20	0.15	0.03	0.23	0.01
-9.13	0.14	0.16	0.01	0.18	0.02
-9.17	0.18	0.22	0.01	0.24	0.03
-9.21	0.59	0.22	0.02	0.45	0.04
-9.26	1.05	0.17	0.05	0.16	0.05
-9.42	0.78	0.19	0.01	0.23	0.01
-9.69	0.35	0.26	0.01	0.46	0.02
-9.73	0.42	0.24	0.02	0.33	0.05
-9.74	1.47	0.11	0.02	0.26	0.06
-10.24	0.40	0.15	0.01	0.43	0.02
-10.60	0.46	0.17	0.03	0.38	0.03
-10.72	0.43	0.22	0.01	0.45	0.02
-10.80	0.75	0.22	0.01	0.41	0.04
-10.83	0.37	0.20	0.02	0.39	0.03
-10.97	0.28	0.15	0.03	0.28	0.06
-11.17	0.28	0.22	0.02	0.41	0.04
-11.20	0.41	0.21	0.01	0.51	0.03

Table 7.14: Retention coefficients for 2-nitrophenol of the measurements at pH 4.

T / °C	ΔT /°C	R_{G_4}	ΔR_{G_4}	R_{B_4}	ΔR_{B_4}
-3.88	0.50	0.03	0.01	0.18	0.03
-4.08	0.63	0.01	0.002	0.06	0.01
-4.41	0.36	0.01	0.002	0.05	0.01
-4.54	0.40	0.01	0.002	0.06	0.01
-4.56	0.59	0.01	0.002	0.05	0.01
-4.69	0.19	0.01	0.002	0.04	0.01
-4.90	0.43	0.05	0.01	0.15	0.03
-4.91	0.47	0.05	0.01	0.10	0.01
-4.94	0.55	0.06	0.01	0.13	0.03
-4.96	0.37	0.04	0.01	0.10	0.01
-5.02	0.40	0.05	0.01	0.13	0.02
-5.07	0.45	0.05	0.01	0.08	0.02
-7.05	0.15	0.12	0.01	0.18	0.01
-7.21	0.68	0.12	0.01	0.23	0.02
-7.45	0.42	0.10	0.01	0.17	0.01
-7.80	0.31	0.12	0.01	0.22	0.03
-7.83	0.87	0.15	0.01	0.34	0.04
-8.11	0.28	0.11	0.01	0.20	0.02
-8.36	0.56	0.06	0.005	0.15	0.01
-8.89	0.34	0.08	0.003	0.15	0.01
-8.96	1.14	0.14	0.004	0.27	0.01
-9.00	0.34	0.08	0.003	0.21	0.01
-9.12	0.32	0.07	0.005	0.14	0.01
-9.54	0.30	0.13	0.004	0.25	0.01
-9.55	0.26	0.06	0.002	0.12	0.00
-9.96	0.25	0.11	0.01	0.25	0.03
-10.00	0.39	0.13	0.02	0.19	0.02
-10.38	0.53	0.13	0.01	0.27	0.03
-10.65	0.39	0.09	0.003	0.21	0.01
-10.93	1.07	0.13	0.02	0.27	0.04
-11.18	0.24	0.07	0.002	0.16	0.01
-11.36	0.38	0.06	0.002	0.09	0.002
-11.41	0.26	0.05	0.003	0.10	0.002

7.2 Supplementary materials chapter 3

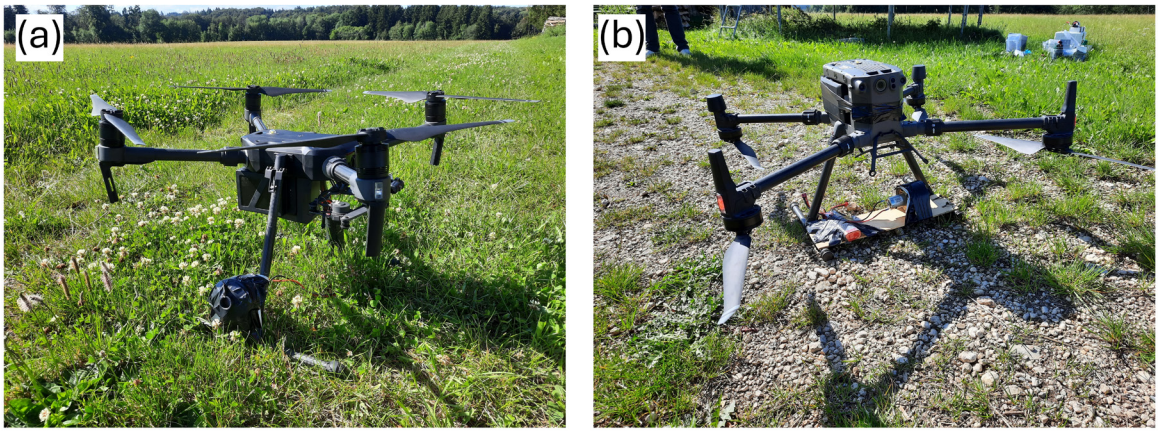

Figure 7.11: Photo of the filter holder attached to the landing gear at the drone dji m300 (a) and at plate between the landing gear of the dji m200 (b).

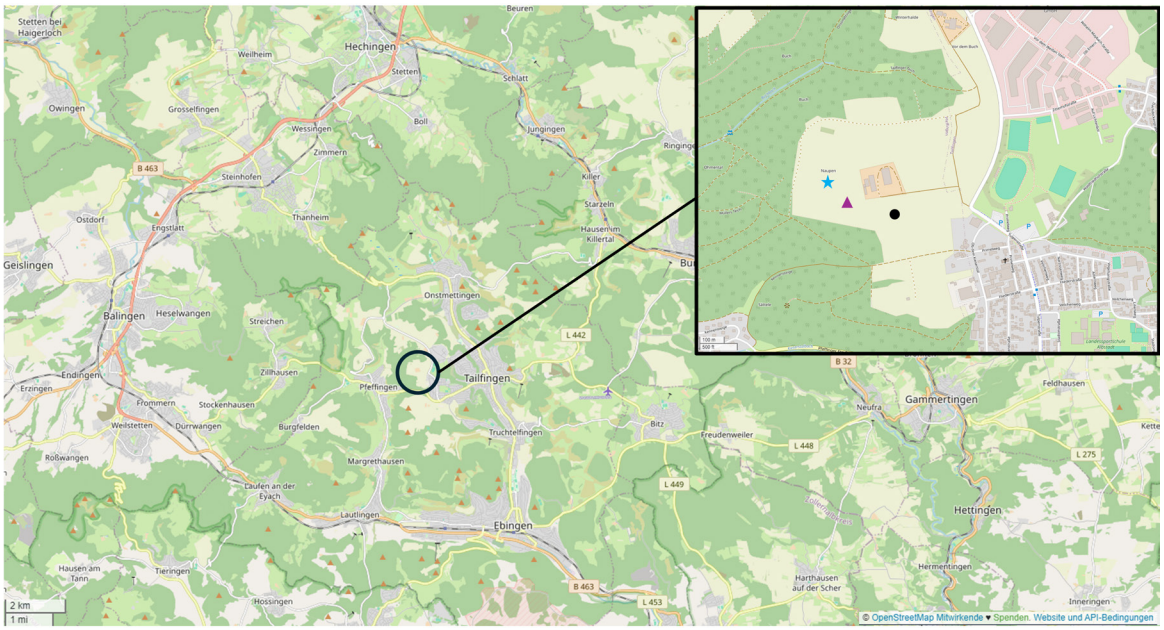

Figure 7.12: Map (© OpenStreetMap contributors) showing the measurement site (close to Albstadt, southern Germany), which is surrounded in all directions by a mixture of forest, agricultural land, and urban infrastructure. The black circle represents the measurement site, which is shown in greater detail within the black box. The symbols indicate the approximate locations for the drone measurements: a blue star (dji m300), a purple triangle (dji m200), and a black dot (FLab).

Determination of the concentration

The extraction solution was not concentrated to dryness to prevent loss of semi-volatile compounds, so the volume prior to HPLC-MS analysis is unknown. To overcome this issue, a known amount of camphor sulfonic acid was added to both the calibration solutions and the samples as internal standard. This ensured that the concentration of all solutions would correspond to 35 ng/mL of the internal standard if the samples had the targeted 50 µL volume. In order to perform the volume correction, the mean value of the signal area of the camphor sulfonic acid of all calibration solutions is calculated. Following this, the ratio of the signal area for the respective sample to this mean value is multiplied by the concentration of the analytes determined by the calibration. This allows the concentration of the analytes to be obtained as if they were dissolved in 50 µL.

As the HPLC-MS analysis only determines the concentration of the sample in the extraction solution it is necessary to determine the concentration in the aerosol (c(compound). This is achieved by first calculating the mass m(compound) on the filter according to the following equation 7.7, with V_{solution} representing the Volume and c_{solution}(compound) symbolizing the blank-corrected concentration of the compound in the extraction solution prior to the HPLC-MS measurement.

$$m(\text{compound}) = c_{\text{solution}}(\text{compound}) \cdot V_{\text{solution}} \tag{7.7}$$

The collected air volume (V_{air}) is then determined by integrating the linear equation of the fit for the flow (Q) (Equation 7.8) through the filter holder, which leads to Equation 7.9. In the following equations t is the sampling time.

$$Q = (-0.027 \pm 0.002)\ \text{L min}^{-2} \cdot t + (18.97 \pm 0.04)\ \text{L min}^{-1} \tag{7.8}$$

$$V_{\text{air}} = \frac{(-0.027 \pm 0.002)}{2}\ \text{L min}^{-2} \cdot t^2 + (18.97 \pm 0.04)\ \text{L min}^{-1} \cdot t \tag{7.9}$$

The concentration of the compound of interest can then be calculated as shown in Equation 7.10.

$$c(\text{compound}) = \frac{m(\text{compound})}{V_{\text{air}}} \tag{7.10}$$

Chemicals

Table 7.15: Chemical compounds used in this study, including their respective purities.

Compound	Label	purity
cis-pinic acid	Synthesized	N/A
terpenylic acid	Synthesized	N/A
terebic acid	Sigma Aldrich	N/A
salicylic acid	Sigma Aldrich	99%
4-hydroxybenzaldehyde	Sigma Aldrich	>97.5%
4-nitrophenol	Alfa Aesar	99%
2,6-dimethyl-4-nitrophenol	Merck KGaA	N/A
2,4-dinitrophenol	Sigma Aldrich	>98%

Table 7.16: Measured concentration of pinic acid, 4-nitrophenol, terebic acid and 2,6-dimethyl-4-nitrophenol, of the three measurement setups (no drone; dji m300; dji m200) during three measurement flights.

Flight	Drone	Pinic acid		Terebic acid		4-Nitrophenol		2,6-Dimethyl-4-nitrophenol	
		Concentration / ng m^{-3}	Error	Concentration / ng m^{-3}	Error	Concentration / ng m^{-3}	Error	Concentration / ng m^{-3}	Error
1	-	10.02	0.28	2.76	0.14	8.76	0.32	1.08	0.02
	Dji m300	7.46	0.31	2.04	0.10	6.29	0.16	0.90	0.02
	Dji m200	8.45	0.36	2.32	0.10	7.65	0.19	0.88	0.02
2	-	8.98	0.25	2.86	0.13	7.49	0.26	1.22	0.05
	Dji m300	8.96	0.35	2.71	0.13	7.45	0.20	1.25	0.03
	Dji m200	9.02	0.42	2.82	0.13	7.97	0.40	1.32	0.06
3	-	9.84	0.49	2.62	0.16	13.84	0.54	3.60	0.12
	Dji m300	10.37	0.41	3.07	0.11	14.35	0.31	3.62	0.08
	Dji m200	10.97	0.33	2.98	0.11	15.22	0.32	4.08	0.11

Table 7.17: Measured concentration of the biogenic marker compounds pinic acid, terpenylic acid and terebic acid at the different heights and times (all times are in UTC+2).

Time	Height / m	Pinic acid		Terpenylic acid		Terebic acid	
		Concentration / ng m^{-3}	Error	Concentration / ng m^{-3}	Error	Concentration / ng m^{-3}	Error
10:35 am	1.5	9.35	0.25	3.75	0.23	5.44	0.16
	120	13.71	0.44	5.18	0.34	8.61	0.28
	500	11.42	0.32	3.95	0.26	6.60	0.19
1:35 pm	1.5	17.48	0.40	6.10	0.25	10.56	0.25
	120	21.32	0.59	7.42	0.34	12.42	0.35
	500	17.87	0.42	6.97	0.27	12.31	0.29
4:30 pm	1.5	22.36	0.50	9.36	0.29	15.81	0.35
	120	25.44	0.67	11.11	0.39	19.26	0.50
	500	16.61	0.39	6.76	0.26	13.59	0.31

Table 7.18: Measured concentration of the biomass burning and anthropogenic marker compounds salicylic acid and 4-hydroxybenzaledhyde at different heights and times (all times are in UTC+2).

Time	Height / m	Salicylic acid		4-Hydroxy-benzaldehyde	
		Concentration / ng m^{-3}	Error	Concentration / ng m^{-3}	Error
10:35 am	1.5	0.09	0.43	0.50	0.30
	120	2.78	0.62	1.71	0.43
	500	0.52	0.49	0.65	0.34
1:35 pm	1.5	1.05	0.43	1.64	0.30
	120	0.00	0.58	1.12	0.40
	500	0.68	0.45	1.15	0.32
4:30 pm	1.5	1.41	0.44	1.60	0.30
	120	0.98	0.55	2.38	0.39
	500	0.32	0.43	1.18	0.30

Table 7.19: Measured concentration of the biomass burning and anthropogenic marker compounds 4-nitrophenol, 2,6-dimethyl-4- nitrophenol, and 2,4-dinitrophenol at different heights and times (all times are in UTC+2).

Time	Height / m	4-Nitrophenol		2,6-Dimethyl-4-nitrophenol		2,4-Dinitrophenol	
		Concentration / ng m^{-3}	Error	Concentration / ng m^{-3}	Error	Concentration / ng m^{-3}	Error
10:35 am	1.5	5.49	0.43	0.14	0.18	0.80	0.39
	120	8.62	0.64	0.22	0.26	1.82	0.57
	500	6.13	0.48	0.15	0.21	1.22	0.44
1:35 pm	1.5	2.58	0.41	0.13	0.18	0.38	0.39
	120	2.96	0.56	0.13	0.24	0.78	0.53
	500	2.42	0.43	0.14	0.19	0.42	0.41
4:30 pm	1.5	2.03	0.42	0.09	0.18	0.32	0.40
	120	2.51	0.53	0.12	0.23	0.42	0.50
	500	1.19	0.42	0.08	0.18	0.25	0.40

FLab

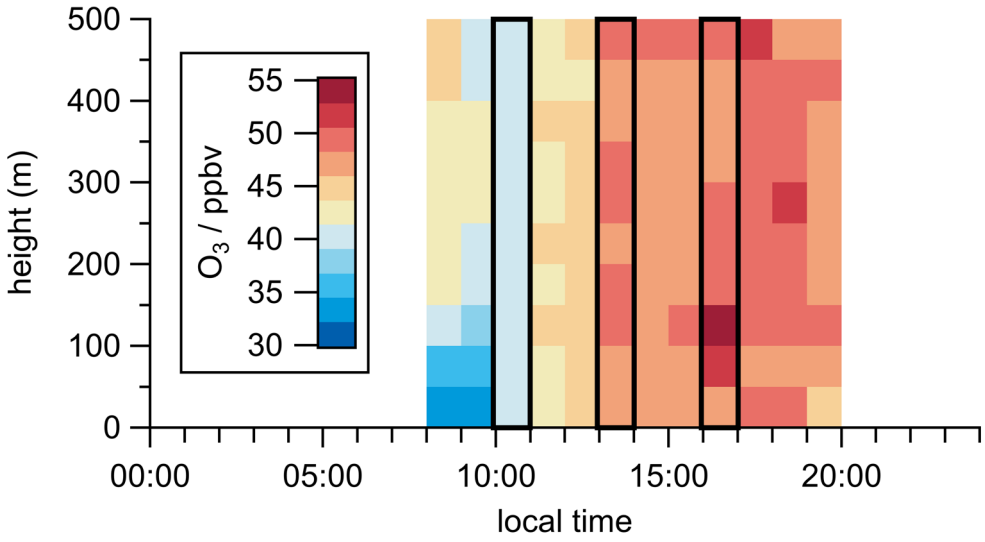

Figure 7.13: Measured ozone concentration versus time of day. The measurements were carried out hourly in an altitude range from 0 to 500 m above ground level (AGL). The black boxes indicate the time intervals during when the parallel drone flights were conducted.

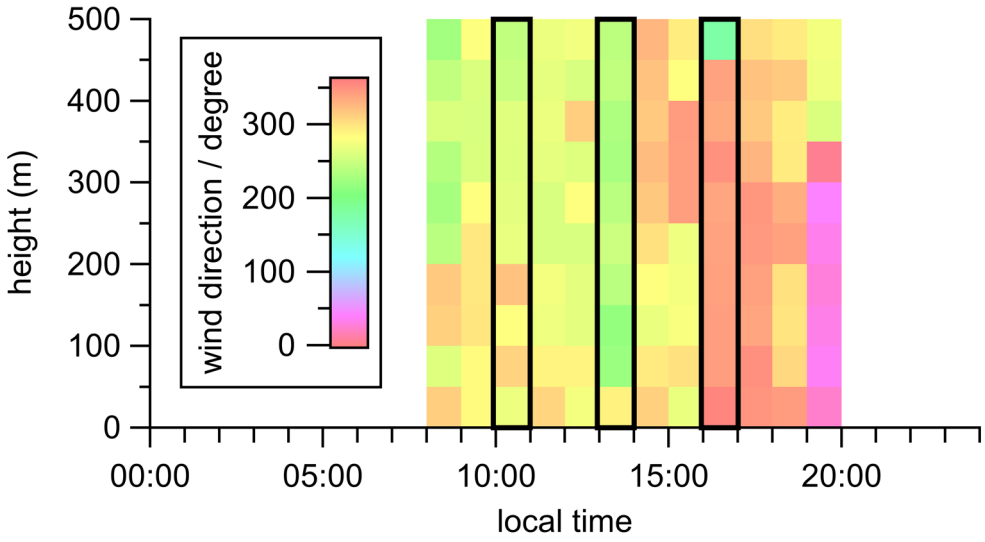

Figure 7.14: Measured wind direction versus time of day. The measurements were carried out hourly in an altitude range from 0 to 500 m. The black boxes indicate the time intervals during when the parallel drone flights were conducted.

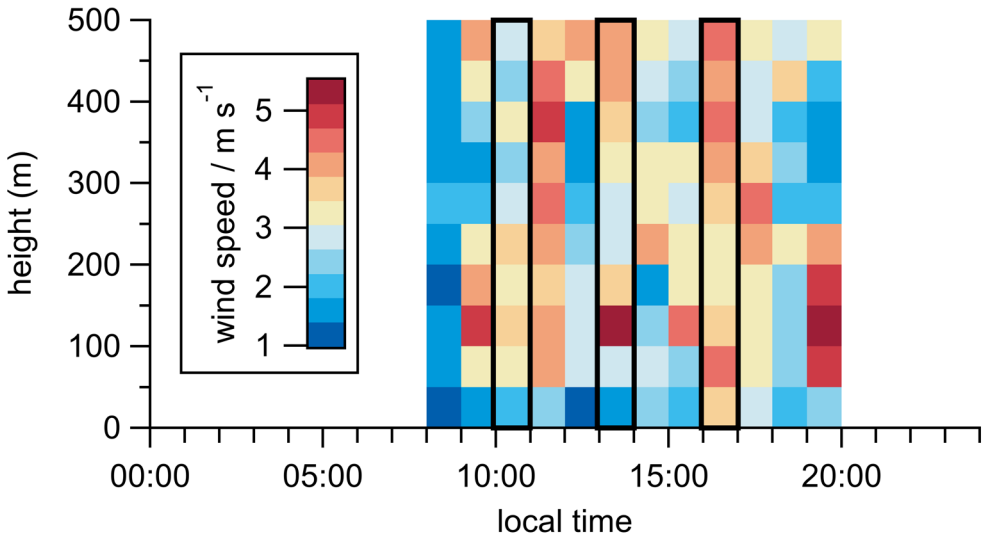

Figure 7.15: Measured wind speed versus time of day. The measurements were carried out hourly in an altitude range from 0 to 500 m. The black boxes indicate the time intervals during when the parallel drone flights were conducted.

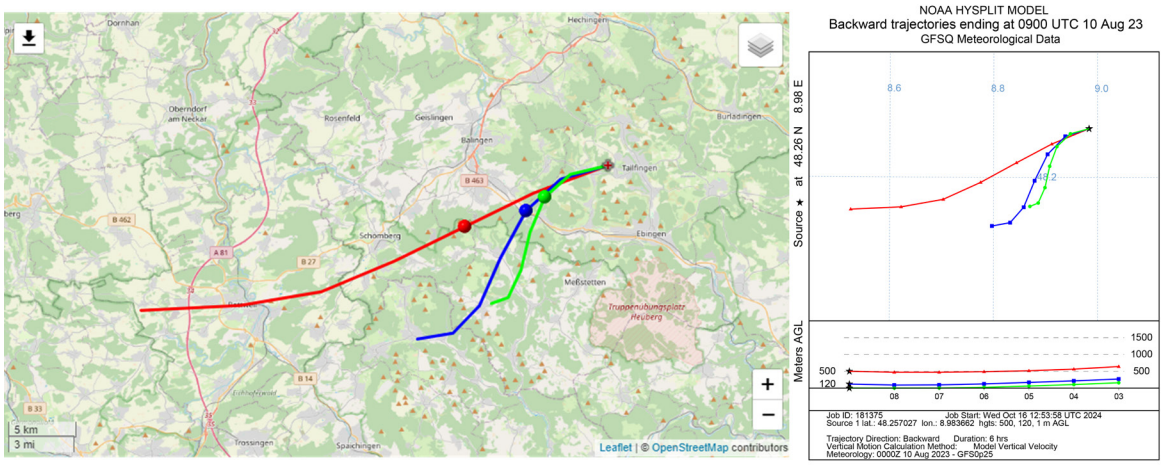

Figure 7.16: Calculated 6 hour back trajectories with HYSPLIT (Rolph et al., 2017; Stein et al., 2015; Draxler and Hess, 1998) for 1 m (green line), 120 m (blue line) and 500 m (red line) for the sampling on 10.08.2023 in the morning. The dots on the map (© OpenStreetMap contributors) indicate the time (8 am local time) at which the air mass at 120 m altitude crosses the main traffic road.

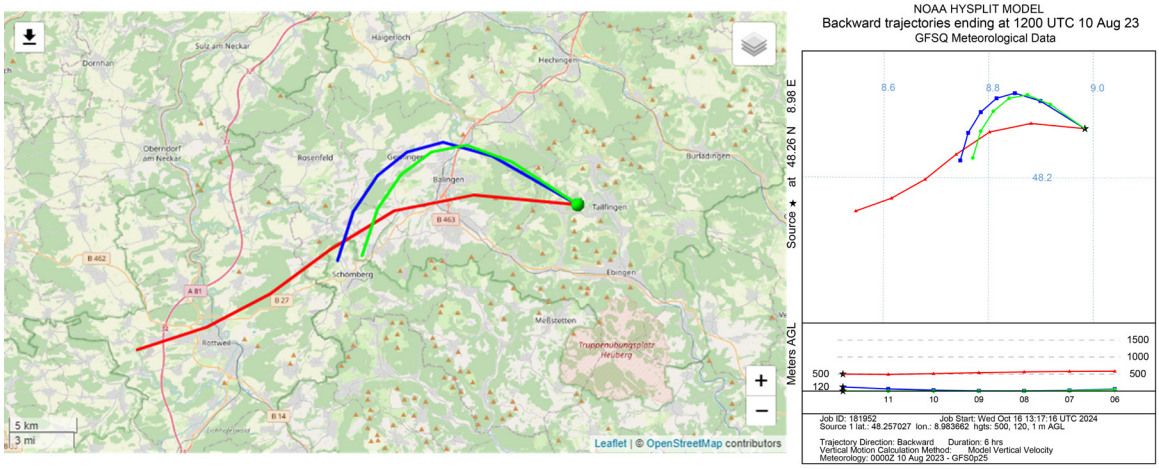

Figure 7.17: Calculated 6 hour back trajectories with HYSPLIT(Rolph et al., 2017; Stein et al., 2015; Draxler and Hess, 1998) for 1 m (green line), 120 m (blue line) and 500 m (red line) for the sampling on 10.08.2023 at noon (© OpenStreetMap contributors).

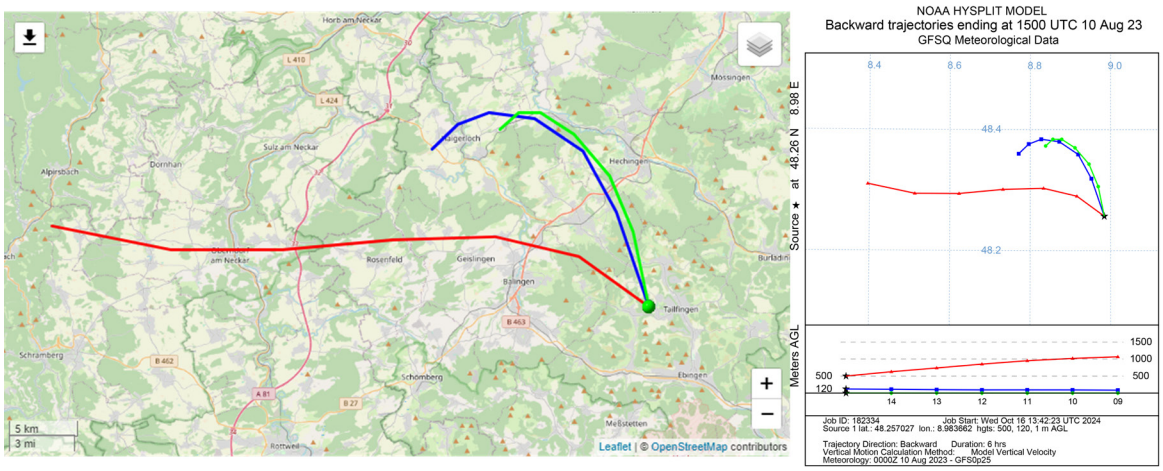

Figure 7.18: Calculated 6 hour back trajectories with HYSPLIT (Rolph et al., 2017; Stein et al., 2015; Draxler and Hess, 1998) for 1 m (green line), 120 m (blue line) and 500 m (red line) for the sampling on 10.08.2023 in the afternoon (© OpenStreetMap contributors).

7.3 Supplementary materials chapter 4

Table 7.20: List of samples with date, collection time, location, sampling flow rate and collection conditions.

Sample	Date	Sampling time / h:min	Approx. location	Flow / $L \cdot min^{-1}$	Comments
ES20C04_LowVol1	10.07.20-11.07.20	5:50	Close to Iceland	50	no cooking but possible influence by engine exhausts
ES20C04_LowVol2	12.07.20	Blank	Close to Iceland	0	Blank
ES20C04_LowVol3	12.07.20-13.07.20	22:58	Close to Iceland	50	no cooking but possible influence by engine exhausts
ES20C04_LowVol4	13.07.20-14.07.20	21:28	Close to Iceland	50	no cooking but influence by engine very likely (wind from back)
ES20C05_LowVol2	20.07.20-21.07.20	21:54	Close to Iceland	50	
ES20C05_LowVol4	22.07.20	1:33	Close to Ireland	50	
ES20C05_LowVol7	22.07.20-23.07.20	20:31	Close to Ireland	40	
ES20C05_LowVol9	24.07.20	Blank	Close to Ireland	0	Blank
ES20C06_LowVol1	07.08.20-08.08.20	21:55	Close to Ireland	50	

Sample	Date	Sampling time / h:min	Approx. location	Flow / $L \cdot min^{-1}$	Comments
ES20C06_LowVol7	09.08.20-10.08.20	9:46	Close to Ireland	50	No cooking, no engine
ES20C06_LowVol8	11.08.20	Blank	Close to Ireland	0	Blank
ES20C06_LowVol10	11.08.20-12.08.20	19:56	Close to Ireland	50	
ES20C06_LowVol12	13.08.20	10:56	Close to Azores	50	
ES20C07_LowVol2	21.08.20-22.08.20	24:05	Close to Azores	50	
ES20C07_LowVol8	24.08.20	11:33	Close to Azores	50	
ES20C08_LowVol9	20.09.20	Blank	Close to Azores	0	Blank
ES20C08_LowVol10	20.09.20	4:15	Close to Azores	50	No cooking, no engine
ES20C09_LowVol3	08.11.20-9.11.20	14:07	Close to Azores	50	
ES21C03_Emfab_blank	22.02.21	Blank	Close to Equator	0	Blank
ES21C03_Emfab	22.02.21	10:00	Close to Equator	45	No cooking, no engine
ES21C06#1	17.04.21	Blank	Close to Equator	0	Blank
ES21C06#2	17.04.21-19.04.21	19:26	Close to Equator	50	
ES21C08_LowVol4	13.05.21-14.05.21	7:21	Close to Equator	50	No cooking, no engine

Sample	Date	Sampling time / h:min	Approx. location	Flow / $L \cdot min^{-1}$	Comments
ES21C08_LowVol8	16.05.21	Blank	Close to Equator	0	Blank
ES21C08_LowVol12	19.05.21-20.05.21	23:24	Close to Equator	50	Exhaust ok, no cooking
ES21C08_LowVol16	22.05.21	Blank	Close to Equator	0	Blank

7.4 Data processing by MZmine 2.53

The software MZmine 2.53 was used for the non-targeted analysis (Pluskal et al., 2010). The following parameters were selected:

1. Mass detection: The noise level for each scan is 10,000. This means that only signals with a signal intensity of more than 10,000 are taken into account in the following steps.
2. FTMS shoulder peak filter: A Gaussian peak model function with a mass resolution of 140,000 at *m/z* 200 was used.
3. ADAP chromatogram builder: A chromatogram is created for each mass. The minimum scan number is 5, the minimum signal intensity is 50,000, and the mass tolerance is 3 ppm.
4. Chromatogram deconvolution: The chromatograms were deconvoluted using the ADAP Wavelet algorithm (S/N threshold 10, coefficient/area threshold 80, peak duration 0.01-1.00, retention time wavelet range 0.00-0.10).
5. Isotopic peak grouper: Removing isotopic peaks (mass tolerance 5 ppm, retention time tolerance 0.2 min, maximum charge of 1).
6. Complex search: Removing complexes (Ionization method $[M-H]^-$, retention time tolerance 0.1 min, mass tolerance 5 ppm, maximum complex peak height 100%.
7. Formula prediction: The formula prediction used $[M-H]^-$ ions. Sum formulas containing C, H, N, O, S, and I were allowed ($C_{0\text{-}35}$; $H_{0\text{-}80}$; $O_{0\text{-}19}$; $N_{0\text{-}15}$; $S_{0\text{-}8}$; $I_{0\text{-}5}$). Elements Counts heuristic (H/C ratio, NOPS/C ratios and multiple element counts) after Kind and Fiehn (2007). The double bond equivalents (DBE) must be an integer between 0 and 30. For the isotope pattern filter, the isotope mass tolerance was set to 5 ppm. A minimum intensity of 1,000 and a score starting at 100% and ending at 70% was used.
8. Join aligner: The peaks detected in different samples were aligned according to the mass tolerance (5 ppm) and retention time tolerance (0.2 min) (weight for *m/z*: 10; weight for RT: 10; minimum score if isotope pattern 70%).
9. Export to csv file: The aligned feature list was exported to a csv file, including the *m/z*, retention time, sum formula, peak height, and peak area. This file can be used for further analysis.

7.5 List of related publications and presentations

Accepted publication:

Borchers, C., Seymore, J., Gautam, M., Dörholt, K., Müller, Y., Arndt, A., Gömmer, L., Ungeheuer, F., Szakáll, M., Borrmann, S., Theis, A., Vogel, A. L., and Hoffmann, T.: Retention of α -pinene oxidation products and nitro-aromatic compounds during riming, Atmos. Chem. Phys., 24, 13961–13974, https://doi.org/10.5194/acp-24-13961-2024, 2024.

Submitted publication:

Borchers, C., Moormann, L., Geil, B., Karbach, N., and Hoffmann, T.: Development and use of a lightweight sampling system for height-selective drone-based measurements of organic aerosol particles, EGUsphere [preprint], https://doi.org/10.5194/egusphere-2024-4015, 2025.

Oral presentations:

05/2022

Borchers, C., Dörholt, K., Theis, A., Vogel, A. L., and Hoffmann, T.: Retention of secondary organic aerosols during riming experiments, European Geoscience Union General Assembly, Vienna, Austria, 2022, DOI: https://doi.org/10.5194/egusphere-egu22-8352.

Poster presentations:

09/2022

Borchers, C., Hrabe de Angelis, I., Pöhlker, C., and Hoffmann, T.: Understanding the sources and processing of atmospheric organic aerosols via non-target analysis, International Aerosol Conference 2022, Athens, Greece.

09/2023

Borchers, C., Karbach, N., Geil, B., Grüner, F. and Hoffmann, T.: Development of a lightweight organic aerosol collection device for drone-based sampling, European Aerosol Conference 2023, Malaga, Spain.

03/2024

Borchers, C., Geil, B., Karbach, N., Moormann, L., Fachinger, F., Drewnick, F., and Hoffmann, T.: Development and deployment of a drone-based sampling system to study altitude profiles of organic aerosols with respect to their molecular composition in the planetary boundary layer, TP-Challenges International Conference, 2024, Mainz, Germany.

7.6 Acknowledgements

7.7 Curriculum vitae